RIKEN Accelerator Progress Report

1981

vol. 15

理化学研究所
the Institute of Physical and Chemical Research

RIKEN Accelerator Progress Report
January-December 1981

理化学研究所
the Institute of Physical and Chemical Research
Wako-shi, Saitama, 351 JAPAN

Editors

This volume contains recent information of the accelerators at RIKEN (IPCR), informal reports and abstracts of papers which will be published at scientific meetings or in publications by staff members, guests, and visitors.

PREFACE

This is the fifteenth issue of the progress reports on research activities at the IPCR Cyclotron. The first beam from the cyclotron was obtained in October in 1966 and the collaborative researches started in 1967. Many important researches on nuclear physics, atomic and solid state physics, nuclear and radiation chemistry and radiation biology have been carried out in these fifteen years. The progress reports on these activities have been issued annually since 1967.

Need for a new accelerator increased in recent years at IPCR to develop researches using the cyclotron, and construction of a new heavy-ion linac started in 1974. It was finished in 1980 and beam acceleration tests are being carried out by now. At the same time the collaborative researches using the linac started and many experimental facilities and devices have been installed at the linac. Research works using the linac are in progress.

Now at IPCR the research activities using accelerators are developing in the new and wider area in the fields of science and technology. Under these circumstances we decided to issue the progress report of the IPCR Cyclotron in a new format. It contains not only the results obtained at the 160 cm cyclotron but also those at the linac and other small accelerators. This new format is to reflect the growing activities in the research fields of basic and applied nuclear science at our Institute. At the same time the name of RIKEN will be used instead of IPCR. RIKEN is a traditional abbreviation of the Institute of Physical and Chemical Research.

This volume summarized studies on nuclear physics, atomic collisions, solid state physics and material engineering, radio chemistry, radiation biology and so on in a period from January to December in 1981. There are also many reports on the developments in the accelerator technology and design study of the new separated sector cyclotron which is now under construction as the post accelerator for the linac.

I would like to acknowledge the effort of Dr. K. Mori to prepare the new format of the RIKEN Accelerator Progress Report.

Hiromichi Kamitsubo

Hiromichi Kamitsubo
Editor

CONTENTS

I. INTRODUCTION

H. Kamitsubo

Nuclear science is one of principal subjects of the research activities at the Institute of Physical and Chemical Research (Riken). Collaborative researches on physical, chemical, biological and other problems using accelerators started at Riken in 1967, when the 160 cm heavy-ion cyclotron was completed and brought into stationary operation. In the early time, most of the beam time was devoted to the studies of nuclear physics and machine development. However shares of the research fields other than nuclear physics in the beam time have gradually increased and many significant results have been obtained in these studies.

Systematic studies of heavy-ion reactions and nuclear structures of heavy nuclei are the typical examples of works in the field of nuclear physics. Charged particle activation analysis of carbon and oxygen impurities in the high purity semiconductors, production of radio-isotopes for medical uses and synthesis of physiological compounds labelled with them, radiolysis studies of inorganic and organic compounds by heavy ions and studies of radiation effects on biological materials at different LETs are also examples of pioneering works in Japan using accelerators in the fields of chemistry and biology. Simulation studies of materials for FBR and thermonuclear fusion reactors by alpha-particle irradiation and those of semiconductor devices for space satellites are the important applications of accelerators and have been promoted at the 160 cm cyclotron.

It has been recognized that energetic heavy ions play an important role to develop new areas in various research fields and there have been increasing demands for accelerators of high quality. In 1974 there started the construction of a heavy-ion linac (Rilac). It was completed in 1979 and is now in test operation. Rilac is designed to be an injector for a big separated sector cyclotron (SSC) with k = 540. The SSC project was granted in 1980 and two sector magnets will be completed in 1982. The SSC is one of the biggest heavy-ion cyclotrons now under construction in the world.

On the other hand a 200 kV ion implanter was installed in 1975 to develop modification and improvement of physical, chemical and mechanical properties of near-surface region of metals, semiconductors and insulators. In addition to this machine a tandem Van de Graaf accelerator (Tandetron) of 1 MV was also installed in 1979 for the studies of characterization of solid materials and particle-induced X-ray spectroscopy (PIXE).

Collaborative and interdisciplinary researches by use of the cyclotron, Rilac, the ion implanter and Tandetron are now in progress. Heavy ion reactions were extensively studied in 1981 as in the preceding years. Search for short-lived α-decays from high spin yrast states was newly started. Studies of atomic collisions were pursued in 1981 using the cyclotron, Rilac and Tandetron. A high resolution electron spectrometer and other measuring devices have been installed at the Rilac. Collaboration with National Research Institute for Metals on the development of metals having low swelling characteristic was continued in this period. Charged particle activation analysis was applied to study the behavior of impurity oxygen on the surfaces of high purity silicon and aluminum. Radiation-biological studies were continued for cultured cells. Brief descriptions of the cyclotron, Rilac, Tandetron and the ion implanter are given in the following.

160 cm Cyclotron

I. Kohno

The 160 cm cyclotron is of a weak focusing type and its project was authorized in 1962. The first beam was accelerated and extracted in October, 1966, and research program started in February 1967. Since that time the cyclotron has been operated for about 42000 h, and has been used for the studies in many fields of research, such as nuclear physics, atomic physics, solid state physics, nuclear chemistry, radiation chemistry, radiation biology, production of radio isotopes for medical use and nuclear fuel study. In Tables 1 and 2 the cyclotron characteristics, and kinds of ions being accelerated at present are shown, respectively.

Table 1. Cyclotron characteristics.

Acceleration system	
Number of dees	2
Dee width	180 deg.
Beam aperture	5 cm
Radio frequency	6 to 12.5 MHz
Tuned by	movable short plus movable panels
Gain max.	400 kV/turn
Dee-gnd. max.	100 kV
RF power input max.	150 kW
Magnet	
Type of Magnet	weak focusing type
Pole tip dia.	162 cm
Extraction radius	73 cm
Gap between pole tips	26 cm
Field at max. excitation	2.0 Wb/m^2
Circular triming coils	4 pairs
Weights Fe (Cu)	310 (20) tons
Magnet excitation	6×10^5 amp-turns
Power max.	400 kW
Ion source	
For light ions (H, He)	Livingston type
For heavy ions (Gas)	Electron bombarded hot cathode PIG type
For heavy ions (Solid)	Same with sputtering electrode

Table 2. Particles, energy ranges and particle yields.

Particle	Energy (MeV)	Extracted beam current (μA)
P	5 – 17	30
d	8 – 26	30
$^{3}He^{++}$	12 – 50	30
$^{4}He^{++}$	16 – 52	30
$^{6}Li^{2+}$	25 – 48	0.2
$^{7}Li^{2+}$	29 – 48	2.0
$^{7}Li^{3+}$	29 – 75	0.05
$^{9}Be^{3+}$	45	0.8
$^{10}B^{3+}$	60	0.3
$^{11}B^{3+}$	66	1.3
$^{12}C^{4+}$	55 – 100	3.0
$^{14}N^{4+}$	65 – 100	3.0
$^{14}N^{5+}$	60 – 125	1.0 (3.0)[a]
$^{16}O^{5+}$	65 – 125	1.0 (3.0)[a]
$^{19}F^{5+}$	80 – 130	0.3
$^{19}F^{6+}$	80 – 150	0.1
$^{20}Ne^{6+}$	82 – 160	0.3[a]

a) Pulsed operation.

RILAC, a Variable Frequency Heavy-Ion Linac

M. Odera

The recently completed RILAC has been designed to accelerate ions of almost all heavy elements in the periodic table. It incorporates a novel variable frequency linac scheme to realize the aim.[1] The scheme also permits a good beam transfer efficiency to the next post-stripper accelerator which is the separated sector cyclotron, by use of the same accelerating rf frequency for both machines.

The reason why the linac was chosen for acceleration of the heavy-ions stems from consideration of the state of art of the ion source technology, the loss of ions by charge exchange collisions during acceleration and the inherent large magnetic rigidity of the fast heavy ions. A large open-air high voltage terminal is used as an external injector to the linac and can house any

ion source of rather complicated and power consuming characteristics.[2] Short accelerating path and the structure which allows to attain high vacuum along the path will minimize charge changing effect by collision of accelerated particles with the residual gas. The straight line of acceleration permits to neglect the large magnetic rigidity effect except for the focusing magnets contained in the accelerating electrodes to counteract the inherent defocusing effect of acceleration in the linac. We have developed the compact and high gradient quadrupole magnets to be installed in the drift tubes (accelerating electrodes) to solve this problem.[3] In addition, the variable frequency scheme is effective to relax the requirements for focusing strength of the quadrupole magnets by use of the lower frequencies for the heavier projectiles.

The variable frequency scheme involves several technical difficulties which hitherto have delayed realization of this type. The largest problems are its cavity structure, rf source and operation by remote control, especially of the high power amplifiers in the variable frequency mode. Firstly, we have developed a suitable structure after studies by the models and calculations.[4] Then, a proty-type amplifier chain was fabricated and made to work in January 1979, though frequency range was between 17 and 35 MHz and was much lower than the final goal of 45 MHz maximum.[5] The first beam using the proto-type amplifier was obtained in that year. Incorporating some modifications found necessary by the operation of the first amplifier, other five amplifiers were ordered and fabricated in a factory including modification of the first one itself. Acceleration of beams by synchronizing a few amplifiers was made in March and the beam by the semi-automatic control of the whole six amplifiers was obtained in October 1981 at 20 MHz. In the semi-automatic control mode, starting up procedures of cavity excitation such as crossing of the multipactoring region, search of the optimum power level and choice of the relative phase difference between cavities are made mannually. After a suitable operating condition is found, the stabilizing circuit of the accelerating voltage and phase is switched in and the automatic mode operation begins. In future, most of the starting up procedures will also become automatic either.

In Table 1 some examples of energy of ions obtainable are shown.

The energy of ions can be varied in three ways. By adjusting frequency, it can be changed continuously. Also, decrease of energy by discrete steps is possible by simply switching off a few sections of the cavity chain. Lastly, energy can be changed continuously but in narrow range by adjusting the relative phase of rf of the last one or two cavities. Probably the third is the most convenient way and takes least time.

There is a relationship among frequency F, charge to mass ratio q/A and total effective acceleration voltage V expressed as $(A/q)F^2/V = \text{const}$. In the initial design, this constant is 500 when the total voltage gain is 16 MV F being given in MHz, A in atomic mass unit and q in electronic charge unit. Ions of charge states within this limit can be accelerated up to q times V MeV. If voltage holding capacity of the cavities is improved in the future, V can be increased and the energy of the large-mass ions may be increased by the same ratio. In that case, the frequency larger by a factor of the square root of the ratio of the energy must be used. Since there is an upper limit for the frequency, this does not apply to light elements for which maximum accelerating frequency is already used.

Table 1. Examples of ions and their energies.

Ion	Charge	Maximum freq.	Maximum energy
Ne- 20	4	40.3 MHz	65 MeV
Ar- 40	4	28.5	65
Ar- 40	7	37.6	114
Kr- 84	8	27.8	130
Xe-132	9	23.5	146

References

1) M. Odera: IPCR Cyclotron Progr. Rep., 4, 24 (1970); M. Odera and T. Tonuma: Proc. 6th Intern. Cyclotron Conf., (Eds. Burgerjon and A. Strathdee), Vancouver (1972); AIP Conf. Proc. No. 9, p. 283; T. Tonuma, F. Yoshida and M. Odera: IEEE NS-23, No. 2, 1031 (1976).

2) M. Hemmi and M. Odera: IPCR Cyclotron Progr. Rept., 9, 111 (1975); M. Odera: Proc. 1976, Proton Linear Accelerator Conf., (Ed. S. O. Schriber), Chalk River, AECL-5677, 62 (1976).

3) M. Odera and M. Hemmi: IPCR Cyclotorn Progr. Rep., 6, 21 (1972); Y. Miyazawa, T. Inoue, and M. Odera: ibid., 9, 113 (1975); I. Takeshita, I. Yokoyama, and M. Odera: ibid., p. 118; M. Hemmi and M. Odera: ibid., 8, 155 (1974); T. Inoue and M. Odera: ibid., p. 159; Y. Miyazawa and M. Odera: ibid., 10, 127 (1976); I. Takeshita and M. Odera: ibid., p. 129; Y. Miyazawa, T. Inoue, M. Hemmi, Y. Chiba, F. Yoshida, and M. Odera: ibid., p. 130; I. Takeshita and M. Odera: ibid., p. 132; I. Takeshita, I. Yokoyama, and M. Odera: ibid., p. 133; I. Yokoyama, I. Takeshita, and M. Odera: ibid., p. 135; I. Yokoyama: ibid., p. 138; I. Takeshita, I. Yokoyama, T. Kambara, and M. Odera: ibid., p. 140; M. Odera: Proc. 1976 Proton Linear Accelerator Conf. (1976).

4) M. Odera: IPCR Cyclotron Progr. Rep., 6, 16 (1972); M. Odera, T. Tonuma, M. Hemmi, and Y. Chiba: ibid., 7, 143 (1973); M. Odera, Y. Chiba, Y. Miyazawa, and M. Hemmi: ibid., 8, 138 (1974); M. Odera and Y. Chiba: ibid., p.139; Y. Chiba and M. Odera: ibid., p. 142; M. Odera: ibid., p. 144; Y. Miyazawa, M. Hemmi, and M. Odera: ibid., p. 146; M. Odera, Y. Chiba, M. Hemmi, T. Inoue, Y. Miyazawa, T. Tonuma, and F. Yoshida: ibid., p. 148; Y. Miyazawa and M. Odera: ibid., p. 150; Y. Miyazawa and M. Odera: ibid., p. 151; S. Takeda: ibid., p. 157; Y. Chiba: ibid., 10, 144 (1976); M. Odera: Proc. 1976 Proton Linear Accelerator Conf. (1976).

5) Y. Chiba: IPCR Cyclotron Progr. Rep., 13, 141 (1979); Y. Chiba: ibid., p. 143; M. Kase, M. Yanokura, Y. Chiba, and T. Tonuma: ibid., 14, 117 (1980); Y. Chiba: ibid., p. 120; T. Kubo and Y. Chiba: ibid., p. 123; M. Odera, Y. Chiba, and T. Kambara: Proc. 1979 Linear Accelerator Conf., (Ed. R. L. Witkover), Montauk, BNL-51134, p. 28 (1979).

Tandetron

H. Sakairi

Tandetron is, as her name suggests, a tandem type ion accelerator, a commercial product of General Ionex Corporation (GIx) in U.S.A. The first machine was supplied to the Hewlett-Packard, California, in 1979 and the second machine was introduced into Riken in Feb. 1980 and licenced to be operated by the Science and Technology Agency in Feb. 1981. Operation for test and scientific experiments started in March.

The tandem type accelerator was preferred because the ion source is held at earth potential. The scheme widens the range of selection of the type of ion sources, which is important in the sense that it can responds to the increasing demand for heavy ions in the field of material science.

The Riken Tandetron is equipped with two ion sources, a duoplasmatron and a sputter source. The former has been used mainly for helium ion production. Positive ions from duoplasmatron are changed to negative ions by passing through a lithium vapour canal. In the latter source, cesium ions are used as primary ions for sputtering to produce negative secondary ions from a solid target.

High voltage for acceleration is generated by a Cockcroft-Walton type circuit. It can be varied between 0.35 MV and 1 MV. The accelerated negative ions are changed to positive ions at the coupler of the tandem, which is a nitrogen gas canal. The ion beam is focused, after final acceleration, by a doublet of electrostatic quadrupole and inflected by $+15^{\circ}$ or $+30^{\circ}$ with an analyzing magnet, the ME value of which is 136 for the 15° port.

Specifications of beams are

H^{+}	:	1 μA at 2.0 MeV,
He^{2+}	:	0.1 μA at 3.0 MeV,
N^{3+}	:	0.5 μA at 4.0 MeV,
Si^{3+}	:	5 μA at 4.0 MeV,
Au^{3+}	:	1 μA at 4.0 MeV.

Main experimental facilities are a Rutherford back scattering (RBS) spectrometer and an ion induced X-ray spectrometer. In the scattering chamber for RBS, a three axis goniometer was installed to make the channeling RBS measurement possible. Scattered ions are energy analyzed by a silicon detecter and Elcor-Northern TN-4000 MCA system. On the downstream of that chamber, another small chamber was placed which was designed to make a quick exchange of a sample holder easy, in the RBS, measurement without channeling effects.

High resolution X-ray spectrometer with double crystals was constructed to observe chemical effect on outer shell electrons, in the peak structure of ion induced X-ray spectra. Crystals used are EDDT, RAP, LSD, Ge, and ADP, and the detecter is a proportional counter of gas flow type. The energy range of measurement covers 0.18 to 3 keV, and the resolving power is, for example, 0.8 and 2.5 eV for Al Kα and S Kα respectively, which is almost equal to the energy band width.

Current subjects of research are depth profiling of implanted ions in solid materials by RBS spectroscopy (performed by Friction and Lubrication Lab., Deformation Processing Lab., Semiconductors Lab., Inorganic Chemistry Lab., and Beam Analysis Center), identification of lattice

location of implanted ions in crystalline solids by channeling RBS spectroscopy (by Metal Physics Lab. and Beam Analysis Center) and study of chemical effect of outer shell electrons in chemical compounds by ion induced X-ray spectroscopy (by Solid-state Chemistry Lab.).

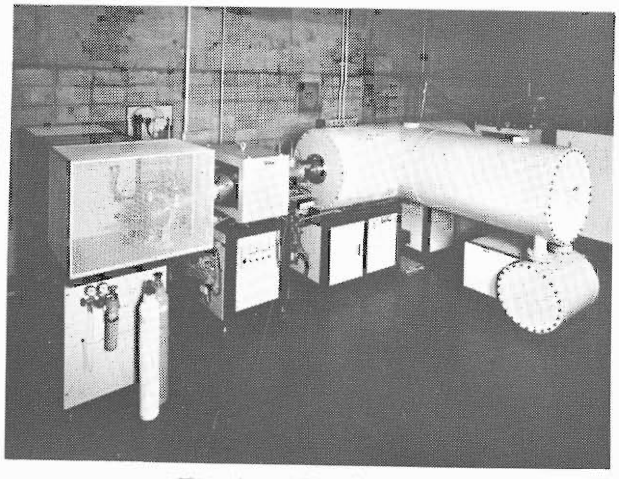

Fig. 1. Tandetron.

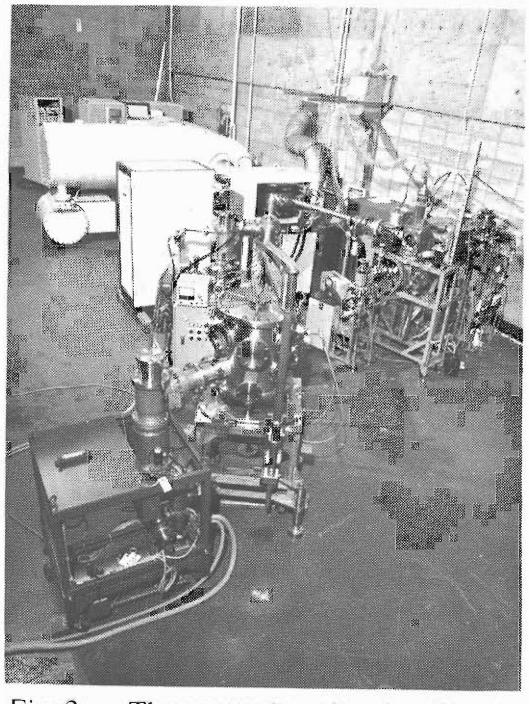

Fig. 2. The scattering chamber for the channeling RBSS (left) and the double crystal X-ray spectrometer (right).

RIKEN 200 kV Low Current Implanter

M. Iwaki

Since the mid-1960s, ion implantation has been used extensively by the semiconductor device manufacturing industry as the method of introducing controlled amounts of dopants into the surface layer of semiconductors. The principal advantages for the application include improved controllability and reproducibility for silicon device fabrication, as compared with thermal diffusion. The remarkable results of research in ion implantation into semiconductors have made an advance in ion implantation equipments (ion implanters).

In general, an ion implanter consists of an ion source, an ion acceleration system, a mass analyzer, a target chamber and a vacuum pumping system. This association can be considered as the particle accelerator combined with the isotope separator used for studies of nuclear physics, high energy physics, etc.. Therefore, an ion implanter, so called, is a kind of ion accelerator whose

acceleration voltage is defined as several tens to a few hundred kilovolts.

The ion implanter constructed in our institute at 1975, was originally planned and built for impurity doping in semiconductors by Central Research Laboratory, Hitachi Ltd. in 1970. Many parts of the present ion implanter were altered for performing modification of the near-surface region of various materials such as metals. A schematic drawing of the present apparatus is shown in Fig. 1. Ions extracted at 20 – 30 kV are focussed by a cylindrical einzel lens, accelerated at 30 – 170 kV, mass-separated by the magnet, swept by the X-Y scanner, and bombard the substrate. The full 200 kV acceleration can be used up to about mass 90. The types of components and characteristics of the implanter are presented in Table 1.

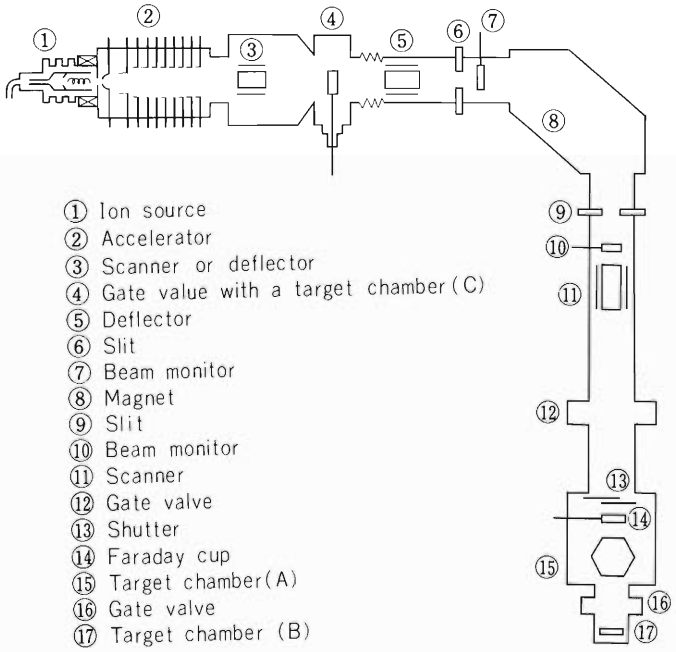

Fig. 1. Schematic drawing of RIKEN 200 kV low current implanter.

Table 1. Types and characteristics of implantation system components presented in Fig. 1.

Ion source	rf type (home-made) Nielsen type (Danfysik Model 910) hollow cathode type (Danfisik Model 911A)
Accelerator voltage	30 – 200 kV
Mass analyzer	Magnet of 90° (mass 90 at 200 kV)
X-Y scanner	~5 kHz(X), ~0.2 kHz(Y) (trianglar waves)
Beam current[a)]	~30 μA (As, Sb)
Pumping	Two sets of oil diffusion pump with rotary pump, one set of molecular pump with rotary pump
Typical pressure	~2 × 10^{-6} Torr during implantation

a) details in Table 2.

The present implanter has the advantage of installing three types of ion sources and owning three target chambers. The following is the description of these equipments.

A variety of ion sources can ionize most of the elements. The rf type ion source has been normally used for gaseous elements such as nitrogen, oxygen and argon. Recently, a new method of utilizing the ion source has been tried for producing metallic ions. For this purpose, the volatile chloride such as $TiCl_4$ or $SiCl_4$ was introduced in the discharge chamber. By using chloride, the erosion takes place at the extraction canal made of aluminum or copper, and the elements of the cathode electrode are included in the ion beams. A beam current of a few microamperes is typically obtained.

Heavy ion sources of the Nielsen and hollow cathode types can be used for the discharge of most of gaseous and metallic elements. Each of the ion sources has its own heating element to allow precise temperature control of the charge oven. The charge oven temperature can be raised up to 900 °C with the Nielsen type ion source and up to 1600 °C with the hollow cathode type ion source. Table 2 presents the typical beam current, the type of the ion sources used to get the beam and the materials inserted in their furnaces.

In this implanter there are three target chambers. Chamber A, which is placed at the normal position of the ion implanter, has six or four target holders for performing ion implantation at the ambient temperature. The target temperature rises from room temperature by the heating effect of the ion beam itself. Maximum implanted area of the sheets is 33 × 30 mm^2 (10 cm^2) for six target holders and 40 × 50 mm^2 (20 cm^2) for four target holders.

Chamber B at the backside of chamber A to the ion beam incidence is provided with one target holder for implantation at any target temperature from liquid nitrogen temperature up to about 400°C. The maximum size of a sheet mounted on the holder is 30 mm in diameter. The exchange of the specimens can be easily done because the volume of the chamber is very small.

Chamber C located between the accelerator and the magnet is also used as the gate valve. A pressure of about 2×10^{-6} Torr can be reached in the chamber by using an oil diffusion pump belonging to the original implanter after an initial pumping down to about 10^{-3} Torr by an oil rotary pump. A cylinder or a plate can be mounted on the target holder. The maximum size of the cylinder is 40 mm in diameter and 30 mm in length, and that of the plate is 30 mm in width and 20 mm in length. The ion beam is scanned in one axis with a trianglar wave voltage and the holder is moved in the perpendicular axis so that the ion beam can strike on the specimen surface uniformly; A cylinder can be rotated at 0.2 to 3.7 r.p.m. and a plate can be moved at 0.4 to 7.4 mm/min. For ion implantation without mass-separation to be carried out, the amount of the desired elements present in the ion beam must be known well. In this implanter, elements of the ion beam can be estimated by using a magnet before performing ion implantation.

The ion implanter has been used for modification of the near-surface region of semiconductors, metals and insulators. Many studies have been made of the physical, electrical, mechanical, tribological and electrochemical properties of implanted materials; depth profiles and lattice location of implanted elements, radiation damage, conductivity, hardness, wear, friction, corrosion, etc. of implanted materials.

Table 2. Typical beam current obtained by the RIKEN implanter.

Element	Current (μA)	Compound	Ion source[a]		
B	5	$B + B_2O_3$			C
C	5	CO_2, CO	A	B	C
N	20	Elem.	A	B	C
O	10	Elem.	A	B	C
Al	20	Elem., $AlCl_3$		B	C
Si	10	$SiCl_4$	A		
P	5	P_2O_5		B	
Cl	50	Chloride	A	B	C
Ar	30	Elem.	A	B	C
Ti	20	$TiCl_4$	A		
Cr	20	Elem., $CrCl_3$		B	C
Ni	20	$NiCl_2$		B	
Cu	20	Cu_2Cl_2		B	
Zn	30	Elem.		B	
Ga	10	GaI_3		B	
Ge	1	$Ge + Ge_2O_3$		B	C
As	30	Elem.		B	
Ag	1	AgCl		B	
Cd	20	Elem.		B	
In	1	Elem.		B	
Sn	1	$SnCl_4$		B	
Sb	30	Elem.		B	
Te	20	Elem.		B	
I	30	Iodide		B	
Pt	0.1	H_2PtCl_4		B	

a) A: rf type, B: Nielsen type, C: Hollow cathode type.

II. OPERATION OF ACCELERATORS

1. Machine Operation

T. Kageyama, S. Fujita, K. Ikegami, S. Kohara,
K. Ogiwara, H. Takebe, and I. Kohno

The cyclotron was operated on the 24 h a day basis during the period from Oct. 23, 1980 to Oct. 22, 1981.

Statistics of machine operation time is shown in Table 1. The total net beam time of 4098.5 h is slightly, i.e. 3.2 % (257.1 h), shorter than that of the last year. This decrease in beam time is due to scheduled shut-down.

Table 1. Machine operation.

	Oscillator	Ion-source	Beam
Reading of time meter on Oct. 23, 1980	66807.1 (h)	70893.8 (h)	37228.7 (h)
Reading of time meter on Oct. 22, 1981	71424.4	75610.8	41327.2
Difference	4617.3	4717.0	4098.5
Percentage of 365 days	52.7 %	53.9 %	46.8 %
Schedule in this period			
Beam time		226 (days)	
Overhaul and installation work		53	
Periodical inspection and repair		26	
Vacation and holidays		47	
Other scheduled shut down		13	

Table 2 shows the beam time allotted to various activities in this period. Although the scheduled beam time (5194 h) was decreased by 284 h compared with that of last year, the beam time allotted to nuclear physics groups was slightly, i.e. 18 h increased and the time to groups of fields other than nuclear physics was decreased by 302 h compared with that of last year.

Table 3 shows the distribution of the scheduled beam time among particles accelerated. In this period, the beam time of highly charged ions such as O^{5+} and Ne^{6+} was greatly increased. The heavy ions were produced and accelerated using a new improved heavy ion source[1] during this period.

Figure 1 shows the beam time of heavy and light ions over the past 7 years. Requests for heavy ion beam continued to increase and cyclotron was operated to accelerate heavy ions for more than 75 % of the total scheduled beam time over the past 4 years.

Table 2. Scheduled beam time and subjects of activity in the period XVI.

Subject		Heavy ion	Light particles	Total
Nucl. Phys.	Nuclear reaction	2722 (h)	240 (h)	2962 (h)
	In-beam spectroscopy	525	24	549
	RI production	61	28	89
Fields others than Nucl. Phys.	Nuclear chemistry	6	262	268
	Radiation biology	185	15	200
	Solid state physics	262	237	499
	Inner atomic shell excitation study	330	22	352
Outside users	Study of radiation damage	0	28	28
	Nuclear fuel study	0	82	82
	RI production	5	160	165
Total		4096	1098	5194
Percent in total		78.9 %	21.1 %	100 %
Maintenance, operation and engineering				
	Exchange of ion sources		79 (h)	
	Machine inspection and repair		624	
	Total		703	

Table 3. Distribution of beam time among particles accelerated.

Particle	(h)	(%)	Particle	(h)	(%)
P	241	4.7	N^{5+}	728	14.1
d	11	0.3	O^{5+}	450	8.8
$^{3}He^{++}$	271	5.3	$^{20}Ne^{6+}$	1316	25.5
$^{4}He^{++}$	581	11.3	$^{15}N^{4+}$ a)	4	0.1
C^{4+}	336	6.6	$^{19}F^{6+}$ a)	48	0.9
N^{4+}	1154	22.4	Total	5194	100.0

a) Newly accelerated ions.

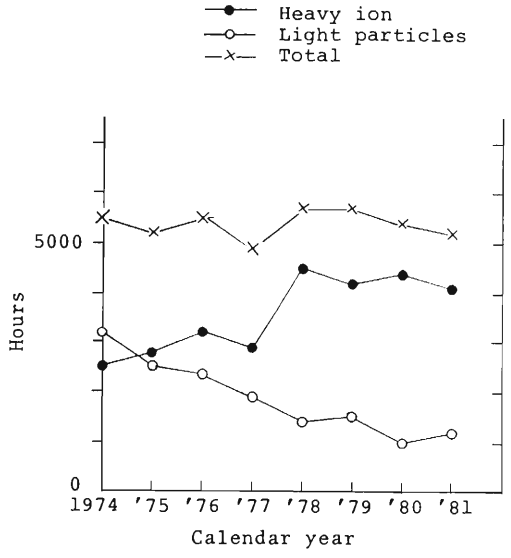

Fig. 1. The cyclotron beam time history.

Reference

1) T. Kageyama, K. Ikegami, and I. Kohno: IPCR Cyclotron Progr. Rep. 14, 4 (1980).

II-2. Operation of Heavy Ion Linear Accelerator

M. Odera

After achieving the test beam acceleration in 1980, effort has been paid to set up and tune the RF control system which is assisted by a computer for synchronized operation of the whole six amplifiers coupled with cavities. In the course of a running test of the individual cavity excitation, a serious vacuum leak and damage was generated in the driving mechanism of the shorting plate of the fourth cavity. Before completion of repair of those defects, acceleration of the singly charged nitrogen ions was tried in March 1981. The results are given in another paper in this Progress Report.[1] Energy resolution was 1.7 % at the exit of the third cavity without use of the chopper or the buncher.

In that operation some defects were found in the power supplies for the amplifiers and other small components of the accelerator such as the beam probe containers or cavity signal pick-ups. Also distribution of the probes for beam diagnosis along the beam line was found desirable to be modified. After improving those parts, acceleration through all the cavities was realized in October.

A pulse excitation method varying the width and repetition rate by a large factor during the starting-up period of the cavity excitation was found to be a convenient means to search resonance of the resonator to the given frequency and to overcome the multipactoring phenomenon. Hitherto, the method of cw excitation at a slightly detuned frequency has been used to cross the multipactoring region. The pulse excitation is also effective for degassing of the cavities at the relatively good vacuum.

In order to get quickly information of the characteristics of the beam being injected, a simple pepper-pot device was fabricated and tested. In combination with a profile monitor, it gives a rough estimation of the emittance of the beam in not complete but intuitive way. It is convenient to indicate to the operator the effect of his adjustment of the parameters of the injection beam line on the beam. A computer program for orbit analysis gives the beam trajectories expected by injection of the beam for assumed parameters of the magnetic lens system in the accelerator on the CRT at the operator console. Also another emittance device which sends digitized signals to allow direct presentation of the emittance figure on the CRT is equipped in the injection line to give a complete information of the beam if necessary. Automatic range switching multichannel current monitors were designed and installed in the control room. The monitors send analog signals of beam current on the slit blades or beam stoppers to the control console. Maximum sensitivity is 10^{-10} A. For the profile monitors which require higher sensitivity, another amplifier systems are provided.

A beam intensity attenuator using the slits with V-slots was fabricated and installed in the beam line downstream of the last cavity. It enables us to attenuate the beam current by a factor of 10^{-5} in combination with a quarupole magnet in front of it. It allows use of a very small current of small diameter for some experiments.

Though the transmission efficiency of the beam through the accelerator is to be improved

further, and the beam buncher and chopper are not working yet, use of the beam was started from November. For a while, only the elements in gaseous state will be accelerated.

In the test bench, PIG ion source equipped with a sputtering electrode is producing ions of solid elements. However, some improvements in the intensity of highly charged ions are still desirable. The first stage of the ECR ion source was completed in early summer and gave singly- and doubly-charged ions of Argon in summer. In that test an uneven spatial distribution of plasma density was found in the ionizing chamber, and the extracted current was smaller than expected. It was disassembled to find the origin and a suitable solution for the insufficient performance.

There occurred two troubles in the injector high voltage power supply. One is a damage in the high frequency transformer of the 50 kHz generator which supplies power to the Cockcroft-Walton voltage multiplier. Another is the damage of one of the rectifier stacks.

Reference

1) T. Kubo, T. Kambara, Y. Miyazawa, M. Hemmi, Y. Gono, T. Inoue, T. Tonuma, M. Kase, M. Yanokura, Y. Chiba, T. Fujisawa, and M. Odera: p. 128 in this report.

II-3. TANDETRON-Operation

H. Sakairi, E. Yagi, A. Koyama, T. Urai, and Y. Yamada

During eight months from March to October, the machine was operated for 74 days in total: 37 days for experiments and 37 days for tests. The machine time for the tests was frequently required because of initial troubles. Part of the machine time for experiments is expected to increase hereafter.

Ions of helium, carbon, nitrogen, silicon and gold were accelerated this year. Some of the conditions of operation and resulted beam intensity are shown in Table 1. For helium and silicon ions, the negative ion beam intensity and the terminal voltage were chosen to be the same for the different charge state of the ions, therefore the difference of accelerated ion beam intensity between the different charge state is considered to depend mostly on the efficiency of charge exchange.

Table 1. Operating conditions and beam intensity.

Ion	Negative Ion beam Intensity (μA)	Terminal voltage (MV)	Acceleration energy (MeV)	Beam intensity (μA)	Ratio of the number of ions
He^{+}	0.6	0.35	0.7	0.2	1
He^{2+}			1.05	0.06	0.15
He^{+}	0.8	0.5	1.0	0.5	1
He^{2+}			1.5	0.1	0.1
Si^{2+}	9	0.8	2.4	2	1
Si^{3+}			3.2	0.8	0.27
Si^{4+}			4.0	0.25	0.08
Au^{3+}	5	0.35	1.4	0.22	
Au^{4+}	5	0.5	2.5	0.18	

Troubles occured this year in the following parts: the logic circuit of the RF driver for the Cockcroft-Walton rectifier, the rectifying circuit of it, the controle circuit of Q-lens and the lithium vapour canal.

For the maintenance of the TANDETRON, Beam Analysis Center took the responsibility supported by Metal Physics Lab., Solid-state Chemistry Lab. and the Work Shop.

III. RESEARCH ACTIVITIES

1. Nuclear Physics

1. Bare Potential DWBA for (d, p) Reactions

M. Ichimura and M. Kawai

NUCLEAR REACTIONS $^{16}O(d,p)^{17}O$, $^{40}Ca(d,p)^{41}Ca$,
Bare potential DWBA, Coupled channel Calculations.

Justification of DWBA is a long standing problem. From analysis of the (p,p′) reaction, Perey and Satchler[1] claimed that DWBA was valid even when strong coupling between the entrance and the exit channels did not warrant the first order approximation to their coupled channel (CC) equations, because the distorting potentials used in the DWBA were the optical potentials and therefore they contained higher-order effects of the coupling.

Starting with the CC formalism, Ascuitto et al.,[2] however, questioned the validity of "conventional" DWBA in which the optical potentials were used for the distorting potentials in both the entrance and the exit, channels, and proposed a new type of DWBA in which the optical potential was used only in the entrance channel while in the exit channel use was made of the bare potential, the distorting potential used in the CC calculations. Such type of DWBA was called bare potential DWBA by Kubo and Hodgson[3] and was shown to work reasonably well for some heavy-ion inelastic scatterings. One can equally consider another type of bare potential DWBA in which the bare potential is used in the entrance channel and the optical potential is used in the exit channel.

A question is then in what situation the bare potential DWBA works. Since strong coupling effects between rearrangement channels have been demonstrated by several authors,[4),5] it is interesting to investigate the validity of the bare potential DWBA for the transfer reactions. Here we study this problem for the cases of $^{16}O(d,p)^{17}O(2s)$ and $^{40}Ca(d,p)^{41}Ca(2p)$ reactions, which have been studied in the previous CC analysis[5] with the finite range form factors and the non-orthogonality terms.

For the present purpose, we considered the CC cross sections of our previous results[5] as the "model" experimental data. With the criterion of best reproducing the "model" elastic cross sections, we searched partial wave (ℓ)-independent local optical potentials, U_d^{opt} and U_p^{opt}, for the deuteron and the proton respectively, which were assumed to have the same functional form of the bare potentials used in the CC calculations. The parameters for U_d^{opt} and U_p^{opt} obtained by the search are listed in Table 1 together with those for the bare potentials, U_d^{bare} and U_p^{bare}, for the deuteron and the proton respectively.

In Fig. 1 the (d,d) and (p,p) cross sections on the oxygen and calcium nuclides obtained by the bare and the searched optical potentials are compared with the CC results. The figure clearly shows the possibility of finding ℓ-independent local optical potentials with reasonable parameters, which reproduce the CC results.

Table 1. Potential parameters.

		V_0(MeV)	r_0(fm)	a(fm)	W_0(MeV)	r_0(fm)	a'(fm)	r_c(fm)
O	U_d^{bare}	118.0	0.934	0.792	5.95	1.58	0.777	1.30
	U_d^{opt}	127.1	0.872	0.831	6.43	1.734	0.661	1.30
	U_p^{bare}	49.3	1.250	0.580	11.1	1.250	0.143	1.25
	U_p^{opt}	43.8	1.276	0.566	12.2	1.365	0.293	1.25
Ca	U_d^{bare}	120.7	0.966	0.846	16.4	1.480	0.492	1.30
	U_d^{opt}	129.1	0.935	0.864	19.5	1.585	0.422	1.30
	U_p^{bare}	52.7	1.200	0.650	11.0	1.250	0.470	1.25
	U_p^{opt}	46.5	1.279	0.704	21.5	1.332	0.379	1.25

The potential form is given by

$$U(r) = V_0\left[1+\exp\left\{(r-r_0A^{1/3})/a\right\}\right]^{-1} + 4iW_0a'\frac{d}{dr}\left[1+\exp\left\{(r-r'_0A^{1/3})/a'\right\}\right]^{-1} + U_c(r),$$

where $U_c(r)$ is the Coulomb potential due to a uniformaly charged sphere of radious $r_cA^{1/3}$.

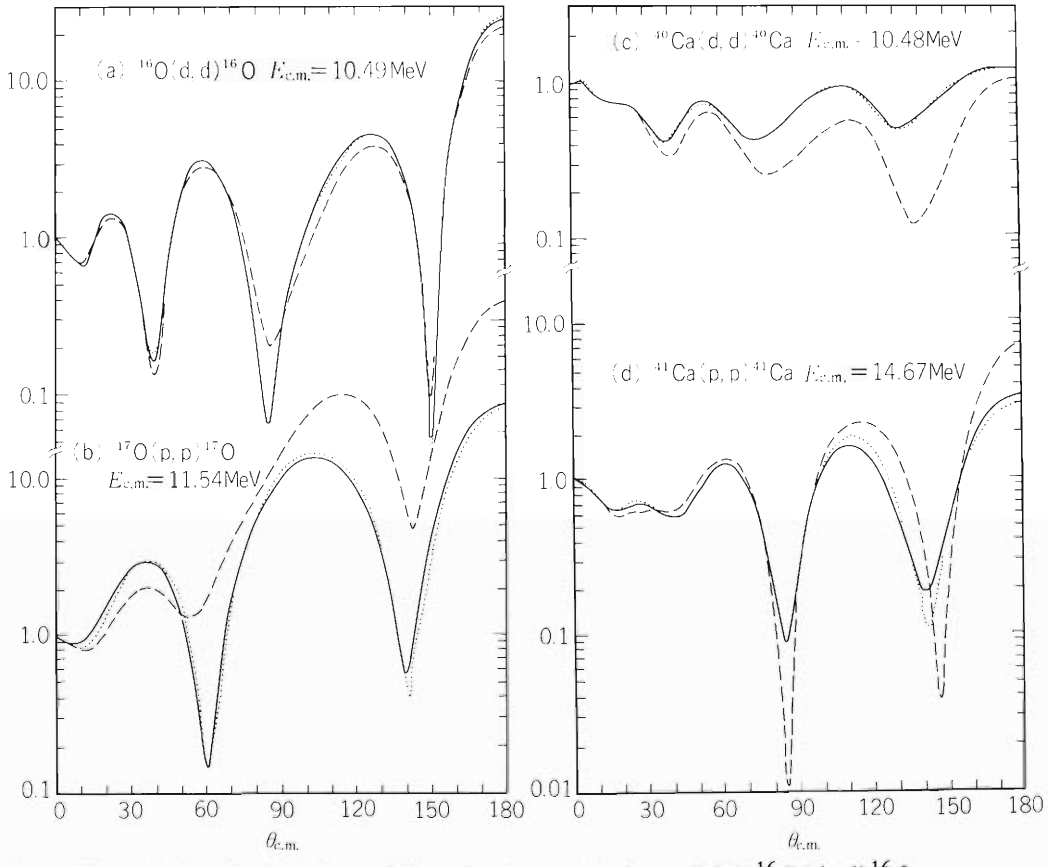

Fig. 1. The Rutherford ratios of the elastic scattering of (a) $^{16}O(d,d)^{16}O$, (b) $^{17}O(2s)(p,p)^{17}O(2s)$, (c) $^{40}Ca(d,d)^{40}Ca$ and (d) $^{41}Ca(2p)(p,p)^{41}Ca(2p)$. The results obtained by the bare potentials (dashed curves) and the searched optical potentials (dotted curves) are compared with the CC results (solid curves).

We then performed four types of DWBA calculations of the (d,p) cross sections in which the distorting potentials were (i) (U_d^{bare}, U_p^{bare}), (ii) (U_d^{opt}, U_p^{opt}), (iii) (U_d^{opt}, U_p^{bare}) and (iv) (U_d^{bare}, U_p^{opt}), respectively. The type (i) corresponds to the first order Born approximation in the CC formalism, the type (ii) to the "conventional" DWBA and the type (iii) and (iv) correspond to two different types of the bare potential DWBA in which the bare potential is used in the channel p and d, respectively.

The results of the four types of DWBA are compared with each other in Fig 2. From the figure one sees that none of the DWBA's reproduces the "model" (d,p) cross sections well. Comparison between Fig. 1 and Fig. 2 shows that the searched ℓ-independent local optical potentials may reproduce the asymptotic behavior of the distorted waves of the CC calculation but they are inadequate for including the channel coupling effects on the (d,p) cross sections. The CC effects associated with the transfer process in light-ion reactions seem to bring about stronger non-locality or ℓ-dependence for the effective potentials which well reproduce the distorted waves of the CC calculation even in the inner region as well as the asymptotic one. The above results are in sharp contrast to the case of the heavy-ion inelastic processes.

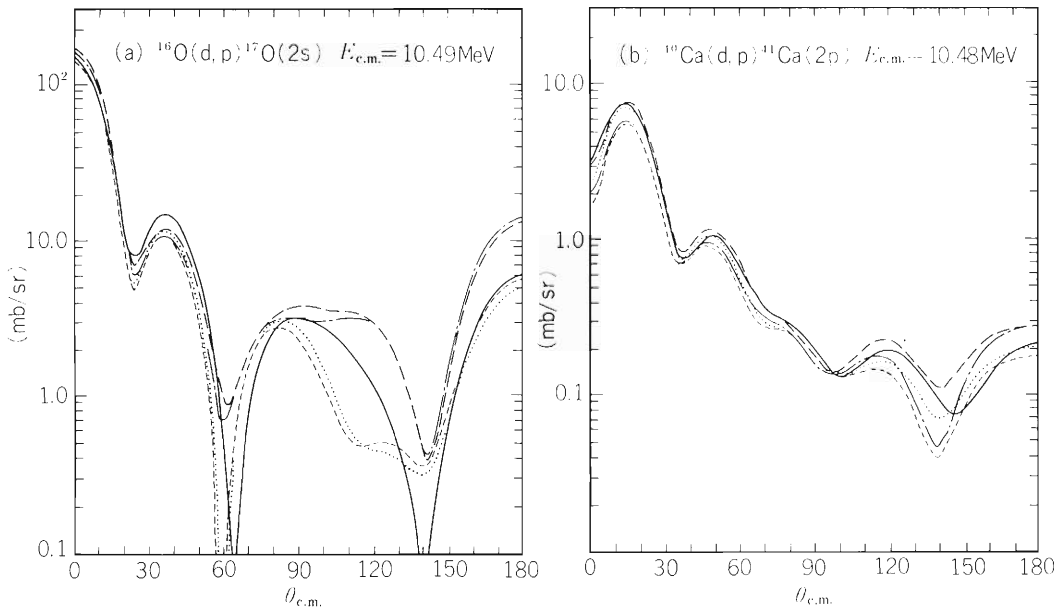

Fig. 2. The (d, p) cross sections of (a) ^{16}O(d, p) ^{17}O(2s) with Q-Value Q = 1.046 MeV and (b) ^{40}Ca(d, p)^{41}Ca(2p) with Q = 4.19 MeV. The CC results are shown by solid curves. The results of the four different types of DWBA are compared. The type (i) is denoted by (——), the type (ii) by (----), the type (iii) by (·····) and the type (iv) by (— · —).

References

1) F. Perey and G.R. Satchler: Phys. Lett., 5, 212 (1963).
2) R.J. Ascuitto, J.F. Petersen, and E.A. Seglic: Phys. Rev. Lett., 41, 1159 (1978).
3) K.-I. Kubo and P.E. Hodgson: Nucl. Phys., A366, 320 (1981).
4) T. Ohmura, B. Imanishi, M. Ichimura, and M. Kawai: Prog. Theor. Phys., 41, 391 (1969); 43, 347 (1970); 44, 1242 (1970); R.S. Mackintosh: Phys. Lett., 44B, 437 (1973).
5) B. Imanishi, M. Ichimura, and M. Kawai: Phys. Lett., 52B, 267 (1974).

III-1-2. Mass Diffusion Coefficients in the Adiabatic Approximation

S. Yamaji, A. Iwamoto,* K. Harada,* and S. Yoshida

[NUCLEAR REACTIONS Microscopic calculation of mass diffusion coefficients, linear response theory, two-center shell model.]

During the past several years, relaxation phenomena in deep inelastic collisions (DIC) have been extensively studied both experimentally[1] and theoretically.[2] The mass transfer in DIC is described on the basis of a non-perturbative statistical treatment which leads to the Fokker-Planck equation for the mass number of projectile-like nucleus A_1.[3)-7)] The diffusion coefficient D_A in the equation is one of the important quantities for this treatment.

Experimentally, the value of D_A has been obtained by the use of the relation $D_A = \chi(\theta)^2/[16\ \ln 2\ \tau_{int}(\theta)]$ with the interaction time estimated on the basis of classical models.[3), 4)] The width $\chi(\theta)$ is obtained from the experimental mass distribution at the deflection angle θ, by assuming the distribution to be gaussian.

Theoretical calculations on D_A have been performed by serveral authors[3)-6)] in the sudden or frozen density approximation. In these treatment, aside from the formation of a neck or window, the two fragments essentially remain spherical. However, the fragments separate with the kinetic energy less than the Coulomb energy of two touching spheres. This suggests the formation of large deformation and the use of adiabatic basis is required for the description of the mass fragmentation.

Therefore, in the present work, we calculate D_A microscopically using the linear response theory,[7)] which is formulated for an adiabatic basis. By neglecting the coupling between mass transfer motion and other motions such as radial and deforming motions, the same type of the Fokker-Planck equation as that in Refs. 3 and 4 is used under the condition of the overdamped motion for the mass transfer, which has been justified numerically for the $^{63}Cu + ^{197}Au$ reaction.[8)] The diffusion coefficient in this formalism is expressed as

$$D_A = T/\gamma_A . \tag{1}$$

Here, T stands for the temperature. The friction coefficient γ_A corresponding to the mass transfer motion is expressed in terms of eigenfunctions $|i>$ with eigenvalues e_i in the two-center potential V by

$$\gamma_A = 4\hbar\Gamma\sum \frac{(e_i - e_j)\left|<i\left|\frac{\partial V}{\partial A_1}\right|j>\right|^2}{\left\{(e_i - e_j)^2 + \Gamma^2\right\}^2} \times \left[\frac{1}{1+\exp\left\{(e_j-\lambda)/T\right\}} - \frac{1}{1+\exp\left\{(e_i-\lambda)/T\right\}}\right]. \tag{2}$$

* Japan Atomic Energy Research Institute.

The two-center potential V depends on the distance between centers of masses of two nuclei R, deformation of two nuclei $\delta(\delta = \delta_1 = \delta_2)$, neck parameter ε and mass number A_1 and A_2, and its specification is given in Ref. 9. The chemical potential λ is determined by the conservation of the total number of nucleons. The smearing width Γ is introduced to take into account the finite width of the energy levels.

The calculations are performed for the reactions $^{20}Ne + ^{27}Al$ at 120 MeV, $^{16}O + ^{58}Ni$ at 92 MeV, $^{32}S + ^{50}Ti$ at 131 and 166 MeV, $^{40}Ar + ^{109}Ag$ at 288 MeV, $^{40}Ar + ^{197}Au$ at 288 and 340 MeV, $^{40}Ar + ^{232}Th$ at 279 and 388 MeV, $^{63}Cu + ^{197}Au$ at 365 and 443 MeV, $^{84}Kr + ^{165}Ho$ at 714 MeV, $^{86}Kr + ^{197}Au$ at 620 MeV, $^{84}Kr + ^{209}Bi$ at 714 MeV and $^{136}Xe + ^{209}Bi$ at 1130 MeV. For the estimation of the temperature T, we use the relation[3)]

$$T = 3.46\sqrt{E^*/A} \quad , \tag{3}$$

where the intrinsic energy E* is assumed to be the difference between the incident energy and measured average kinetic energy of DIC products.[1)] The dependence of the diffusion coefficient per unit temperature D_A/T on the parameters A_1, T and Γ are examined and the results show that it does not depend much. In the further calculation, therefore, A_1 is fixed to be the projectile mass number, T to be the average of temperatures determined by Eqn. (3) in the cases of more than two different incident energies and Γ to be 0.4 $\hbar\omega_0$ ($\hbar\omega_0 = 41\ A^{-1/3}$ MeV).

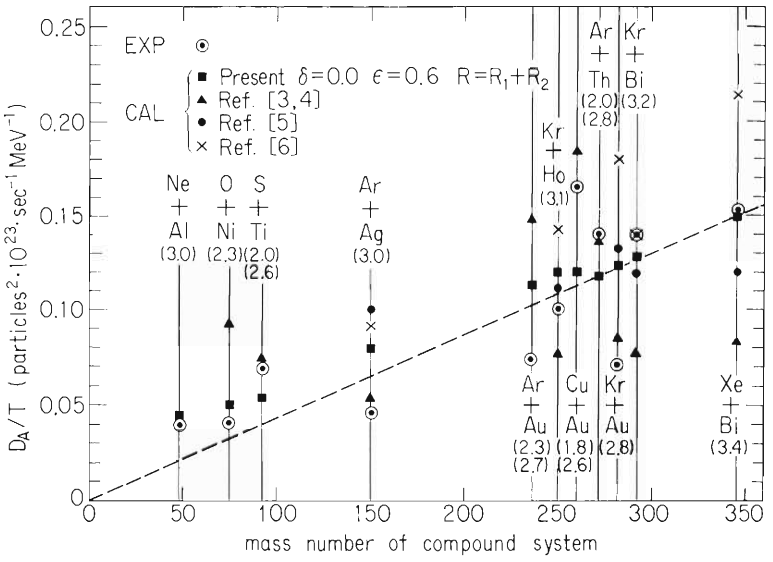

Fig. 1. Comparison between experimental and calculated mass diffusion coefficients per unit temperature. The present calculated results and experimental ones[3), 4), 11)] are shown by the points ■ and ⊙. The other points ▲, ● and × show the calculated results taken from Refs. 3 and 4, Refs. 5 and 6, respectively. The values of temperature estimated from Eqn. (3) are written in the parentheses in units of MeV. The average values are taken in the cases when more than two different values exist for both experimental and calculated results.[3), 4)] The values calculated at S = 0.5 are taken from Ref. 6.

The dependence of D_A/T on the parameters δ, R and ε are also examined and the results show that it is strong. The smooth increase in D_A/T is found with the increase of δ, the decrease of R and the decrease of ε. This trend is consistent with the physical intuition that the mass transfer occurs more rapidly under the situation of deeper penetration of two nuclei and larger neck-radius. The calculation is found to give a rough magnitude of the experimental result.

Since the calculated values of D_A/T depend strongly on R, we have to fix the value of R in order to compare the calculated results with the experimental ones. For that purpose, we assume that the mass transfer occurs while two nuclei form a rotating composite system at $R = R_1 + R_2$ ($R_i = 1.18\ A_i^{1/3}$ fm) in the same way as in Ref. 4. A comparison at $R = R_1 + R_2$ shows that the values of $\varepsilon = 0.6$ and 0.8 seem to give overall good fits to the experimental results for the cases of $\delta = 0.0$ and 0.2, respectively. The latter value of δ is the average of the deformations which are obtained at the distances of the closest approach in the calculation for the 120 MeV $^{20}Ne + {}^{28}Si$ reaction.[10]

In Fig. 1, the present calculated results are compared with both the experimental ones[3), 4), 11)] and the other calculated ones.[3)-6)] A dashed line is drawn between the origin and our calculated value for the reaction $^{136}Xe + {}^{209}Bi$ to help to see the trend that both the calculated and experimental values of D_A/T increase with the mass number of the compound system A. Agreements between our calculated and experimental results are satisfactory in view of the uncertainty of experimental results which comes from the uncertainty in the determination of the interaction time. It should also be noted that our calculation based on the adiabatic approximation and other ones[3)-6)] based on the sudden approximation give rather similar results.

References

1) M. Lefort and C. Ngô: Ann. Phys., 3, 5 (1978).
2) H.A. Weidenmüller: Progr. in Particle and Nucl. Phys., 3, 49 (1980).
3) S. Ayik, B. Schürman, and W. Nörenberg: Z. Physik, A279, 145 (1976).
4) G. Wolschin and W. Nörenberg: ibid., A284, 209 (1978).
5) C.M. Ko, G.F. Bertsch, and D. Cha: Phys. Lett., 77B, 174 (1978).
6) M. Prakash, S. Shlomo, V.S. Ramamurthy, S.S. Kapoor, and S.K. Kataria: ibid., 98B, 413 (1981).
7) H. Hofmann and P.J. Siemens: Nucl. Phys., A275, 464 (1977).
8) S. Yamaji, A. Iwamoto, K. Harada, and S. Yoshida: Proc. Intern. Conf. on Nucl. Phys., Berkeley (1980).
9) K. Sato, A. Iwamoto, K. Harada, S. Yamaji, and S. Yoshida: Z. Physik, A288, 383 (1978).
10) K. Sato, S. Yamaji, K. Harada, and S. Yoshida: ibid., A290, 149 (1979).
11) S. Yamaji: IPCR Cyclotron Progr. Rep., 13, 42 (1979).

III-1-3. Non Perturbation Effect on the Nucleon Transfer Amplitudes in Close Contact Heavy-Ion Collisions

N. Takigawa, T. Uchiyama,* and K. Sato

NUCLEAR REACTION DIC, nucleon transfer amplitude non perturbation effect, Green's function.

In deep inelastic heavy ion collisions (DIC) the scattering nuclei come in close contact with each other for a long period. Accordingly, the amplitudes of single nucleon transfer, which govern the mass transport coefficients, cannot be estimated by the lowest order perturbation treatment.[1),2)] In order to go beyond the lowest order perturbation approximation we introduce the single particle Green's function $G(t, t_0)$ that describes the time evolution of a nucleon in the unified mean field created by the scattering nuclei. The matrix element of $G(t, t_0)$ with respect to the i-th and j-th single particle states of the scattering nucleus A, Φ_{Ai} and Φ_{Aj}, is given by

$$G_{AjAi}(t,t_0) = \sum_{\alpha} <\Phi_{Aj}|\chi_\alpha><\chi_\alpha|\Phi_{Ai}> \exp\left\{-iE_\alpha(t-t_0)/\hbar + ie_{Aj}t/\hbar - ie_{Ai}t_0/\hbar\right\}$$

$$\simeq \delta_{ij}\sum_{\alpha}<\Phi_{Ai}|\chi_\alpha><\chi_\alpha|\Phi_{Ai}> \exp\left\{-i(E_\alpha - e_{Ai})(t-t_0)/\hbar\right\}, \qquad (1)$$

where $|\chi_\alpha>$ is the α-th single particle bound state of the combined system, E_α is the corresponding eigenenergy, and e_{Ai} is the energy of the single particle state $|\Phi_{Ai}>$. We use all the bound states of the colliding nuclei A and B, i.e. $\{|\Phi_{Ai}>\}$ and $\{|\Phi_{Bk}>\}$, as the working space and deal with the scattering in the static approximation. Namely, we disregard the change of the relative distance between the colliding nuclei during the period when the nucleon transfer takes place. The transition amplitude t_{ki} for the transfer of a nucleon from $|\Phi_{Ai}>$ to $|\Phi_{Bk}>$ is then given by

$$t_{ki}(t) \simeq (1/i\hbar)\int_{t_0}^{t} ds \left\{\sum_j <\psi_{Bk}(s)|U_A(\underset{\sim}{r} - \underset{\sim}{R}_A(s))|\psi_{Aj}(s)> G_{AjAi}(s,t_0)\right.$$

$$\left. + \sum_l <\psi_{Bk}(s)|U_A(\underset{\sim}{r} - \underset{\sim}{R}_A(s))|\psi_{Bl}(s)> G_{BlAi}(s,t_0)\right\}, \qquad (2)$$

where U_A is the single particle potential of the fragment A, and $\psi_{Aj}(s) = \Phi_{Aj} \times \exp\{-e_{Aj}t/\hbar\}$ etc. The lowest order perturbation approximation for t_{ki} corresponds to putting $G_{ji}(s-t_0) \equiv G_{AjAi}(s,t_0) \simeq \delta_{ji}$ and $G_{BlAi}(s,t_0) \simeq 0$ in Eqn. (2). In the following we study the behavior of the Green's function $G_{ii}(t)$ by considering one dimentional scattering problem. We assume the Woods-Saxon potential for each separated fragment and choose 50 MeV, 1.2 $A^{1/3}$ fm (A being the mass) and 0.65 fm to be the values of depth, range and diffuseness parameters, respectively. The separation distance between the centers of the scattering nuclei, R, is chosen so as to correspond to the distance of closest approach for typical partial waves of DIC.

In Fig. 1 we consider a symmetric system, i.e. $A_1 = A_2 = 90$. The left and the right of Fig. 1 (a) show the single particle energy spectrum of each separated fragment. The middle shows the energy spectrum for the unified system when R = 12.0 fm. Each of the energy levels can be distinguished by the number of nodes of the corresponding level of the separated fragment and the parity. The thick bar at −27.8 MeV represents the height of the potential barrier V_B between the scattering nuclei. Figure 1 (b) shows the absolute values of the diagonal matrix elements of the corresponding Green's function as functions of time. Roughly speaking, each of $|G_{ii}(t-t_0)|$ behaves like $|\cos\omega_i(t-t_0)|$. The frequency can be easily estimated by two level approximation, i.e. by keeping only the parity doublets χ_{i+} and χ_{i-} that correspond to Φ_{Ai} in the sum over α in Eqn. (1). In this approximation,

* Department of Physics, Tohoku University.

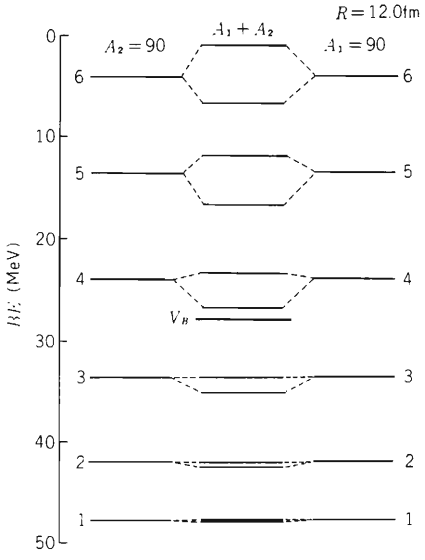

Fig. 1 (a). Energy spectra for separated fragments and for the unified system. Symmetric system.

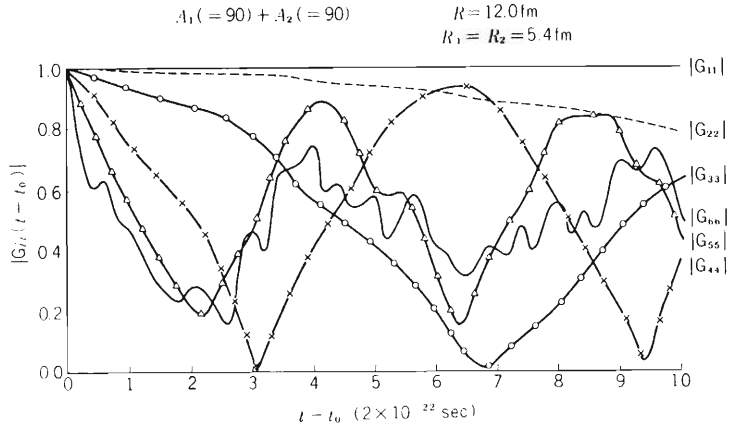

Fig. 1 (b). Matrix elements of the single particle Green's function as functions of time.

$$\left|G_{ji}(t-t_0)\right| \simeq \delta_{ji}\left|\cos\left\{(1/2)\,\Delta E_i\,(t-t_0)/\hbar\right\}\right| \qquad (3)$$

$$\text{and}\quad \left|G_{BlAi}(t-t_0)\right| \simeq \delta_{li}\left|\sin\left\{(1/2)\,\Delta E_i\,(t-t_0)/\hbar\right\}\right|,$$

where ΔE_i is the energy splitting between the parity doublets. This and Fig. 1 (a) explain the feature of Fig. 1 (b) that the frequency of $|G_{ii}(t)|$ becomes larger as the energy of the single particle state Φ_{Ai} becomes higher. The remarkable point is that the matrix elements of the Green's function with respect to high lying states, which dominantly contribute to the mass transport, show a few oscillations within the typical reaction time ($\simeq 2 \times 10^{-21}$ sec) of DIC. This clearly shows the importance of non perturbation effect in close contact heavy ion collisions. The energy difference between any parity doublets becomes smaller for larger separation distance R. This leads to less oscillations in the matrix elements of the Green's function. Accordingly, the use of the lowest order perturbation treatment becomes more justifiable. Our calculation shows that only $|G_{66}|$ has an oscillation within the time interval of 2×10^{-21} sec when R = 15 fm.

Figure 2 shows the energy spectra and the matrix elements of the Green's function for a very asymmetric system, i.e. $A_1 = 40$ and $A_2 = 232$. The separation distance R has been chosen to be 12.6 fm. Only the matrix elements with respect to 8 single particle states of the heavy fragment B ($A_2 = 232$) are shown. Their time dependence is more complicated than that for the symmetric system. This reflects the lower regularity in the level sequence. Without question, however, Fig. 2 again shows the necessity of taking the Green's function into account when we estimate the nucleon transfer amplitudes for DIC. A difference from the case of symmetric system is that the non-diagonal matrix elements of the Green's function have to be properly taken into account for the scattering of very asymmetric nuclei.

In this report we have demonstrated the importance of non perturbation effect on the nucleon transfer amplitudes in close contact collisions. The mass transport coefficients will be characteristically influenced if the non perturbation effect on each single nucleon transfer amplitude adds up coherently. Such coherent process is expected to be important in close contact collisions of, especially, identical and nearly identical nuclei. This is because, in such collisions there is an intimate correspondence between the energy spectra of the scattering nuclei. As one of such examples, we compare in Fig. 3 the single particle energy spectra of ^{92}Zr and ^{98}Mo in the actual 3 dimensional case calculated for the single particle potential given by Eqns. (2.181) and (2.182) of Ref. 3.

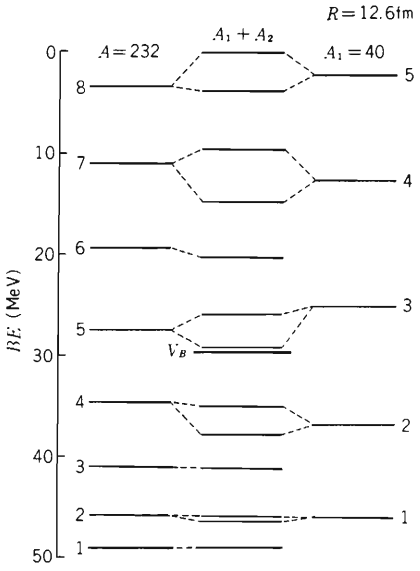

Fig. 2 (a). The same as Fig. 1 (a). Asymmetric system.

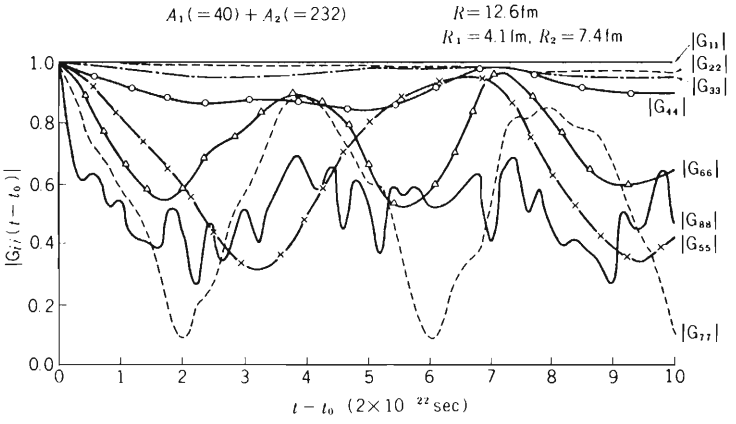

Fig. 2 (b). Matrix elements of the single particle Green's function as functions of time. Only the matrix elements with respect to 8 single particle states of the heavy fragment B (A_2 = 232) are shown.

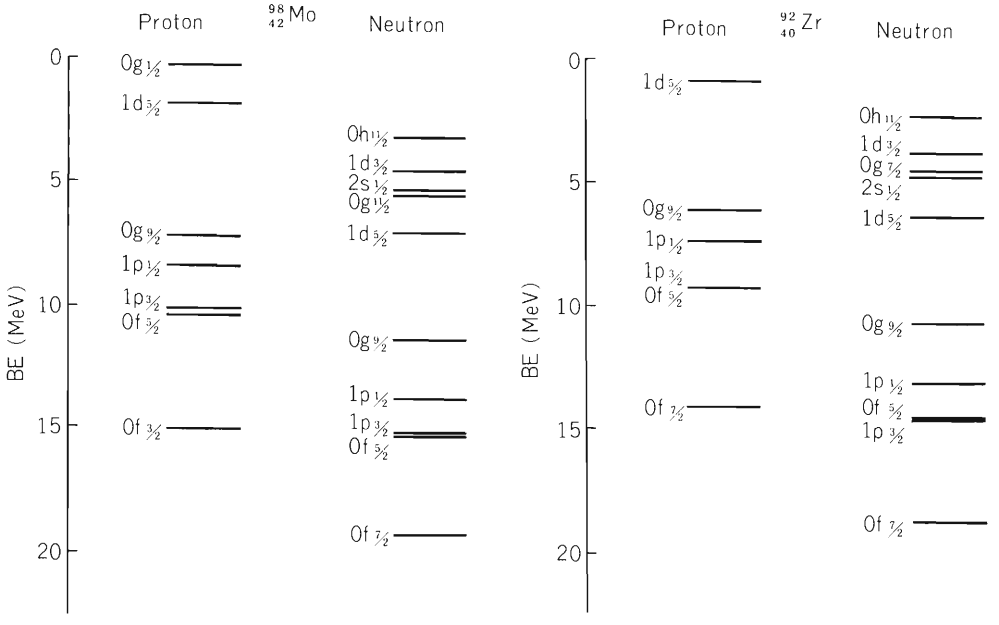

Fig. 3. Comparison of the single particle energy levels of ^{92}Zr and ^{98}Mo.

References

1) K. Sato, N. Takigawa, and S. Yoshida: Soryushiron Kenkyu (Kyoto), 63, C-38 (1981).
2) D.H.E. Gross and K.M. Hartmann: Preprint HMI (1981).
3) A. Bohr and B.M. Mottelson: Nuclear Structure, New York, Amsterdam, Benjamin, 1, 239 (1969).

III-1-4. Full Finite-Range CCBA Analysis of the ^{22}Ne (p, t) ^{20}Ne Reaction

T. Takemasa

NUCLEAR REACTION ^{22}Ne(p, t)^{20}Ne, E = 39.8 MeV; ground state rotational band, finite-range, zero-range, CCBA.

Exact finite-range (EFR) coupled-channel Born approximation (CCBA) calculation for the reaction ^{22}Ne(p, t)^{20}Ne at E_p = 39.8 MeV to the 0^+, 2^+, and 4^+ states of the ground-state (g.s.) rotational band has been carried out. The analysis of this reaction has already been attempted by Olsen et al.[1] and by King et al.[2] within the framework of zero-range (ZR) CCBA, who showed that the effects of indirect transitions via inelastic processes are of importance in this reaction. No physical justification, however, has been given to the ZR assumption. The purpose of the present work is to investigate the finite-range effects in performing EFR calculation for this reaction.

The spectroscopic amplitude was taken from the work of Olsen et al.[1], where they adopted the adiabatic assumption for the rotational wave function of the g.s. members, and the internal wave functions were constructed from Nilsson-BCS model. The interaction responsible for the two-neutron transfer process was assumed to be a finite-range, central, spin-dependent force between the proton and the two individual neutrons. The triton wave function used in this calculation was obtained by a variational calculation. The depth of bound-state potential was chosen to give each bound neutron half of the two-neutron separation energy using a Woods-Saxon well with standard geometry (r_0 = 1.25 fm, a_0 = 0.65 fm). The inelastic matrix elements used were obtained on the basis of macroscopic rotational model. The calculation included $0^+ - 2^+$ inelastic coupling in the incident channel and $0^+ - 2^+ - 4^+$ inelastic coupling in the exit channel. The nuclear deformation parameters β_2 and β_4 for neon isotopes were taken from an analysis of proton scattering.[3] For comparison, the ZR-CCBA calculation was also carried out by using the Gaussian triton wave function. The parameters used in the ZR-CCBA calculation were the same as those used in the EFR-CCBA calculation.

The results of the EFR-CCBA and ZR-CCBA calculations are shown in Fig. 1 together with the data of Olsen et al. The single normalization constant was chosen to give the best visual overall fit for the 0^+, 2^+, and 4^+ curves. The magnitude of the experimental cross section is about a factor of 2 larger than that calculated in the EFR-CCBA. It is evident from Fig. 1 that the EFR-CCBA calculations give a good reproduction of the experimental relative strengths of the three transitions.

A comparison with the ZR-CCBA calculations shows that the finite-range effect improved agreement with experiment in the shapes of angular distributions of the 0^+ and 4^+ transitions. However, the agreement between the 2^+ curve and the experimental data is rather poor. In order to find out the reason for the discrepancy between the experimental cross section and the CCBA prediction for the 2^+ transition, we investigated the dependence of the cross section on reasonable variations of deformation and optical-model parameters. It was found that such variations in deformation and optical-model parameters result in non-negligible changes in the shape of the

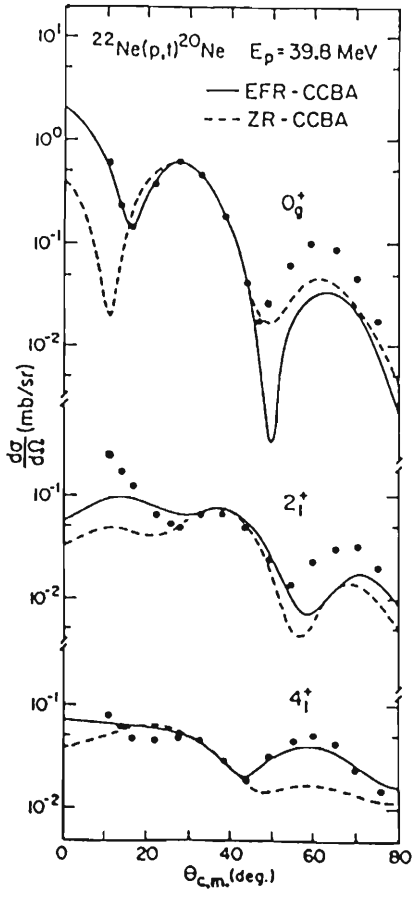

Fig. 1. Comparison of EFR-CCBA (solid lines) and ZR-CCBA (dashed lines) calculations with the data[1] for the differential cross sections to the 0^+ (g.s.), 2^+ (1.63 MeV), and 4^+ (4.25 MeV) states of ^{20}Ne.

angular distribution, but some differences between the theory and experiment for the 2^+ transition still remained. The result points out that other higher-order reaction mechanisms such as successive transfer processes not included in the CCBA calculation could account for some of the remaining discrepancies.

References

1) D.K. Olsen, T. Udagawa, T. Tamura, and R.E. Brown: Phys. Rev. C, 8, 609 (1973).
2) C.H. King, M.A.M. Shahabuddin, and B.H. Wildenthal: Nucl. Phys., A270, 399 (1976).
3) R. de Swinarski, A.D. Baher, F.G. Resmini, G.R. Plattner, D.L. Herndrie, and J. Raynal: Phys. Rev. Lett., 28, 1139 (1972).

III-1-5. Extended Brink Model and Its Derivation from Distorted Wave Born Approximation

A. Ichimura, M. Ichimura, and S. Yamaji

[NUCLEAR REACTIONS Cluster transfer reaction, matching conditions.]

The optimum particle transfer in heavy-ion reactions has been treated by Brink using a classical model.[1] The method can be extended to cluster transfer with general mass as shown by Ichimura et al.[2] This schematic model predicts the optimum excitation energy and spin of the residual nucleus. However, it does not give the strength distribution of the cross section and the validity of the model is not warranted.

In the present work we derive the extended Brink model from the formalism of DWBA (distorted wave Born approximation) which is a completely quantum mechanical one. It enables us to clarify the origin of the matching conditions and to estimate the width of the distribution as well as the optimum conditions. In the following we summarize the logic of the derivation. It is similar to that shown by Gross,[3] but he derived only the optimum conditions for light particle transfer.

We start from the DWBA transition amplitudes for the cluster transfer reaction,

$$T_{\beta\alpha}(\mathbf{k}_\beta, \mathbf{k}_\alpha) = \int \chi_\beta^{(-)*}(\mathbf{k}_\beta) F_{\beta\alpha} \chi_\alpha^{(+)}(\mathbf{k}_\alpha), \qquad (1)$$

where $F_{\beta\alpha}$ is a nonlocal form factor determined by the clustering bound-state wave functions and by the coupling interaction. First we express the distorted wave $\chi^{(+)}$ and $\chi^{(-)}$ according to the geometrical optics approximation (three-dimensional WKB approximation). They are constructed by the set of classical trajectries with incident momenta $\mathbf{k}_\alpha$ and $\mathbf{k}_\beta$, respectively. It should be noted here that an arbitrary point is passed in general by many classical trajectries and that the wave function is a superposition of many components. We further make an approximation, however, to take only one component with the largest impact parameter. Because the flux of the other components is absorbed more rapidly, this procedure is reasonable particularly when the transition occurs near the point of closest approach for the grazing trajectory.

The absolute value $|\chi_\beta^{(-)*} F_{\beta\alpha} \chi_\alpha^{(+)}|$ of the integrand has a maximum when the transferred cluster is placed between the other two clusters in the reaction plane. It is the very configuration to be expected when the transition is assumed to occur in the schematic model.[1), 2)] Then we expand the exponent of the integrand around this configuration and approximate it by a six-dimensional complex quadratic form.

Thus the integral (1) is reduced to a product of six Gauss integrals and finally we obtain the approximate expression for the transition probability

$$\left| T_{\beta\alpha} \right|^2 = \exp \left\{ - \sum_{\mu=1}^{6} (A_{\mu\nu} \cdot \Delta P_{\mu})^2 \right\} . \qquad (2)$$

Here $A_{\mu\nu}$ denotes a real regular transformation and ΔP_{μ} transferred momenta between three clusters by the transition. The expression (2) has a maximum when

$$\Delta P_{\mu} = 0 \qquad (\mu = 1, \ldots, 6) , \qquad (3)$$

namely when each cluster takes no recoil. The conditions (3) are nothing but the optimum matching conditions of the extended Brink model. The width of the distribution can be also estimated from the expression (2).

References

1) D. M. Brink: Phys. Lett., 40B, 37 (1972).
2) M. Ichimura, E. Takada, T. Yamaya, and K. Nagatani: ibid., 101B, 31 (1981).
3) D.H.E. Gross: ibid., 43B, 371 (1973).

III-1-6. Angular Distribution of Reaction Products in Preequilibrium Process

M. Takahashi,* Y. Nagame, K. Sueki,* H. Nakahara, and I. Kohno

NUCLEAR REACTIONS $^{59}Co(^{3}He, n)$; cross section, recoil range, angular distribution, preequilibrium model.

The preequilibrium process in light-particle-induced reactions has been successfully explained by the exciton model originally proposed by Griffin.[1] However, the model is restricted to the explanation of energy spectra and cross sections of emitted particles. Only recently, the model has been extended to include the angular behavior of the preequilibrium process by Weidenmüller and his collaborators,[2] and also by Akkermans et al.[3] The new model has been tested for angular distributions of neutrons emitted in such reactions as (n, n'), (p, n), and (α, n). But since the number of data available is still scant, it is necessary to accumulate more data in order to check the validity of the model.

In this work, angular distributions of the residual nuclei produced in the $^{59}Co(^{3}He, n)^{61}Cu$ reaction at the incident energies of 17.5 MeV and 30 MeV were investigated in order to study the angular behavior in pre-equilibrium reaction process. Excitation functions and mean recoil ranges projected onto the beam direction were also measured to aid the understanding of preequilibrium process. A similar work was carried out by Fujiwara and Porile[4] for the reaction system of $^{64}Cu(^{3}He, n)^{66}Ga$; they varied the incident energy from 16.9 MeV to 31.9 MeV, and covered the angular range of 0° to 42°, but the detection angles were taken at only in coarse steps.

Excitation functions and recoil ranges were measured by the stacked-foil technique. Self-supporting target foils 4–8 mg/cm^2 thick prepared by an electrodeposition method were used. The recoil catchers consisted of 0.0025 cm thick aluminum foils of high purity (99.997 %). The target stack was constructed by inserting 8–12 target foils in between aluminum catcher foils as well as appropriate aluminum energy degrading foils. The range-energy relation for ^{3}He reported by Williamson et al.[5] was used to determine the bombarding energy at each target position in the stack. Irradiations were performed at the cyclotron with the initial beam energies of 40 MeV and 27 MeV. The beam current was ~1.2 μA.

After the bombardment, the reaction products recoiled into the catcher foil were chemically separated and their activities were determined by measurement of γ-rays with a 40 cc Ge(Li) detector. The γ-rays from products

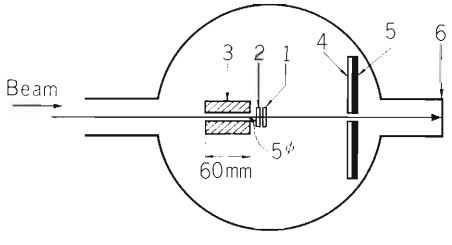

Fig. 1. Schematic diagram of irradiation arrangement used in the angular distribution study.
1. Target, 2. flux monitor, 3. carbon collimator, 4. aluminum catcher foil, 5. catcher foil backing, 6. Faraday cup.

* Faculty of Science, Tokyo Metropolitan University.

remaining in the target foil could be directly measured without chemical separation. The experiments on the angular distribution studies were carried out in a scattering chamber by using the target and the catcher foil arrangement depicted in Fig. 1. A 30 $\mu g/cm^2$ thick ^{59}Co target of 99.99 % was prepared by vacuum deposition onto a 4.5 mg/cm^2 thick aluminum foil of 99.997 % purity. The catcher foil used was of the same quality as the one used in the stacked-foil experiments. Irradiations were performed at the ^3He energy of 17.5 and 30 MeV with the beam current of 0.3 to 0.5 μA. The beam was collimated by a 5 cm long cylindrical carbon block with a 5 mm ϕ hole which was placed at 2.5 cm upstream from the target. The distance between the target and the catcher foil was varied from 15 cm to 62 cm depending on the angular range to be measured. The angular resolution obtained with this setup was typically about 1° in the angular range of 0° to 15°, and about 3° in the 15° to 40°. The activity of ^{61}Cu recoiled into each ring was determined by the γ-ray spectrometry after proper chemical separation and purification.

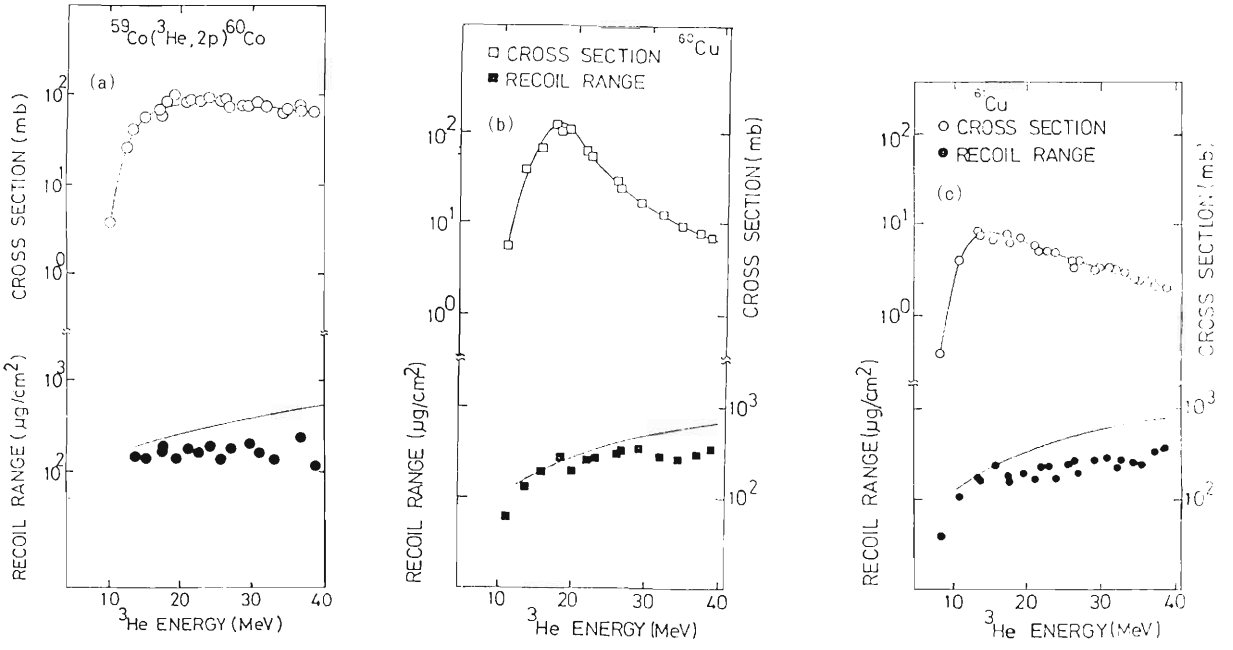

Fig. 2. Excitation functions and projected mean recoil ranges of residual nuclei. (a), (b), and (c) show those of (^3He, 2p), (^3He, 2n), and (^3He, n) reactions, respectively.

In Fig. 2 are shown the excitation functions and projected recoil ranges of residual nuclei produced by the (^3He, 2p), (^3He, n), and (^3He, 2n) reactions. It was found that the energy dependence of the ratio between the observed σ (^3He, n) and the total reaction cross section (calculated by the optical model) could be well explained by the hybrid model[1] if the initial exciton number of four was assumed. The ratio of the observed projected mean recoil ranges to those expected by the compound nucleus formation followed by evaporation are plotted in Fig. 3 as a function of bombarding energy for three kinds of reaction. The energy-range conversion was performed by the prescription of Lindhard et al.[6] The ratio for the (^3He, n) reaction fall in between those for the (^3He, 2n) and (^3He, 2p) reactions. This trend is consistent with the expectation that the (^3He, 2n) reaction would be compound-like and that the most of the (^3He, 2p) reaction would be accounted for by the one-neutron stripping process. The contribution from the direct reaction (two proton stripping) to the total (^3He, n) reaction cross section was estimated to be less than 10 % from the published work[7] on the (^3He, n) direct reactions.

Angular distributions of the $^{59}Co(^3He, n)$ reaction products obtained at the energies of 17.5 MeV and 30 MeV are given in Fig. 4. The solid lines are calculated curves with the assumption of isotropic neutron emission from the compound nucleus in the center of mass system, and the dashed lines are the results of the preequilibrium calculations for $n = n_0$ where n_0 stands for the initial exciton number. The vertical lines "excite" and "ground" show the kinematically allowed maximum laboratory angles when emitted neutron energies are assumed to be

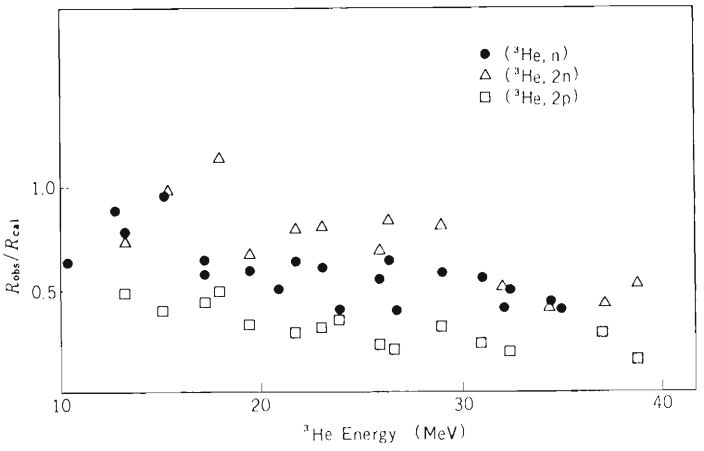

Fig. 3. The ratios of the observed projected mean ranges to those expected by compound nucleus formation followed by evaporation.

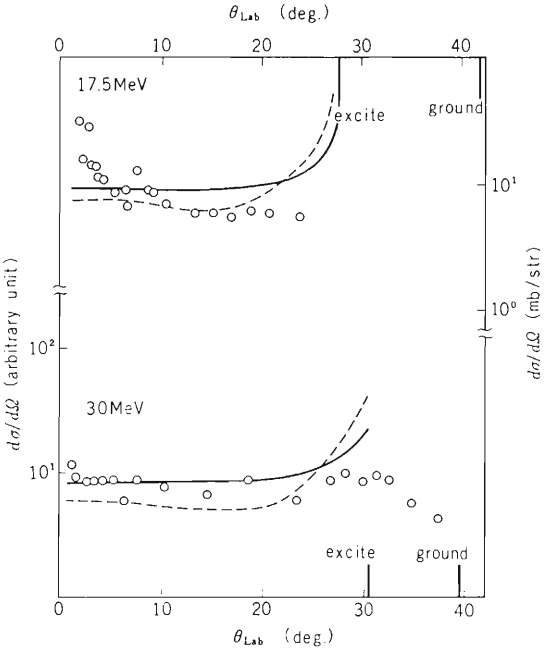

Fig. 4. Angular distributions of ^{59}Co(^{3}He, n) reaction product obtained at the incident energies of 17.5 MeV and 30 MeV.

($Q_{gg} + E_i - B_n$) and ($Q_{gg} + E_i$), respectively. E_i and B_n are the incident energy and the neutron binding energy of ^{61}Cu. According to Akkermans et al.,[3] the angular distribution of emitted neutrons from the $n = n_0$ state in the center of mass system can be expressed by

$$d\sigma/d\Omega \propto 1/4\pi \left\{ P_0(\cos\theta) + 2P_1(\cos\theta) + 5/4\, P_2(\cos\theta) \right\} ,$$

where $P_\ell(\cos\theta)$ is the Legendre function of the ℓth order. The observed differential cross sections in larger angles that contribute to most of the total cross section are, however, less than those calculated. This discrepancy indicates that neutron emissions in the (^{3}He, n) reaction are more forward peaking in the center of mass system than expected from the preequilibrium model proposed by Akkermans et al.[3]

References

1) J.J. Griffin: Phys. Lett., 24B, 5 (1967).
2) G. Mantzouranis, D. Agassi, and H.A. Weidenmüller: ibid., 57B, 220 (1975).
3) J.M. Akkermans and H. Gruppelaar: Phys. Rev., C 22, 73 (1980).
4) I. Fujiwara and N.T. Porile: Phys. Rev., 173, 1055 (1968).
5) C.M. Williamson, J.P. Boujot, and J. Picard: Saclay Report CER-R, 3042 (1966).
6) J. Lindhard, M. Scharff, and H.E. Schiott: Mat. Fys. Medd. Dan. Vid. Selk., 33, No. 14 (1963).
7) M.B. Greenfield and C.R. Bingham: Phys. Rev. C, 6, 1756 (1972).

III-1-7. Strongly Damped Components in the Reaction of $^{20}Ne + {}^{50}Cr$ and $^{20}Ne + {}^{54}Cr$ Systems

Y. Nagame, I. Kohno, H. Nakahara, H. Kudo*,
K. Sueki,* M. Takahashi,* and M. Yanokura

NUCLEAR REACTIONS $^{20}Ne + {}^{50}Cr$, $^{20}Ne + {}^{54}Cr$, strongly damped component, bombarding energy dependence, target isotope dependence, rotating liquid drop model, diffusion model.

The reactions of $^{20}Ne + {}^{50}Cr$ and $^{20}Ne + {}^{54}Cr$ systems were investigated. The strongly damped components, especially, symmetric mass fragmentation products were analyzed in terms of the diffusion model[1] as well as the rotating liquid drop model[2] for fission. The interpretation was performed from the following two systematic features: i) bombarding energy dependence (angular momentum effect); ii) target isotope dependence. The systems studied in this work, the conditions for compound nucleus formation and its decay by fission are summerized in Table 1.

Table 1. Summary of the conditions for compound nucleus formation and its decay by fission.

Reaction	Compound nucleus	Fissility (Z^2/A)	E_L (MeV)	E_X^{CN} [a] (MeV)	ℓ_{crit} [b] (h)	$\ell_{Bf=Bn}$ [c] (h)	Bf at ℓ_{crit} (MeV)
$^{20}Ne + {}^{50}Cr$	^{70}Se	16.5	146	108.6	53	44	5.0
		16.5	120	90.0	47	44	10.3
		16.5	93	70.7	40	44	19.0
$^{20}Ne + {}^{54}Cr$	^{74}Se	15.6	146	114.8	55	50	7.0

a) compound nucleus excitation energies.
b) Ref. 3.
c) $\ell_{Bf=Bn}$ characterises the ℓ value at which the fission barrier Bf coincides with neutron binding energy.

The details of the experimental procedure have already been reported in a previous report.[4]

The trends of the energy spectra and angular distributions obtained in the 120 MeV $^{20}Ne + {}^{50}Cr$ and 146 MeV $^{20}Ne + {}^{54}Cr$ systems are similar to those observed for the 146 MeV $^{20}Ne + {}^{50}Cr$ reaction.[4]

The charge distributions of the target isotope and bombarding energy dependence are shown in Figs. 1 and 2, respectively.

As shown in Fig. 1, there are difference in the cross sections of the strongly damped products between the 146 MeV $^{20}Ne + {}^{50}Cr$ reaction and 146 MeV $^{20}Ne + {}^{54}Cr$ reaction. The yields for

* Faculty of Science, Tokyo Metropolitan University.

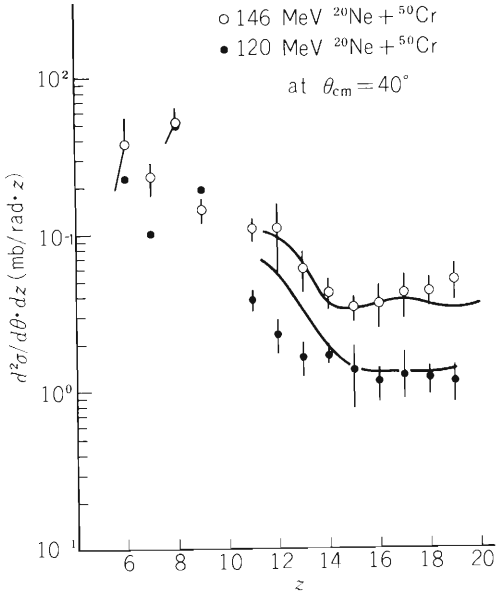

Fig. 1. Charge distributions at two reaction system. These cross sections are integrated over an angular range from 30° to 60° in the center-of-mass system.

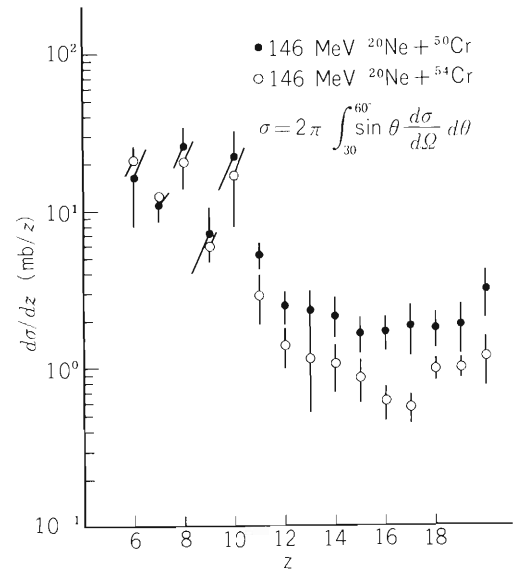

Fig. 2. Charge distributions at two different bombarding energies at $\theta_{cm} = 40°$. The solid lines show calculated charge distribution with $t_{1/2} = 10 \times 10^{-22}$ sec. The calculations are normalized to the data at Z = 15.

the ^{20}Ne + ^{50}Cr system were found to be about twice to three times larger than for the ^{20}Ne + ^{54}Cr system, while the difference was not observed in the products lighter than the projectile. This isotopic effect in the strongly damped components is similar to that observed between the system ^{14}N + ^{58}Ni and ^{14}N + ^{64}Ni.[5] As shown in Fig. 2, the difference of the yield in the strongly damped components were observed even between the reactions 120 MeV ^{20}Ne + ^{50}Cr and 146 MeV ^{20}Ne + ^{50}Cr. The excitation function of the symmetric fission-like products (Z = 17) is given in Fig. 3. These results of the isotopic and bombarding energy dependence can be qualitatively explained by the fission barrier height predicted by rotating liquid drop model[2] as shown in Table 1.

If it is supposed that the transfer of charge Z or mass A conforms to the diffusion phenomena,[1] the total charge distribution is given by the integration over ℓ-value from critical angular momentum ℓ_{crit} to maximum angular momentum ℓ_{max} as follows;[6]

$$\frac{d\sigma}{dZ_1} = \frac{2\pi}{k^2} \int_{\ell_{crit}}^{\ell_{max}} \ell P \left\{ Z_1, \tau_{int}(\ell) \right\} d\ell \qquad (1)$$

with asymptotic wave number k and the ℓ-dependent interaction time $\tau_{int}(\ell)$. The probability distribution $P\{Z_1, \tau_{int}(\ell)\}$ is given by a gaussian function,[6]

$$P\left\{ Z_1, \tau_{int}(\ell) \right\} = \left\{ 4\pi D_z \tau_{int}(\ell) \right\}^{-\frac{1}{2}} \exp\left\{ -\frac{Z_1 - Z_p - v_z \tau_{int}(\ell)}{4 D_z \tau_{int}(\ell)} \right\}, \qquad (2)$$

where Z_p is the projectile charge, v_z and D_z are drift velocity and diffusion constant, respectively.

The interaction time $\tau_{int}(\ell)$ can be generally obtained from angle of observation using an angular velocity. Supposing that the composite system rotates, it is possible to calculate the angular velocity of the system by taking a rigid-body sticking model. An additional parameter which is the probability of survival of a composite system after time $\tau_{int}(\ell)$ would be given by $\exp(-\lambda\tau_{int}(\ell))$,[7] where λ ($= 0.693/t_{1/2}$) is the decomposition probability constant and $t_{1/2}$ is the half-life time of the composite system. Thus the contribution of projectile-like fragments to the probability of obtaining a charge Z_1 at an angle θ can be given by the following equation:[7]

$$P(Z_1, \theta)_p = \sum_{n=1}^{n} \exp\left\{-\lambda\tau_{int}(\ell)_n\right\} P\left\{Z_1, \tau_{int}(\ell)_n\right\}, \quad (3)$$

where if $\theta_{gr} < \theta$

$$\tau_{int}(\ell)_1 = \frac{1}{\omega}(\theta_{gr} + \theta), \quad \tau_{int}(\ell)_2 = \frac{1}{\omega}(\theta_{gr} + \theta + 2\pi),$$

$$\tau_{int}(\ell)_3 = \frac{1}{\omega}\left\{2\pi - (\theta - \theta_{gr})\right\}, \cdots\cdots\cdots$$

ω being the ℓ-dependent angular velocity of the composite system. It has been assumed that the strongly damped components are associated with negative scattering angles. One charge can have contributions from projectile-like fragments, and also it can have contributions from target-like fragments. The total probability of observing a charge Z_1 at an angle θ will be given by

$$P(Z_1, \theta) = P(Z_1, \theta)_p + P(Z_1, \theta)_t \quad (4)$$

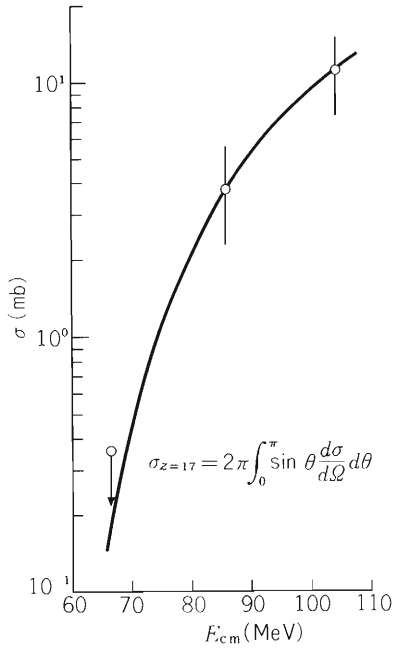

Fig. 3. Exciation function for the symmetric fission-like products (Z = 17). The curve show calculated values. The calculations are normalized to the data at E_{cm} = 104 MeV.

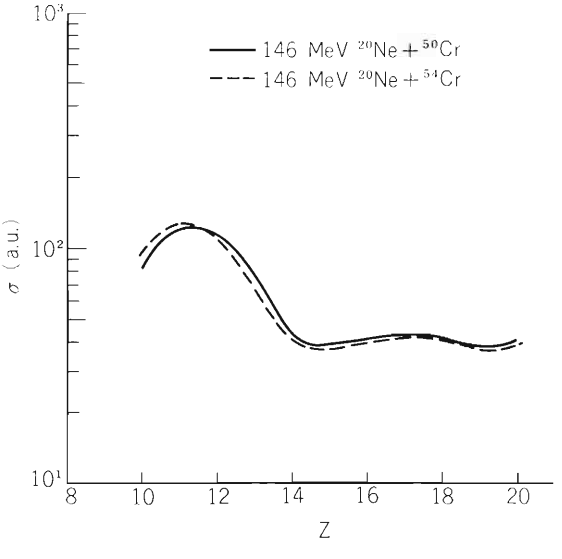

Fig. 4. Liquid drop potential energy curves of two touching spheres relative to the rotating composite system as a function of mass asymmetry for different orbital angular momentum ℓ. The arrows indicate the injection points.

The differential cross section will be given by

$$\frac{d^2\sigma}{d\theta dZ_1} = \frac{2\pi}{k^2} \int_{\ell_{crit}}^{\ell_{max}} \ell P(Z_1, \theta) d\ell \quad . \tag{5}$$

Transport coefficients v_z and D_z used in this calculation were obtained from theoretical expressions.[1)]

Figures 2 and 3 show that the bombarding energy dependence reproduce the relative enhancement of symmetric fragmentation at high energy. This is due to the strong drift towards symmetry for high angular momenta caused by the deep minimum at symmetry in the potential energy curves as shown in Fig. 4. The charge distributions calculated with Eqn. (5) at $\theta = 40°$ and $t_{1/2} = 10^{-21}$ sec indicate that the isotopic dependence in the strongly damped components between $^{20}Ne + {}^{50}Cr$ and $^{20}Ne + {}^{54}Cr$ is not observed as shown in Fig. 5. Therefore, this isotopic effect in the strongly damped components, especially symmetric mass fragmentation products, is considered to reflect the contribution of the fissility parameter (Z^2/A), i.e., fission barrier height.

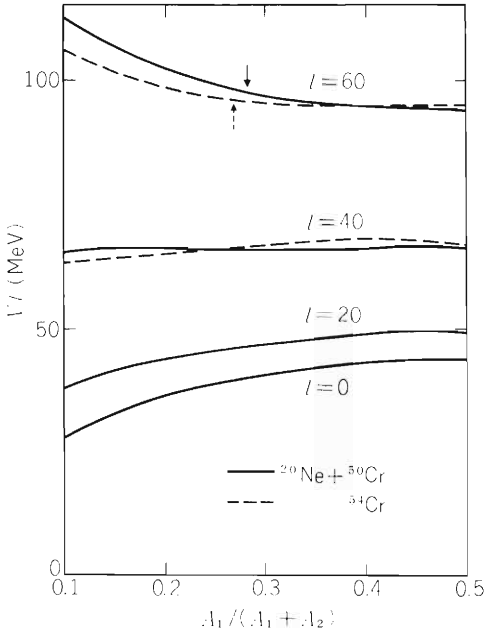

Fig. 5. Calculated charge distributions for two reaction systems.

References

1) W. Nörenberg: J. Phys. C5, 37, 141 (1976).
2) S. Cohen, F. Plasil, and W.J. Swiatecki: Ann. Phys., 82, 557 (1974).
3) R. Bass: Nucl. Phys., A231, 45 (1974).
4) Y. Nagame, I. Kohno, M. Yanokura, H. Kudo, and H. Nakahara: IPCR Cyclotron Progr. Rep., 14, 34 (1980).
5) M. Yanokura, H. Nakahara, and I. Kohno: J. Phys. Soc. Japan, 50, 369 (1981).
6) G. Wolshin and W. Nörenberg: Z. Phys., A284, 209 (1978).
7) S. Agarwal: ibid., A297, 41 (1980).

III-1-8. Incident Energy Dependence of Heavy-Residue Products in $^{14}N + ^{62}Ni$

K. Sueki,* Y. Nagame, M. Takahashi,* H. Nakahara, and I. Kohno

[NUCLEAR REACTION $^{62}Ni(^{14}N, X)$; measured cross section, its energy dependence.]

The aim of the present work is to study the incident energy dependence of yields of heavy-residue products in heavy-ion induced reactions of a relatively light mass system. The reaction system chosen was (^{14}N + ^{62}Ni) and the ^{14}N energy incident on each enriched self-supporting ^{62}Ni target foil (1 – 2 mg/cm^2) was varied by the stacked-foil method. Aluminum catcher foils (5.53 mg/cm^2) of 99.997 % purity were inserted in between target foils in order to collect the recoiling products. Irradiations were performed using the cyclotron for 6 h with the beam intensity of 0.5 μA. The energy range covered was from 85 to 120 MeV.

Three kinds of heavy-residue products were investigated: (1) those with masses close to the compound mass, (2) cobalt isotopes which could be considered as pxn transfer products from the target, and (3) scandium isotopes whose atomic number is smaller than that of the target by seven units. The yields of the first kind of products could be determined by directly measuring γ-rays with a Ge(Li) detector whereas those of the other kinds could be determined only after proper chemical separations.

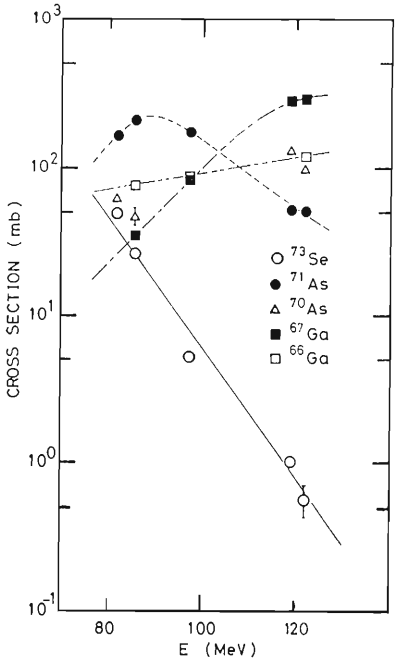

Fig. 1. Excitation functions of fusion residue products.

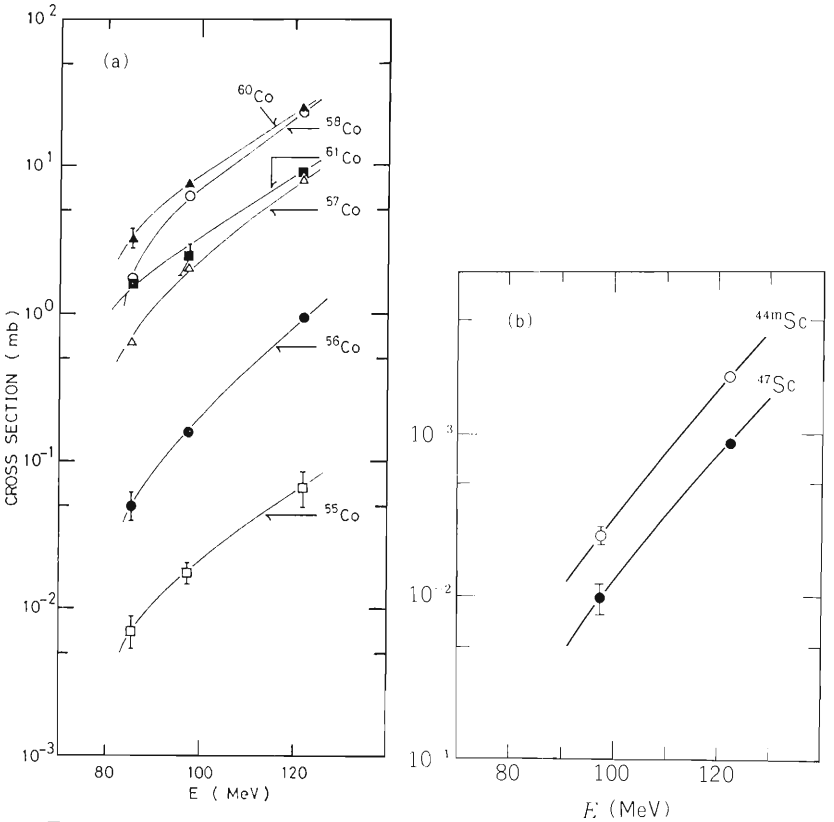

Fig. 2. Incident energy dependence of cross section: (a) Cobalt isotopes; (b) Scandium isotopes.

* Faculty of Science, Tokyo Metropolitan University.

Theoretical understanding of the data is still in progress, and only important features of the experimental data observed are presented in this report.

Excitation functions obtained for the first kind of products are shown in Fig. 1. The lines drawn in the figure are simply to guide the eye. The yield of ^{73}Se which was produced either by three neutron emission followed by β^+ decay or by one proton and two neutron emission from the fused nucleus could not be fitted by the evaporation calculation. The mean projected range of ^{73}Se in nickel metal observed by the conventional thick-target thick-catcher foil method[1] also turned out to be only a half of what was expected for full-momentum transfer reactions. The preequilibrium process may, therefore, be effective for the formation of ^{73}Se.

Excitation functions of cobalt isotopes and scandium isotopes are shown in Fig. 2 (a) and (b), respectively. The cross sections are not corrected for the contribution from the parent nuclides in β-decay chains. However, cobalt and scandium isotopes ^{61}Co, ^{60}Co, ^{58}Co, and ^{44}Sc, ^{46}Sc, ^{47}Sc, ^{48}Sc are shielded nuclides in β^+-decay chains and they can be considered free from the effect of parents. Although yields of the parent nuclides of ^{57}Co and ^{56}Co, namely, ^{57}Ni (36.1 h) and ^{56}Ni (6.10 d) were tried to obtain, they were found below the detection limit. Consequently, contributions from parent nuclides can also be considered negligibly small even for ^{57}Co and ^{56}Co. From the figures it is found that the energy dependence of yields of cobalt isotopes is similar to that of scandium isotopes although the latter seems to be somewhat steeper.

In Fig. 3 are shown the ratios of the activity of the respective isotope recoiled into the forward catcher foil, C, to that found remaining in the target foil, T. They are related to the mean projected ranges, and therefore, to the amounts of linear momenta transferred to the product nuclides. The figure shows that the amount of linear momentum transfer becomes larger as the number of neutrons stripped off from the target nuclide becomes larger. The ratio for ^{55}Co, however, does not follow this trend.

The isotopic yield distributions of cobalt isotopes observed at three different incident energies are shown in Fig. 4. They can be well fitted by Gaussian curves. The charge density of each isotope is shown in terms of N/Z on the horizontal scale given at the top of the figure. Also indicated by arrows are the N/Z values of the target nuclide (TN) and of the compound nucleus (CN). The most probable N/Z value of the present reaction

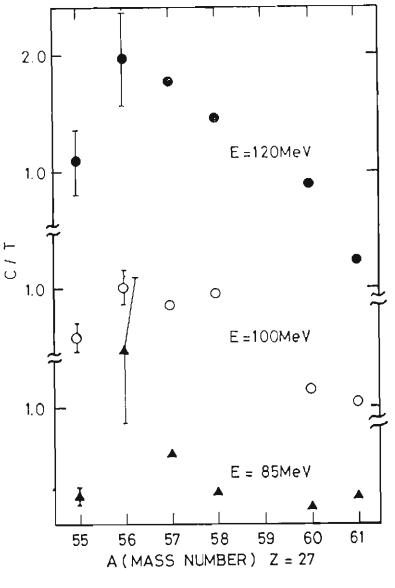

Fig. 3. C/T ratios for cobalt isotopes.

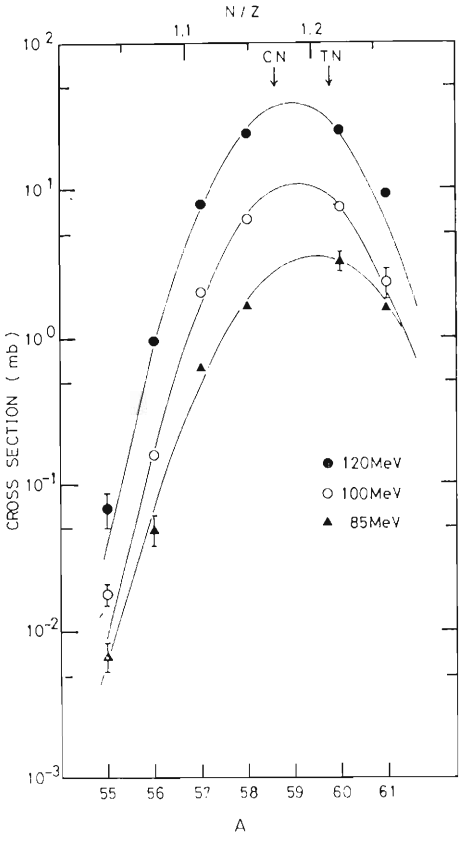

Fig. 4. Isotopic yield distribution of cobalt isotopes.

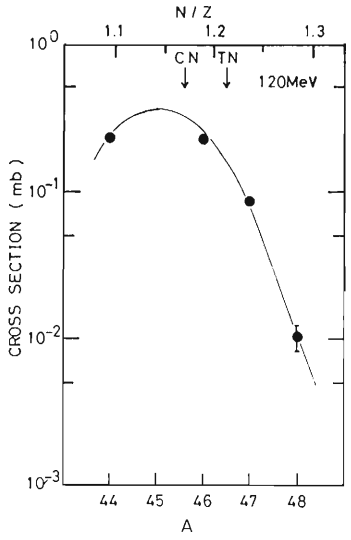

Fig. 5. Isotopic yield distribution of scandium isotopes at 120 MeV.

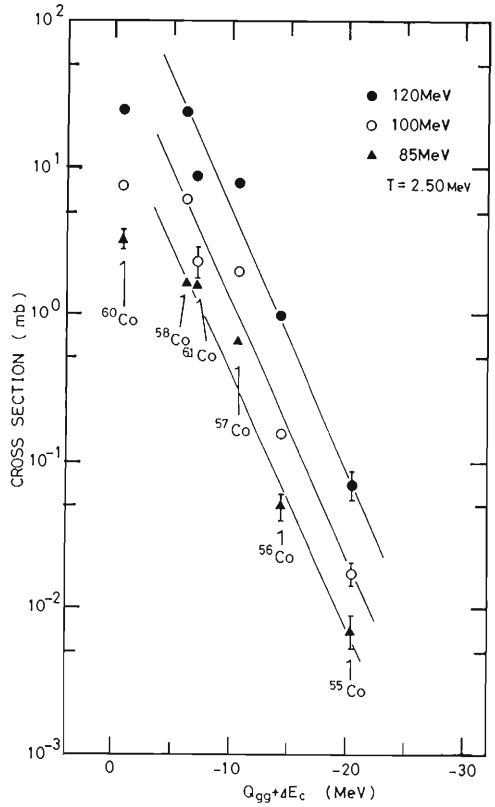

Fig. 6. The Q_{gg} dependence of cabalt isotopes. ΔE_c indicates the difference in Coulomb interaction energy between the entrance and exit channels.

system for cobalt products seems to shift from the TN to CN as the incident ^{14}N energy is increased. Similar plots were made in Fig. 5 for scandium isotopes. The most-probable N/Z value is found a little smaller than the CN value. This fact may suggest that a larger number of neutrons are emitted in the reaction process producing scandium isotopes. However, it is to be noted that the width of the scandium distribution at 120 MeV is not very different from that of the cobalt distribution observed at the same energy as shown in Fig. 4.

In Fig. 6 are plotted the cross section for cobalt isotopes as a function of the (Q_{gg} + ΔE_c) value. All but ^{60}Co seem to show the so-called Q_{gg} dependence fairly well. The temperature deduced from the slope of the lines[2] is 2.5 MeV, and it is rather independent of the incident ^{14}N energy within the range investigated in the present work.

Similar studies are in progress for the nickel targets of different mass numbers.

References

1) Y. Nagame, M. Watanabe, H. Kudo, H. Nakahara, I. Kohno, and M. Yanokura: IPCR Cyclotron Progr. Rep., 14, 37 (1980).
2) V.V. Volkov: Phys. Rep., 44, 93 (1978).

III-1-9. Light-Particle Emissions in the $^{93}Nb + ^{14}N$ Reaction in the Region of ~7 to ~15 MeV/A

M. Ishihara, T. Fukuda,* M. Tanaka,** H. Ogata,***
I. Miura,*** T. Shimoda,* and K. Katori*

NUCLEAR REACTIONS $^{93}Nb(^{14}N, X)$ with X = p, d, t, α, E = 132, 160, 210 MeV; measured $\sigma(E, \theta)$.

The strong emission of fast-light particles is one of characteristic aspects of heavy-ion reactions in a broad region of the projectile energy. Several mechanisms have been proposed to account for these emissions. Apparently, the phenomenon bears different features as the incident energy varies from low to high energies. In the low-energy region of ~5 MeV/nucleon, the energy spectrum shows a Maxwellian-line shape, which may favour treatments in terms of "hot-spot" model and "exciton" models. On the other hand, in the high-energy region of some 100 MeV/nucleon, the aspect of projectile fragmentation dominates. In the intermediate region, the competition among such different mechanisms is likely.

The present work is aimed at investigation of energy dependence of the light-particle emission in the $^{93}Nb + ^{14}N$ reaction in the energy range of ~7 to ~15 MeV/nucleon. The ^{14}N beam of 132, 160, and 210 MeV from the RCNP cyclotron (Research Center for Nuclear Physics at Osaka) was used to irradiate a metalic target of ^{93}Nb. Energy spectra and angular distributions of light-charged particles, i.e., p, d, t, and α were measured using telescopes of Si-detectors and those incorporating intrinsic Ge detectors.

Figure 1 shows some energy spectra of α particles taken at different incident energies. The spectra shown are those obtained after subtracting the equilibrium components whose intensities and spectral shapes are estimated from the data at backward angles. The spectra at 115 MeV are characterized by their shapes, which may be fitted by Maxwellian shapes. At higher incident energies, the spectral shapes no longer exhibit such a monotonic structure; typically, for the 210 MeV data at forward angles, the energy spectra clearly show an extra enhancement in the higher energy region and particularly in the energy region corresponding to the incident velocity of the projectile. Recently an alpha-particle-emission mechanism[1] associated with the projectile breakup was proposed. The enhancement at the higher energy region is suggestive of such a mechanism.

The angular distributions of p, d, t, and α taken at 132 MeV are compared in Fig. 2. The equilibrium components are again subtracted. The slope of the distribution is rather similar among p, d, t, while that of α is considerably steeper. The significant deviation observed for the alpha particles may characterize a particular feature of the alpha-particle emission.

A detailed description of data and comparison of the results with various models are in preparation.

* Department of Physics, Osaka University.
** Kobe Tokiwa Junior College.
*** Research Center for Nuclear Physics, Osaka University.

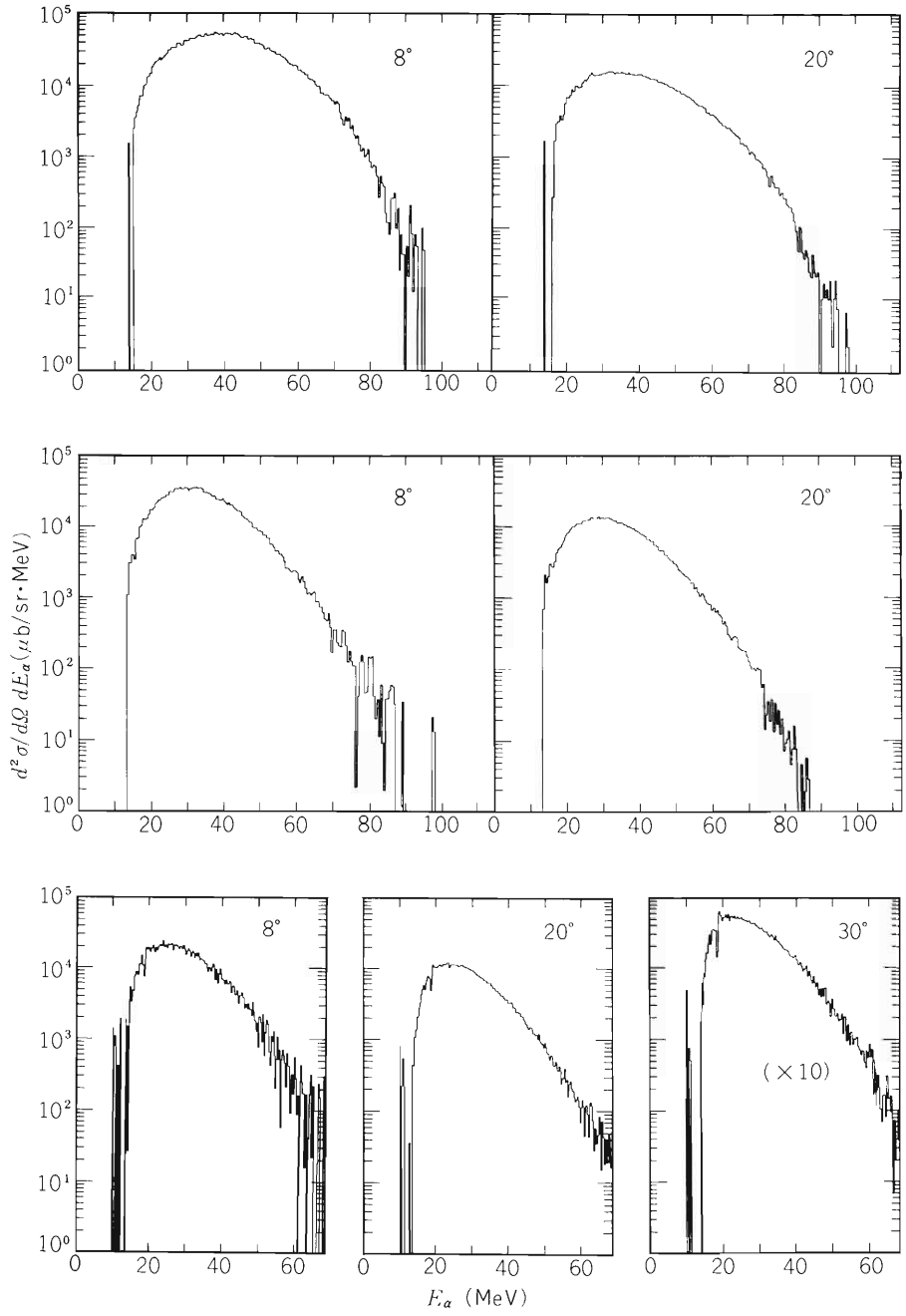

Fig. 1. Examples of alpha-particle energy spectra for E(^{14}N) = 210, 160, and 132 MeV shown, respectively, in the top, middle and bottom rows. The vertical axices represent the differential cross section, $d^2\sigma/d\Omega dE_\alpha$, in unit of μb/sr·MeV, and the horizontal axies the alpha-particle energy E_α in unit of MeV.

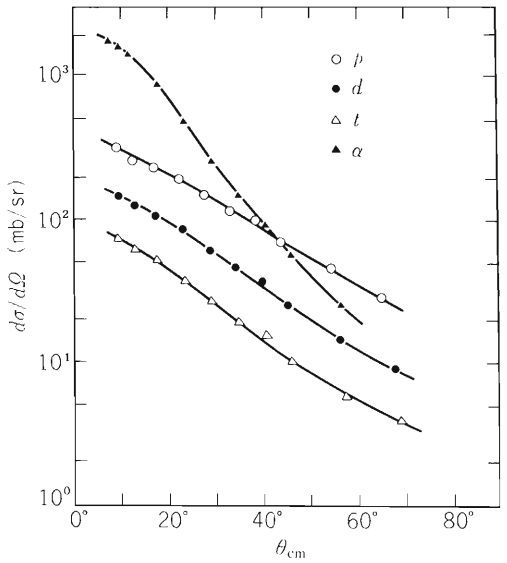

Fig. 2. Angular distributions of p, d, t, and α in the $^{93}Nb + ^{14}N$ reaction at 132 MeV.

Reference

1) T. Udagawa and T. Tamura: Phys. Rev. Lett., 45, 1311 (1980).

III-1-10. Alpha Particle vs. Ejectile Correlations in the $^{93}Nb + {}^{14}N$ Reaction at 208 MeV

M. Ishihara, T. Fukuda,* M. Tanaka,** H. Ogata,***
I. Miura,*** T. Shimoda,* and K. Katori*

[NUCLEAR REACTION $^{93}N(^{14}N, \alpha X)$ with X = Li – O, E = 208 MeV; measured correlations between α and X.]

The present note is to report on the correlation between alpha particles and ejectiles measured in the heavy ion reaction ^{93}Nb + 208 MeV ^{14}N. A large number of experiments on such correlations have been reported for various reactions, being followed by suggestions of different mechanisms to account for the phenomena. The accumulated data now indicate two types of mechanisms to be significant for the correlation observed. The first is a sequential emission of alpha particles from excited ejectiles produced in the primary heavy ion reaction.[1] The second bears a feature of direct ternary process and is argued[2] to have characteristic behaviour of cross sections as described by the factorized form

$$d^4\sigma/d\Omega_1\, d\omega_2\, dE_1\, dE_2 = k\cdot(d^2\sigma/d\Omega_1\, dE_1)_{singles}\cdot(d^2\sigma/d\Omega_2\, dE_2)_{singles}, \qquad (1)$$

where subscripts 1 and 2 refer to ejectile and alpha particle, respectively. The important property involved in this formula is that the energy and angular dependence of each of the coincident particles are identical with those of singles. This particular property involved a conjecture that the direct-like mechanism may consist of a two-step process, i.e., the projectile breakup followed by deep-inelastic-type reaction.

The primary aim of the present work is to obtain further information on the direct-like process. In the experiments so far performed, the counter for ejectiles was usually placed at forward angles. This resulted in significant contamination of the ejectile-decay component in the observed spectra so that the validity of (1) is hard to be tested. In the present measurement, the correlation has been observed for three ejectile angles, 22°, 50°, and 80°. For the data of the backward angles, 50° and 80°, the kinematic conditions allowed to isolate the two components fairly well. Moreover, the present data provides extended information on the direct-like process over a wider angular range.

The experiment was performed using ^{14}N ions from the RCNP cyclotron at Osaka University. The alpha particles and ejectiles were detected in coincidence using conventional Si-detector telescopes. The energy and angular correlations were recorded. A detailed report on the experiment will be published elsewhere. Here we only describe some of the characteristic features of the experimental results.

* Department of Physics, Osaka University.
** Kobe Tokiwa Junior College.
*** Research Center for Nuclear Physics, Osaka University.

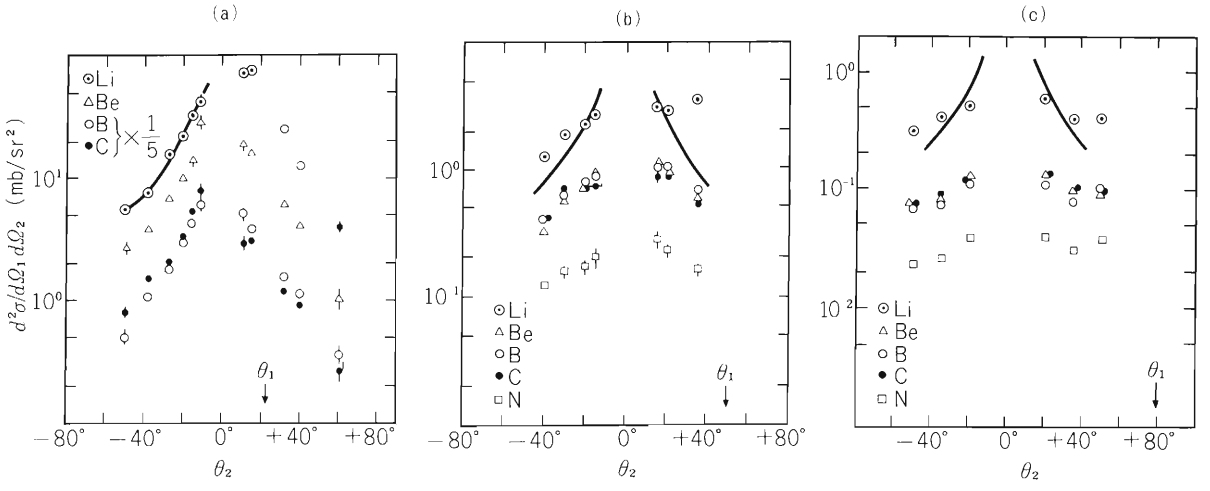

Fig. 1. Energy integrated angular distributions of alpha particles in coincidence with various ejectiles for ejectile angles of 22° (a), 50° (b) and 80° (c). The solid line indicates the slope of the singles angular distribution. Note that contributions from sequential ejectile breakup are significant in the angular range of $\theta_2 > 0$ for (a), at $\theta_2 = 35°$ for (b), and at $\theta_2 = 45°$ for (c).

Figure 1 compares the energy integrated angular distributions of alpha particles (angle θ_2) in coincidence with ejectiles which were detected at $\theta_1 = 22°$, 50°, and 80°. According to the relation (1), the same shapes of angular distributions are expected. This feature is apparently missing in the observed distributions, which show gradual flattening of the slope as the ejectile angle becomes more backward. In spite of such difference, the angular distributions have a common feature. The peak angle is close to 0°, i.e., the direction of the beam. This aspect, which is also implied by Eqn. (1), is suggestive of a reaction mechanism, in which alpha particles are emitted prior to the ejectiles.

The coincidence energy spectra of alpha particles and ejectiles were also compared with Eqn. (1). For the result for $\theta_2 = 22°$, alpha-particle spectra are similar in shape with singles in accordance with Eqn. (1). For the more backward angles of θ_1, however, the coincidence alpha-particle spectra become more deviated from singles spectra, being attenuated in the higher energy region. Apparently higher-energy alpha particles contribute more to events involving forward angle emission of ejectiles. The different behaviours of low- and high-energy alpha particles are suggestive of the coexistance of varied reaction mechanisms.

References

1) M. Bini, C.K. Gelbke, D.K. Scott, T.J.M. Symons, P. Doll, D.L. Hendrie, J.L. Lavilla, J. Mahoney, M.C. Mermaz, C. Olmer, K. Van Bibber, and H.H. Wieman: Phys. Rev., C 22, 1945 (1980).

2) R.K. Bhowmik, E.C. Pollaco, N.E. Sanderson, J.B.A. England, and G.C. Morrison: Phys. Lett., 80B, 41 (1978); Phys. Rev. Lett., 43, 619 (1979).

III-1-11. Projectile Dependence of Fast Light-Particle Emission in Heavy-Ion Reaction

K. Ieki, M. Ishihara, T. Inamura, and S. Kohmoto

NUCLEAR REACTIONS ^{93}Nb(X, α), X = ^{14}N, ^{16}O, ^{19}F, and ^{20}Ne, E = 7.3 MeV/amu; measured energy spectra and angular distribution; compound component subtraction, projectile dependence.

This work is concerned with light-particle emission in light heavy-ion reactions. Such emission is characterized by following features: (a) high energy component is enhanced in energy spectra in comparison with evaporation spectra; (b) differential cross section is forward peaked.

These features suggest that fast light-particles are emitted in an early stage of reaction and several models (hot spot, massive transfer, exciton, etc.) have been proposed. To study this phenomenon more systematically, we have measured differential cross sections and energy spectra of light-particle emissions for several different projectiles.

Various heavy ion beams (^{14}N 106 MeV, ^{16}O 120 MeV, ^{19}F 136 MeV, ^{20}Ne 139 MeV) from the cyclotron were used to bombard ^{93}Nb foil of 3.4 mg/cm^2. We chose as projectile energy about 7.3 MeV per nucleon for all ions. We measured angular distributions and energy spectra of emitted light particles (p, d, t, α, etc.) with a counter telescope consisting of 30 μm and 5 mm Si detectors. We here report the results for α particles.

Angular distributions are shown in Fig. 1. For every projectile, the angular distribution is forward peaked. At backward angles, energy spectra are well reproduced with Maxwellian shape. Nuclear temperatures extracted from energy spectra are nearly constant for $\theta \geqq 120°$, so we

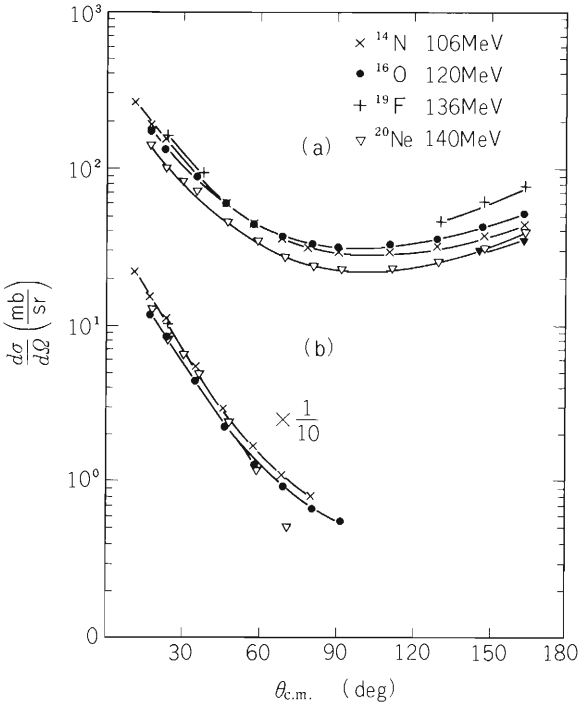

Fig. 1. Angular distribution of emitted α-particles.
(a) measured distribution.
(b) compound component subtracted distribution.

assumed that particles emitted backward are evaporated from compound nucleus. Particles emitted forward originate both from compound process and from non-compound process. The non-compound component of present interest was deduced by subtracting the compound component; the subtraction was made by assuming 90° symmetry of the compound cross sections. Figure 1(b) shows angular distributions of non-compound component. They all look very similar both in shape and magnitude. Initially we anticipated that difference of transfered mass or difference of grazing angular momentum would reflect on the cross section, but such differences are not so distinct.

Figure 2 shows typical energy spectra for non-compound component. Energy spectra exhibit some difference in width. In order to display the difference more quantitatively, we fitted energy spectra to Maxwellian shape. Though high energy part ($E \geqq 35$ MeV) deviates, main part of the spectrum is well characterized by the Maxwellian shape. The fitted values of nuclear temperature (T)

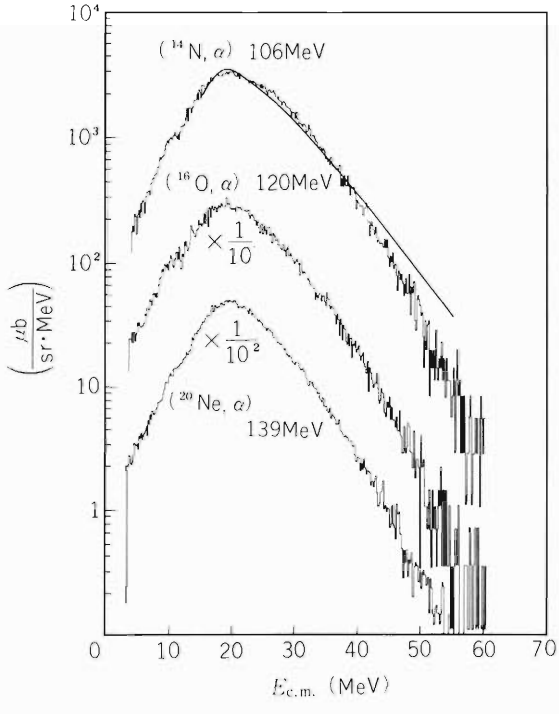

Fig. 2. α-particle energy spectra at $\theta_{c.m.} = 35°$ in log scale. Line is fitted curve to Maxwellian shape.

are shown in Fig. 3(a). The projectile dependence of T is rather smooth and T is larger for smaller mass of projectile. Note that the total energy brought on the target is smaller for smaller mass of projectile so that lower T is expected for the case of an equilibrated process. It is also noted that the variation of T with projectile does not show a particular dependence on the projectile structure with respect to whether or not the projectile is a 4N nucleus.

With temperature T, one may derive effective level density parameter a by

$$a = U/T^2,$$

where U is total excitation energy. The parameter a may represent the effective number of degrees of freedom involved in the preequilibrium excitation. To see the relation of a to projectile mass number A, we plot the values of a/A in Fig. 3(b). For heavier projectile, the ratio a/A is slightly larger and the gradient is steeper. This fact may imply that relaxation occurs faster for heavier projectile.

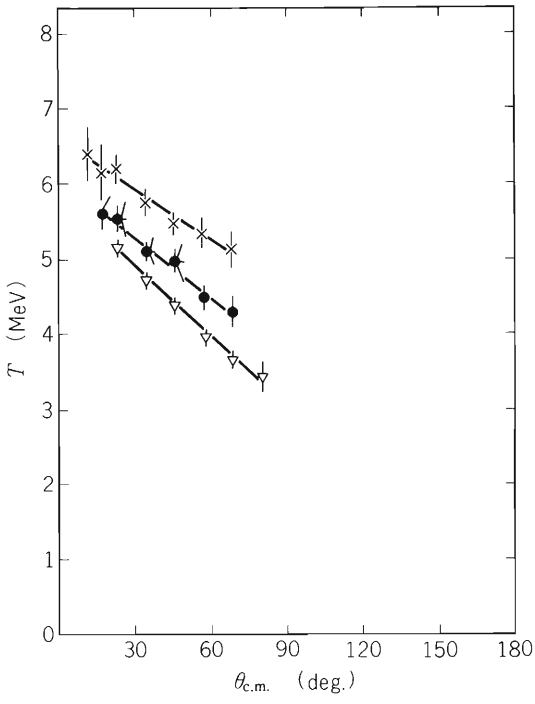

Fig. 3 (a). Nuclear temperature of residual nucleus.

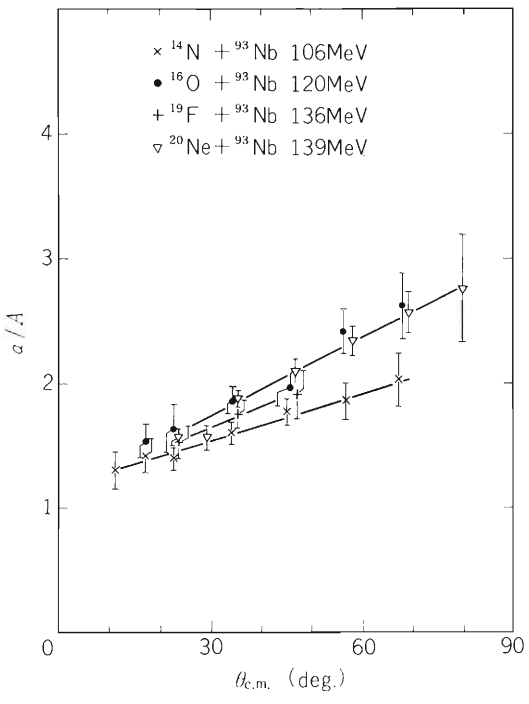

Fig. 3 (b). Effective level density parameter a divided by projectile mass number A.

III-1-12. Polarization of Continuous Protons Emitted at 40° in the $^{93}Nb + ^{14}N$ Reaction

T. Sugitate,* T. Nomura, H. Utsunomiya,
M. Ishihara, K. Ieki, and S. Kohmoto

NUCLEAR REACTION $^{93}Nb(^{14}N, p)$, E = 95 MeV; measured spin polarization (θ = 20°). double scattering method.

The polarization measurement for protons emitted at 40° in the $^{93}Nb + ^{14}N$ reaction at 95 MeV has been carried out by the double scattering method. The experimental method is the same as that described previously.[1] The result is given in Fig. 1. The measured value of polarization is small for low energy protons but increases with the increasing proton energy, reaching about 20 % at $E_{c.m.} \simeq 20$ MeV. This tendency is similar to the case observed at 20° in the same reaction reported in Ref. 1 and is considered to be due to the fact that the proportion of a preequilibrium (PE) component in a continuous energy spectrum at 40° increases with the increasing energy.[1] The upper part of Fig. 2 shows energy spectra of protons emitted at θ_{lab} = 40° and 134°, which roughly correspond to those at $\theta_{c.m.}$ = 43° and 137°, respectively. Since the spectrum at $\theta_{c.m.}$ = 137° approximately represents an equilibrium (EQ) component at $\theta_{c.m.}$ = 43° as explained in Ref. 1, the difference between the two spectra in Fig. 2 gives a PE component at $\theta_{c.m.}$ = 43°. The lower part of Fig. 2 shows this proportion as a function of energy. If we assume that the EQ component is completely unpolarized, and that the polarization (P) of the PE component is independent of energy, the experimental polarization has been well fitted by using the proportion of the PE component mentioned above. The result is shown by a solid curve in Fig. 2, from which we obtain P = 38 ± 10 %.

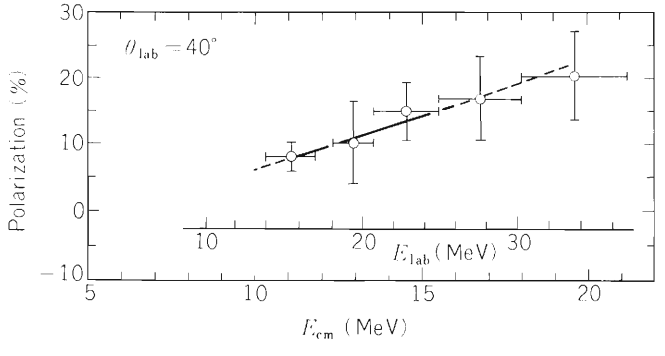

Fig. 1. The measured (circles) and estimated (solid curve) values of proton polarization observed at 40°.

* Present address : Department of Physics, Hiroshima University.

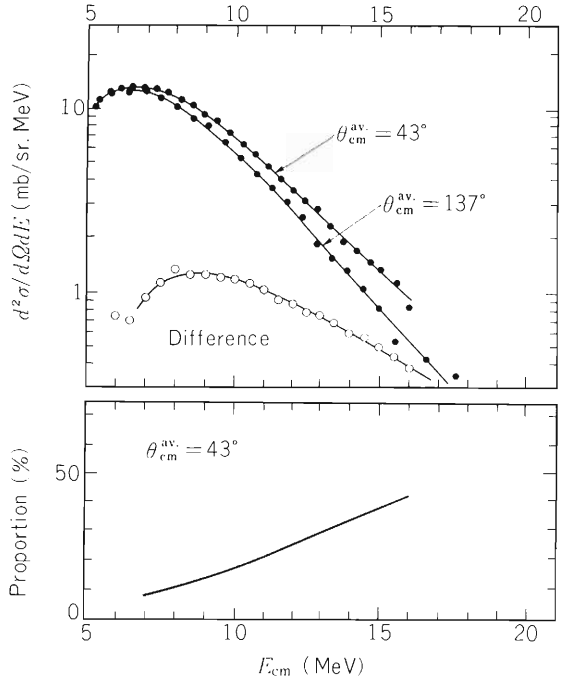

Fig. 2. Upper: Experimental energy spectra of protons at θ_{lab} = 40° and 134°, which roughly correspond to those at $\theta_{c.m.}$ = 43° and 137°, respectively. The difference of the two spectra is also given. Lower: The proportion of the preequilibrium component deduced as explained in the text.

Reference

1) T. Sugitate, T. Nomura, M. Ishihara, Y. Gono, H. Utsunomiya, K. Ieki, and S. Kohmoto: IPCR Cyclotron Progr. Rep., 14, 28 (1980).

III-1-13. Light-Particle Emission Following ^{7}Li-Induced Reactions

H. Utsunomiya, S. Kubono,* M. Tanaka,*
K. Morita,* M. Sugitani,* and T. Nomura

[NUCLEAR REACTION ^{93}Nb(^{7}Li, x), ^{159}Tb(^{7}Li, x), ^{232}Th(^{7}Li, x), E = 49, 77 MeV, x = p, d, t, α, f; measured $\sigma(E, \theta)$, angular correlations.]

The light-particle emission has been studied in ^{7}Li-induced reactions on ^{93}Nb, ^{159}Tb, and ^{232}Th targets. The experiment has been carried out at beam energy of 49 MeV at Riken and of 77 MeV at Institute for Nuclear Study. The following measurements have been done: 1) energy and angular distributions of protons, deuterons, tritons and α particles measured between 20° and 160°; 2) angular correlations of two light particles emitted at forward angles (mainly between 20° and 50°); 3) angular correlations between light particles and fission fragments in order to study angular-momentum transfer and alignment in the case of ^{232}Th target.

The analysis of the experimental results is now in progress.

* Institute for Nuclear Study, University of Tokyo.

III-1-14. Influence of Chemical Environment on Outer-Shell Internal Conversion in ^{119}Sn

H. Muramatsu, T. Miura, H. Nakahara, M. Fujioka,
E. Tanaka,* and A. Hashizume

RADIOACTIVITY ^{119}Sb; measured E_{ce}, I_{ce}; deduced chemical effect, O/N_1, 5s electron density, $CaSnO_3$, white tin. Iron free magnetic spectrometer. Enriched targets.

In a number of experiments[1] chemical states have been shown to affect the rate of radioactive decay. These effects are related with the sum of electron densities of several electron orbitals near the nucleus, that is, with the so-called electron contact densities. However, quantitative analysis of these results is almost impossible because of the lack of knowledge of the effects of chemical binding on the related electron wave functions. On the other hand, observations of the internal conversion probabilities of the outermost shell electrons give more direct information on the effects of chemical binding on each individual electron wave function. Chemical effects on internal conversions of the outermost shell electrons was investigated by several groups in the past.[2]

For experiments of this type with a high resolution beta-ray spectrometer, it is necessary that the transition energy is less than about 50 keV in order for the conversion line due to the electrons in the outermost shell to be separated from that due to the electrons in the next-inner shell. This requirement comes from the fact that the best momentum resolution of the spectrometer is about 0.05 % in this energy region and the energy difference between the conversion line of the outermost shell electrons and that of the next-inner shell electrons is 137 eV. It is also preferable that the transition multipolarity is that of a magnetic dipole (M1) since such conversion can be interpreted simply in terms of the s-orbital electron density. Therefore, we chose the 23.87 keV M1 transition of ^{119}Sn that follows decay of ^{119}Sb ($T_{1/2}$ = 38.1 h) in our investigations. In this case, the energy of the conversion electron is so low and energy losses of such electrons are considerably large that high resolution measurements of the conversion electron spectra become extremely difficult, and the most essential problem is how to prepare a source sufficiently thin, e.g. 10 μg/cm^2.

Internal conversion sources with different chemical environments, namely, white tin and $CaSnO_3$, were prepared by the implantation of ^{119}Sb using the electromagnetic isotope separator at Tohoku University. The ^{119}Sb was obtained by the milking method from ^{119m}Te produced by proton irradiation of the natural antimony at AVF cyclotron of Tohoku University. Implantation of the radioactive ^{119}Sb was carried out at the terminal potential of 20 kV at room temperature. The dose rate was $\lesssim 10^7$ atoms/cm^2 for the mass number 119. From the radioactivity of the implanted sample, the number of implanted ^{119}Sb atoms was determined to be $\lesssim 10^{12}$ atoms/cm^2. In order to identify the final chemical state of the samples, emission Mössbauer spectra were measured with a $CaSnO_3$ absorber at 77 and 150 K.

Measurement of conversion electron spectra was made with a 50 cm, double focusing, iron-free beta-ray spectrometer at the Riken. A resolution of 0.14 % in momentum (full width at half maximum measured at L_I line of the 23.87 keV transition) was achieved with a 1 mm × 20 mm source and 1 mm × 20 mm final detector aperture. The detector was a gas-flow proportional counter with a thin polypropylene window (~ 100 μg/cm^2). All the conversion lines of the 23.87 keV transition were measured. In Fig. 1 there are shown the conversion electron spectra in the region of N and O lines from sources of white tin and $CaSnO_3$. The spectra have been normalized to equal N_I line intensity and K-LM Auger lines of tin are also shown. The N_I line and O lines with the energy difference of 137 eV could be clearly resolved from each other. The relative intensities of the N and O lines were evaluated using the computer code, ACSEMP[3] whose function essentially a least-squares analysis

* Faculty of Science, Tohoku University.

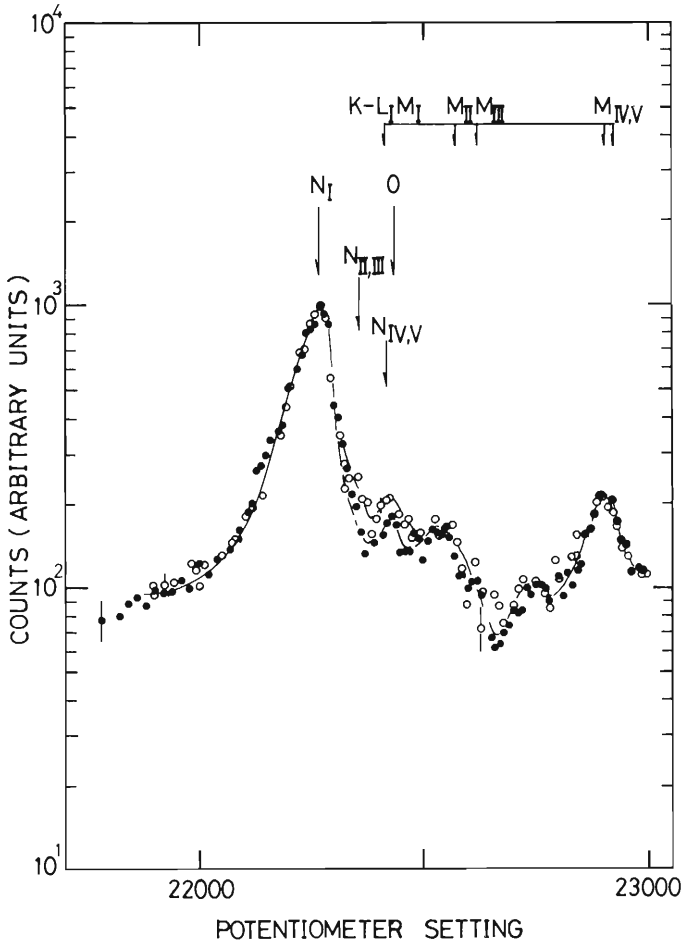

Fig. 1. Conversion electron spectra from two different ^{119}Sb sources. The curves have been normalized to equal N_1 line intensity.

- ● source No. 8 ($CaSnO_3$)
- ○ source No. 9 (white tin)

using empirical profiles. The K-LM Auger spectra, on which the 23.87 keV N and O lines are super-imposed in the energy region 23.7 to 24.0 keV, were independently observed by using a radioactive tin isotope, ^{117m}Sn and they were subtracted from the conversion electron spectra as a background in the spectral analysis of conversion lines.

Results of the analyses of two different sources are listed in Table 1. For the source No. 8, the Mössbauer spectrum indicated that only 47 % of the ^{119}Sb doped in the material was in the form of $CaSnO_3$. Therefore, the O/N_I intensity ratio was corrected on the assumption that the rest, which had an isomer shift similar to that

Table 1. Relative intensity ratios (O/N_I) from internal conversion of the 23.87 keV M1 transition in ^{119}Sn.

Source	O/N_I
No. 8 ($CaSnO_3$)	0.086 ± 0.015
	→ 0.066 ± 0.013
No. 9 (white tin)	0.12 ± 0.015

of white tin, was of the chemical composition of the source No. 9. If the effects of the change in the 5s electron density on the inner s-electron densities are small, one can deduce the 5s electron density at the nucleus from the observed O/N_I ratios by using the formula

$$\left|\psi(0)_{5s}\right|^2_x = \left|\psi(0)_{4s}\right|^2 \cdot (O/N_I),$$

where $|\psi(0)_{5s}|^2_x$ is the 5s electron density at the nucleus for the chemical medium x and $|\psi(0)_{4s}|^2$ is the 4s electron density of the tin atom. We adopted a value of 719 a.u. for the $|\psi(0)_{4s}|^2$ reported by Band et al.[4] who carried out relativistic Dirac-Fock calculations for the tin atom and ions. The difference in the 5s electron density between white tin and $CaSnO_3$ is then evaluated as

$$\Delta\left|\psi(0)_{5s}\right|^2 = \left|\psi(0)_{5s}\right|^2_{CaSnO_3} - \left|\psi(0)_{5s}\right|^2_{Sn}$$

$$= -38 \text{ a. u.}$$

This result shows that the presence of more electrophilic oxgen atoms around the tin atoms causes the reduction of the valence s-electrons in the tin atom. The change of the lifetime of the 23.87 keV level is also calculated to be about 0.12 %, that is, the lifetime of the 23.87 keV state of ^{119}Sn in $CaSnO_3$ is expected to be about 0.12 % longer than that of white tin.

References

1) See, for example, R.F. Leininger, F. Segre, and C. Wiegand: Phys. Rev., 76, 897 (1949); 81, 280 (1951).
2) See, for example, J.-P. Bocquet, Y.Y. Chu, O.C. Kistner, M.L. Perlman, and G.T. Emery: Phys. Rev. Lett., 17, 809 (1966); T.A. Carlson, P. Erman, and K. Franson: Nucl. Phys., A111, 371 (1968).
3) M. Fujioka and M. Takashima: J. Phys., 40, C2–32 (1979).
4) I.M. Band and V.I. Fomichev: Atomic Data and Nuclear Data Tables, 23, No. 4, p. 295 (1979).

III-1-15. Highly Neutron Deficient Nuclei ^{157}Yb

A. Hashizume, T. Katou, Y. Tendow,
and H. Kumagai

NUCLEAR REACTIONS ^{144}Sm(^{16}O, 4n) E = 80 – 120 MeV, n-γ, γ-γ coin, ^{157}Yb deduced levels, Ge(Li) detectors, enriched target.

In a series of experimental studies carried out on the excited states in Yb isotopes by (HI, xnγ) reactions,[1] the most neutron deficient nucleus whose states has been known is ^{158}Yb. To study the levels of more neutron deficient nuclei, states of ^{157}Yb were populated by means of the compound-evaporation reaction ^{144}Sm(^{16}O, 4nγ)^{157}Yb.

A self-supporting enriched ^{144}Sm target was prepared by vacuum evaporation where $^{144}Sm_2O_3$ was reduced by thorium. Excitation functions in the incident energy range of 80 to 120 MeV were studied by observing γ-ray singles spectra and also spectra of γ-rays in coincidence with neutrons. Since nothing is known of the excited states of ^{157}Yb, precaution was taken to assure the observation of the (^{16}O, 4n) reaction by compairing the excitation function with those of ^{147}Sm(^{16}O, 3n)^{160}Yb and ^{147}Sm(^{16}O, 4n)^{159}Yb. Levels of reaction products of the latter are well known.[2] It was also found that the n-γ coincidence technique was a good means to select neutron emitting channels.[3] The four fold coincidence spectra of $E_{\gamma 1} - E_{\gamma 2} - t - T$ have been

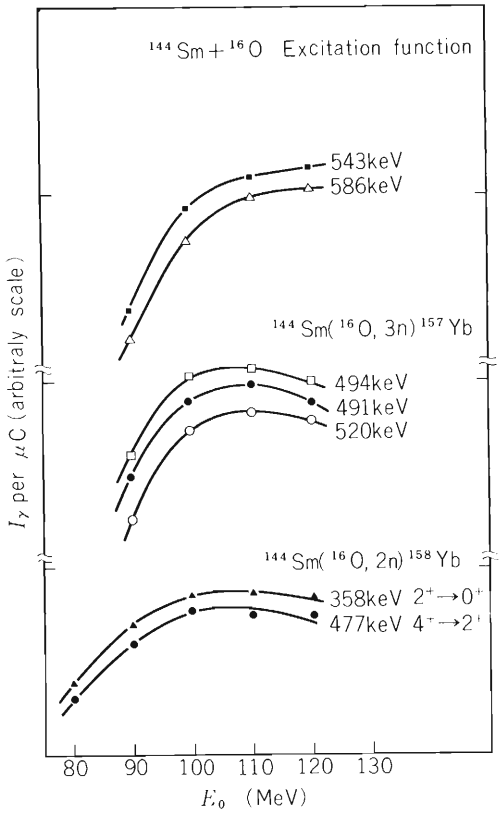

Fig. 1. Excitation functions of ^{157}Yb and ^{158}Yb.

measured where $E_{\gamma 1}$ and $E_{\gamma 2}$ are the γ-ray energies, t is the time between two γ-rays, and T is the time from a natural bunched beam of the cyclotron.

Figure 1 shows excitation function for the (^{16}O, $3n\gamma$) reaction observed with some γ-rays and Fig. 2 shows a spectrum of γ-rays coincident with neutrons when ^{144}Sm was bombarded by 100 MeV ^{16}O. As shown in Fig. 2, three intense γ-rays, 491, 543, and 586 keV, which coincide with neutrons were observed. When the gate was opened by 491 keV in γ-γ coincident spectrum, those γ-rays coincide as shown in Fig. 3. It was also shown that all of those γ-rays are emitted in coincidence.

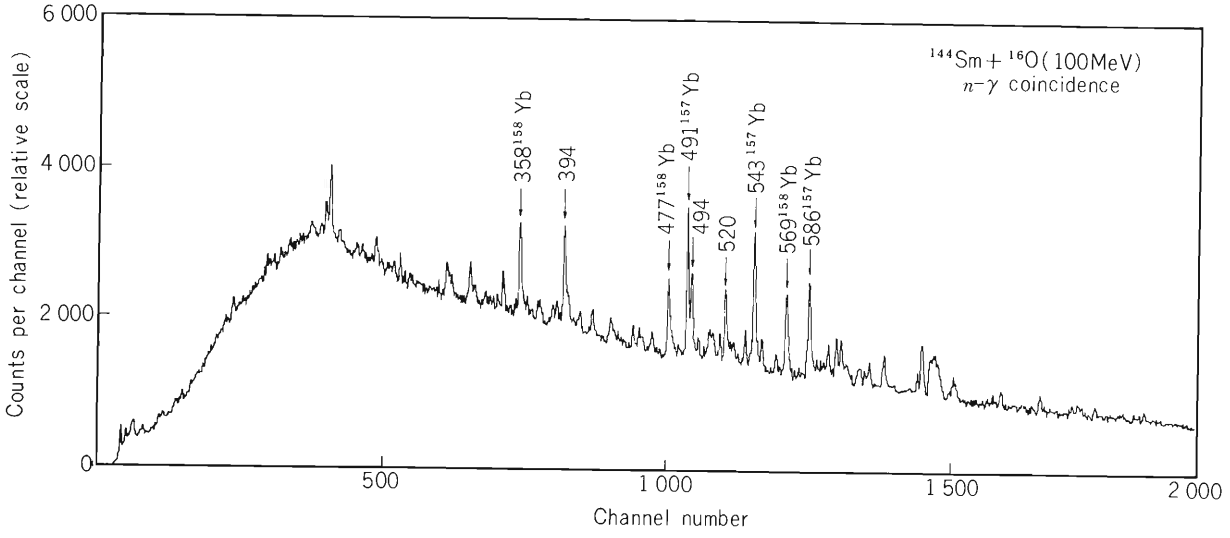

Fig. 2. Spectrum of γ-rays which coincides with neutrons.

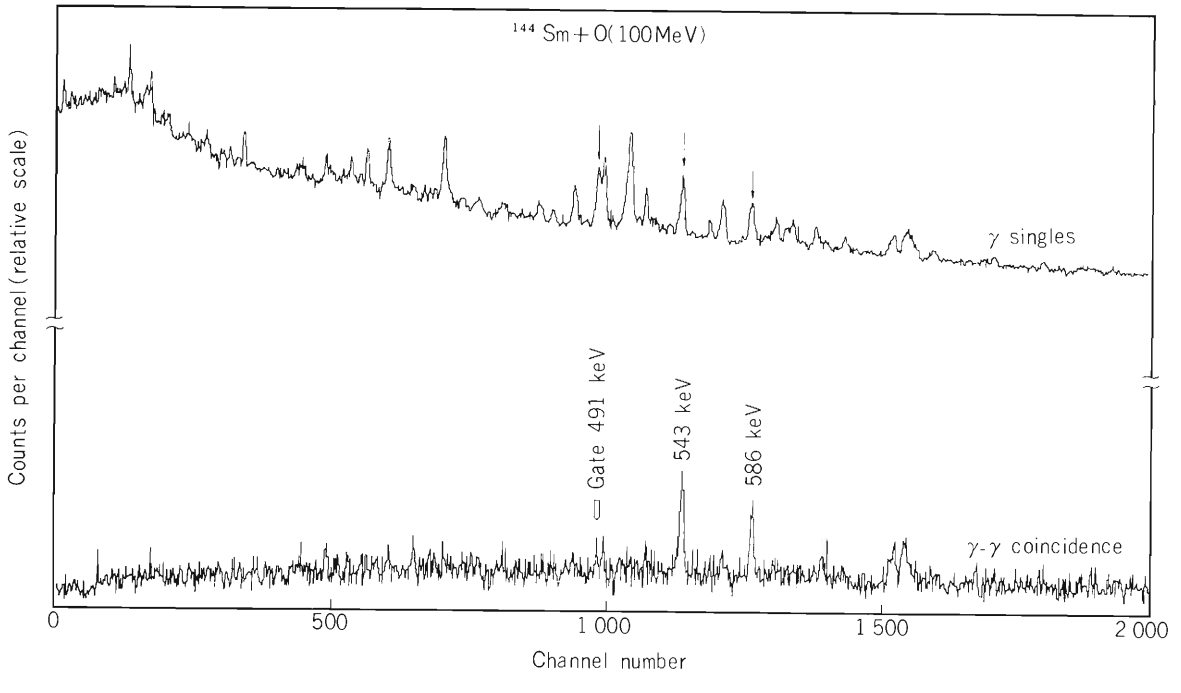

Fig. 3. γ-γ coincidence spectrum gated by the 491 keV γ-ray.

We tentatively propose the excited states in ^{157}Yb shown in Fig. 4. Since ^{157}Yb is an odd nucleus, it is not yet evident if the proposed band corresponds to the ground band. However, in view of these three γ-rays being most intense lines in n-γ spectrum, it is probable that the band is the ground band of (7/2), (9/2), (11/2), and (13/2) states. Further study is in progress.

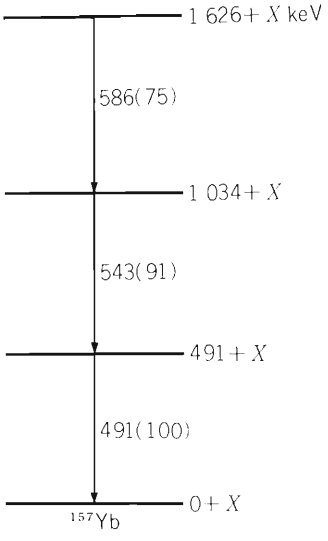

Fig. 4. Proposed level scheme in ^{157}Yb. Relative γ-ray intensities observed at 90° in the case of 90 MeV incident energy are shown in parenthesis.

References

1) A. Hashizume, T. Katou, Y. Tendow, and H. Kumagai: IPCR Cyclotron Progr. Rep., 14, 59 (1980); A. Hashizume, T. Katou, Y. Tendow, and H. Kumagai; ibid, 12, 74 (1978).

2) F.A. Beck, E. Bozek, T. Byrski, C. Gehringer, J.C. Merdinger, Y. Schutz, J. Styczen, and J.P. Vivien: Phys. Rev. Lett., 42, 493 (1979); W. Trautmann, D. Proetel, O. Hausser, W. Hering, and F. Riess: ibid., 35, 1694 (1975).

3) A. Hashizume, H. Kumagai, Y. Tendow, and T. Katou: p.121 in this report.

III-1-16. Calculation of Gamma-Ray Multiplicity Moments Associated with Massive-Transfer Reactions

T. Inamura and M. Wakai*

NUCLEAR REACTIONS $^{154}Sm(^{12}C, \alpha 4n)^{158}Dy$, E = 85, 109 MeV; $^{159}Tb(^{14}N, \alpha 5n)^{164}Yb$, E = 115 MeV; $^{159}Tb(^{10}B, 5n)^{164}Yb$, E = 69 MeV; massive transfer and fusion evaporation; γ-ray average multiplicity, variance, skewness calculated; E and J distribution effects.

The most distinctive feature predicted for the massive-transfer (or incomplete-fusion) reaction is the localization of ℓ values in the entrance channel leading to fusionlike products.[1),2)] Consequently it is interesting to study the γ-ray multiplicity distribution (m_γ distribution) which depends on excitation energy and angular momentum distributions of the entry states, i.e., the excited states prior to γ decay.

We have made a statistical model calculation to estimate the first three moments of the m_γ distribution for the following systems from which the massive transfers were observed accompanying energetic α-particle emission:[2)] 85 MeV ^{12}C + ^{154}Sm, 109 MeV ^{12}C + ^{154}Sm, and 115 MeV ^{14}N + ^{159}Tb. The first three moments μ_1, μ_2, and μ_3, which are defined as $\mu_n = < (m_\gamma - \langle m_\gamma \rangle)^n >$, have been converted into the shape parameters for convenience as presented in Table 1: the average γ-ray multiplicity $\langle m_\gamma \rangle$ the width (standard deviation) $\sigma_\gamma = \sqrt{\mu_2}$, and the skewness $s_\gamma = \mu_3/\sigma_\gamma^3$.

Computation was made by combining the second part of the Monte Carlo treatment code ICARUS (Region II)[3)] and the code GROGI2.[4)] The time-consuming first part of ICARUS (Region I), which treats the multiple-particle evaporation, was replaced by GROGI2 because we found that when it is normalized, the entry-state population P(E, J) produced by the first part is not substantially different from that obtained with GROGI2. α particles are treated as those emitted prior to successive particle evaporation from the system of interest.

Since there is no established way to construct the entrance-channel energy ϵ and angular momentum ℓ distribution $p(\epsilon, \ell)$, we assumed that $p(\epsilon, \ell) = p(\epsilon) \cdot p(\ell)$, $p(\epsilon)$ and $p(\ell)$ being given by Gaussian forms. This assumption is considered reasonably good for the present stage because gross properties of deexcitation process are mainly governed by the average values of ϵ and ℓ, and by the widths σ_ϵ and σ_ℓ. These values were estimated from experimental information[2)] and theoretical prediction.[5)] Here we confine our remarks to the sign of skewness s_γ.

As is seen from Table 1, the sign of s_γ is likely to be positive in the case of massive transfer, while being negative in the case of complete fusion. It should be reminded that the value of μ_3 is generally quite large and the sign of s_γ is determined by the sign of μ_3. To test the present result we repeated calculations for all cases presented in Table 1, changing the level density and the ratio of γ-transition strengths $C_{E1} : C_{M1} : C_{E2} : C_{E2}^{coll}$. We have found that the sign of s_γ is not changed although its absolute value is affected.

Needless to say, the sign of s_γ depends on the asymmetry of J distribution. But it is not known whether the sign of s_γ is determined independently of the E- and J- widths of P(E, J). We examined how s_γ changes as a function of P(E, J), using $P(E, J) = P(E) \cdot P(J)$ where P(E) and P(J) were Gaussian distributions with fwhm ΔE and ΔJ, and mean values $< E >$ and $< J >$. It should be stated that the existance of the yrast line is taken into account in the γ-deexcitation process (Region II). The result is, as illustrated in Fig. 1 by using typical values $< E >$ = 14.0 MeV and $< J >$ = 24.0 $\hbar$ for ^{164}Yb: The narrower J distribution tends to give a positive s_γ, while the broader one tends to reduce its value so that it becomes even negative; and the reverse is true of the E distribution

* Department of Physics, Osaka University.

Table 1. Shape parameters of γ-ray multiplicity distribution for products of massive-transfer and complete-fusion reactions.

Reaction	Product	$<m_\gamma>$	σ_γ	s_γ
85 MeV ^{12}C + ^{154}Sm [a]	^{158}Dy	11.2	2.3	0.12
109 MeV ^{12}C + ^{154}Sm [a]	^{158}Dy	12.9	2.6	0.07
115 MeV ^{14}N + ^{159}Tb [b]	^{164}Yb	14.6	3.1	0.25
69 MeV ^{10}B + ^{159}Tb [c]	^{164}Yb	13.7	3.7	−0.10
115 MeV ^{14}N + ^{159}Tb [d]	^{164}Yb	18.4	4.6	−0.05

a) The transferred fragment is ^{8}Be.
b) The transferred fragment is ^{10}B.
c) Fusion. The energy of ^{10}B gives the excitation energy of the system that corresponds to the excitation energy at the most probable energy of α particles emitted in the massive-transfer reaction $^{159}Tb(^{14}N, \alpha 5n)^{164}Yb$ at 115 MeV.
d) Fusion evaporation.

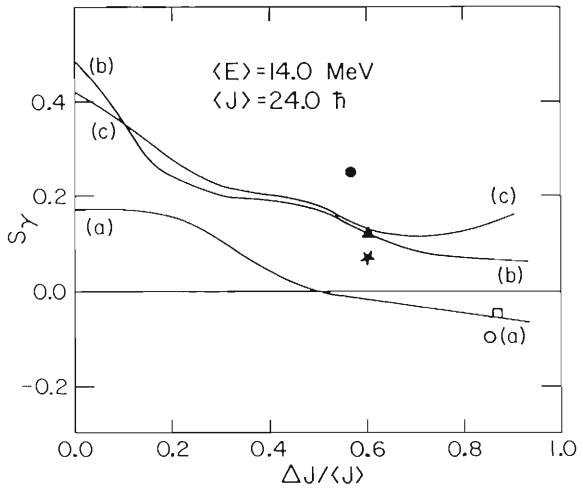

Fig. 1. Dependence of skewness s_γ on the entry-state E and J distributions: (a) $\Delta E/<E> = 0.0$, (b) $\Delta E/<E> = 0.6$, and (c) $\Delta E/<E> = 0.9$. Solid and open points represent s_γ specifically calculated for massive transfer and for complete fusion, respectively (see Table 1): massive transfer, $^{159}Tb(^{14}N, \alpha 5n)^{164}Yb$ at 115 MeV (solid circle), and $^{154}Sm(^{12}C, \alpha 4n)^{158}Dy$ at 85 MeV (solid triangle) and at 109 MeV (solid star); fusion, $^{159}Tb(^{10}B, 5n)^{164}Yb$ at 69 MeV (open circle), and $^{159}Tb(^{14}N, \alpha 5n)^{164}Yb$ at 115 MeV (open square).

effect. (These tendencies are enhanced as $<J>$ increases.) Therefore, in general, s_γ becomes positive if σ_ℓ is small and σ_ϵ is large, i.e., when ℓ values are localized in the entrance channel whose energy distribution is broad.

In summary, the m_γ distribution is expected to possess a positive s_γ in the case of massive transfer (or incomplete fusion), being contrary to the case of complete-fusion reaction. In the light of the present study it is quite understandable that s_γ measured by Geoffroy et al.[6] seems to change its sign from negative to positive as the emitted α-particle energy increases, reflecting the effect of reaction mechanisms. It is interesting to note that, in the ^{86}Kr + ^{144}Sm reaction at 490 MeV, s_γ of the m_γ distribution was found to be positive for the quasielastic region, while to be negative for the deep inelastic region.[7] Although the reaction system is very much different from the present examples, there may be some similarities in the reaction mechanisms if the sign of s_γ is the same. It would be very desirable to study the sign of skewness (or third moment) of the m_γ distribution systematically in the heavy-ion reaction.

This study was initiated at the Cyclotron Institute, Texas A & M University.

References

1) T. Inamura, M. Ishihara, T. Fukuda, T. Shimoda, and K. Hiruta: Phys. Lett., 68B, 51 (1977).

2) T.T. Sugihara: Proc. of Nobel Symp. 50, Sweden, June 23–27 (1980); Physica Scripta, 24, 108 (1981), and references therein.
3) M. Wakai and A. Faessler: Nucl. Phys., A307, 349 (1978); M. Wakai, M. Muraoka, and A. Faessler: Phys. Lett., 93B, 232 (1980).
4) J. Gilat and J.R. Grover: Phys. Rev., C3, 734 (1971); J. Gilat: Brookhaven Natl. Lab. Rep., No. BNL 50246.
5) T. Udagawa and T. Tamura: Phys. Rev. Lett., 45, 1311 (1980).
6) K.A. Geoffroy, D.G. Sarantites, M.L. Halbert, D.C. Hensley, R.A. Dayras, and J.H. Baker: ibid., 43, 1303 (1979).
7) P.R. Christensen, F. Folkmann, Ole Hansen, Q. Nathan, N. Trautner, F. Videbæk, S.Y. van der Werf, H.C. Britt, R.P. Chestnut, H. Freiesleben, and F. Pühofer: ibid., 40, 1245 (1978).

III-1-17. Angular-Momentum Transfer and Alignment Following Preequilibrium α-Particle Emission in Heavy-Ion Reactions

H. Utsunomiya, T. Nomura, S. Kohmoto, and M. Sasagase

[NUCLEAR REACTION ^{209}Bi(^{16}O, αf), E = 120 MeV, ^{209}Bi(^{20}Ne, αf), E = 134, 146 MeV; measured angular correlations.]

If a fissile nucleus is produced in a nuclear reaction as one of the reaction products, angular correlations of the fission fragments in coincidence with the other product are known to give information on the magnitude and alignment of angular momenta transferred in the reaction. We have applied this method to the study of "fast" α-particle emission in heavy-ion fusionlike reactions in order to study the reaction mechanism relevant to this phenomenon. A series of α-f angular correlation measurements were performed in ^{14}N-, ^{16}O- and ^{20}Ne-induced reactions on ^{209}Bi. We have already reported a result of the ^{209}Bi(^{14}N, αf) reaction at 115 MeV,[1] which indicates that the preequilibrium α-particle emission mainly originates from entrance angular momenta smaller than the critical angular momentum for complete fusion.

The present measurements in the ^{16}O- and ^{20}Ne-induced reactions were made at bombarding energies of 120 and 134 MeV, respectively. The grazing angular momentum is estimated to be 60 $\hbar$ in both reactions, being nearly equal to that in the ^{14}N-induced reactions mentioned above. These reactions are therefore conveniently utilized to study projectile dependence on the angular-momentum transfer and alignment following the fast α-particle emission. In addition, the measurement was performed in the ^{209}Bi(^{20}Ne, αf) reaction at 146 MeV to see an effect of the different incident energies. The experimental α-f angular correlations obtained in the ^{16}O- and ^{20}Ne-induced reactions have been found to be apparently very similar to those reported in Ref. 1. A detailed quantitative analysis similar to that in Ref. 1 is now in progress.

Reference

1) H. Utsunomiya, T. Nomura, M. Ishihara, T. Sugitate, K. Ieki, and S. Kohmoto: Phys. Lett., 105B, 135 (1981).

III-1-18. Search for α-Decay from High Spin Yrast Region

M. Sasagase, Y. Gono, Y. Itoh,* T. Kubo,
M. Sugawara,** and S. Hayashibe

NUCLEAR REACTIONS: $^{12}C + ^{208}Pb$, E_{lab} = 80 MeV and $^{14}N + ^{141}Pr$, E_{lab} = 88 MeV; α-X-ray coin., E – ΔE counter telescope and LEPS detector, enriched target.

Typical life time of equilibrium or preequilibrium α-particle emissions in heavy-ion reactions is roughly estimated to be in the order of 10^{-21} second. On the other hand, α-emissions from longer-lived ($\sim 10^{-12} - 10^{-13}$ second) high-spin states near the yrast line are also expected as reported by Grover et al.[1] We refer to the former case as type 1 and the latter as type 2. It is very useful for nuclear spectroscopy to identify these longer-lived α-emitting states of type 2. Coincidence experiments between α-particles and X-rays were performed for this purpose.

In nuclear reactions concerning medium weight nuclei, the compound nuclei de-excite emitting neutrons, γ-rays and α-particles etc. It is known that the vacancies produced in the K-shell of the atoms on occasion of nuclear reactions[2] will be occupied by electrons with the life time of about 10^{-16} second, emitting the associated K X-rays. Thus the α-particles of type 2, emitted from the compound nuclei after neutron emissions, should be coincident with the K X-rays of the compound nuclei, although the α-particles of type 1 should be coincident with those of the daughter nuclei of the α-decay.

According to the above idea, α-X-ray coincidence measurements were done for the two systems: ^{12}C(80 MeV) + ^{208}Pb and ^{14}N(88 MeV) + ^{141}Pr. We used $^{12}C^{4+}$ and $^{14}N^{4+}$ beams accelerated by the cyclotron and self-supporting ^{208}Pb enriched target of about 1 mg/cm^2 and ^{141}Pr target of about 2 mg/cm^2. Emitted α-particles were detected with a counter telescope of 26.7 – 1000 μm Si detectors. Coincident X-rays were measured with a 1 cm^3 LEPS detector. The four fold coincidence spectra of E – ΔE – E_X – $T_{X\alpha}$ have been measured, where E and ΔE are the signals from the α-counter, E_X is the X-ray energy signal, and $T_{X\alpha}$ is the time relation between the X-ray and α-particle.

Examples of α-singles and coincidence spectra are shown in Fig. 1. For the $^{12}C + ^{208}Pb$ system, some of known α-decay lines[3] from the ground and excited states of ^{216}Ra were observed to be coincident with the K X-rays of Ra and not with those of Rn. The level scheme of ^{216}Ra and α-decay lines are presented in Fig. 2. The ground state of ^{216}Ra decays with the life time of 0.18×10^{-6} second and the life times of the excited states are in the order of 10^{-9} second. Thus the α-decay lines from the excited states are relatively enhanced in Fig. 1(c). The multiplicity of K X-ray of Ra for the α-decay line from the ground state of ^{216}Ra can be obtained from the intensity ratio of the coincidence spectrum relative to the singles spectrum of α-particles. It is deduced to be $\sim$ 0.8.

* Faculty of Science, Tohoku University.
** Chiba Institute of Technology.

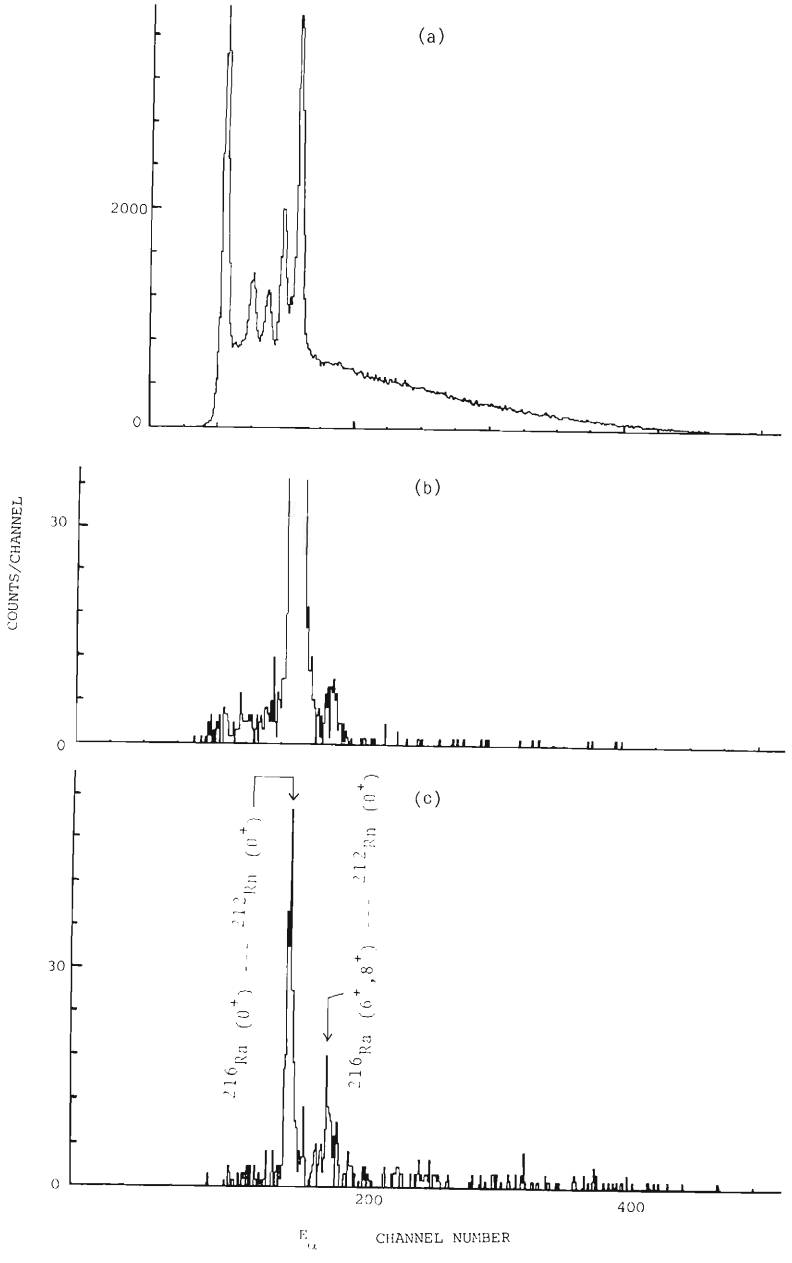

Fig. 1. (a) α-singles spectrum for the $^{208}Pb(^{12}C, \alpha)$ reaction (b) and (c) α-spectra coincident with K X-rays of Ra: (b) delayed component ($20ns \lesssim T_{X\alpha} \lesssim 230ns$) and (c) prompt component ($T_{X\alpha} \lesssim 20ns$).

For the $^{14}N + ^{141}Pr$ system, a definite evidence of the α-emission of type 2 is not obtained yet. An X-ray spectrum coincident with α-particles is shown in Fig. 3. In the K X-ray region of Dy, unassigned γ-ray peak may exist and the exact yield of Dy X-ray could not be obtained. The coincident yield of the K X-rays of Dy is estimated to be less than 1/2000 of that of Gd, where the former is expected to associate with the type 2 α-particles and the latter with the type 1.

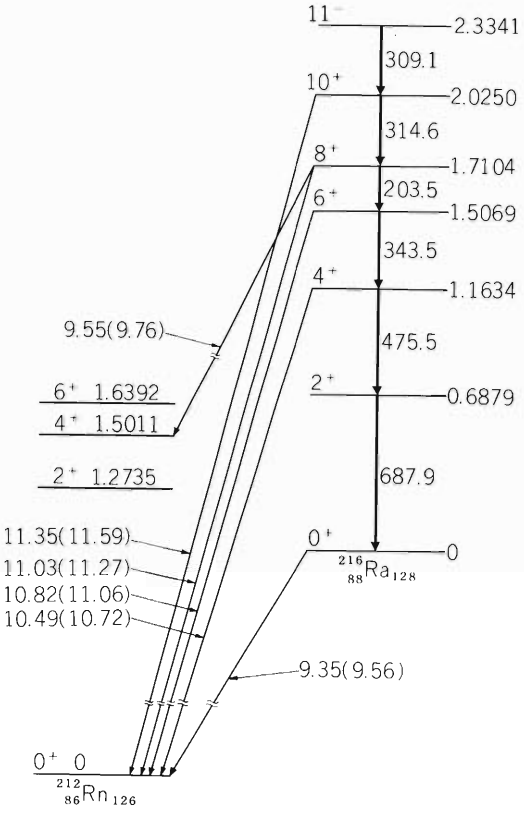

Fig. 2. Level scheme of ^{216}Ra (Ref. 3). The γ-ray transition energies are given in keV unit, whereas the α-decay energies and the level energies are given in MeV unit. The Q-values of the α-decays are given in parentheses in MeV unit.

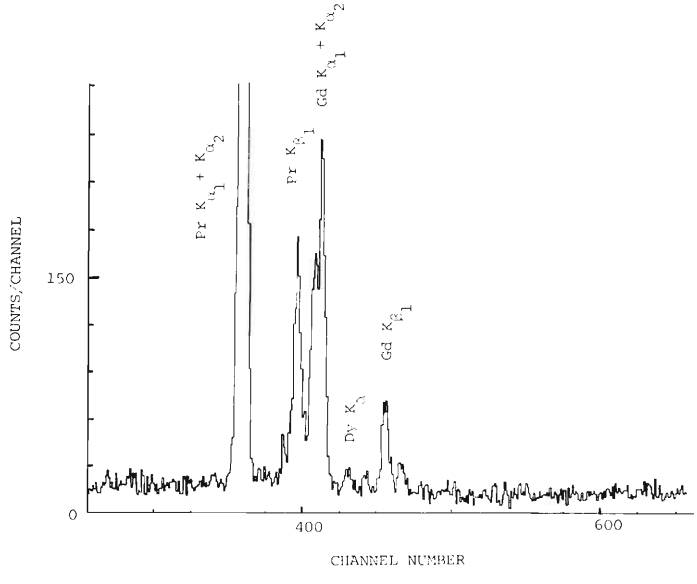

Fig. 3. X-ray spectrum coincident with α-particles for the ^{141}Pr(^{14}N, α) reaction.

References

1) J.R. Grover and J. Gilat: Phys. Rev., 157, 823 (1967).
2) J.U. Andersen, E. Lægsgarrd, M. Lund, and C.D. Moak: Nucl. Instr. and Methods, 132, 507 (1976).
3) T. Nomura, K. Hiruta, M. Yoshie, H. Ikezoe, T. Fukuda, and O. Hashimoto: Phys. Lett., 58B, 273 (1975).

III-1-19. In-Beam γ-Ray Spectroscopy of ^{216}Ra

Y. Itoh,* Y. Gono, M. Sasagase, T. Kubo,
M. Sugawara,** S. Hayashibe, K. Hiruta, and T. Nomura

NUCLEAR REACTIONS ^{208}Pb(^{12}C, 4n) E = 80 MeV; γ-γ coin., $I_\gamma(\theta)$, $I_\gamma(t)$, linear polarization (γ). ^{216}Ra deduced levels. Ge(Li) and LEPS detectors, enriched target.

This study is one of a series of experiments on high-spin states of nuclei in the translead region. In this report we give a preliminary result of in-beam γ-ray spectroscopy on ^{216}Ra.

We performed measurements of singles γ-ray spectra, angular distributions, time spectra, γ-γ coincidences, and linear polarizations. States in ^{216}Ra were populated via the ^{208}Pb(^{12}C, 4nγ) reaction at E = 80 MeV.

Angular distributions of γ-rays were measured at five angles from θ = 34° to 90° with 72 cm^3 Ge(Li) and 1 cm^3 LEPS (Low Energy Photon Spectrometer) detectors. The LEPS detector was used especially to resolve 344 keV doublet (343.5 keV and 344.2 keV) and to observe 51.4 keV γ-ray with good statistics. This low energy 51.4 keV transition in ^{216}Ra was found for the first time in the α-γ coincidence study.[1] The data were fitted to the equation $W(\theta) = A_0 + A_2 P_2(\cos\theta) + A_4 P_4(\cos\theta)$, where P_2 and P_4 are Legendre polynomials. The γ-ray intensities were obtained from the angular distribution coefficients A_0. Time spectra of γ-rays with respect to RF signals of the cyclotron were measured with 1 cm^3 LEPS and no long-lived ($\gtrsim$ 10 ns) component was observed. The γ-γ coincidences were measured with Ge(Li) – Ge(Li) and Ge(Li) – 15 cm^3 LEPS combinations. The latter combination was useful to confirm the 51.4 keV transition. Linear polarizations of γ-rays were measured by using a Compton polarimeter with a pair of high-purity Ge diodes.[2]

Figure 1 shows a preliminary level scheme of ^{216}Ra. The order of transitions was determined considering the total transition intensities taking account of the internal conversion coefficients (ICC).[3] Up to (14^+) level, we referred to Nomura et al.[4] The result of the linear polarization measurements indicates that all transitions except the 344 keV doublet below the (14^+) level are electric ones. This confirms the parity of these levels. In Fig. 1, the order of 344.2 keV and 613.3 keV transitions is reversed comparing to that of Nomura et al.[4] based on their transition intensities.

Above the (14^+) state, we assumed E2 modes for quadrupole transitions (220.5 keV and 290.1 keV). Half-lives for M2 transitions calculated from the Weisskopf estimate[5] are longer than 100 ns for both Eγ = 220.5 keV and 290.1 keV with the ICC corrections[3] while those for E2 ones are shorter than 10 ns. The M2 assignments to these transitions are therefore thought to be improbable because of the absence of the long-lived ($\gtrsim$ 10 ns) component in the observed time spectra. The angular distribution of the 51.4 keV transition shows a dipole character. We assigned an E1 mode to it because its transition intensity for M1 case should exceed that of the 688.2 keV, $2^+ \rightarrow$ g.s. transition. The order of the 220.5, 398.6, and 556.9 keV transitions could

* Faculty of Science, Tohoku University.
** Chiba Institute of Technology.

not be determined definitely since it depends on whether two dipole transitions (398.6 keV and 556.9 keV) are E1 or M1. In Fig. 1, three transitions were located according to their γ-ray intensities. More detailed analysis is in progress.

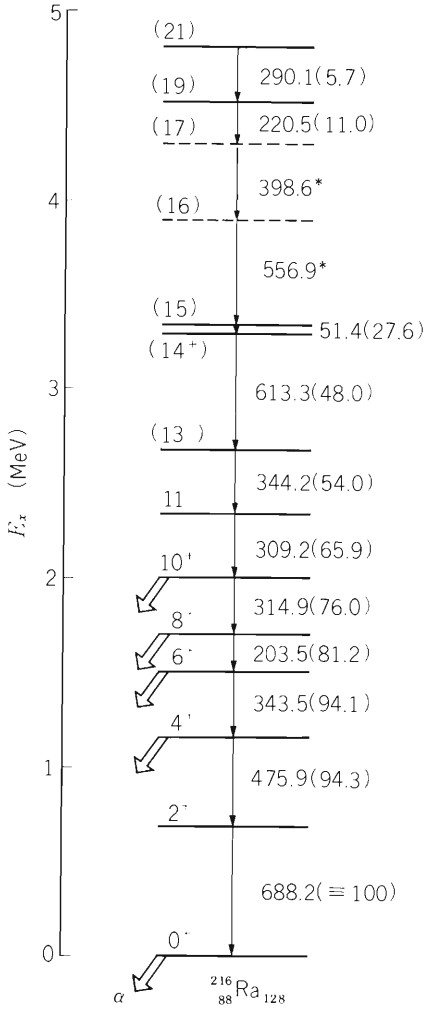

Fig. 1. A preliminary level scheme of ^{216}Ra. The blank arrows indicate α-decay.[4] Transition energies are in keV unit. The numbers in parentheses are relative transition intensities. Errors of these intensities are less than 10 %. Two intensities denoted by asterisks could not be given definitely. See the text.

References

1) M. Sasagase, Y. Gono, Y. Itoh, T. Kubo, M. Sugawara, and S. Hayashibe: p. 61 in this report.
2) T. Matsuzaki, H. Taketani, M. Ishii, and M. Oshima: Nucl. Instr. and Methods, 188, 63 (1981).
3) F.Rösel, H.M. Fries, K. Alder, and H.C. Pauli: A.D. and N.D.T., 21, 292 (1978).
4) T. Nomura, K. Hiruta, M. Yoshie, H. Ikezoe, T. Fukuda, and O. Hashimoto: Phys. Lett., 58B, 520 (1975).
5) C.M. Lederer and V.S. Shirley (ed.): "Table of Isotopes, 7th ed.", John Wiley & Sons, Inc., New York, Chichester, Brisbane, and Tronto (1978).

III-2. Atomic and Solid-State Physics

1. A Broad Range Crystal Spectrometer

Y. Awaya, A. Hitachi, and H. Kumagai

A broad range crystal spectrometer has been designed and constructed for the purpose of studying the X-rays following the heavy-ion atom collisions with high resolution and high efficiency. It analyses the X-rays of energies in the range from E_1 to E_2 simultaneously ($|\theta_1 - \theta_2| \approx 10°$, θ_1 and θ_2 being Bragg angles corresponding to E_1 and E_2, respectively). A flat crystal and a position sensitive proportional counter (PSPC) were used. The whole system of the spectrometer is shown in Fig. 1.

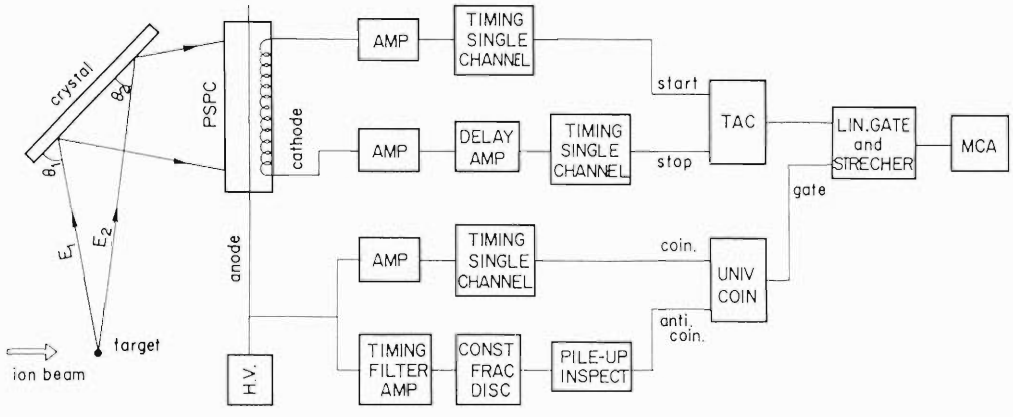

Fig. 1. The whole system of the spectrometer.

Fig. 2. A photograph of the spectrometer in the scattering chamber.

The PSPC is of a gas-flow type and operated at the pressure of 3 atm. The size of its window is 10 cm × 1 cm and covered with 500 μm Be sheet. A position signal is obtained from the cathode (multiwire cathode connected with a delay line of 1.6 μsec) and is gated by a pulse height signal from the anode. This reduces the background caused by the γ-rays induced by nuclear reactions and the X-rays with different energies. Spurious position signals caused by photons incident within 4 μsec are eliminated by using a pile-up inspector circuit.

The PSPC was mounted on an arm which can be rotated around the center of the surface of the crystal. This unit was set on a turn arm of the 75 cm-diameter scattering chamber,[1] so that the angular distribution of the X-rays can be measured. A photograph of the spectrometer in the scattering chamber is shown in Fig. 2.

As an example of the spectrum obtained by using this spectrometer, the spectrum of Ti K X-rays induced by 81.2 MeV N ions is shown in Fig. 3. A strip target of 1 mm wide and 4 μm thick was used. The energy resolution of the spectrometer depends on the width of the X-ray source, as well as the distance between the target and the crystal and that between the crystal and the PSPC, which were 14.5 cm and 13 cm in the case shown in the figure. The crystal of LiF(200) was used. The energy resolution of the spectrometer is comparable to that of the step-scanning crystal spectrometer[2), 3)] reported previously with a flat crystal and Soller slits and the data taking time is significantly reduced, e.g. by a factor of 20 in this case.

The detailed report on this spectrometer will be given elsewhere.[4)]

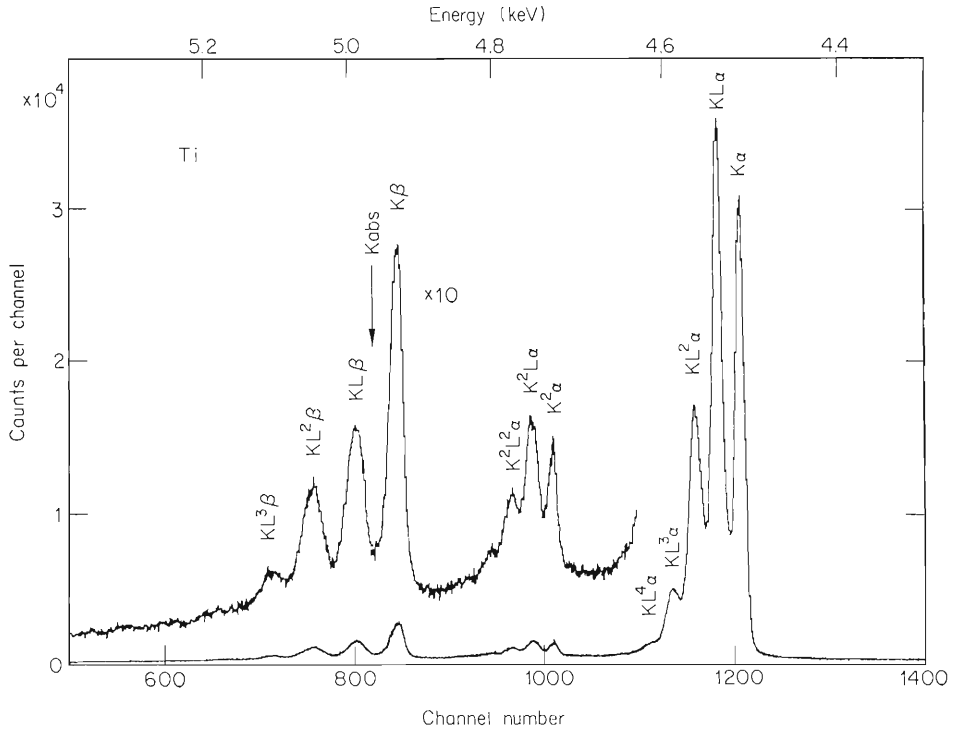

Fig. 3. Spectrum of Ti K X-rays induced by N ions obtained by this spectrometer. The symbol $K^m L^n$ denotes the m K-shell and n L-shell vacancies in the initial state.

References

1) T. Fujisawa and Y. Awaya: IPCR Cyclotron Progr. Rep., 1, 54 (1967).
2) Y. Awaya, A. Akiba, T. Katou, H. Kumagai, Y. Tendow, K. Izumo, T. Takahashi, A. Hashizume, M. Okano, and T. Hamada: ibid, 10, 78 (1976).
3) Y. Awaya, M. Akiba, T. Katou, H. Kumagai, Y. Tendow, K. Izumo, T. Takahashi, A. Hashizume, M. Okano, and T. Hamada: Phys. Lett., 61A, 111 (1977).
4) A. Hitachi, H. Kumagai, and Y. Awaya: Nucl. Instr. and Methods, (in press).

III-2-2. Angular Distribution of X-Rays Following Multiple Inner Shell Ionization

A. Hitachi, Y. Awaya, T. Kambara, M. Kase,
H. Kumagai, T. Tonuma, and A. Yagishita

Angular distributions of Ti K X-rays and Sn L X-rays induced by N-ion bombardment have been measured using a broad range X-ray crystal spectrometer.[1), 2)] Ti (1 mm wide and 4 μm thick) and Sn (1 mm wide and 1 μm thick) targets were excited by 81.2 MeV N^{7+} ion beam from the cyclotron. A flat crystal of LiF (200) was used for the dispersion of X-rays.

Typical spectrum obtained for Ti is shown elsewhere.[1)] The relative intensities of Kα and Kβ satellite lines to that of Kα diagram line are plotted as a function of emitted photon angles in Fig. 1. These satellite lines are found to be isotropic within experimental errors assuming that Kα line is isotropic.

Spectra obtained for Sn L X-rays at various photon angles are shown in Fig. 2. Anisotropy was observed for some satellite lines. The analysis of the data is in progress.

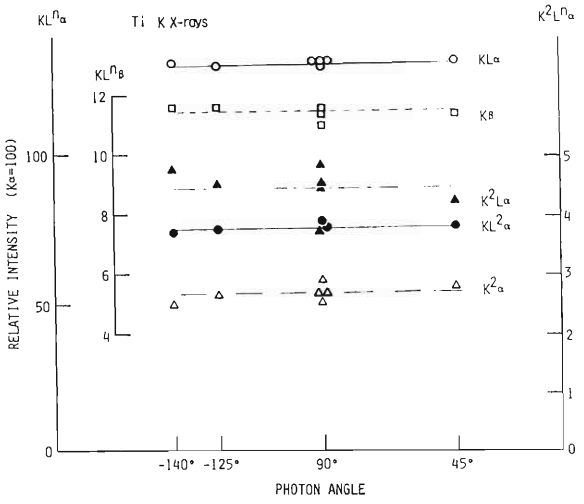

Fig. 1. Angular distribution of Ti K satellite lines following 81.2 MeV N^{7+} bombardment relative to Kα diagram line.

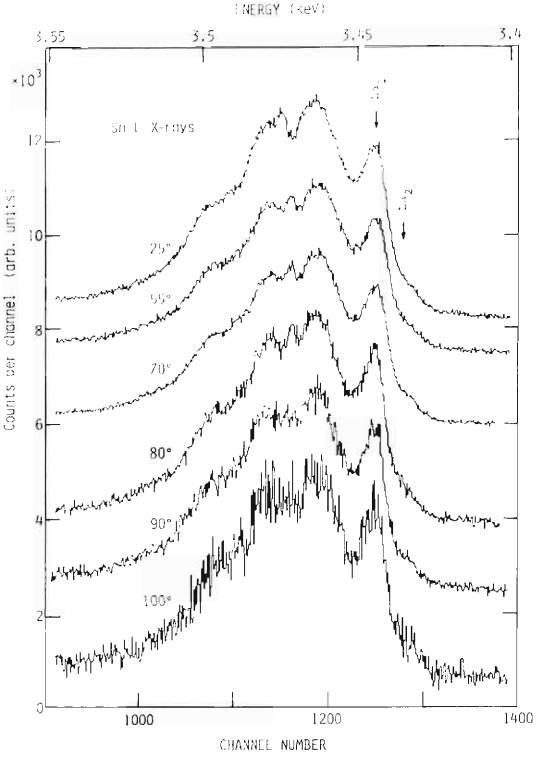

Fig. 2. Sn L X-ray spectra at various photon angles excited by 81.2 MeV N^{7+} ions.

References

1) Y. Awaya, A. Hitachi, and H. Kumagai: p. 66 in this report.
2) A. Hitachi, H. Kumagai, and Y. Awaya: Nucl. Instr. and Methods, (in press).

III-2-3. Ionization of Gases by Ion Bombardment

T. Tonuma, A. Yagishita, M. Kase, T. Kambara,
Y. Awaya, H. Kumagai, and I. Kohno

In order to obtain information on multiple ionization in ion-atom collisions, we set up an experimental apparatus to measure charged ions of gas targets by ion bombardment. The apparatus used in producing charged ions is shown in Fig. 1. A beam of ions is crossed by a gas target emerging from a gas jet of 1 mm in diameter and ionizes gas atoms. Charged ions are extracted in the direction perpendicular to the beam direction by an extraction electric field produced by parallel plate electrodes with a slit and are focused by an Einzel lens and an analyzer magnet. Charge-analyzed ions, which are deflected through 90° along the curve of 16 cm radius by the analyzer magnet, are detected by a channeltron detector. The magnetic field of the analyzer magnet is kept constant and charge spectrum of the ionized gas target is observed by scanning electric potentials of the parallel plate electrodes. The apparatus has two 6″ oil diffusion pumps (P_1,P_2) and one 2″ oil diffusion pump(P_3).

Figure 2 shows the Ar charge spectrum produced by 84 MeV N^{4+} ions obtained by the cyclotron. The magnetic field was kept at 1.1 kG. The background pressure was 3×10^{-6} Torr. When Ar gas was introduced at a rate of 1 cc/min, the pressure rose to about 8×10^{-5} Torr. Charge states up to Ar^{7+} were observed.

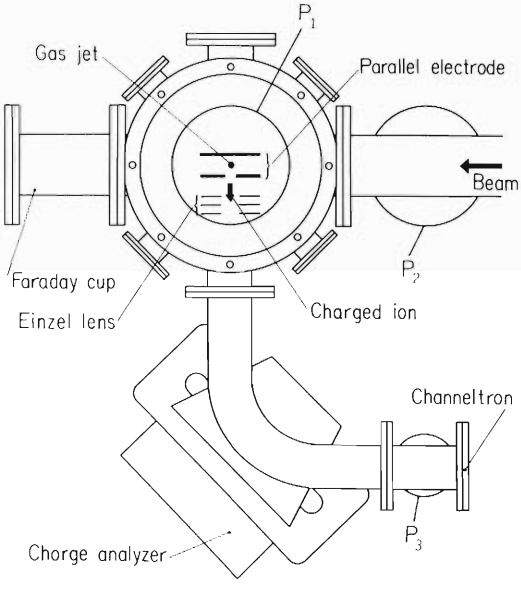

Fig. 1. Schematic diagram of the apparatus. P_1, P_2, and P_3 are pumps.

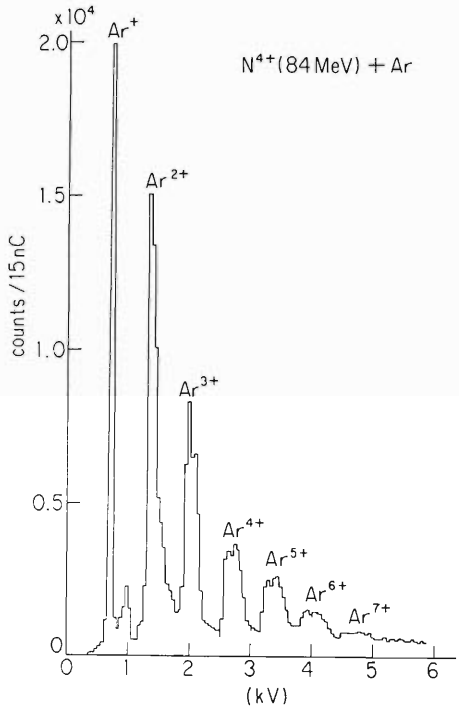

Fig. 2. Ar charge spectrum by 84 MeV N^{4+} ions.

III-2-4. Target Gas Pressure Dependence of X-Rays from 110 MeV Ne^{9+} Ions

T. Kambara, Y. Awaya, A. Hitachi, M. Kase,
I. Kohno, H. Kumagai, and T. Tonuma

The energy spectra of K X-rays from 110 MeV Ne^{9+} ions (hydrogen-like) in gaseous targets were measured at various gas pressures ranging from 0.5 to 300 Torr. The targets were H_2, He, CH_4, N_2, O_2, Ne, and CH_3OH. A Si(Li) detector with a resolution of 240 eV (FWHM) for 6.4 keV X-rays was used for the measurements. The experimental set-up was reported previously.[1)]

In the spectra of the X-rays, two peaks appear around 1 keV which correspond to the K X-rays from the Ne^{9+} ions. The X-rays from the 2p – 1s transition (1.02 keV) make one peak at lower energy and those from the np – 1s transitions with n greater than 2 (1.21 – 1.36 keV) make another peak at higher energy. The resolution of the detector could not resolve the latter peak to each transition but high resolution measurement with a crystal spectrometer verified that the excited states up to n = 6 contribute to the peak.[1)]

The spectra obtained were fitted to the sum of two Gaussian curves by the least square fitting. The position, width and yield of each peak were compared for various gas species and their pressures.

We have found some differences in the pressure dependence of the spectra among gas species. For light gas targets (H_2 and He), the yield of the X-rays for both peaks are not proportional to the pressure but the yield normalized to the pressure decreases greatly when the pressure increases,

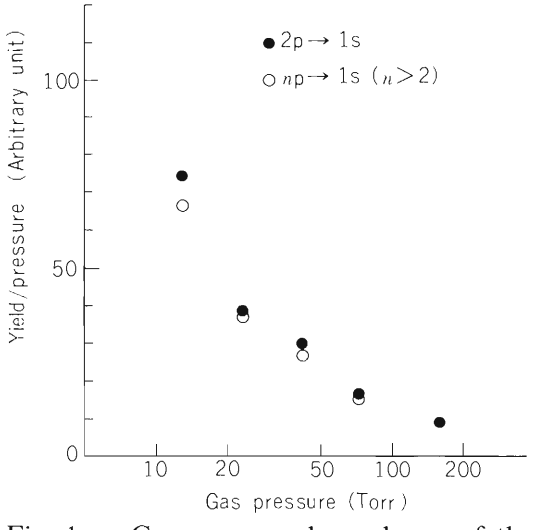

Fig. 1. Gas pressure dependence of the yield of X-rays normalized to the pressure of He gas target. Closed circle: 2p – 1s transition; open circle: sum of np – 1s transitions (n > 2).

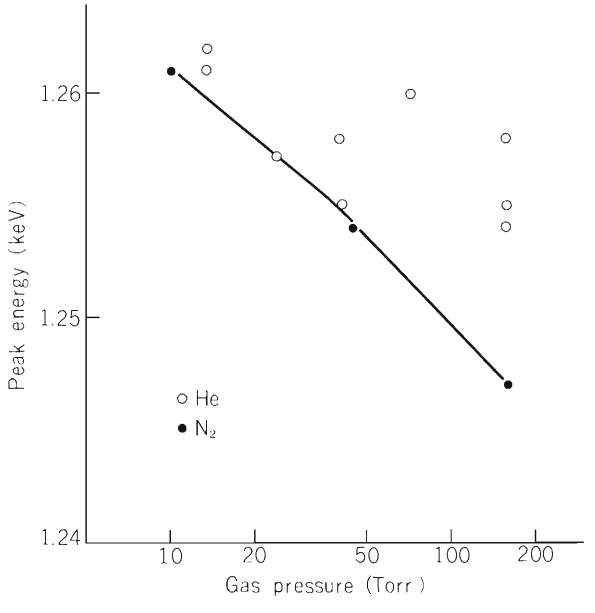

Fig. 2. Gas pressure dependence of the peak position from np – 1s transitions (n > 2). Open circle: He gas target; closed circle: N_2 gas target.

as shown in Fig. 1. For the other targets, the yield seems to be proportional to the pressure. The position of the peak from the 2p – 1s transition does not change with the change of pressure, but the peak at higher energy, which is a superposition of the unresolved peaks from the np – 1s transitions ($n > 2$), shifts to lower energy when the pressure increases. One exception is the case of He gas target where both the peaks do not shift greatly. Figure 2 shows the pressure dependence of the position of the peak at higher energy in N_2 and He targets.

The non-linear pressure dependence of the X-ray yield in the light targets is considered to be due to small electron transfer probability from the target molecules into the projectile ions. The OBK model[2] predicts the cross section values of about 10^{-20} cm^2 for H_2 and He targets, which are smaller than those for the other targets by 10^{-3} – 10^{-4}. Therefore projectile ions in the lighter gases do not exchange electrons with the gas molecules frequently enough to reach the equillibrium charge state distribution in the gas before they get to the detection area. The fraction of Ne^{9+} ions in the projectiles may be smaller for higher target pressure which means larger target thickness from the entrance of the target cell, and the K X-rays from the Ne^{9+} ions may not increase in proportion to the gas pressure.

The energy shift of the peak from the np – 1s transitions ($n > 2$) is considered to come from the collisional quenching[3] of the higher excited states of the Ne^{9+} ions. When the ions are in higher excited states, they have longer lifetime and larger cross section of collisions with the target molecules than those in lower states, and they can more easily be changed to other states by collisions before they emit X-rays. The collisional quenching process becomes more dominant for smaller mean free path of the ions in the gas, which is inversely proportional to the gas pressure. The X-rays following the transitions from higher levels disappear when the gas pressure increases and the observed peak shifts to lower energy. The small shift of the peak in the case of He target may be interpreted by assuming that the collision cross section between the excited Ne ions and He atoms is smaller than those between the Ne ions and other molecules. We expect to obtain the information of the collision cross section between excited ions at high charge state and various gas molecules by making more detailed experiments and analyses of the X-ray spectra.

References

1) T. Kambara, Y. Awaya, A. Hitachi, M. Kase, I. Kohno, and T. Tonuma: IPCR Cyclotron Progr. Rep., 14, 88 (1980).
2) H.D. Betz: "Method of Experimental Physics", (Ed. L. Marton and C. Marton), Academic Press, New York, 17, 96 (1980).
3) D.L. Matthews, R.J. Fortner, and G. Bissinger: Phys. Rev. Lett., 12, 664 (1976).

III-2-5. Chemical Effects on F, Al and Si Kα, and Cu Lα Satellite Spectra Produced by 2.4 MeV He^{++}

M. Uda, K. Maeda, Y. Sasa, and A. Koyama

Chemical effects have been reflected in intensity distributions of X-ray satellite spectra related to the multiple ionization. Rather pronounced change in the intensity distribution has been observed in F Kα spectra [1)-3)] which are originated from the electron transition between the outermost and 1s shells. However, the change has been depressed in the innershell-innershell transitions, such as Al, Si, S, and Cl Kα's.[4),5)] It is difficult to compare the change in the intensity distributions for these elements directly because the experiments have been carried out under different conditions. In the present experiment, the same excitation condition (2.4 MeV He^{++}) was employed for all the elements studied.

He^{++} was accelerated by the Tandetron (General Ionex Corp.). A Bragg spectrometer was equipped with a rubidium acid phthalate (010) flat crystal. NaF, AlF_3, CuF_2 for F Kα, Al and AlF_3 for Al Kα, Si and SiO_2 for Si Kα, and Cu and CuF_2 for Cu Lα, β were used.

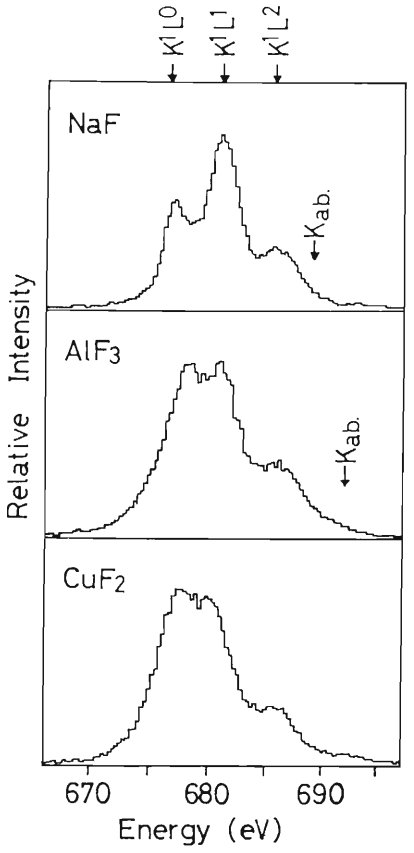

Fig. 1. F Kα satellite spectra produced by 2.4 MeV He^{++}. $K_{ab.}$ means the K absorption edge.

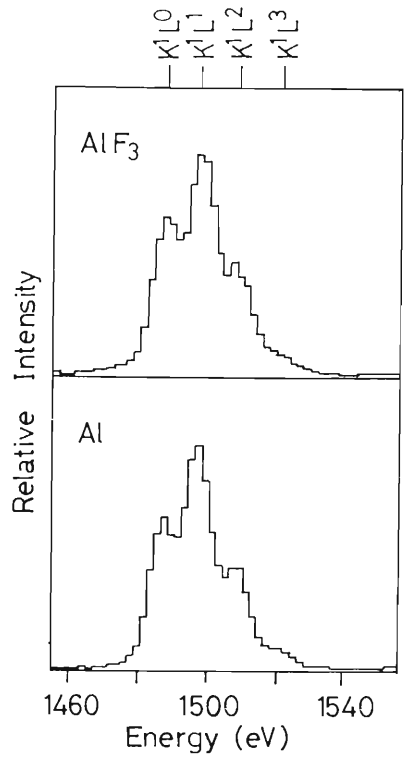

Fig. 2. Al Kα satellite spectra produced by 2.4 MeV He^{++}.

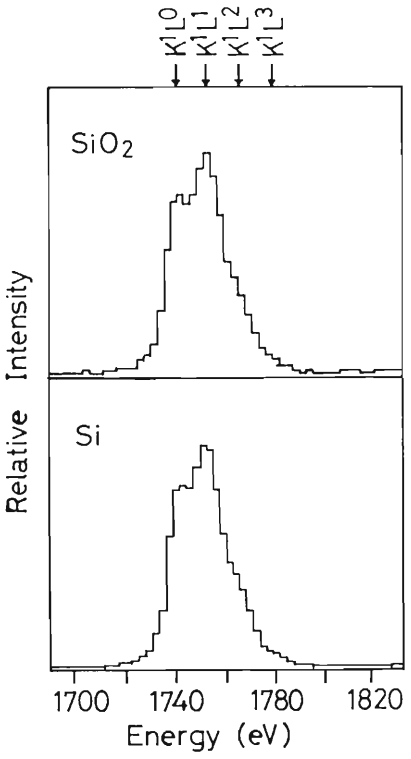

Fig. 3. Si Kα satellite spectra produced by 2.4 MeV He^{++}.

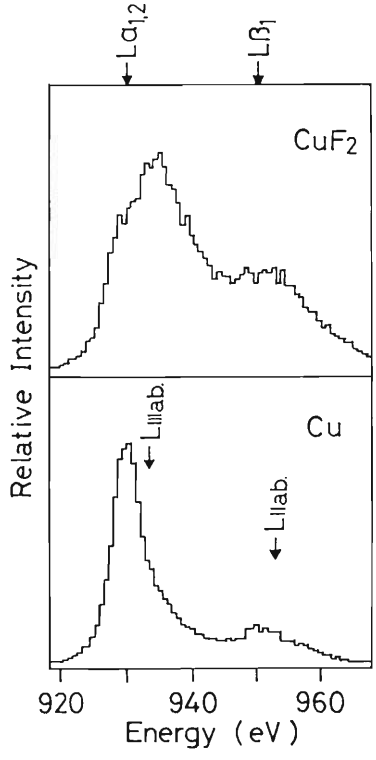

Fig. 4. Cu Lα, β satellite spectra produced by 2.4 MeV He^{++}.

Prior to the X-ray emission, electron vacancies produced in the valence band are expected to be filled with valence electrons localized on ligand atoms. Enhanced chemical effect should then be observed on the intensity distribution of the X-ray satellite spectra which are originated from the transition of the valence electrons to the inner shell (Fig. 1 for F Kα and Fig. 4 for Cu Lα, β). For elements whose X-ray emission relates indirectly to the electron vacancy transfer between the atoms of interest and surrounding atoms, much smaller chemical effect than that of the former is expected to be seen. This is indeed the case in Al Kα and Si Kα as shown in Figs. 2 and 3, respectively.

References

1) M. Uda, H. Endo, K. Maeda, Y. Awaya, M. Kobayashi, Y. Sasa, H. Kumagai, and T. Tonuma: Phys. Rev. Lett., 42, 1257 (1979).
2) H. Endo, M. Uda, and K. Maeda: Phys. Rev., A22, 1436 (1980).
3) M. Uda, H. Endo, K. Maeda, Y. Sasa, and M. Kobayashi: Z. Physik A., 300, 1 (1981).
4) P. G. Burkhalter, A. R. Knudson, D. J. Nagel, and K. L. Dunning: Phys. Rev., A6, 2093 (1972).
5) R. L. Watson, A. K. Leeper, B. I. Sonobe, T. Chiao, and F. E. Jenson: ibid., 15, 914 (1977).

III-2-6. Chemical Effect on O Kα Satellite Spectra Induced by 2.4 MeV He^{++} Ions

K. Maeda, Y. Sasa, K. Fuwa, and M. Uda

We have extensively investigated the chemical effects on the intensity distributions of the X-ray satellites due to multiple ionization.[1)-4)] The present paper deals with the He^{++}-ion induced O Kα satellite spectra obtained from a series of oxygen compounds.

2.4 MeV He^{++}-ion beams accelerated by the Tandetron (General Ionex Corp.) were used to generate the K^1L^n states for oxygen, where K^1L^n denotes a configuration with a single K and n L vacancies. Target materials used were films of MgO, Al_2O_3, SiO_2, CuO, and Na_2SO_4, all in 1–6 mg/cm^2 thickness. The emitted X-ray spectra were recorded on a Bragg spectrometer equipped with a flat analyzing crystal.

The intensities of the O Kα satellites are supposed to be weak because in the compounds of small ionicity such as oxides, considerable number of the L shell vacancies generated at the time of ion impact may be filled with the valence electrons of the surrounding atoms prior to the X-ray emission.[1)] Therefore, we magnified the O K^1L^2 satellite intensity utilizing a particular analyzing crystal, rubidium acid phthalate (RAP) to make clear the small change in the satellite intensities. RAP has a reflectivity spike at 532 eV where the O K^1L^2 satellite is just situated. Electron induced O Kα spectra of MgO analyzed with two kinds of crystals, RAP and clinochlore, are shown in Fig. 1 to demonstrate such an anomalous reflectivity of RAP. The spectrum obtained by RAP shows a peak at 532 eV, whereas no peak is detected at this energy region when the clinochlore is used, whose reflection coefficient is almost constant within the measured energy range.[5), 6)] The energies of K^1L^1 and K^1L^2 satellites given in the figure were calculated, on the basis of the sudden approximation, by the DV-Xα method[7)] and were determined by referring to the energy of the diagram line (K^1L^0). The reflection coefficient of RAP at 532 eV was evaluated to be about 4

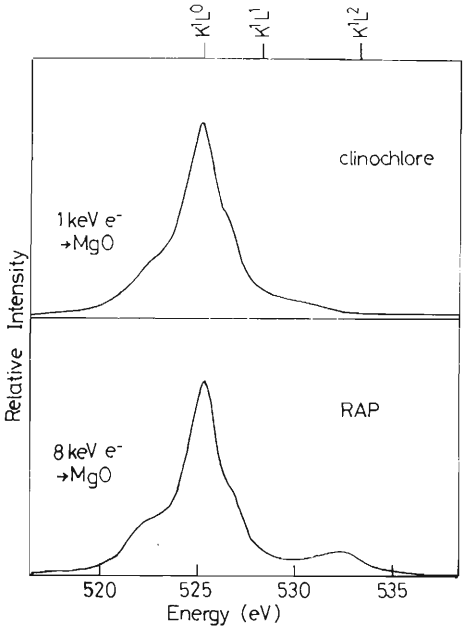

Fig. 1. Electron induced O Kα spectra of MgO analyzed with RAP and clinochlore.

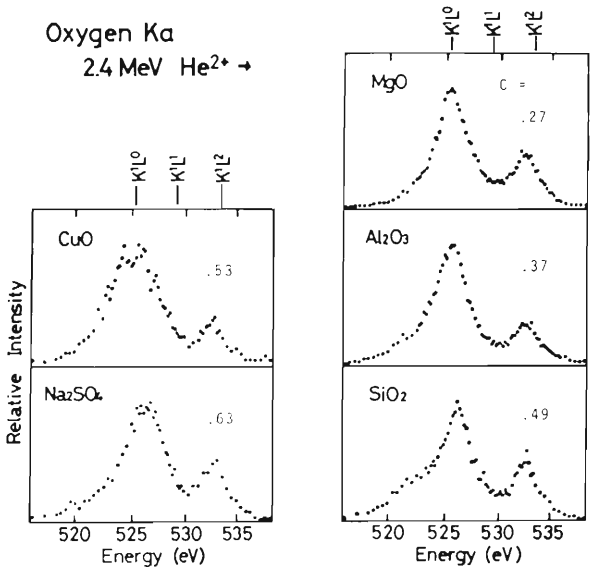

Fig. 2. O Kα spectra of MgO, Al_2O_3, SiO_2, CuO, and Na_2SO_4 induced by 2.4 MeV He^{++} ions. RAP was used as the analyzing crystal. C means the covalency calculated from the relation, C = 1 − I, where I is the Pauling ionicity.[8]

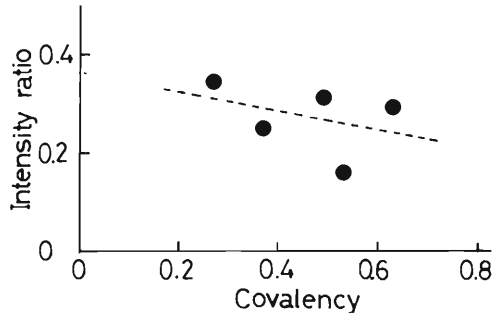

Fig. 3. The observed intensity ratio of the K^1L^2 satellite to the diagram line of O Kα against the covalency.

times larger than that in the neighbouring energy region.

The He^{++}-ion induced O Kα spectra analyzed with RAP are shown in Fig. 2. A strong peak identified as the O K^1L^2 satellite is found in each spectrum. The observed intensity ratios of the satellites to the diagram lines are plotted, in Fig. 3, against the covalency of the compounds. The intensity ratios tend to decrease with the increase of the covalency. Such a trend is consistent with the results for F Kα spectra.[1)-3)]

The crystals such as RAP and KAP, which have a reflectivity anomaly, have been considered to be unsuitable for X-ray analysis. However, making use of RAP as the analyzing crystal, we could magnify the weak O K^1L^2 satellite and could detect the chemical effect reflected in the O Kα satellite spectra, successfully.

References

1) M. Uda, H. Endo, K. Maeda, Y. Awaya, M. Kobayashi, Y. Sasa, H. Kumagai, and T. Tonuma: Phys. Rev. Lett., 42, 1257 (1979).
2) H. Endo, M. Uda, and K. Maeda: Phys. Rev., A22, 1436 (1980).
3) M. Uda, H. Endo, K. Maeda, Y. Sasa, and M. Kobayashi: Z. Physik A, 300, 1 (1981).
4) M. Uda, K. Maeda, H. Endo, Y. Sasa, and M. Kobayashi: IPCR Cyclotron Progr. Rep., 13, 86 (1979).
5) R.L. Blake: Adv. X-ray Analysis, 13, 352 (1970).
6) K. Maeda and M. Uda: Adv. X-ray Chemical Analysis (Japan), 8, 19 (1976).
7) H. Adachi, M. Tsukada, and C. Satoko: J. Phys. Soc. Japan, 45, 875 (1978).
8) L. Pauling: "The Nature of the Chemical Bond", 3rd ed., Cornell Univ. Press, N. Y. (1960).

III-2-7. Preliminary Experiments for PIXE

K. Maeda, Y. Sasa, and M. Uda

Preliminary experiments have been carried out to obtain optimum conditions for PIXE

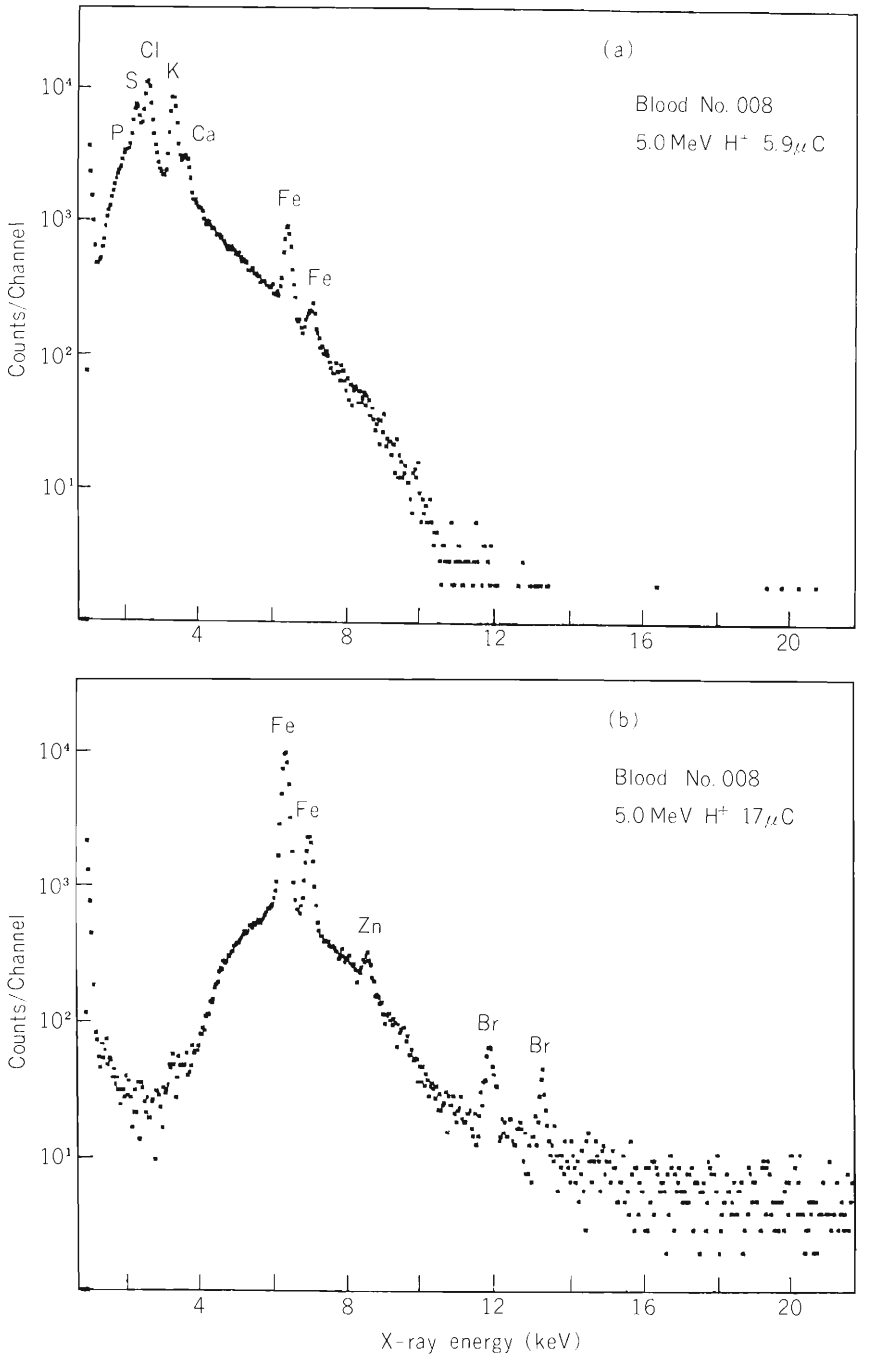

Fig. 1. X-ray spectra of blood from a healthy person induced by 5.0 MeV H^+ ion impact; (a) without absorber and (b) with a 60 μm Al absorber. Backings are Mylar foils.

(particle induced X-ray emission) analysis.

Our present interest is in finding the correlations between diseases and trace element concentrations in biological tissues. At the first step we chose healthy whole blood as samples to estimate the mean composition of normal human blood. The blood samples treated with anticoagulant were deposited on 4 μm thick Mylar films or 250 μm thick Be foils. The anticoagulant used was potassium salt of EDTA. The impurities contained in the backings are as follows: Ca in Mylar; Al, Si, Fe, and Ni in Be. Two kinds of ion beams, 5.0 MeV H^+ and 2.4 MeV He^{++} accelerated by the cyclotron and the Tandetron (General Ionex Corp.), respectively, were utilized to induce characteristic X-rays. The emitted X-rays were detected by a Si(Li) detector (FWHM = 200 eV at 5.9 keV) and processed by a multichannel analyzer. In some cases X-ray absorbers were inserted between the sample and the detector to depress undisired X-rays.

A dozen of the samples were analyzed with this method. Typical spectra taken with an without X-ray absorber for the blood sample induced by 5.0 MeV H^+ ion impact are represented in Fig. 1. Eight elements, P, S, Cl, K, Ca, Fe, Zn, and Br, were detected. No significant difference in the elemental concentrations was observed among the samples used here. The ability of the Tandetron for PIXE analysis was also checked by use of one of the blood samples. The spectrum shown in Fig. 2 indicates that the Tandetron is particularly suitable for the analysis of light elements. Further investigation is in progress for the choice of appropriate experimental parameters, such as bombarding energy, particle type, absorber, backing etc.

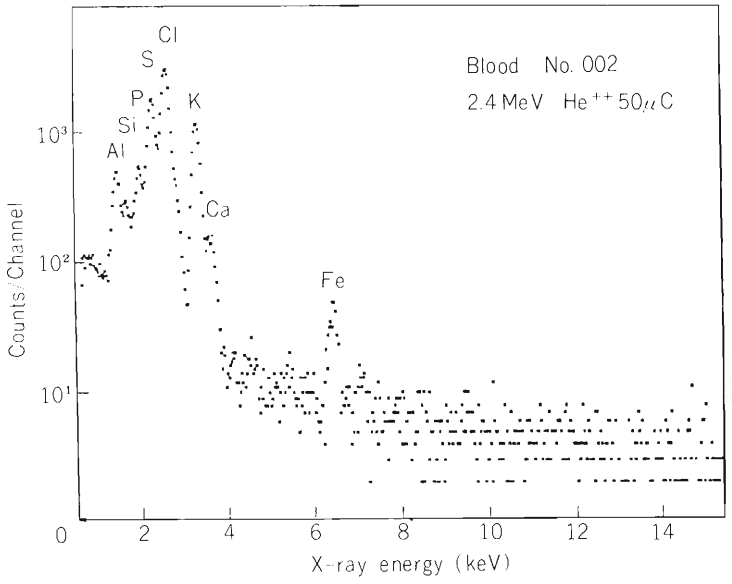

Fig. 2. X-ray spectrum of blood from a healthy persons induced by 2.4 MeV He^{++} ion impact without absorber. A Be backing is used.

III-2-8. Backscattering Spectra from Silicides

M. Uda, K. Hirose, N. Yokoyama, N. Imajo,
I. Odomari, K. Fuwa, and Y. Sasa

The Schottky barrier is formed at the interface between a metal and a semiconductor. Its height for Si and silicide contact has been reported to be related linearly to the heat of formation[1] and the work function[2] of silicides. However, Pt-Si and Ir-Si systems are exceptions to such empirical law. To get the general rule, bonding natures or electronic structures of outermost shells of the silicides have to be investigated and classified systematically. For this purpose the efforts to measure ESCA spectra of the silicides are indispensable.

A series of silicides is formed on Si by evaporating various metals on Si (111) in vacuum and allowing them to diffuse into the substrate silicon. Thickness of the silicides formed is governed by annealing temperature and duration. A degree of silicide formation was checked by the backscattering technique for which the Tandetron (General Ionex Corp.) was used. 2.1 MeV He^{++} beams were focused on specimens, whose diameter was 1 mmϕ.

Backscattering spectra taken from a Ni-Si system are shown in Fig. 1 (a)–(c). When the

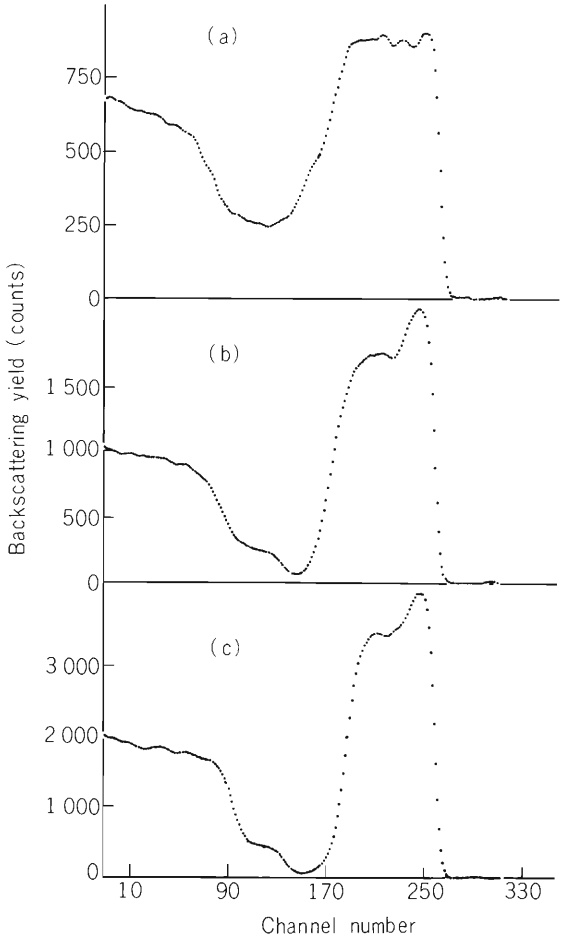

Fig. 1 (a). Backscattering spectrum for a Ni-Si system annealed at 325° C for 2 h. A peak at the right hand side is that of pure Ni at the outermost layer. The second peak which looks like a shoulder to the first peak is that of Ni in Ni_2Si. The third one is that of Si in Ni_2Si. The forth one is that of pure Si which is the substrate. (b) Backscattering spectrum for the system annealed at 300 °C for 17 h. (c) Backscattering spectrum for the same system, but annealed at 500° C for 1 h.

annealing temperature was low, pure nickel layer still remains at the outermost surface of the specimen. Thus, the surface structure is described as Ni-Ni_2 Si-Si in regular sequence from the surface. After high temperature annealing, for example at 500°C, diffusion between Ni and Si is almost completed as shown in Fig. 1 (c). The sample thus heat-treated will be submitted to ESCA measurement.

References

1) J.M. Anderews and J.C. Phillips: Phys. Rev. Lett., 35, 56 (1975).
2) J.L. Freeouf: Solid State Commun., 33, 1059 (1980).

III-2-9. High Resolution Electron Spectrometer

A. Yagishita, M. Saito, and K. Nishi

Design, construction, and preliminary testing of the Auger Electron Spectrometer (AES) have been previously reported.[1] The AES was constructed on the crossed-beam principle, and consists basically of a molecular gas beam target, a high resolution electron energy analyzer, and a high intensity electron gun which is installed to calibrate the electron analyzer. The analyzer can be rotated relative to an incident ion-beam about the axis of the gas beam, to enable ejected electron spectra to be studied over the range of ejection angles from 20° to 160°.

The electron gun was designed to produce a well defined image of an electron source (in this case a tungsten hairpin filament) that could be focused onto the target gas beam in the energy range from 200 eV to 7000 eV. This image is typically formed by a current between 1 μA and 10 μA, depending primarily on a space charge limitation imposed by the energy of the electrons.

The molecular beam flows out from a thin stainless steel tube of inside diameter 0.5 mm and length 10 mm. In the target region, the pressure is typically 10^{-3} Torr, while the background pressure in the system is two order of magnitude lower. This situation is maintained by two turbo molecular pumps, one with a pumping speed of 510 ℓ/sec and another of 360 ℓ/sec.

Electrons emitted from the small interaction region enter into the entrance of the analyzer which consists of electron-optical lenses and an electrostatic energy filter of hemispherical shape.

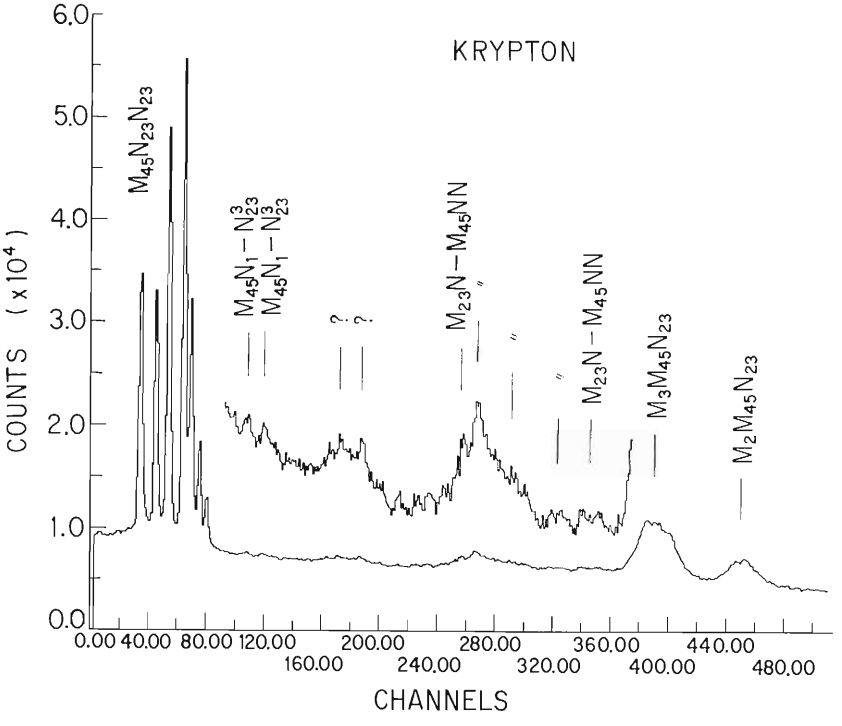

Fig. 1. The MNN Auger and MMN Coster-Kronig spectrum of krypton by 2000 eV-electron impact.

The electrons having the correct energy to pass through the energy filter are detected with a channel electron multiplier operating in the pulse-counting mode. Pulses from the detector are accumulated in a multichannel scaler which performs the function of signal averaging. A linear ramp voltage, synchronized with the horizontal sweep of the multichannel scaler, is used to define certain potential energy such as the ejected-electron energy within the analyzer.

Figure 1 shows the MNN Auger and MMN Coster-Kronig spectrum of Krypton by electron impact. The energy of incident electrons is 2000 eV and the electron-ejection angle is 108° with respect to the primary beam direction. Some experimental results on those Auger and Coster-Kronig processes induced by electron impact have been already published.[2), 3)]

Figure 2 shows the KLL Auger spectrum of neon by electron impact. Because the spectrum has been studied by many investigators, we can easily estimate the energy resolution of the AES. From the spectrum, we deduce the energy resolution to be a few parts in 10^4.

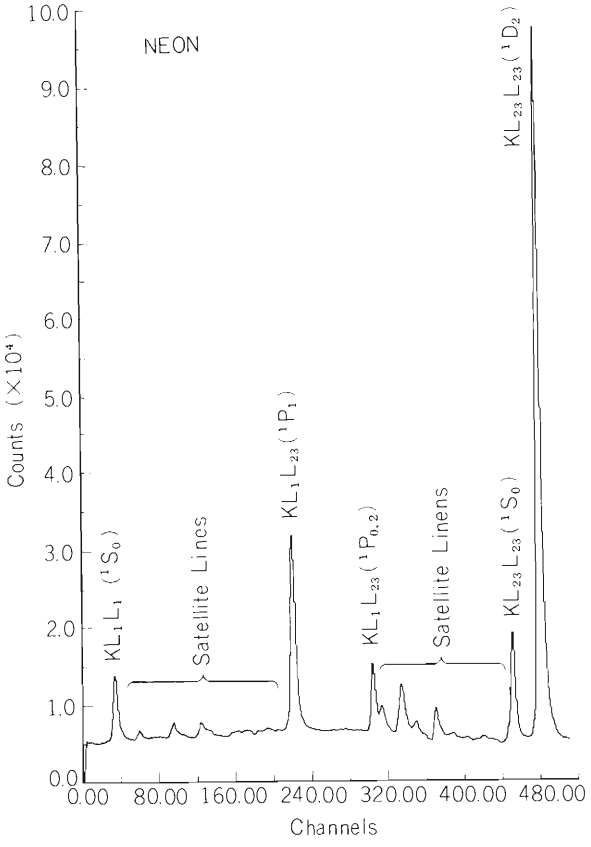

Fig. 2. The KLL Auger spectrum of neon by 2000 eV-electron impact.

References

1) A. Yagishita and T. Nakamura: IPCR Cyclotron Progr. Rep., 14, 143 (1980).
2) A. Yagishita: Phys. Lett., 87A, 30 (1981).
3) A. Yagishita, H. Hanashiro, S. Ohtani, and H. Suzuki: J. Phys. B, 14, L777 (1981).

III-2-10. Parallel Plate Electrostatic Spectrograph Using MCP and PSD

A. Yagishita and K. Agata

Conventional spectrometers usually involve using an energy or mass analyzer, which produces dispersion, and scanning an image across a slit. This procedure detects at one time only a small part of the spectrum. The resolving power of the instrument is determined by the width of the slit: the narrower the slit, the better the resolution; but this must be paid for by a reduction in sensitivity since only a part of the available signals will now be transmitted through the slit. To remedy this situation and make use of the whole image, a multidetector system is needed that can simultaneously detect all the events.

The system we are developing uses a microchannel plate (MCP) image intensifier to amplify the extended image produced by an electron energy analyzer. The electrons produced by the MCP are accelerated on to the surface of a position sensitive device (PSD; manufactured by Hamamatsu TV Co., Ltd.). The electronic charges are divided by the resistance of the PSD's surface into two parts, q_A and q_B, which are inversely proportional to the resistances, $R_L - R_X$ and R_X, to the electrodes A and B, respectively (see Fig. 1). One can determine the position of the incident electrons by calculating $q_A/(q_A + q_B)$ and the data are stored in a multichannel pulse height analyzer.

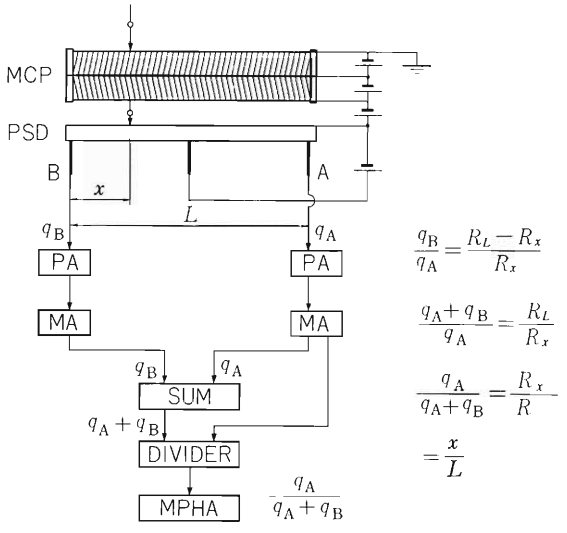

Fig. 1. Schematic diagram of position analyzing electronics.

For the operation of this multidetector system, we have newly designed a simple parallel plate electrostatic electron-energy analyzer. Our design of the analyzer has mostly followed the idea developed by Green and Proca.[1] Their consideration of the focusing properties of a parallel plate analyzer indicated that it is possible to select a given angle θ of entry into the field for which second order focusing can be attained giving rise to an angular aberration term proportional to $(\Delta\theta)^3$. In fact, for $\theta = 30°$, the angular aberrations are minimized, allowing one to built an analyzer of reasonable resolution with a wide angular acceptance.

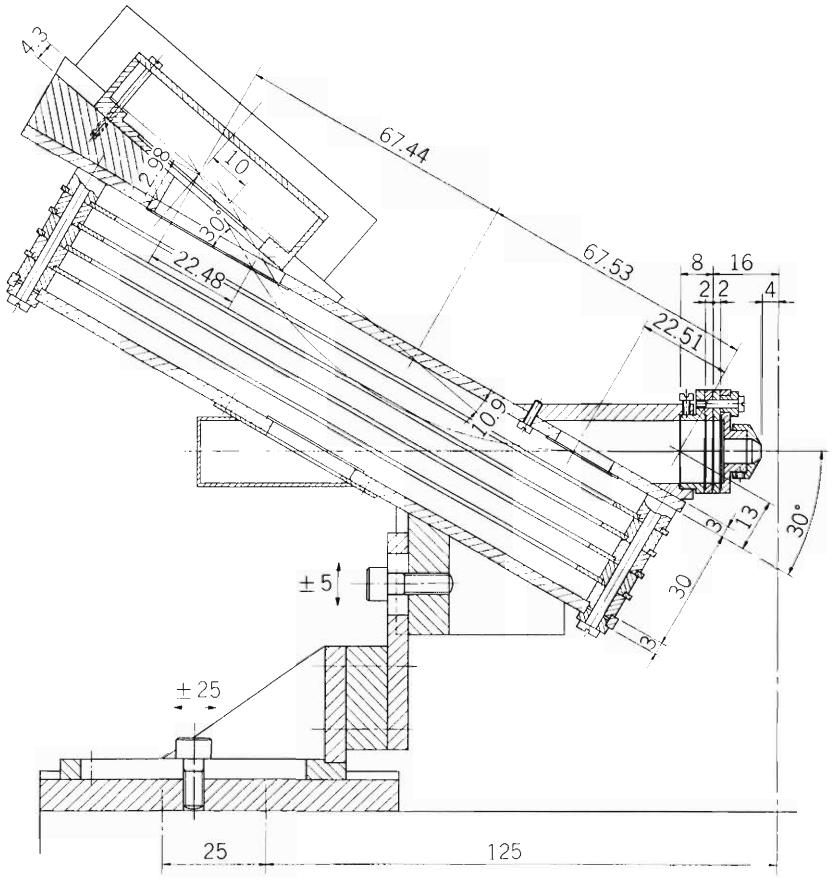

Fig. 2. Schematic drawing of the parallel plate electrostatic electron-energy analyzer.

Figure 2 shows the schematic drawing of the analyzer designed according to the prescription mentioned above. Design parameters of the analyzer are written in Fig. 2 in units of mm. The position sensitive detector system (MCP and PSD) is settled on the exit focal plane and the whole spectrum can be obtained at once.

Reference

1) T.S. Green and G.A. Proca: Rev. Sci. Inst., 41, 1409 (1970).

III-2-11. Beam-Foil Spectroscopy

K. Ando and K. Mori

An automatic system for measurement of spectral intensities against wavelength or foil position has been prepared and is schematically shown in Fig. 1.

Two modes of measurements are selected on a control panel. The first mode is for measurement of spectrum emitted from the excited ion beam transmitted through a carbon foil. The second mode is for measurement of decay curves of spectral line intensities against the distance from the foil position. In each mode, the wavelength or the foil position is automatically changed by a given amount by means of the stepping motor connected with the scanning system of the spectrometer or the foil carriage, after each scanning system receives a trigger signal. This trigger signal is produced by a preset counter whenever the number of ion particles which are collected in a Faraday cup reaches the preset value of the counter so as to normalize the spectral intensities by the number of ion particles.

The data in the measurement, that is, foil position, wavelength, photon number, etc., are stored by data aquisition system of a computer.

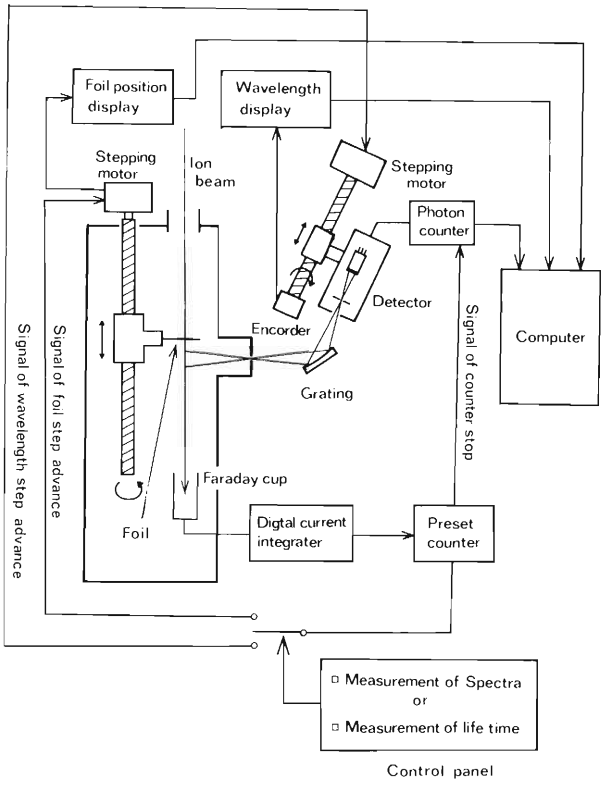

Fig. 1. An automatic measuring system for the beam-foil spectroscopy.

III-2-12. Optical Detection of Atomic and Nuclear Spin Polarization Produced by Beam-Foil Interaction

S. Kohmoto, M. Ishihara, T. Nomura,
Y. Gono, and M. Sasagase

It has been shown[1] that low energy ($\lesssim$ few MeV) ion beam after passage through a thin foil whose normal is tilted relative to the beam axis is not only atomically excited but also polarized. This polarization can be determined by measuring the circular polarization of light emitted from the excited ion beam. The atomic polarization is then transferred to the nucleus via hyperfine interaction. An optical detection of the nuclear spin polarization is also shown[2] to be possible with the aid of a second thin foil placed downstream vis-à-vis the first and perpendicularly to the beam direction.

We are interested in, with use of these techniques,

(1) to generate nuclear spin polarized ion beams and to accelerate them moreover to energies which are suitable for the study of nuclear physics

(2) and to measure the nuclear polarization of particles which are produced in nuclear reactions.

In an attempt to look for these possibilities, we are going to measure the circular polarization of light emitted from the ^{14}N beam accelerated to few hundreds keV by the injector of the Linac Accelerator (Fig. 1). The interference filter is used for the purpose to select a particular transition in nitrogen atom. Single photon counting measurement will be done by the aid of a photo-multiplier (PM) with low dark counts (<1 cps). Preliminary tests are in progress.

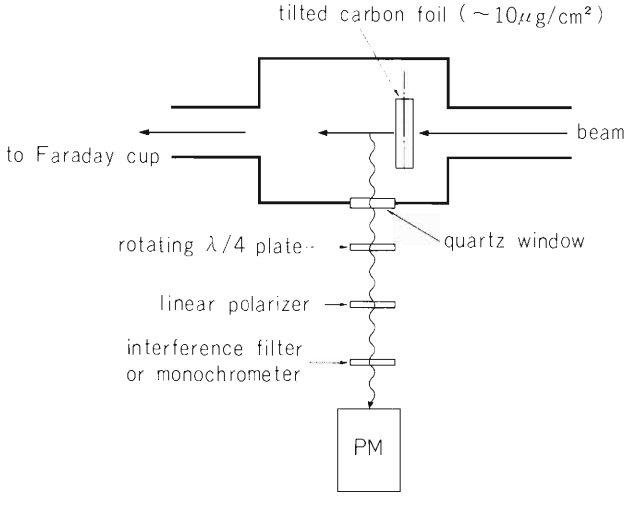

Fig. 1. Schematic experimental arrangement to measure the circular polarization of light emitted from the beam passing through the carbon foil. Photons are observed in a direction perpendicular to the beam axis and to the normal of the tilted foil.

References

1) H.G. Berry, L.J. Curtis, D.G. Ellis, and R.M. Schectman: Phys. Rev. Lett., 32, 751 (1974).
2) H.J. Andrä, H.J. Plöhn, A. Gaupp, and R. Fröhling: Z. Phys., A281, 15 (1977).

III-2-13. Lattice Location of Sn Atoms Implanted into Al Crystals as Investigated by Means of Channeling Method

E. Yagi, A. Koyama, H. Sakairi, and R.R. Hasiguti*

Some kinds of impurity atoms implanted into Al crystals occupy interstitial sites. Therefore the investigation on the lattice locations of such impurities will give information on the interstitial sites or the configurations of interstitials in an Al crystal. In the present study, the lattice location of Sn atoms implanted into Al crystals is investigated by means of channeling method. The implantation was carried out at room temperature and at 150 kV with various doses. Axial channeling effect was investigated with respect to <100>, <110>, and <111> axes by means of backscattering with 1 MeV He^+ ions. Figure 1 shows the normalized backscattering yields from Al and Sn atoms as a function of the angle between the incident beam direction and the <110> crystal axis for a specimen implanted with the dose of 1×10^{14} Sn/cm^2. The backscattering yield from Sn atoms gives a shallower and narrower dip than the Al-dip. In the <111> angular scan, it gives also a narrower dip than the Al-dip. These results suggest that the Sn atoms occupy interstitial sites which are different from those of Sn atoms in Al crystals implanted with the higher dose, 1×10^{16} Sn/cm^2,[1] and also implanted Ni atoms in Al crystals.[2] A detailed investigation is in progress.

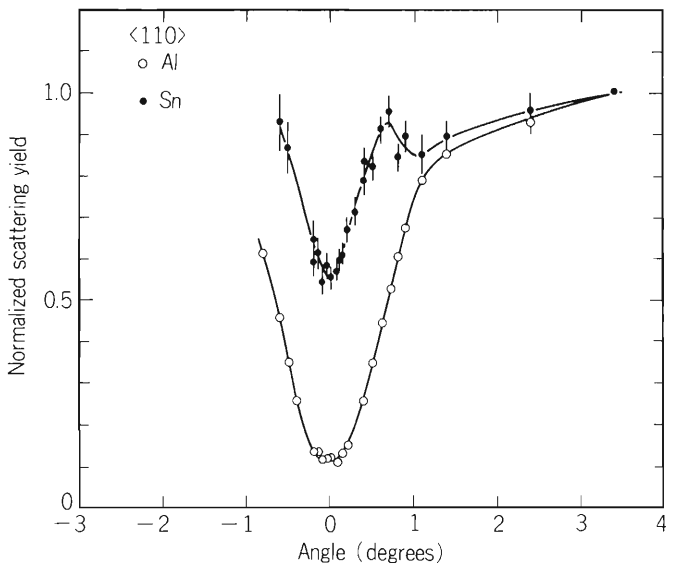

Fig. 1. Normalized backscattering yields from Al and implanted Sn atoms as a function of the angle between the incident beam direction and the <110> crystal axis. The implantation dose is 1×10^{14} Sn/cm^2.

References

1) A. Koyama and H. Sakairi: IPCR Cyclotron Progr. Rep., 13, 92 (1979).
2) E. Yagi, A. Koyama, H. Sakairi, M. Iwaki, and R.R. Hasiguti: J. Phys. Soc. Japan, 50, 873 (1981).

* The Science University of Tokyo.

III-2-14. Secondary Electron Emission from Metal Targets under Heavy-Ion Bombardment

A. Koyama, T. Shikata,
H. Sakairi, and E. Yagi

The secondary electron emission coefficients γ for in-situ vacuum deposited Al, Cu, Ag, and Au targets are measured under bombardment with He^{2+}, C^{4+}, C^{6+}, N^{4+}, N^{5+}, N^{7+}, O^{5+}, and O^{8+} ions in the energy region of 4.5 – 8 MeV/amu. Ion currents are 0.5 – 1 nA. The experimental apparatus and conditions were described in our previous reports.[1),2)]

Figure 1 shows the energy dependences of γ for Al and Ag targets under bombardment with N^{4+}, N^{5+}, and N^{7+} ions. It shows that the energy dependence of γ is rather insensitive to the variation of the projectile charge state. The energy dependences of γ under bombardment with these ions are expressed as,

$$\left.\begin{aligned} &\gamma \propto E^{-0.36}, \text{ for Al,} \\ &\gamma \propto E^{-0.45}, \text{ for Ag,} \end{aligned}\right\} \qquad (1)$$

where E is the incident energy of these ions in MeV/amu.

The decrease of γ with E is gentler than that of the electronic stopping power S. Thus γ/S increases with incident ion energy, which is the same as the experimental result by Oda and Lyman.[3)]

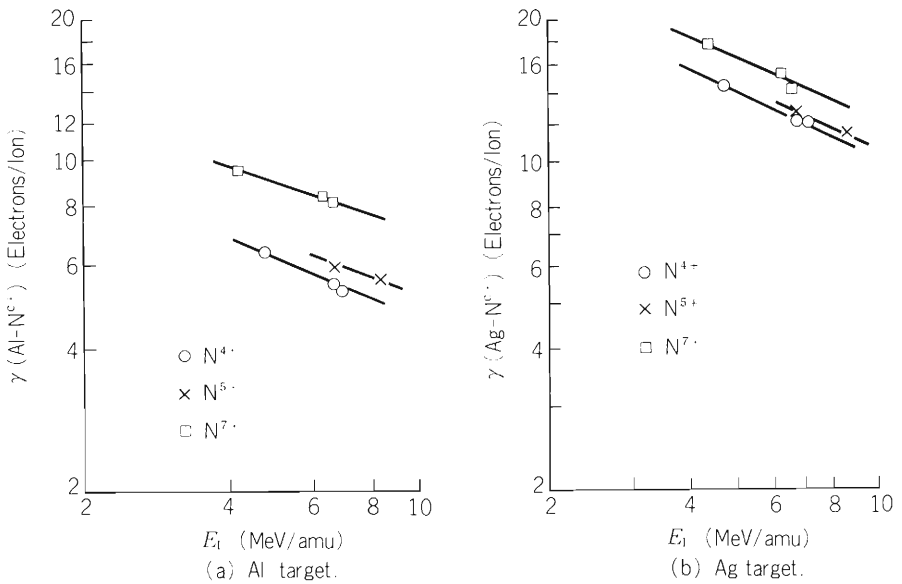

Fig. 1. Energy dependences of γ for N^{4+}, N^{5+}, and N^{7+} projectiles.

Table 1 shows values of the ratio $R(z_1, c; Z_2) \equiv \gamma(z_1, c; Z_2)/\gamma(z_1, z_1; Z_2)$, where $\gamma(z_1, c; Z_2)$ is for a target of atomic number Z_2 under bombardment with a partially stripped projectile of atomic number z_1 and electric charge c, and $\gamma(z_1, c; Z_2)$ for the same target under bombardment with a fully stripped one of the same atomic number z_1. The first column is for the specification of the projectile system used for obtaining the value of $R(z_1, c; Z_2)$. The second column shows the values of R for the targets used. The third column shows the values

Table 1. Dependence of γ on the projectile charge state. z_1 is the atomic number of the projectile and c is its electric charge. N_p is the number of electrons bound to the projectile and is equal to $z_1 - c$.

	$R(z_1, c; Z_2)$				$\frac{c^2}{z_1^2}$	$\frac{z_1^2 + c^2}{2z_1^2}$	$\frac{z_1^2 + c^2 + 2N_p}{2z_1^2}$
	Al	Cu	Ag	Au			
C^{4+}/C^{6+}	0.71		0.79		0.44	0.72	0.78
N^{4+}/N^{7+}	0.75	0.83	0.86	0.89	0.33	0.66	0.72
N^{5+}/N^{7+}	0.82		0.90		0.51	0.76	0.80
O^{5+}/O^{8+}	0.74		0.84		0.39	0.70	0.74

of c^2/z_1^2. The fourth column shows the values of $(z_1^2 + c^2)/2z_1^2$. $R(z_1, c; Z_2)$ is much larger than c^2/z_1^2, but is nearly equal to $(z_1^2 + c^2)/2z_1^2$. Thus, $\gamma(z_1, c; Z_2)$ is nearly proportional to $(z_1^2 + c^2)/2$.

Figure 2 shows $R(z_1, c; Z_2)$ as a function of target atomic number Z_2. The Z_2-dependence of $R(z_1, c; Z_2)$ is expressed by

$$R(z_1, c; Z_2) = AZ_2^{0.1}, \tag{2}$$

where A is independent of Z_2 and is equal to 0.6 in the case of the ratio of γ for N^{4+} ions to that for N^{7+} ions.

According to Schou,[3] γ is nearly proportional to S at the target surface for the projectile. If the ratio γ/S is independent of the charge state of projectiles, $R(z_1, c; Z_2)$ is equal to the ratio of the square of the effective charge at the surface of the target for the partially stripped projectile, $Z_{eff}^2(z_1, c; Z_2)$, to that for the fully stripped one, $Z_{eff}^2(z_1, z_1; Z_2)$. The square of the effective charge for a partially stripped ion was theoretically given by Kim and Cheng.[4] By refering to this theory, $Z_{eff}^2(z_1, c; Z_2)$ is deduced semiempirically from the values of $R(z_1, c; Z_2)$ and is expressed in terms of z_1, c and Z_2, as follows:

$$Z_{eff}^2(z_1, c; Z_2) = (z_1^2 + c^2)/2 + N_p + \alpha N_p Z_2^{2/3}, \tag{3}$$

where N_p is the number of the bound electrons and is equal to $z_1 - c$, and α is the numerical factor and is equal to 0.16 for N^{4+} ions. The fifth column of Table 1 shows the value of $(\frac{z_1^2+c^2}{2} + N_p)/2z_1^2$. It agrees well with the value of $R(z_1, c; Z_2)$. The Z_2-dependence of R originates from the third term on the right hand side of Eqn. (3).

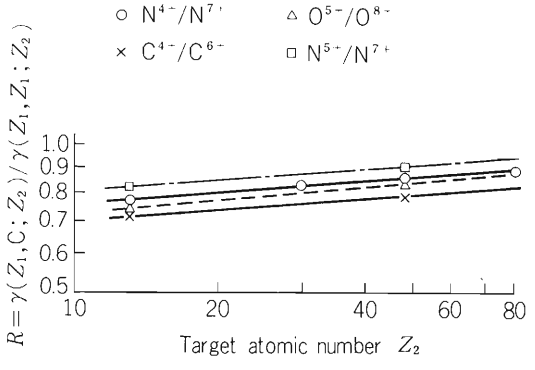

Fig. 2. Dependence of $R(z_1, c; Z_2) \equiv \gamma(z_1, c; Z_2)/\gamma(z_1, z_1; Z_2)$ on target atomic number Z_2, where $\gamma(z_1, c; Z_2)$ is for a target of atomic number Z_2 under bombardment with a partially stripped projectile of atomic number z_1 and electric charge c, and $\gamma(z_1, z_1; Z_2)$ is that for the same target under bombardment with a fully stripped projectile of the same atomic number z_1. Incident energy of the projectiles is 6.2 MeV/amu.

References

1) A. Koyama, T. Shikata, H. Sakairi, and E. Yagi: Jpn. J. Appl. Phys., 20, 65 (1981).
2) A. Koyama, T. Shikata, and H. Sakairi: IPCR Cyclotron Progr. Rep., 13, 83 (1979).
3) N. Oda and J. T. Lyman: Radiat. Res., 7, Suppl., p. 20 (1967).
4) Y. K. Kim and K. Cheng: Phys. Rev., A 22, 61 (1980).

III-2-15. Distributions of the Hyperfine Magnetic Field at ^{119}Sn ($\leftarrow$ ^{119}Sb) on the Surfaces of α-Fe_2O_3

T. Okada, H. Sekizawa, F. Ambe, and S. Ambe

The present work aims to utilize emission Mössbauer measurement of the supertransferred hyperfine (hereafter abbreviated as STHF) magnetic fields in studying the chemical state of very dilute antimony ions "adsorbed" onto the surfaces of oxides. In the actual work, the technique of emission Mössbauer spectroscopy of ^{119}Sn, with ^{119}Sb as the source nuclide, has been applied to the study of carrier-free pentavalent antimony ions adsorbed on the surfaces of corundum type antiferromagnetic oxide, α-Fe_2O_3 (Néel temperature: 950 K). In the measurement, Mössbauer analysis was made on the 23.8 keV γ-rays emitted by ^{119}Sn nuclei in the first excited state (^{119}Sn*, half life: 17.8 ns) arising from ^{119}Sb (half life: 38.0 h) by the EC decay.

The nature of the chemical bonds formed by ^{119}Sb ions on the oxide surfaces is explicitly reflected in the emission spectra as the STHF interaction of ^{119}Sn* ($\leftarrow$^{119}Sb) with its magnetic environment.

Experimental procedures and a part of the experimental results have already been reported in a previous report.[1] The present report is concerned with the results of subsequent detailed research.

Emission Mössbauer spectra of the "as adsorbed" (A) and 2 h heat-treated (B to E) α-Fe_2O_3 – $^{119}Sb^{5+}$ specimens at liquid nitrogen temperature are shown in Fig. 1. The temperatures of heat treatments were 200°C (B), 400°C (C), 500°C (D), and 700°C (E). The spectrum of a specimen (F), obtained by coprecipitating carrier-free $^{119}Sb^{5+}$ with Fe^{3+} from an aqueous solution with subsequent calcination in air at 700°C for 2 h, is also given in Fig. 1.

Even in the "as adsorbed" specimen (Fig. 1 A), there can be seen a remarkably broadened emission line, which transforms gradually into the six-line magnetic hyperfine pattern (B – E) with elevation of temperature of the isochronal heat treatment. We attribute the observed broadening and splitting to magnetic interaction of the ^{119}Sn ($\leftarrow$^{119}Sb) ions with the magnetically ordered Fe^{3+} ions of the α-Fe_2O_3 substrate. The distributions of hyperfine magnetic fields (H_{hf}) obtained by analyzing the spectra by means of the method of Hesse[2] are shown in Fig. 2. The spectra were also analyzed by the method of Window[3] and the results were in good agreement with those by the method of Hesse. Measurements at room temperature gave distributions of H_{hf} similar in trend to those at liquid nitrogen temperature. This similarity is compatible with the fact that the Néel temperature of α-Fe_2O_3 (950 K) is much higher than the above two temperatures of measurement

The other parameters were also derived from Mössbauer emission spectra. From the values of isomer shift it is certain that the ^{119}Sn ions resulting from $^{119}Sb^{5+}$ were tetravalent in all the α-Fe_2O_3 specimens. The isomer shifts showed a temperature dependence expected from the second order Doppler shift. The ratios of the adsorption areas of the spectra at room temperature to that at liquid nitrogen temperature were in the range of 0.7 – 0.8 in the coprecipitated (F), in the heat-treated (B to E), and even in the "as adsorbed" specimens (A). It means that the

adsorbed ^{119}Sb ions have unexpectedly high Debye temperatures.

As can be seen in Fig. 2 A, no peak was observed explicity at $H_{hf} = 0$ in the hyperfine field distribution of nominally diamagnetic $^{119}Sn^{4+}$ ($\leftarrow {}^{119}Sb$) ions in the "as adsorbed" specimen.

In order to analyze the effect of heat treatment, the ranges of H_{hf} in Fig. 2 were divided equally into three regions called I, II, and III respectively in order to intensity of the fields. Variations of weights of the regions are plotted against the heating temperature in Fig. 3. The weight of region I which is dominant before the heat treatment (A) decreases monotonically with the heating temperature. Weight of region II increases slowly up to about 500°C (D) and

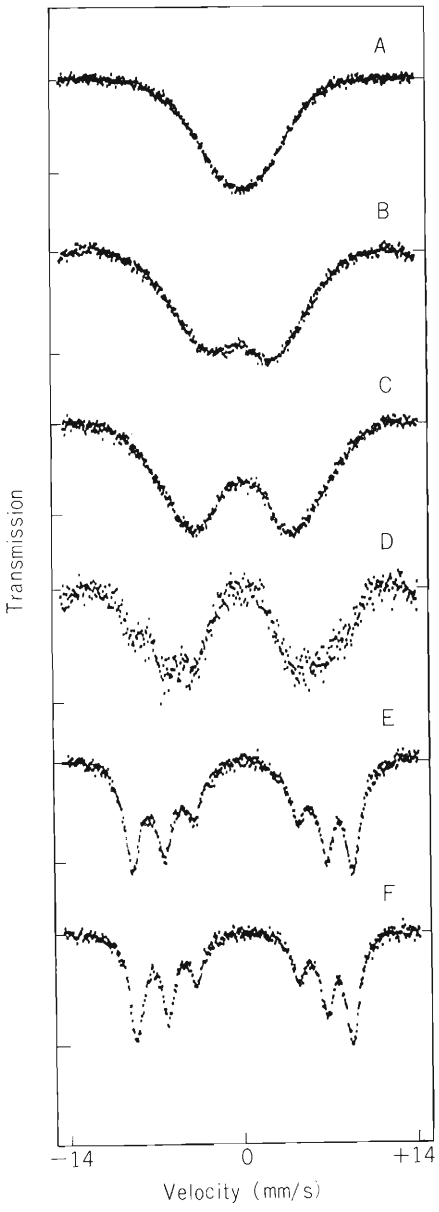

Fig. 1. Mössbauer spectra of the α-Fe_2O_3-^{119}Sb at liquid nitrogen temperature.

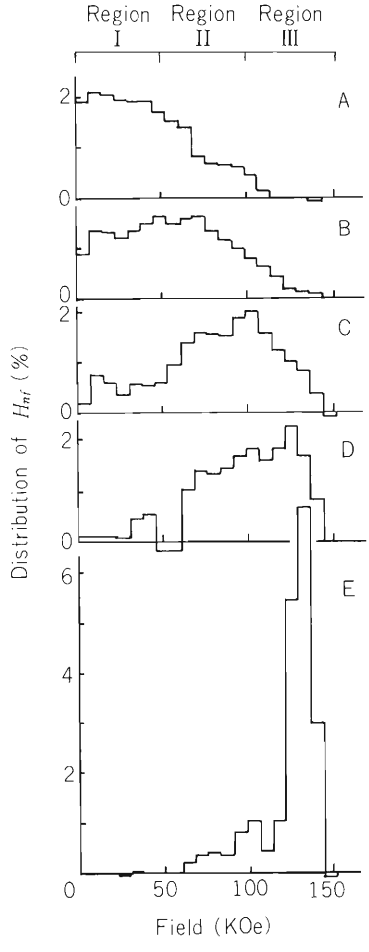

Fig. 2. The distributions of the hyperfine magnetic fields obtained by analyzing the spectra of α-Fe_2O_3-^{119}Sb by means of the method of Hesse.

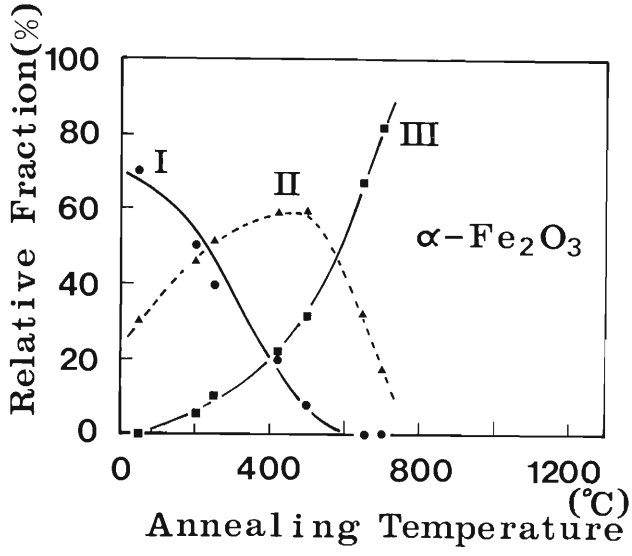

Fig. 3. Dependence of the relative fraction of the distribution on the heating temperature.

decreases abruptly above it. The decrease in the weight of region II is accompanied with rapid increase in the weight of region III, which dominated at the heating temperature of 700°C (E). The distribution of specimen (E) is almost equal to that of the coprecipitated specimen (F), which means that the adsorbed ^{119}Sb ions diffused into the substrate deep enough by 2 h heat treatment at 700°C so as to make the daughter ^{119}Sn nuclei to feel the same hyperfine magnetic fields as the ones on the daughter ^{119}Sn of the coprecipitated ^{119}Sb ions. These variations of hyperfine field distribution by heat treatment were interpreted in terms of the STHF interactions on $^{119}Sn^{4+}$ ($\leftarrow^{119}$Sb) ions diffused into various sites of the surface structure of α-Fe_2O_3. The detailed discussion on the experimental results will be published elsewhere.

A similar investigation of Cr_2O_3 – ^{119}Sb is in progress.

References

1) T. Okada, H. Sekizawa, F. Ambe, and S. Ambe: IPCR Cyclotron Progr. Rep., 14, 86 (1980).
2) J. Hesse and A. Rübartsch: J. Phys. E: Sci. Instrum., 7, 526 (1974).
3) B. Window: ibid., 4, 401 (1971).

III-2-16. Angular Correlation Measurements on Nb-Mo System

N. Shiotani, T. Okada, H. Sekizawa, and T. Nakamichi

Niobium and molybdenum have nearly the same electronic band structure, especially at and below the Fermi level. The Fermi level is higher in Mo than in Nb because of the extra valence electron per atom. Consequently, measurements of the angular correlation of positron annihilation radiation in a series of binary Nb-Mo alloys should provide information on how the addition of d electrons to the unfilled d band changes the geometry of the Fermi surfaces.

Single crystals of $Nb_{80}Mo_{20}$ and $Nb_{50}Mo_{50}$ were grown by zone melting in an argon arc furnace. The angular correlation curves were measured by a parallel slit system at room temperature. The results are shown in Fig. 1(a) – 1(c). The effects of alloying can be seen in changes of fine structures of the observed angular correlation curves.

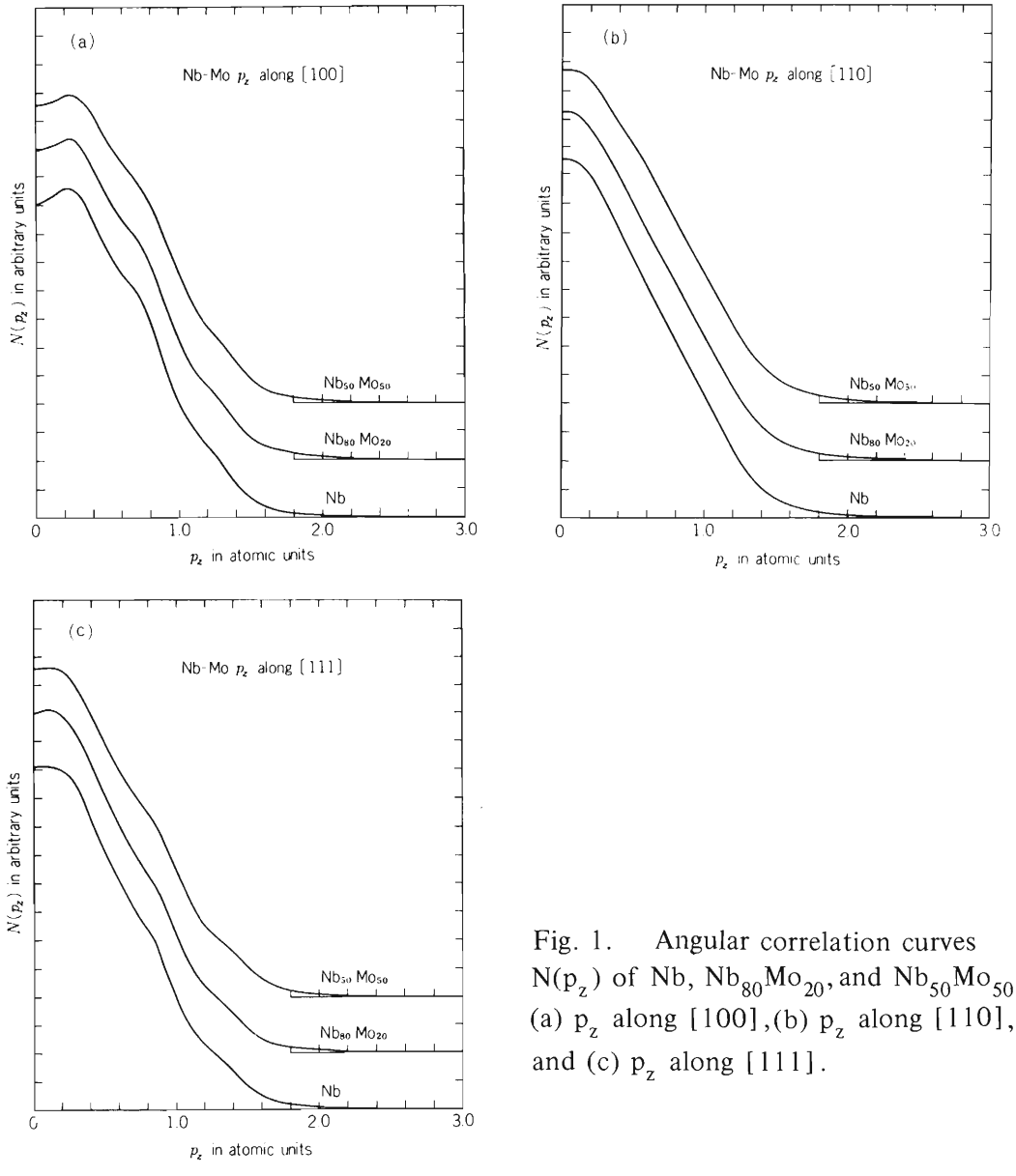

Fig. 1. Angular correlation curves $N(p_z)$ of Nb, $Nb_{80}Mo_{20}$, and $Nb_{50}Mo_{50}$, (a) p_z along [100], (b) p_z along [110], and (c) p_z along [111].

III-2-17. Creep Properties in Helium-injected SUS 316 and γ''-Precipitation Strengthened Alloy

N. Yamamoto,* H. Shiraishi, H. Yoshida,*
H. Kamitsubo, I. Kohno, and T. Shikata

Helium generated by (n, α) reactions has long been identified as the main cause of the neutron irradiation embrittlement of alloys used in fast breeder and future fusion reactors. The presently accepted mechanism is that helium bubbles form and weaken the grain boundary of the material and thus the intergranular fracture easily occurs. Among the experimental methods to study this phenomenon, helium injection by using an accelerator is conventional because the required amount of helium can be introduced into the specimen in a short time period, and the induced radioactivity of the specimen is low. In the present study, we took this method, and effects of helium on creep properties were studied for SSU 316 and γ''-precipitation strengthened alloy.

Results of chemical analysis of the alloys used are presented in Table 1. SUS 316 is a typical fast breeder structural material, and 7818 alloy is a γ'' Ni_3Nb precipitation strengthened alloy which has exhibited excellent tensile properties after helium injection.[1] The virgin raw materials were melted using a vacuum induction furnace, and 17 kg ingots were fabricated. Then, these ingots were hot forged and hot rolled at 1200°C. Finally, 0.2 mm thick plates were prepared by repeating cold rolling and intermediate annealing (1050°C, 30 min). Creep test

Table 1. Chemical composition of used samples. (wt %)

Alloy	C	Ni	Cr	Mo	Ti	Nb	Si	Mn	B
SUS 316	0.043	13.9	16.1	2.50	–	–	0.44	1.42	0.0006
7818	0.024	39.9	14.7	3.03	0.31	2.96	0.48	0.19	0.0048

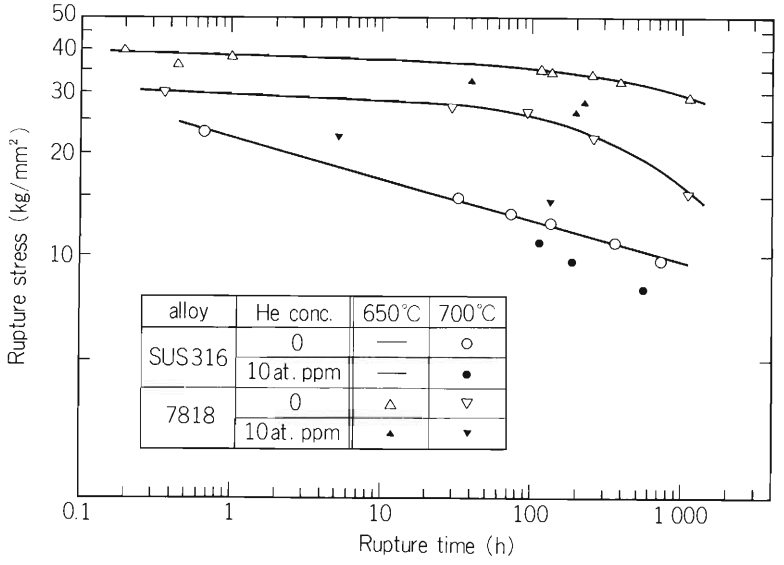

Fig. 1. Creep rupture curves for SUS 316 and 7818 alloy in which helium was uninjected and injected to 10 at. ppm.

* National Research Institute of Metals.

Table 2. Creep rupture properties of helium injected SUS 316 and 7818 alloy.

Alloy	Test temp. (°C)	He conc. (at. ppm)	Stress (kg/mm²)	Rupture time (h)	Rupture elong. (%)
SUS 316	700	0	23.0	0.7	49.7
			15.1	33.2	57.2
			13.3	73.4	61.4
			12.5	134.7	55.2
			11.0	364.2	59.5
			9.8	724.2	53.3
		10	11.0	113.5	17.7
			9.7	185.8	12.7
			8.0	552.5	14.5
7818	700	0	30.0	0.4	28.6
			28.0	29.9	26.1
			26.5	94.4	24.3
			22.5	265.0	18.2
			15.4	1128.7	11.8
		10	22.5	5.2	6.4
			14.5	137.6	1.8
	650	0	40.1	0.2	29.8
			38.0	1.0	30.2
			36.0	0.5	35.0
			35.1	114.9	31.6
			34.5	135.4	41.8
			34.0	253.4	31.1
			32.5	387.8	28.2
			29.0	1134.5	20.7
		10	32.5	38.4	0.8
			28.0	225.5	4.7
			26.6	202.6	2.9

specimens were die-stamped out from these specimens. The dimension of gauge section was 10 mm long, 4 mm wide. and 0.2 mm thick. Then, the specimens were solution treated for 30 min at 1050°C for SUS 316 and at 1100°C for 7818 alloy. This treatment resulted in the mean grain size of 46 μm and 69 μm, respectively. Helium was injected at constant high temperature (650°C or 700°C), using the cyclotron. The injected helium content of each specimen was about 10 at. ppm. The creep tests were carried out on the uninjected and injected specimens at the same temperature with that for helium injection in flowing Ar gas of 99.999 % up purity. The elongation at rupture was determined after testing by using a profile projector. The fracture surface of ruptured specimens was examined by a scanning electron microscope. Transmission electron microscope examinations on the fractured specimens were made mainly to study the morphology of helium bubbles.

The results of creep tests are shown in Table 2. As illustrated in Fig. 1, the decrease of the creep rupture strength by helium in 7818 alloy was much higher than that in SUS 316 at 700°C, but appreciably improved at

650°C test. The rupture elongation was greatly reduced after injection, although the extent of the deterioration varied between two alloys. Fractographs by SEM revealed that while the fracture occured in ductile mode in helium free reference materials, the helium injected specimens showed an intergranular brittle fashion, and as illustrated in Fig. 2(a), large helium bubbles were found out at grain boundaries in the creep ruptured specimens. These observations show the direct evidence of helium embrittlement. On the other hand, Fig. 2(b) shows that small helium bubbles were trapped at NbC precipitates in the matrix. This result implies that the helium embrittlement can be reduced if it is possible to trap more helium bubbles in the matrix by adjusting the size and distribution of NbC precipitates.

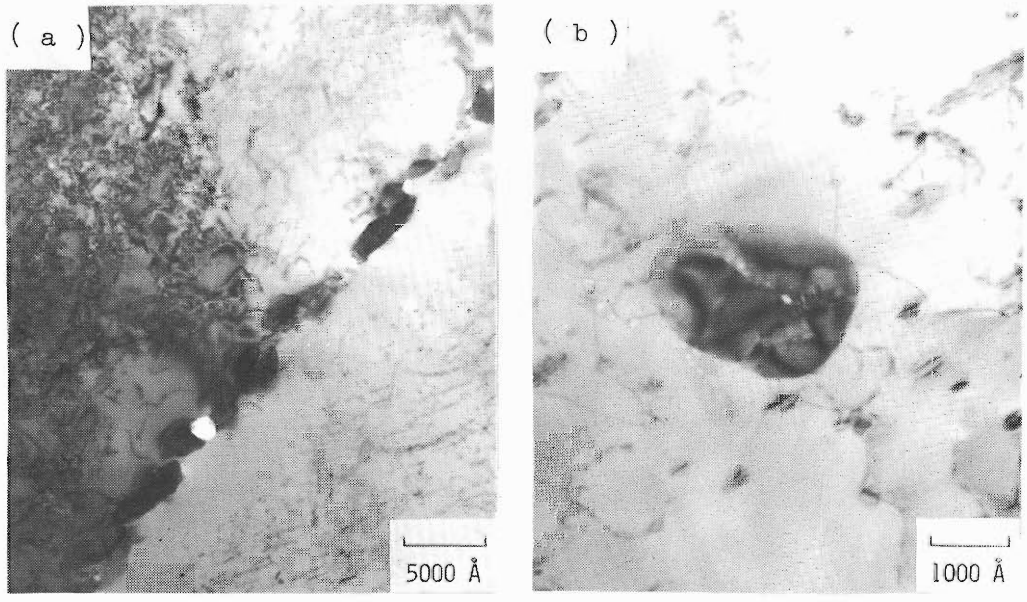

Fig. 2. Transmission electron micrographs of the 10 at. ppm helium injected and creep ruptured 7818 alloy. Test temperature: 700° C, creep stress: 22.5 kg/mm^2, rupture time: 5.2 h. (a) Large helium bubbles in a grain boundary; (b) small helium bubbles at the NbC precipitate in the matrix.

Reference

1) H. Shiraishi, H. Shinno, N. Yamamoto, H. Yoshida, H. Kamitsubo, I. Kohno, and T. Shikata: IPCR Cyclotron Progr. Rep., 14, 79 (1980).

III-2-18. Channeling in Argon-Implanted Diamond

M. Iwaki and H. Sakairi

A study has been made of radiation damage and depth profile of argon implanted diamond by means of the 1 MeV ^4He channeling technique with the use of the Tandetron.

Substrate used were natural and colorless diamonds with the surface nearly parallel to the (111) plane. Before ion implantation, the surfaces of all specimens were mirror-polished and sputtered by 5 keV Ar^+ ion beams coming at an angle of 75° from the normal. Ion implantation was performed with the dose of 1×10^{16} Ar/cm^2 at the energy of 150 keV at $\sim 2 \times 10^{-6}$ Torr. The beam current density was about 1 μA/cm^2. The target temperature during ion implantation rose from room temperature to about one hundred degrees of centigrade by the heating effect of the ion beam itself. The ion beam was sent in the direction deviating by a few degrees from the <111> crystal axis in order to reduce the deep penetration of implanted argon by channeling.

Channeling measurements (Rutherford backscattering) were done by using 1 MeV $^4He^+$ with the fluence of 5 μQ. Backscattered particles at an angle of 150° were detected and analyzed by a solid state detector and conventional electronics. The samples were mounted on a 3 axis goniometer in a target chamber, which was at a pressure below 5×10^{-6} Torr.

Figures 1 and 2 show the <111> aligned and random spectra observed for argon implanted diamond. The leading edge of the diamond target is at channel number 442 (located at harf-height) and the energy edge of argon at the diamond surface at channel number 1145. The energies at channel numbers 442 and 1145 are 0.273 and 0.687 MeV, respectively. The spectra obtained for backscattered particles from argon implanted in diamond do not exhibit any difference between random and channeling spectra as shown in Fig. 1. Moreover, as shown in

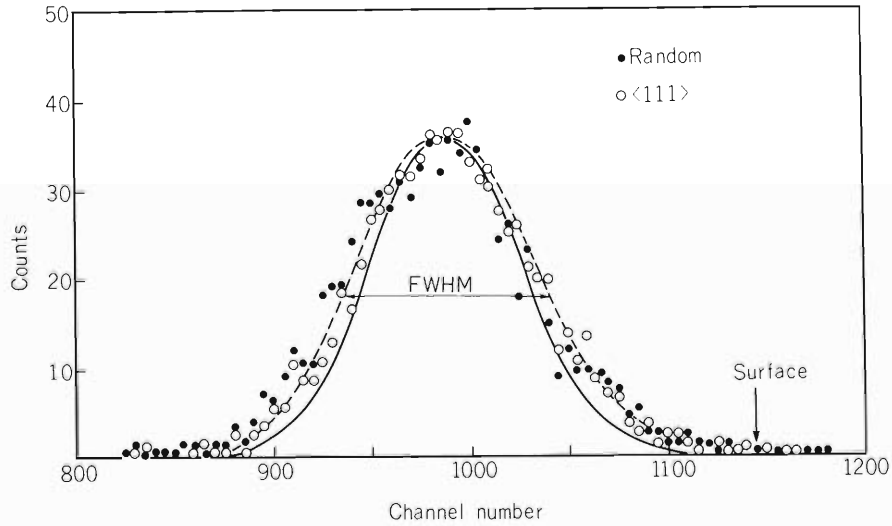

Fig. 1. Random (•) and <111> aligned (○) spectra of argon implanted in diamond.

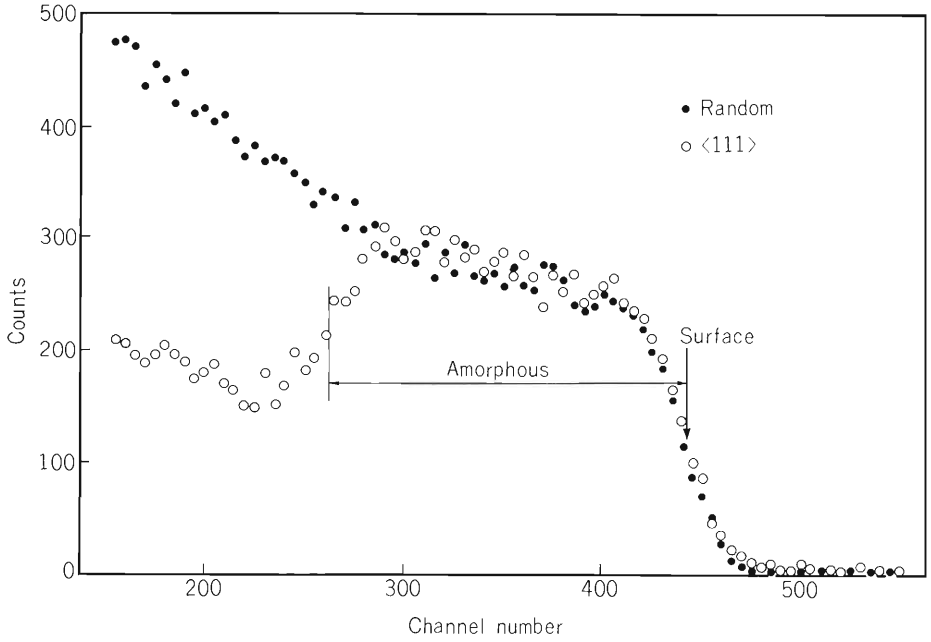

Fig. 2. Random (•) and $<111>$ aligned (○) spectra of diamond implanted with argon.

Fig. 2, the channeling spectrum overlaps with the random spectrum at channel number above 285. These results display that argon implantation in diamond produces the amorphous layer near its surface, where implanted argon atoms are located at random sites.

The depth profile of implanted argon and the thickness of the amorphous layer can be obtained from Figs. 1 and 2 by using a zero-order analysis. The solid line in Fig. 1 indicates the depth distribution predicted by the range theory. The depth corresponding to the peak obtained from the spectra is about 770 Å, which is in good agreement with the predicted range of 772 Å. The standard deviation calculated from the FWHM of the spectra is about 220 Å, which is a little larger than the predicted value of 190 Å. Because the FWHM of the spectra contains not only the depth distribution of the argon, but also the energy resolution of the backscattering system and the energy straggling of the ^{4}He ions, the calculated standard deviation may be a little smaller and close to the predicted value. The results suggest that the depth profile of argon implanted in diamond can be predicted by the range theory.

The thickness of the amorphous layer is, if it is assumed to be the region from 262 to 442 channels as indicated in the figure, about 1340 Å, which is 1.8 times as large as the average projected range. The amorphous layer of the diamond surface produced by argon implantation exhibited the electrical conductivity, which was measured by means of a four point probe method. The sheet resistivity of the specimen was about 170 Ω/cm^2. If the conductivity is assumed to be attributed to the amorphous layer, the resistivity is $170 \times 1340 \times 10^{-8} = 2.3 \times 10^{-3}$ $\Omega \cdot$cm, which is almost the same as that of the glassy carbon (produced by Tokai Carbon Company Ltd.).

It is concluded that the average predicted range and standard deviation of argon implanted in diamond are in fairly good agreement with those predicted by the range theory. By argon implantation with 1×10^{16} ions/cm^2 at 150 keV, the surface layer of diamond becomes amorphous and induces electrical conductivity. The resistivity of the amorphous layer is almost the same as that of the glassy carbon on the market.

III-2-19. Ion Beam Mixing of the Aluminum Film-Iron Substrate Interface

M. Iwaki and K. Takahashi

In the field of modification of the near-surface region of metals by ion implantation, considerable attention has been directed toward the change of physical and chemical properties of the metal, such as improvements of friction, wear and corrosion. Recently, the doping of the given species in metals has been carried out not only by direct implantation but also by the ion beam mixing. The doping technique by mixing is as follows: One deposits a thin film of the given species on the substrate and then intermix the film and substrate by ion bombardment of energetic ions which penetrate through the film-substrate interface. In this report, the effect of ion implantation into aluminum deposited iron plates is investigated on the depth profile of aluminum and iron, and the corrosion behavior.

The iron substrates used were mirror-polished by buffing wheel and ultrasonically cleaned in trichloroethylene, and moreover sputtered by 5 keV Ar^+ beams at an angle of 75° from the normal at a pressure of $\sim 2 \times 10^{-6}$ Torr. Aluminum thin films a hundred angstroms thick, were prepared on the iron substrates by sputter coating at room temperature by using IMMI-V (Commonwealth Scientific Co. Ltd.) at $\sim 2 \times 10^{-6}$ Torr. In this process, several iron substrates were placed in such a way as to make an angle of 30° with an aluminum plate and the aluminum was sputtered at an angle of 60° from the incidence of 5 keV Ar^+ beams. The iron targets were rotated at random so that sputtered aluminum can be deposited on the iron surface uniformly.

Ion implantation with oxygen and argon was performed with the dose of $1 \times 10^{16}/cm^2$ at the energy of 150 keV at $\sim 2 \times 10^{-6}$ Torr by using the RIKEN 200 kV Low Current Implanter. The conditions of the dose and energy were selected in such a way so as to reduce the thickness of material removed by sputtering during ion implantation and for most implanted atoms to penetrate into the deeper region than the film-substrate interface. The target temperature during ion implantation rose to a temperature slightly higher than room temperature by the heating effect of the ion beam itself.

Depth profiles of aluminum and iron were measured by means of secondary ion mass analysis, which was carried out by Ion Beam Surface Mass Analyzer (ISMA, produced by Commonwealth Scientific Co. Ltd.). ISMA includes the facility to produce primary bombardment ions of both active oxygen and inert argon, a quadrupole mass analyzer and a provision for automatically recording individual masses for depth profiling. The sputtering removal rates used for measuring the depth profiles were ~10 Å/min for aluminum and ~20 Å/min for iron with the primary oxygen ion energy of 7 – 8 keV at a sputtering angle of 45°.

Figure 1 shows the depth profiles of aluminum and iron in unimplanted (as-coated), oxygen implanted and argon implanted specimens. In the unimplanted specimen, it seems that aluminum has invaded the iron substrate, but no sharp interface appeared. This may have been caused by the unexpected islands of the deposited thin films, the roughness of the based iron plates and the

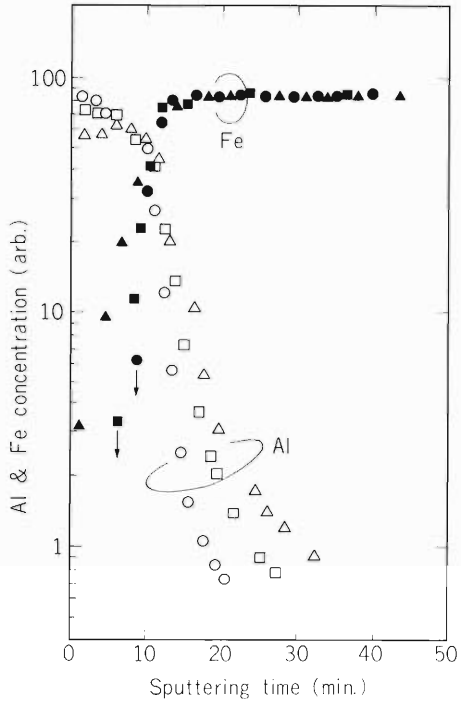

Fig. 1. Depth profiles of aluminum and iron in unimplanted (○, ●), oxygen implanted (□, ■) and argon implanted (△, ▲) specimens, which are pure iron plates coated with aluminum.

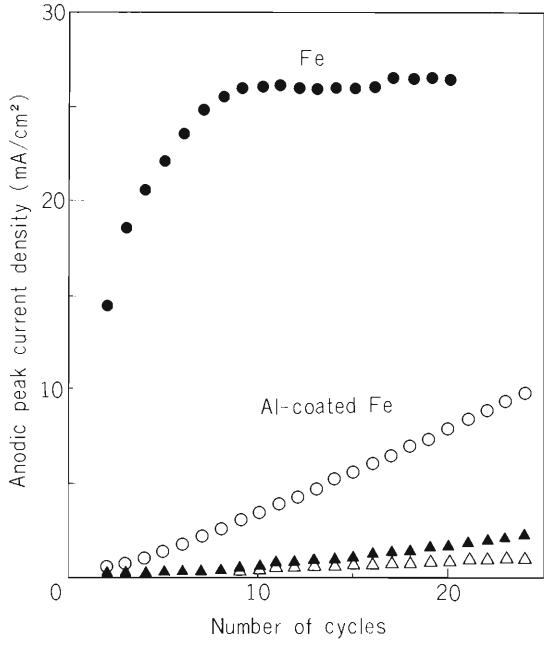

Fig. 2. Relationship between anodic peak current density and number of potential sweep cycles with un-coated (●) as-coated (○) and oxygen (△) or argon (▲) implanted specimens after coating aluminum

ion beam mixing during depth profiling. By ion implantation through the thin film, especially by argon implantation, it is obvious that iron moves into the aluminum thin film and aluminum penetrates into the iron substrate, as compared with the depth profile of the unimplanted specimen. The results show that the ion beam mixing of the thin film-substrate interface can occur by ion implantation through the interface.

The corrosion behavior of these specimens was investigated by means of the cyclic voltammetry in 0.5 M acetate buffer solution (pH 5.0). The cell construction and the instrument for the experiment were given in detail in Ref. 1. Cyclic-voltamograms show the anodic dissolution current peak and the depressed current region with passivation. The anodic peak current density corresponds to the reactivity of the anodic dissolution reaction of the metal surface. Figure 2

shows the relationship between anodic peak current density and number of potential sweep cycles, which shows the change of reactivity of the surface with repeat of the potential sweep cycles. The peak current density of iron is relatively high and that of aluminum is very low. By depositing aluminum on iron the anodic peak current density becomes low, and even lower by subsequent ion implantation. The results show that the ion beam mixing is an important technique for the improvement of corrosion.

In conclusion, ion implantation through the deposited thin film results in making the sharp interface of the thin film-substrate dispersed and improving the corrosion resistance.

Reference

1) K. Takahashi, Y. Okabe, and M. Iwaki: Nucl. Instr. and Methods, 182, 1009 (1981).

III-3. Radiochemistry and Nuclear Chemistry

1. Charged Particle Activation Analysis of Semiconductor Materials

T. Nozaki, Y. Terai, H. Emori,* M. Takeya,*
T. Masui,** S. Muraoka,** M. Watanabe,*** and T. Usami***

Utilization of charged particle activation analysis has been continued for the study on carbon, nitrogen and oxygen in semiconductor materials in collaboration with the following companies: Mitsubishi Metals Co., Shinetsu Semiconductor Co., Toshiba Electric Co., and Hitachi Ltd. Oxygen content of gallium arsenide crystals was studied in correlation with their preparation conditions, and nitrogen in silicon was analyzed in order to determine the calibration curve for its infrared spectrophotometry and to examine nitrogen contamination into silicon crystals pulled from crucibles covered with silicon nitride. Charged particle activation analysis was also used for oxygen depth profiling and for surface oxygen analysis; these are presented as separate reports in this volume.

Gallium arsenide is one of the most difficult matrices in oxygen analysis by activation with the $^{16}O(^{3}He,p)^{18}F$ reaction, because its oxygen content is usually very low and because high activities of radio-germanium, radio-arsenic, radio-selenium and radio-bromine are formed from the matrix itself. We have developed a satisfactory method of separating the ^{18}F from various matrices, converting the ^{18}F into $KB^{18}F_4$ precipitate.[1] By this method, as low as a few wt ppb of oxygen in semiconductor GaAs has been determined successfully. Gallium arsenide crystals prepared from its melt under various conditions were analyzed in order to get information about (1) oxygen concentration range for commercial GaAs crystals, (2) dependence of oxygen concentration on the preparation methods and dopants, (3) effective distribution coefficient of oxygen between solid and liquid GaAs, and (4) possibility of oxygen doping to the crystal by the addition of Ga_2O_3 to the melt.

Oxygen concentration in semi-insulating GaAs bulk grown both by the liquid encapsulated Czochralski process and by the holizontal Bridgeman method was found to vary from 3 wt ppb to 18 wt ppb. No oxygen level lower than these has ever been reported for any other high-purity substance and for GaAs itself. The low oxygen content is probably due to the ease of oxygen escape by vaporization as arsenic oxide and, in the Czochralski process, by extraction into coexisting B_2O_3 melt as oxides of silicon and chromium which were added as dopants. No marked difference in oxygen content was found in chromium-doped crystals due to the difference in the crystal-formation method. Silicon-doped crystal did not exhibit any elevated oxygen concentration. Effective distribution coefficient of oxygen between solid and liquid GaAs was estimated to be about 2 from the change of oxygen content of the crystal along with the solidified fraction in the encapsulated Czochralski process. The measurement of oxygen levels at three different portions of holizontal Bridgeman crystals formed from Ga_2O_3-added GaAs melt has indicated that intentional oxygen doping to the GaAs single crystal is quite inefficient. More details of this study will be published.[2]

Nitrogen in silicon is known to exhibit sharp infrared absorption peaks at 963 cm^{-1} and 764 cm^{-1}. In heat treatment, less dislocation has been shown to be formed in nitrogen-doped float-zone silicon than in ordinary Czochralski silicon.[3] We previously determined the phase diagramme of the N-Si system in the extremely low nitrogen concentration range[4] and recently the calibration curve for infrared spectrophotometry of nitrogen in silicon by charged particle activation with the $^{14}N(p, \alpha)^{11}C$ reaction. In our recent experiments, the previous procedure has been used with the following modifications:[5] in the chemical separation of the ^{11}C, a larger amount of Na_2CO_3 carrier is added and converted into the counting form of Li_2CO_3 by precipitation from a methanolic solution. By this modification, the interference of non-radioactive carbonate contamination can be made negligible

* Mitsubishi Metals Co.
** Shinetsu Semiconductor Co.
*** Toshiba Electric Co.

and the carrier recovery can be determined reliably by simple weighing. Various silicon samples with and without nitrogen doping were prepared and subjected to the infrared absorption measurement and activation analysis. The calibration curve thus obtained is shown in Fig. 1. Further work is under progress with more care to elevate the reliability of the calibration curve.

Use of a crucible covered with silicon nitride is thought to be effective for the preparation of Czochralski silicon with reduced oxygen contents.[6] Nitrogen contents of silicon crystals prepared from melts in such crucibles under slightly different conditions have been measured by the activation analysis. Contents of about 100 wt ppb have often been found. This work will be continued further.

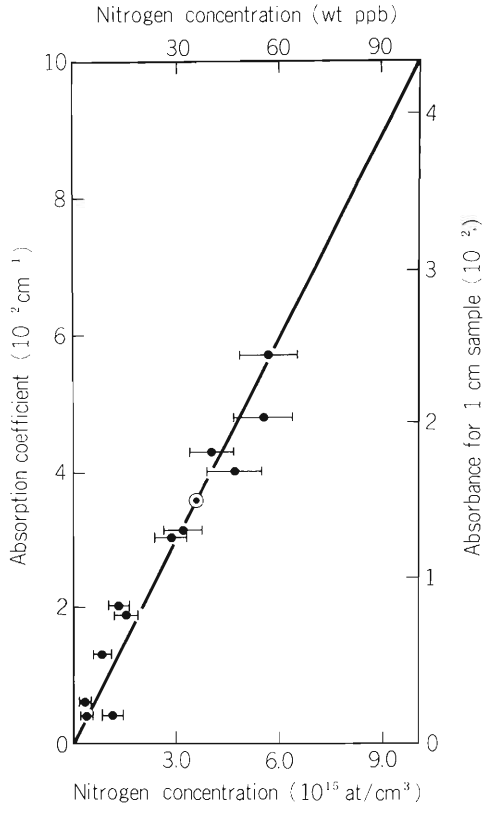

Fig. 1. Calibration curve for infrared spectrophotometry of nitrogen in silicon.

References

1) T. Nozaki: J. Radioanal. Chem.(in press).
2) H. Emori, M. Umehara, M. Takeya, Y. Terai, and T. Nozaki: Proc. 1981 Intern. Symp. Gallium Arsenide and Related Comp.(in press).
3) T. Abe, K. Kikuchi, S. Shirai, and S. Muraoka: Semiconductor Silicon 1981, (Ed. by H.R. Huff et al.), Electrochem. Soc., Pennington, p. 54, (1981).
4) Y. Yatsurugi, N. Akiyama, Y. Endo, and T. Nozaki: J. Electrochem. Soc., 120, 975 (1973).
5) T. Nozaki, Y. Yatsurugi, and N. Akiyama: J. Radioanal. Chem., 4, 87 (1970).
6) M. Watanabe, T. Usami, H. Muraoka, Y. Imanishi, and H. Nagashima: Semiconductor Silicon, (Ed. by H.R. Huff et al.), Electrochem. Soc., Pennington, p. 126 (1981).

III-3-2. Charged Particle Activation Analysis for Surface Oxygen on Silicon and Aluminum

T. Nozaki and M. Iwamoto

Although most methods of surface analysis are applicable only to sample in a high vacuum, it is more important to study surfaces under atmospheric pressure, particularly in the analysis of surface oxygen. Charged particle activation analysis is useful for this purpose, by the use of a suitable target assembly. We initiated this study in 1977[1] and have continued it after some interval.

The apparatus we used is shown in Fig. 1. The sample in a form of two plates in intimate contact with each other is placed on a water-cooled target holder in a bombardment vessel, which can be evacuated by oil-free pumps. The reaction of $^{16}O(^{3}He, p)^{18}F$ has been adopted for radioactivation, and the incident particle energy is so adjusted as to give the maximum cross section for the reaction on the inside surface of the sample plates.

We analyzed high-purity silicon and aluminum. Silicon wafers for the sample were pretreated with a mixture of $HF\text{-}HNO_3$ (1 : 3) at room temperature, washed in pure water with the aid of ultrasonic waves and dried. Aluminum wafers were pretreated with acetone or a mixture of $H_3PO_4 - H_2SO_4$ (1 : 3) at 95 °C in the same manner. Two of these wafers were set in the bombardment vessel and bombarded with charged particles (1～2 μA, 20 min) under three conditions: atmospheric pressure, about 10 Pa and 10^{-3} Pa.

Only the wafer forward to the incident particle direction was taken for the measurement of the ^{18}F activity, because ^{18}F produced in the backward wafer is known to be pushed into the forward wafer almost completely.[2]

The inside surface of about 5 mg cm^{-2} thickness was ground off from the bombarded silicon, and transferred into a polyethylene tube for activity measurement. The annihilation radiation was measured with a well-type scintillation crystal and a single channel analyzer, and the decay was followed. Each of the aluminum sample after the bombardment, was sandwiched between two card plates. Annihilation radiation from the sandwich was then measured with a Ge(Li) detector and a multi-channel analyzer. As an activation standard, a stack of five or six Mylar films were bombarded and the ^{18}F activity in each films was measured under the same conditions as those sample, to give an apparent activation curve. The results of the analysis are shown in Table 1.

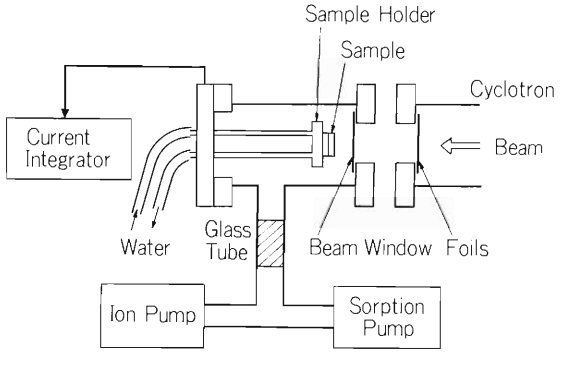

Fig. 1. Apparatus for radioactivation.

Table 1. Surface oxygen quantities ($\mu g\ cm^{-2}$) for different environmental pressures.
(Mean values for repeated measurements, with the numbers of repetitions indicated in the parentheses)

Sample / Pretreatment / Pressure	Si		Al			
	$HF-HNO_3$		Acetone		$H_3PO_4-H_2SO_4$	
Atmospheric	0.7	(8)	7	(4)	3	(1)
about 10 (Pa)	0.2	(11)	6	(2)	2	(1)
about 10^{-3} (Pa)	0.09	(3)	4	(2)	0.4	(2)

References

1) T. Nozaki and M. Iwamoto: IPCR Cyclotron Progr. Rep., 11, 116 (1977).
2) T. Nozaki, M. Iwamoto, and K. Usami: ibid., 14, 93 (1980).

III-3-3. Heat Treatment Behaviour of Oxygen in Silicon as Measured by Charged Particle Activation Analysis

Y. Itoh and T. Nozaki

Since control of oxygen and carbon in silicon wafers has been suggested to be one of the keys to the successful future of VLSI (very large scale integrated curcuit) processing,[1] there has been an explosion of articles published in this field. Gaps remain in our fundamental knowledge of the properties of oxygen in silicon, such as its solubility and diffusion coefficient. However, the depth profiling of oxygen in silicon at trace levels has been a very difficult analytical problem. We developed a simple and reliable method of oxygen depth profiling using charged particle activation analysis with the $^{16}O(^{3}He, p)^{18}F$ reaction.[2), 3)] This new method has been applied to the observation of oxygen distribution after heat treatment of silicon under various conditions. Using these results we estimated the diffusion coefficient and determined the solubility of oxygen in silicon.

Samples used are CZ silicon $<111>$ B-doped p-type and P-doped n-type with resistivities of $2-5\ \Omega$ cm and oxygen concentrations of $6-15 \times 10^{17}\ cm^{-3}$ and FZ silicon $<111>$ B-doped p-type with resistivities of $7000\ \Omega$ cm and oxygen concentrations of $5 \times 10^{15}\ cm^{-3}$. The samples were kept at given temperatures between 900 and 1250°C in an atmosphere of Ar, N_2 or O_2 for

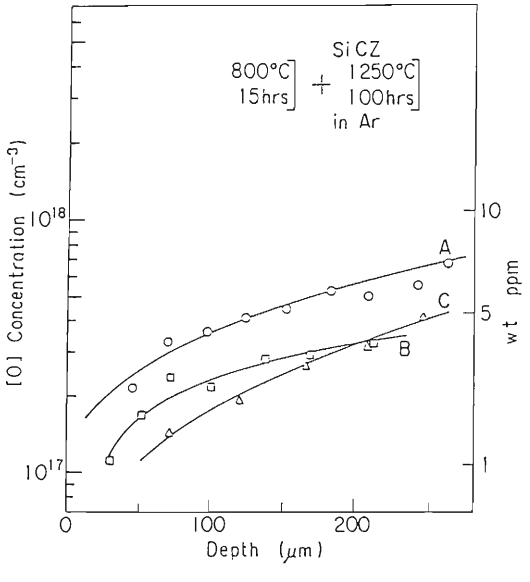

Fig. 1. Oxygen depth profiles in CZ-silicon heat treated in argon. (Initial oxygen concentration: A, $9.5 \times 10^{17}\ cm^{-3}$; B, $6 \times 10^{17}\ cm^{-3}$; C, $8.5 \times 10^{17}\ cm^{-3}$).

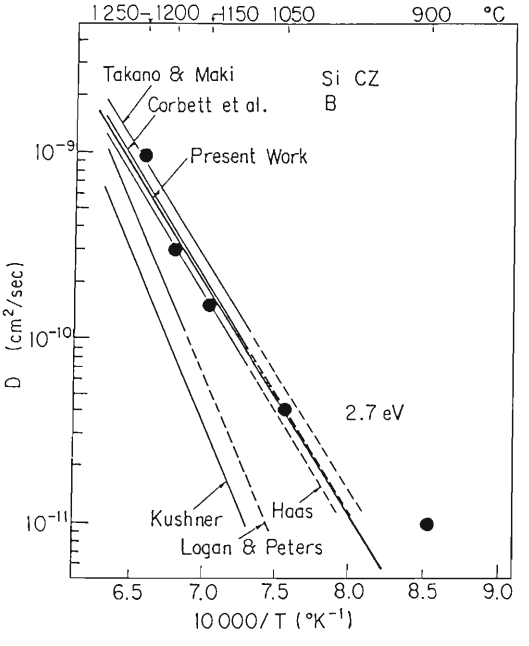

Fig. 2. Diffusion constant as a function of reciprocal temperature in comparison with measurements of other authors.

16 to 144 h. Oxygen depth profiles were obtained by the method reported in our previous paper.[2] The resultant oxygen out-diffusion is shown in Fig. 1 for CZ silicon of various initial oxygen concentrations after heat treatment at 1250°C for 100 h in Ar. Similar profiles were measured for heat treatment at 900, 1050, 1150, 1200, and 1250°C in Ar. The diffusion coefficients of oxygen were estimated from these experimental results for the given temperatures; they are shown in Fig. 2, together with those reported by other workers. The activation energy calculated on the basis of our curve in Fig. 2 is 2.7 eV. The diffusion coefficient is thus given by

$$D = 0.58 \exp(-2.7/kT).$$

These results have frequently been extrapolated to temperatures as low as 450°C, where any small error in their determination at the high temperatures would be magnified. Further results at low temperatures are needed in order to obtain more reliable formula for the diffusion coefficient.

In Fig. 3 we show the oxygen depth profiles of the samples with different initial oxygen concentrations after heat treatment in oxygen atmosphere at 1100°C for 144 h. In sample A and B, the oxygen profiles were variable depending on the initial oxygen concentration. The profile in sample F is for a low initial oxygen concentration, demonstrating the uptake of oxygen from the atmosphere. When these three curves are extraporated to the surface of the sample, they give the same oxygen concentration. This concentration should be the solubility of oxygen in solid silicon at this temperature. It is $(3.6 \pm 0.5) \times 10^{17}$ cm^{-3}. Similar profiles were measured for heat treatments at several other temperatures in oxygen atmosphere. Figure 4 shows the

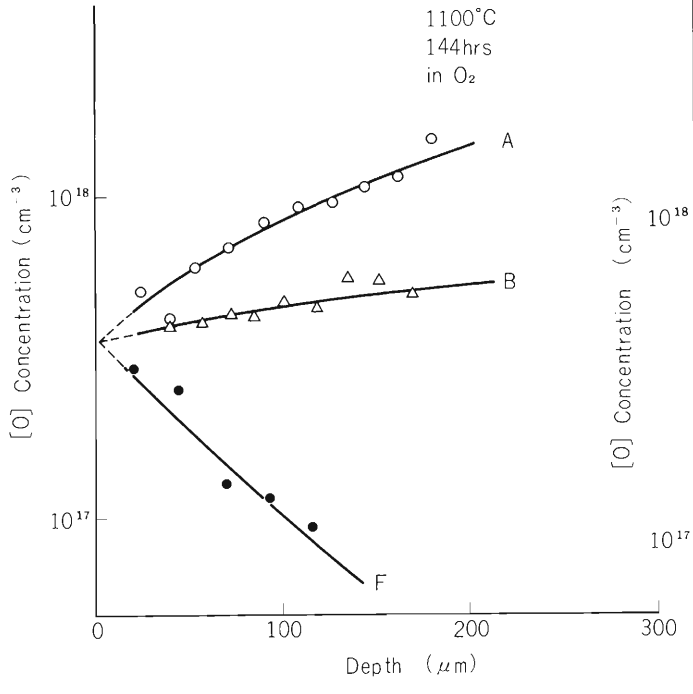

Fig. 3. Oxygen depth profiles of three samples with different initial oxygen concentrations. (A, 9.5×10^{17} cm^{-3}; B, 6×10^{17} cm^{-3}; F, 0.5×10^{17} cm^{-3}).

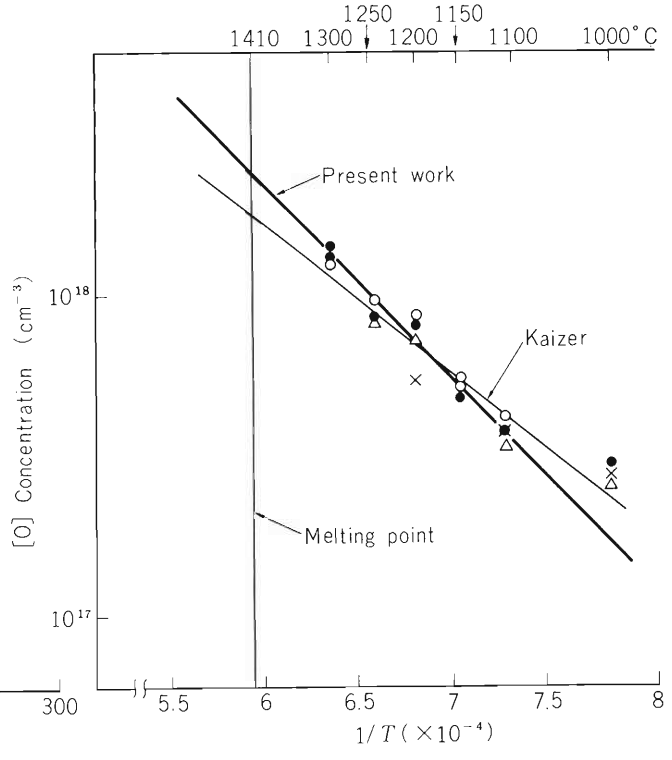

Fig. 4. Solubility of oxygen in solid silicon. (●: FZ, △: CZ; 6×10^{17} cm^{-3}; ○: CZ; $\gtrsim 10^{18}$ cm^{-3}, ×: by Kushner).

oxygen solubility as a function of the reciprocal temperature. The results obtained by the present experiments are slightly different from the results of Kaiser obtained by IR spectrophotometry and those of Kushner by charged particle activation analysis with the $^{18}O(p, n)^{18}F$ reaction. Further experiments will be needed to confirm our results.

References

1) J.R. Patel: Proc. 3rd Intern. Symp. on Si Mater. Sci. and Tech., p. 521 (1977); Proc. 4th Intern. Symp. on Si Mater. Sci. and Tech., p. 189 (1981).
2) T. Nozaki and Y. Itoh: IPCR Cyclotron Progr. Rep., 14, 94 (1980).
3) Y. Itoh and T. Nozaki: J. Radioanal. Chem., 70, 329 (1982).

III-3-4. Effect of Carbon Precipitation on Gold Diffusion in Silicon

Y. Itoh and T. Nozaki

It is well recognized that carbon in Czochralski-grown silicon crystals, when its concentration exceeds a certain critical value, precipitates in a high-temperature heat treatment. The precipitation of carbon exhibits harmful effects on silicon devices, such as lowering of breakdown voltage of p-n junction.[1] The precipitation is also suspected to have certain influence on gold diffusion in silicon. Since carbon in silicon is electrically inactive, it has been investigated mainly by infrared absorption due to substitutional carbon. To get the total amount of carbon content, we used charged particle activation analysis with the $^{12}C(^{3}He, \alpha)^{11}C$ reaction. By combination of this method and usual infrared (IR) spectrophotometry, the precipitation of carbon was investigated.

Samples used were dislocation free CZ-grown silicon $<111>$, B-doped p-type with resistivities of from several $\Omega \cdot$cm to tens of $\Omega \cdot$cm. Dislocation-free float-zone silicon with resistivity of several $k\Omega \cdot$cm was also used for comparison. These samples with different initial oxygen and carbon contents were kept at 1250°C for 100 h in argon. Since little change in the carbon content after the heat treatment was found by charged particle activation analysis, decrease in the substitutional carbon peak in 607 cm^{-1} is regarded as a result of precipitation of carbon. As for oxygen in silicon, both activation analysis and IR spectrophotometry showed certain decreases of its concentration in heat treatments. Gold was diffused into the samples with or without heat treatment at 1000°C in vacuum of 1×10^{-8} Torr for 2.5 h. The results are shown in Fig. 1, where $[O]_D$ is the decrease in oxygen concentration caused by the heat treatment. $[C]_P$ is the quantity of the precipitated carbon estimated from the reduction of substitutional carbon measured

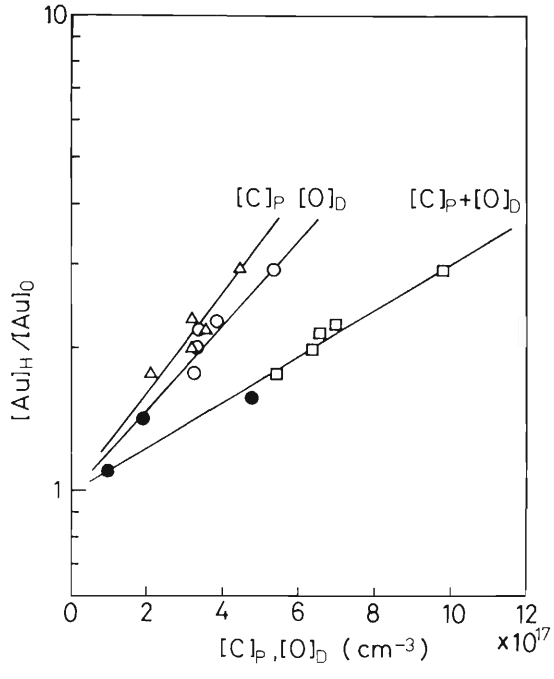

Fig. 1. Effect of decreases of IR-sensitive carbon and oxygen concentrations on gold diffusion in silicon.

by IR spectrophotometry, and $[Au]_H$ and $[Au]_0$ are the central gold concentrations of the samples with and without heat treatment, respectively. The ratios of $[Au]_H$ to $[Au]_0$ are plotted against $[C]_P$ and $[O]_D$ in Fig. 1, by Δ and $\circ$, respectively. The plots $\bullet$ are for $[O]_D$ in samples with low-carbon contents. A linear relationship exists between $[C]_P + [O]_D$ and $[Au]_H/[Au]_0$ as shown in Fig. 1 (plotted by $\square$), indicating that both precipitation of carbon and escape of oxygen have similar acceleration effect on the gold diffusion. Details of this study will be presented elsewhere in the near future.

Reference

1) N. Akiyama, Y. Yatsurugi, Y. Endo, Z. Imayoshi, and T. Nozaki: Appl. Phys. Lett., 22, 630 (1973).

III-3-5. Separation and Purification of Carrier-Free ^{119}Sb from ^{119m}Te Produced by the Sn(α, xn) Reaction

S. Ambe, F. Ambe, and T. Okada

We have been studying the electronic states of ^{119}Sn arising from cyclotron-produced 38.0 h ^{119}Sb in bulk solids by Mössbauer emission spectroscopy.[1-4] Recently, a new series of investigations have also been started on chemical states of carrier-free ^{119}Sb hydrolytically adsorbed on a variety of surfaces.[5-7] In such experiments, not only non-radioactive antimony but also hydrolyzable metal ions which compete with ^{119}Sb in adsorption must be kept minimum in the starting ^{119}Sb solution employed. As reported previously,[5] ^{119}Sb free from non-radioactive antimony contained in the target can be obtained by milking from 4.68 d ^{119m}Te produced by the Sn(α, xn) reaction. Needless to mention, the most probable undesirable impurity in the ^{119}Sb solution obtained is tin which originates in the target. Formerly, we eliminated tin from the solution by anion exchange of ^{119}Sb(V).[8] But, partial loss of ^{119}Sb due to reduction of ^{119}Sb(V) to ^{119}Sb (III) in the resin phase was inevitable in this method.

In the course of adsorption studies of this year, we found that carrier-free ^{119}Sb(V) is hardly adsorbed by active charcoal in the pH range 4-10. Since most hydrolyzable metal ions including Sn(IV) are effectively adsorbed by active charcoal in this pH range, the above finding could be readily utilized in the purification procedure of ^{119}Sb in place of the anion exchange of ^{119}Sb(V).

To 20 ml of 0.25 M LiOH containing carrier-free ^{119}Sb(V) or ^{113}Sn(IV) with a small amount of tin carrier, 100 mg of active charcoal was added. The suspension was shaken for 1 h at room temperature. The active charcoal was separated by filtration or centrifugation and the percentage of ^{119}Sb or ^{113}Sn adsorbed on the charcoal was determined by radioactivity measurement. As shown in Fig. 1, essentially all the ^{113}Sn was adsorbed by the active charcoal from the solutions of pH 4-8, while practically no adsorption of ^{119}Sb was observed at pH 4-10. When the concentration of Sn was larger than 0.8 mM, a part of ^{119}Sb was lost from the solution probably due to co-adsorption with Sn(IV). However, the use of active charcoal can be regarded as quite profitable for elimination of trace of tin from a solution of ^{119}Sb in its final stage of purification.

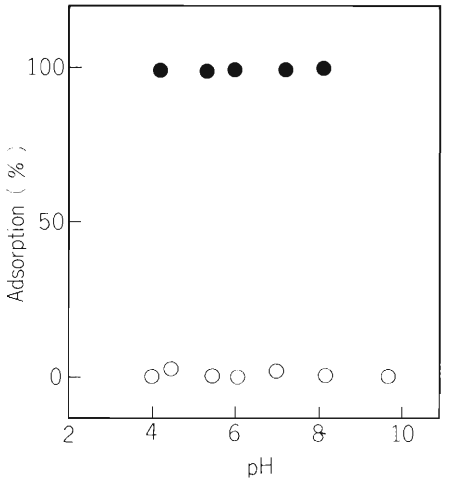

Fig. 1. Percentage of ^{119}Sb(V) (○, carrier-free) and ^{113}Sn(IV) (●, carrier: 6×10^{-5} mM) adsorbed onto 100 mg of active charcoal from 20 ml of 0.25 M LiOH after 1 h of shaking at room temperature.

Our present procedure for the separation and purification of ^{119}Sb from the tin target containing ^{119m}Te is as follows:

A tin plate (1 × 36 × 50 mm, about 13 g, content of antimony 2 ppm) is irradiated with 40 MeV α-particles from the cyclotron in a specially designed target box. The target is dissolved in aqua regia. After evaporation to almost dryness, ^{119m}Te produced by the Sn(α, xn) reaction is precipitated as metal from 3 M HCl with an appropriate amount of Te carrier by reduction with sodium sulfite and hydrazine dihydrochloride. After repetition of dissolution and precipitation, the ^{119m}Te metal is left standing for a few days to allow accumulation of ^{119}Sb by the EC decay of ^{119m}Te. The metal is then dissolved in aqua regia and dried up. The residue is dissolved in 3 M HCl and ^{119m}Te is again reduced to metal, ^{119}Sb being left in the solution. After filtration, a small amount of Te carrier is added to the solution and Te metal is precipitated to ensure removal of ^{119m}Te. The filtrate (3M in HCl) containing ^{119}Sb(III) is passed through a column of anion exchanger, Dowex 1-X8. After thorough washing with 3 M and 0.5 M HCl, ^{119}Sb is eluted with 0.5 M LiOH and oxidized to ^{119}Sb(V) by air bubbling. Active charcoal is added to the solution after neutralization with 0.5 M HCl to pH 6. The suspension is shaken for 1 h at room temperature and filtered. The carrier-free ^{119}Sb solution thus obtained is used for various tracer and Mössbauer studies. Antimony in the solution was determined to be 1 – 4 ppb by neutron activation analysis. The separation of ^{119}Sb from the ^{119m}Te metal could be repeated every two or three days.

Further experiments are now under way in order to establish the conditions for eliminating Sn(IV) with a column of active charcoal.

References

1) F. Ambe and S. Ambe: J. Chem. Phys., 73, 2029 (1980).
2) F. Ambe and S. Ambe: IPCR Cyclotron Progr. Rep., 14, 96 (1980).
3) S. Ambe and F. Ambe: ibid., p. 98.
4) F. Ambe and S. Ambe: J. Chem. Phys., 75, 2463 (1981).
5) T. Okada, H. Sekizawa, F. Ambe, and S. Ambe: IPCR Cyclotron Progr. Rep., 14, 86 (1980).
6) T. Okada, H. Sekizawa, F. Ambe, and S. Ambe: p. 91 in this report.
7) S. Ambe, F. Ambe, and T. Okada: p. 114 in this report.
8) F. Ambe, S. Ambe, and H. Shoji: Radiochem. Radioanal. Lett., 15, 349 (1973).

III-3-6. Adsorption Kinetics of Carrier-Free ^{119}Sb(V) onto α-Fe_2O_3 Surfaces

S. Ambe, F. Ambe, and T. Okada

Recently, we have clarified chemical states of ^{119}Sb(V) adsorbed on α-Fe_2O_3 surfaces by Mössbauer emission spectroscopy.[1), 2)] Here, the adsorption kinetics of carrier-free ^{119}Sb(V) ions from an aqueous solution onto α-Fe_2O_3 is reported.

Kinetic study on hydrolytic adsorption of metal ions from aqueous solutions has been payed little attention because of rapid precipitation of hydrolyzed metal ions after neutralization of the solutions. Antimony(V) ion is one of the most hydrolyzable metal ions and gives various hydrolyzed species dependending on the pH of the solution and the concentration of the ion.[3), 4)] In this work, the troublesome hydrolytic precipitation of antimony(V) ions was avoided by using a carrier-free radioisotope of antimony. Its adsorption onto α-Fe_2O_3 surfaces has been shown to obey an unexpectedly simple kinetic law.

As the tracer, ^{119}Sb was separated from ^{119m}Te produced by α-particle irradiation of tin by the cyclotron.[5)] Suspension of α-Fe_2O_3 in 0.25 M LiCl solution containing carrier-free ^{119}Sb(V) ions was shaken at constant temperatures. An aliquot of the suspension was taken in every one minute for determination of the fraction of ^{119}Sb adsorbed. α-Fe_2O_3 in the aliquot was separated by filtration with glass fiber paper. The radioactivities of ^{119}Sb in each filtrate were counted with an NaI scintillation counter.

Percentage of adsorbed ^{119}Sb after 1 and 3 h is plotted against pH value in Fig. 1. Maximum adsorption was observed at pH around 4, showing almost 100 % adsorption after 1 h shaking.

Adsorption process of ^{119}Sb(V) from the solutions of pH 4.1 at 30, 40, 50, and 60 °C is

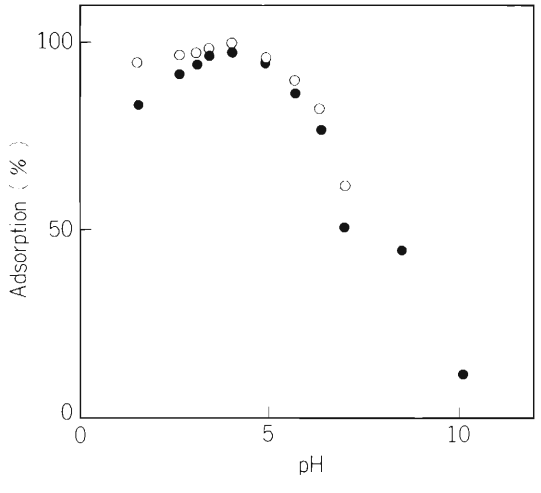

Fig. 1. pH dependence of adsorption of ^{119}Sb(V) on α-Fe_2O_3 at 50 °C: ● 1 h shaking ○ 3 h shaking.

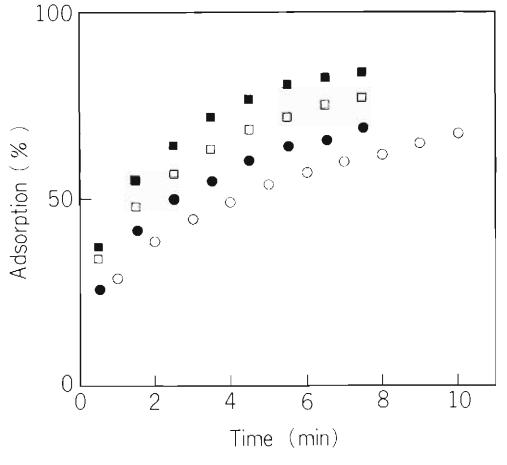

Fig. 2 Increase in percentage of adsorbed ^{119}Sb(V) on α-Fe_2O_3 with time. Adsorption temperature: ■ 60 °C, □ 50 °C, ● 40 °C, ○ 30 °C.

shown in Fig. 2. Temperature dependence of the adsorption indicates that the adsorption of $^{119}Sb(V)$ on α-Fe_2O_3 is a chemisorption. The adsorption was found to follow the rate equation:

$$\frac{dx}{dt} = k(a-x)^2$$

where "a" represents the initial radioactivity of ^{119}Sb and "k" is the rate constant of adsorption. As shown in Fig. 3, the relation between $1/(a-x)$ versus t exhibits a good linearity, giving the rate constant k from the slope. The plot of $\ln(k \times 10^6)$ versus $1/T$ is shown in Fig. 4. From the slope, the activation energy of adsorption was calculated to be 37 kJ/mol using Arrhenius equation.

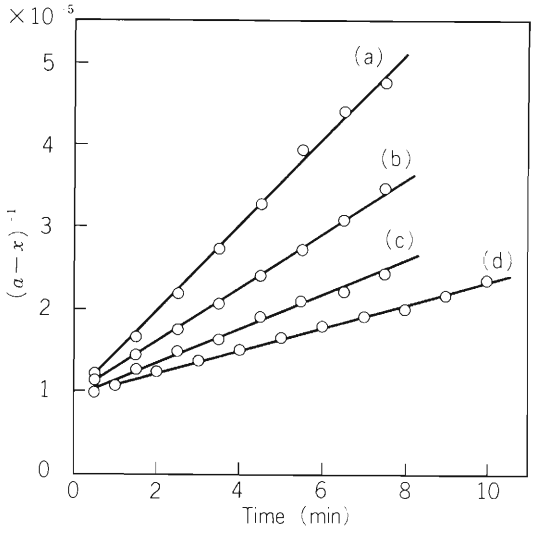

Fig. 3. Relation of $1/(a-x)$ versus time. Adsorption temperature: (a) 60 °C, (b) 50 °C, (c) 40 °C, (d) 30 °C.

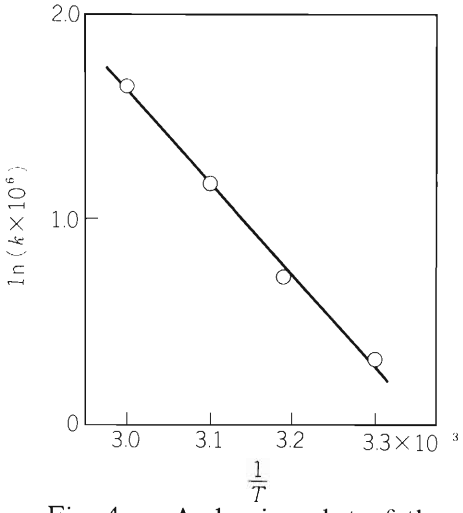

Fig. 4. Arrhenius plot of the adsorption.

The chemical form of dilute Sb(V) ion in a weakly acidic aqueous solution is reported to be $Sb(OH)_6^-$,[4] while the surfaces of α-Fe_2O_3 suspended in the solution are known to be positively charged due to adsorption of protons.[6] The adsorption is considered, therefore, to be initiated by the electrostatic attraction between the negatively charged complex ions in the solution and the positively charged oxide surfaces and then leads to the formation of Sb-O-Fe bonds on the surfaces as shown by Mössbauer spectroscopy.[1),2)]

References

1) T. Okada, H. Sekizawa, F. Ambe, and S. Ambe: IPCR Cyclotron Progr. Rep., 14, 86 (1980).
2) T. Okada, H. Sekizawa, F. Ambe, and S. Ambe: p. 91 in this report.
3) S.H. Gate and E. Richardson: J. Inorg. Nucl. Chem., 23, 257 (1961).
4) G. Jander and H.J. Ostmann: Z. Anorg. Allg. Chemie, 315, 241 (1962).
5) S. Ambe, F. Ambe, and T. Okada: p. 112 in this report.
6) G.A. Parks and P.L. de Bruyn: J. Phys. Chem., 66, 967 (1962).

III-4. Radiation Chemistry and Radiation Biology

1. Inactivation of B. Subtilis Spores by Heavy Ions

T. Takahashi and F. Yatagai

Inactivation of B. subtilis spores has been studied using accelerated He, C, and O ions, and several attempts were made for the interpretation of the results. To get better understanding of inactivation, we are doing experiments using Ne ions which became available recently. The inactivation cross sections preliminarily obtained for Ne ions are shown in Fig. 1, with our cross sections for He, C, N, and O ions.[1), 2)] In Fig. 1 are also shown cross sections for Pb and U ions recently published by Schäfer et al.[3)] Analyses are in progress based on Chatterjee and Schaefer's track structure model[4)] as well as Katz's theory.[5), 6)]

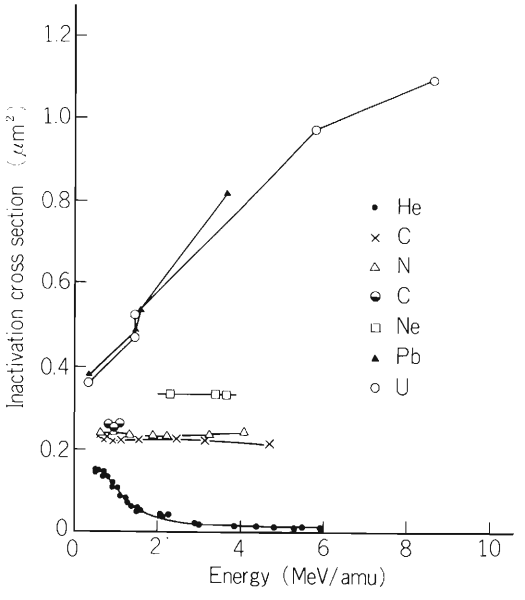

Fig. 1. Relation between the energy of ions and the inactivation cross sections. Lines are to guide the eye.

References

1) F. Yatagai, T. Takahashi, and A. Matsuyama: J. Radiat. Res., 15, 90 (1974).
2) F. Yatagai, T. Takahashi, and A. Matsuyama: ibid., 16, 99 (1975).
3) M. Schäfer, R. Facius, K. Baltschukat, and H. Bücker: Proc. 7th Symp. on Microdosimetry (1980).
4) A. Chatterjee and H.J. Schaefer: Radiat. Environm. Biophys., 13, 215 (1976).
5) R. Katz, B. Ackerson, M. Homayoonfer, and S.C. Sharma: Radiat. Res., 47, 402 (1971).
6) T. Takahashi, F. Yatagai, and A. Matsuyama: Sci. Papers I.P.C.R., 74, 51 (1980).

III-4-2. Relative Biological Effectiveness of Nitrogen Ions on Inactivation of Cultured Mammalian Cells

I. Kaneko, T. Nishimura, T. Ohno, K. Eguchi,
K. Nakano, and T. Inada

Heavy-ions have been shown to have higher biological effectiveness, and are expected to be superior to X- or γ-rays for cancer therapy.

The present study, performed with nitrogen ions, concerns (1) the relative biological effectiveness (RBE) on the inactivation of mammalian cells and (2) the expression and repair of the heavy ion-caused damage in the mammalian cells in culture.

Normal human fibroblasts, IMR 90 cells were maintained and treated as described previously.[1] Human melanoma HMV cells were cultured in F-12 medium supplemented with 5 % calf serum and 0.05 % heat infusion broth (Difco).[2] Human epitheloid carcinoma HeLa S3, mouse Balb/c 3T3, and Chinese hamster V79 cells were cultured in MEM medium containing 10 % fetal bovine serum. Colony-forming IMR 90 3T3 cells were cultured with feeder cells previously irradiated with 5500 rad of ^{60}Co γ-rays. The expression and repair of the damage after nitrogen-ion irradiation were performed by incubating these cells at their saturation density.

Five hours before nitrogen-ion irradiation, the cells were seeded onto 25 mm cover glass set in 35 mm glass petri-dishes. The dishes were incubated in a humidified CO_2-incubator until the time of irradiation. Cell-handling procedures for the irradiation and cultivation were similar to those described previously[1] except for the size of the dishes and without replating after irradiation because the irradiation dishes with cells were directly incubated for the colony formation. A new dish holder for 35 mm petri dish was used for irradiation.

Table 1 shows the radiosensitivities for three human cell lines.

The relationship between RBE and LET for inactivation of human IMR 90, HeLa S3, and HMV cells by nitrogen-ion irradiation was found to be similar to that of human fibroblast HF 19

Table 1. Radiation quality and radiosensitivity of three human cell lines.

Cell line	Parameters	γ-rays	Nitrogen ions (E=4.7 MeV/amμ)	RBE
Normal human fibroblast,	D_0 (rad)[a]	153	98	1.5
IMR 90	n[b]	1.6	1.1	
Human epitheloid carcinoma,	D_0 (rad)	180	140	1.3
HeLa S3	n	2.0	1.0	
Human melanoma,	D_0 (rad)	130	95	1.4
HMV	n	9.1	0.4	

a) The dose required to reduce the number of clonogenic cells to 37 % of their former value.
b) A measure of the width of the initial shoulder in the survival curves.

and Chinese hamster V79 cells.[3)]

The patterns[4)] of the recovery from the potentially lethal damage in IMR 90 and Chinese hamster V79 cells after nitrogen-ion irradiation were found to be different from the well-known pattern for the recovery from the potentially lethal damage after γ-ray irradiation. Studies on the potentially lethal damage repair of HeLa S3, HMV, and Balb/c 3T3 cells after nitrogen-ion irradiation are under way.

References

1) I. Kaneko, T. Ohno, K. Nakano, and F. Yatagai: IPCR Cyclotron Progr. Rep., 14, 102 (1980).
2) T. Inada, K. Kawachi, T. Kanai, and I. Nojiri: J. Radiat. Res., 22, 143 (1981).
3) R. Cox and W. K. Masson: Int. J. Radiat. Biol., 36, 149 (1979).
4) I. Kaneko, T. Ohno, I. Suzuki, T. Taira, K. Nakano, and F. Y. Yatagai: J. Radiat. Res., 22, 26 (1981).

III-5. Instrumentation

1. Gamma-Ray Circular Polarimeter

K. Ieki and M. Ishihara

NUCLEAR INSTRUMENT Forward scattering type Compton polarimeter; conical shape magnet, variable detection angle of emitted particle, calculated analyzing power and transmission

In an attempt to study heavy ion reaction mechanism, several methods have been employed to determine spin polarizations of residual nuclei. These methods utilize β-decay asymmetry of ^{12}B,[1] double scattering of protons[2] and circular polarization of γ-rays.[3] Much knowledge was given to light fragment polarization by the first two methods, whereas information on heavy fragment polarization can be taken only via the third method.

In order to pursue the study of heavy fragment polarization, we are now constructing forward scattering type Compton circular polarimeter. The main features of the setup are similar to those of Trautmann et al.,[3] but following modifications have been incorporated:

1) Trautmann et al. detected emitted particles with ionization chamber and Si detector at fixed angle. To study reaction mechanism, however, detection at variable angles is favorable. In our setup counter telescopes can be set symmetrically with beam axis in vacuum chamber at varied angles. Setting angle can be changed in 5° step. To gain detection efficiency, the telescope with solid angle of 20 – 40 msr can be installed and serveral sets of the telescopes can be set at the same time.

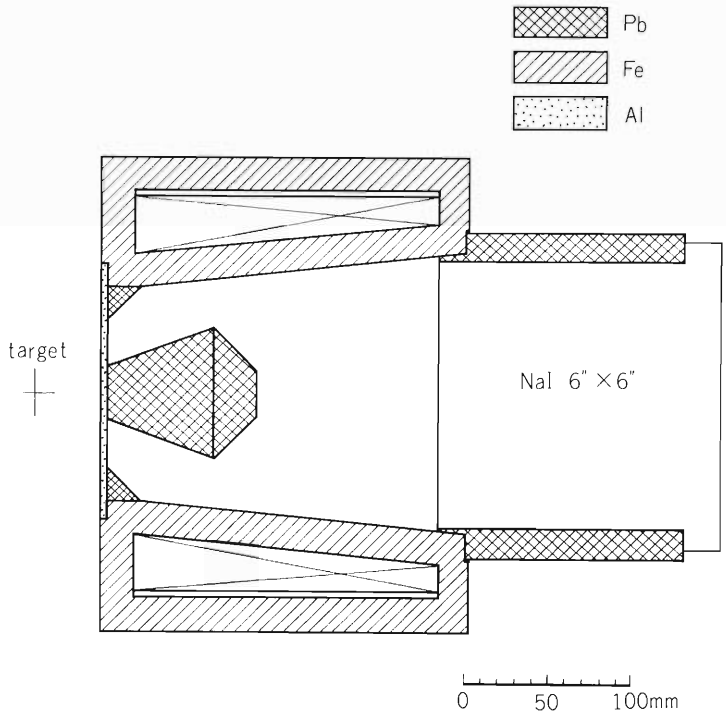

Fig. 1. Cross sectional view of the polarimeter.

2) The room required for installation of particle detectors causes the size of chamber to become rather large. Hence, we chose a relatively large volume NaI detector ($6''^{\phi} \times 6''$) to obtain sufficient efficiency.

3) Trautmann et al. chose a rather complicated shape of the magnet surface. Our setup adopts a simple conical shape to facilitate easy construction (Fig. 1). The acceptance angle for incoming γ-rays ranges $20^{\circ} - 45^{\circ}$ which is the same as for Ref 3. To calculate figure of merit of the setup, we made Monte Carlo simulation code "POL" which includes multi-scattering effect. Calculated results are shown in Fig. 2. Though the analyzing power of our setup is smaller than that of Ref 3, transmission is larger, and the figure of merit is comparable.

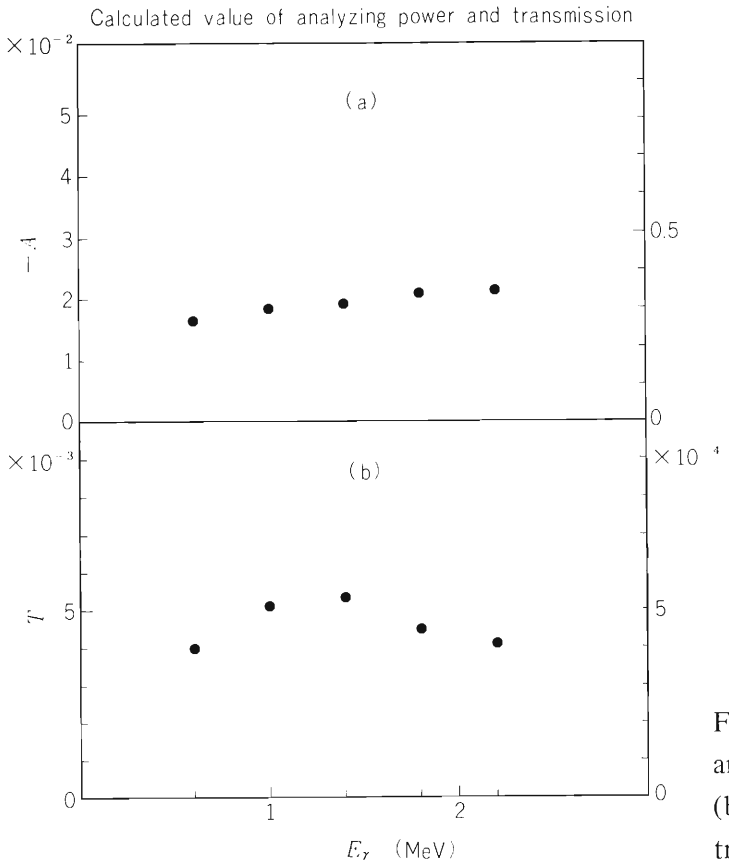

Fig. 2. Calculated value of analyzing power (a) and transmission (b). Right-hand scale of transmission is relative to 4-π.

References

1) K. Sugimoto, N. Takahashi, A. Mizobuchi, Y. Nojiri, T. Minamisono, M. Ishihara, K. Tanaka, and H. Kamitsubo: Phys. Rev. Lett., 39, 323 (1977).

2) T. Sugitate, T. Nomura, M. Ishihara, Y. Gono, H. Utsunomiya, K. Ieki, and S. Kohmoto: IPCR Cyclotron Progr. Rep., 14, 28, 64 (1980).

3) W. Trautmann, C. Lauterbach, J. de Boer, W. Dunnweber, G. Graw, W. Hamann, W. Hering, and H. Punchta: Nucl. Instr. and Methods, 184, 449 (1981).

III-5-2. Neutron Detection in In-Beam Spectroscopy

A. Hashizume, H. Kumagai, Y. Tendow, and
T. Katou

To study the states in neutron deficient nuclei excited by (HI, xnγ) reactions by in-beam γ-ray spectroscopy, it is important to distinguish other types of reactions such as charged particle emitting reactions. The n-γ coincidence technique is a useful means to define the neutron emitting reaction channel.

A liquid plastic scintillation neutron detector has been successfully used for this purpose. The detector consists of a RCA 8854 photomultiplier optically coupled to liquid plastic scintillator of 5″ diam.×3″ NE213. To distinguish the neutrons from γ-rays a pulse shape discrimination technique has been used. The block diagram used for the n-γ coincidence is shown in Fig. 1. The selection of pulses caused by neutrons from those by γ-rays is made by the difference of zero-crossing time of pulses. A typical time spectrum from the pulse shape discriminator system

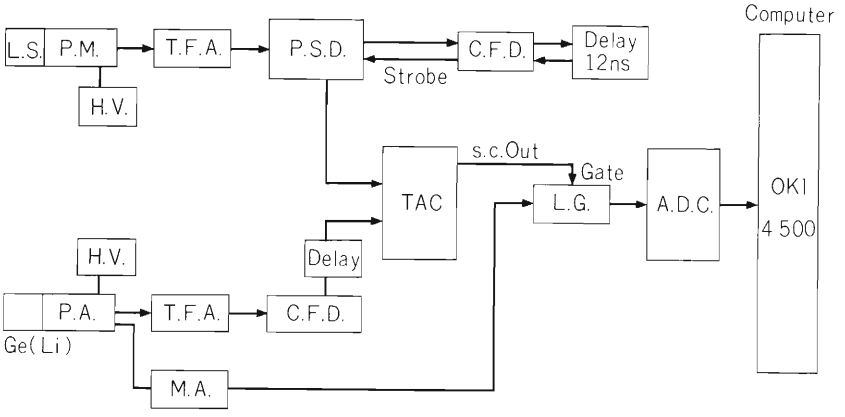

C.F.D. : Constant fraction discriminator
P.S.D. : Pulse shape discriminator
T.F.A. : Timing filter amplifier

Fig. 1. The block diagram of the electronic system to obtain n-γ coincidence spectrum.

is shown in Fig. 2. Californium 252 was used for the γ-ray and neutron source. The time resolution was considerably improved when the liquid scintillator and the photomultiplier were cooled to 0° C.

Figure 3 shows γ-ray energy spectra in coincidence with neutrons obtained when ^{147}Sm was bombarded by 100 MeV ^{16}O. For comparison a γ-ray singles spectrum is also shown. If one takes the ratios of peak areas between γ-ray singles and n-γ coincidence for the 2^+ 0^+ transition in (^{16}O, 3n) and the $17/2^+$ $13/2^+$ transition in (^{16}O, 4n) reactions, the peak of the $17/2^+$ $13/2^+$ transition is 1.3 times larger than that of 2^+ 0^+ transition in the n-γ coincidence spectrum. This fact reflects the emission of one more neutron in (^{16}O, 4n) than in (^{16}O, 3n) reaction. Thus, to observe the change of intensity of peaks in singles and n-γ spectrum is a good means to distinguish a (HI, xn) reaction from (HI, (x−1)n) or other charged particle emitting reactions.

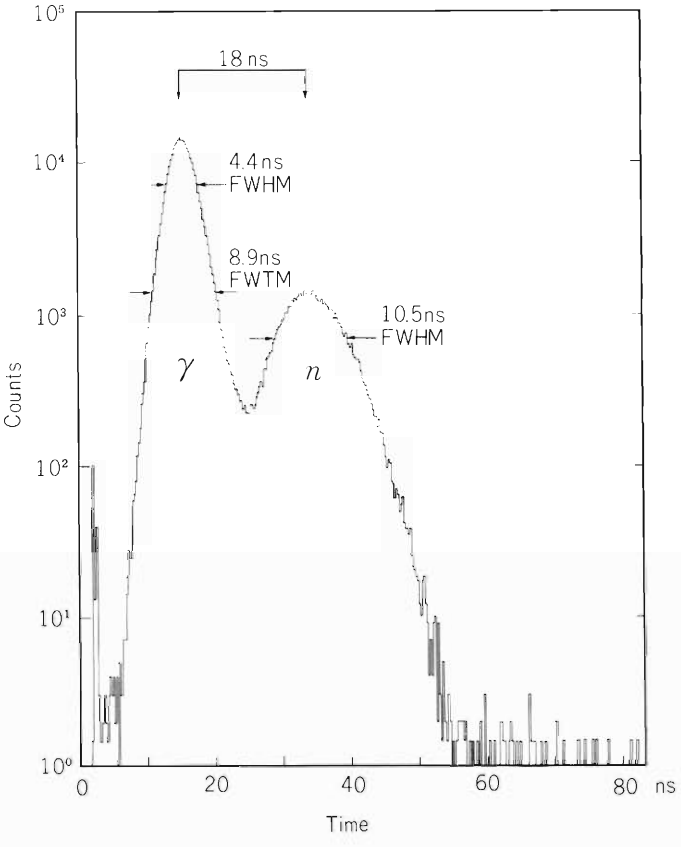

Fig. 2. A time spectrum from pulse shape discriminator system using γ-rays and neutrons emitted from ^{252}Cf.

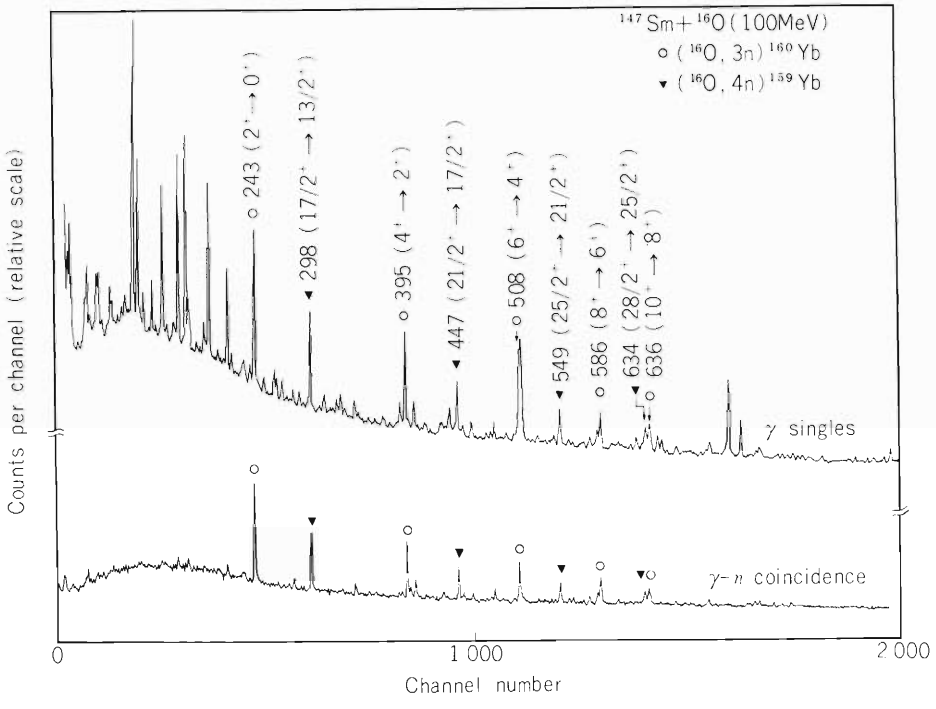

Fig. 3. A spectrum of γ-ray singles and of γ-rays in coincidence with neutrons observed in the ^{147}Sm + ^{16}O (100 MeV) reaction.

III-5-3. Data Processing System at RILAC

H. Kumagai and M. Sasagase

Construction of the on-line data taking and data processing system[1] at RILAC is in progress. An 8-parameter multi-channel scaler (MCS) interface, a LIST mode interface and a control panel interface were installed, and another PERKIN ELMER model 3220 super mini-computer has also been introduced in 1981, for off-line data processing. The present configuration of the on-line and off-line data processing systems is shown in Fig. 1. Both users of the on-line computer and the off-line one can make use of the common line printer, digital plotter and magnetic tape controller by switching the input/output switches.

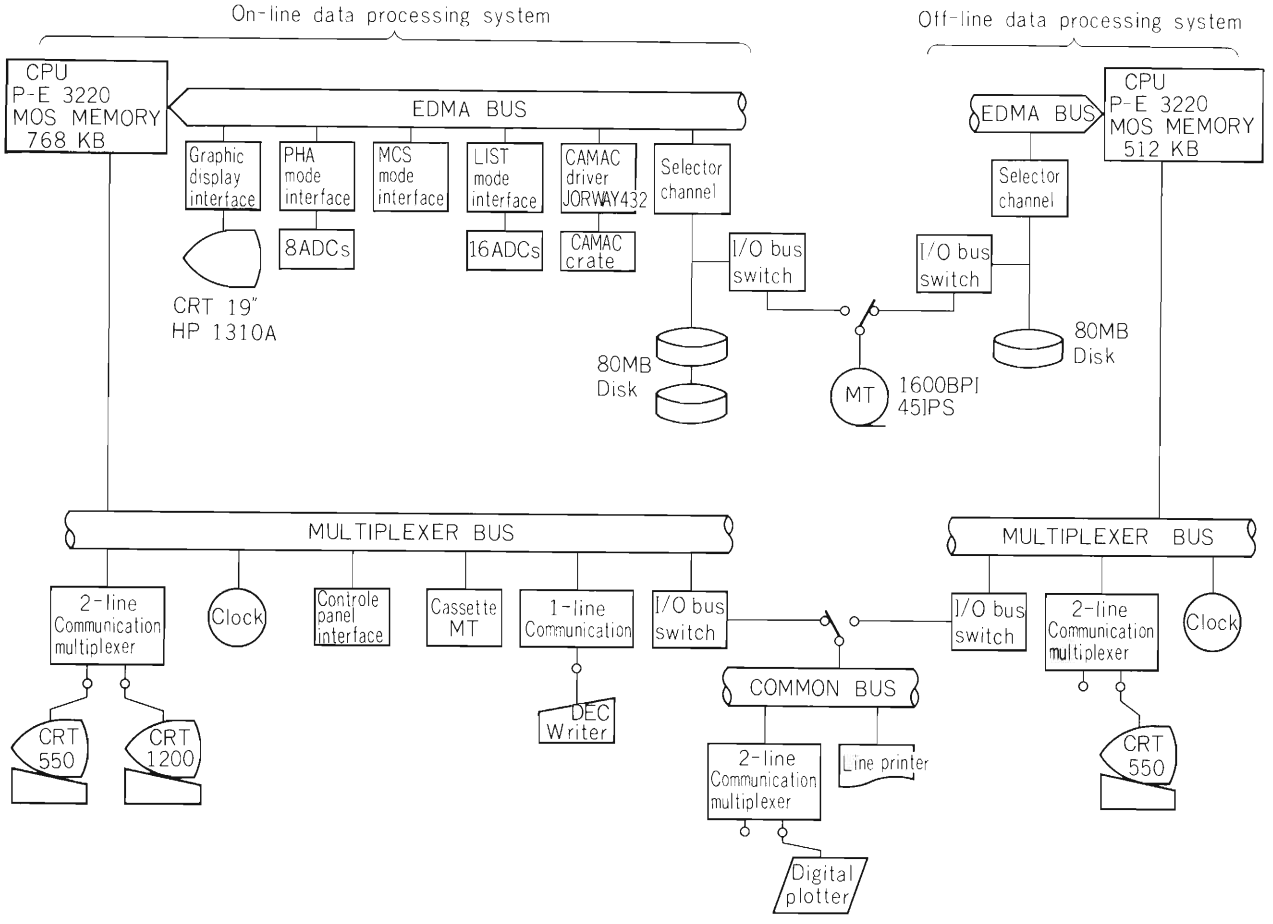

Fig. 1. The data processing system.

The specifications of the custom made interfaces are described below.

For the MCS interface:

1) Eight independent scalers (24 bit, 100 MHz) are included so that 8 input pulses can be counted simultaneously.

2) Data address on the main memory is appointed with a universal logic interface (ULI).

3) Readout and modification of the contents of the main memory are performed with DMA channel.

4) It is possible for a user-written program to control the interface ignoring the condition of several switches on the front panel.

For the LIST mode interface:

1) Maximum 15 NIM-ADC's can be connected and coincidence data are sent to the main memory event by event.

2) There are two coincidence modes, the internal coincidence mode and the external coincidence mode. For the internal coincidence mode, coincident data are taken into the interface when some ADC signals are input within a coincidence time, which is previously defined by a user. For the external coincidence mode, gate signals for each ADC are generated by supplying an external coincidence signal to the interface. Coincident data are simultaneously taken into the interface for maximum 16 combinations of the ADC's in this mode.

3) Coincidence data are sent to the main memory from the interface through DMA channel.

4) There are two buffer areas of 16 k byte on the main memory. The data on the buffer area are recorded on a magnetic tape or a disk when one of these buffer areas is filled up with data.

For the control panel interface:

1) This interface is designed to enable a user to control the PHA, MCS, and LIST interfaces and to do I/O operation to a disk, the magnetic tape, the line printer or the plotter by pressing the butten switches on the panel.

Development of softwares to control the above-mentioned interfaces is in progress. Because many functions are required to the system, these functions are shared with many separated tasks and care is taken so that close communication is possible among these tasks. The on-line data processing system is planned to be accomplished by the end of February in 1982.

Reference

1) H. Kumagai and T. Wada: IPCR Cyclotron Progr. Rep., 14, 156 (1980).

Ⅳ. ACCELERATOR DEVELOPMENT

1. New Gas-Feed System and Acceleration Test of Heavy Ions with Gas Mixing

K. Ikegami, K. Ogiwara, and I. Kohno

A gas-feed system was improved for stable operation of the ion source. A method of mixing gas[1] through the gas-feed system was applied in the production and acceleration of heavy ions such as C^{4+}, O^{5+}, N^{4+}, N^{5+} or Ne^{6+} ions, to increase beam intensity and stability of source operation.

Figure 1 shows a block diagram of the new gas-feed system. This system consists of four reservoirs, additional valves and two gas-feed lines having a gas flow controller. The reservoirs and additional valves are placed in the control room. Two gas controllers are installed in the underground room of the cyclotron vault, because the ion source must respond quickly to the change of gas flow without picking up RF noise. Figure 2 shows a block diagram of a gas flow controller system. This system is composed of a piezoelectric valve[2] PV-10 made by VEECO, a gas flow controller made by RIKEN and a mass flow meter by HASTING. The valve PV-10 is operated by an electric pulse with a repetition rate of 300 Hz and an amplitude of 80 – 100 V supplied by a controller. By varying the pulse duration from 0 to 6 % one gas flow controller can be remotely controlled over a range of 0 to 10 cc/min and the other from 0 to 5 cc/min.

In the case of mixed gas, the main gas was supplied to the ion source through one gas-feed line and the support gas was supplied through the other line. Rare gases, such as He, Ne, Ar, Kr, and Xe, were mainly used as the support gas. To investigate the gas mixing effect, heavy ion source of electron-bombarded hot cathode type[3] was used. In the test run the electron-bombarding power was switched off after the source was ignited to avoid effect the other than the

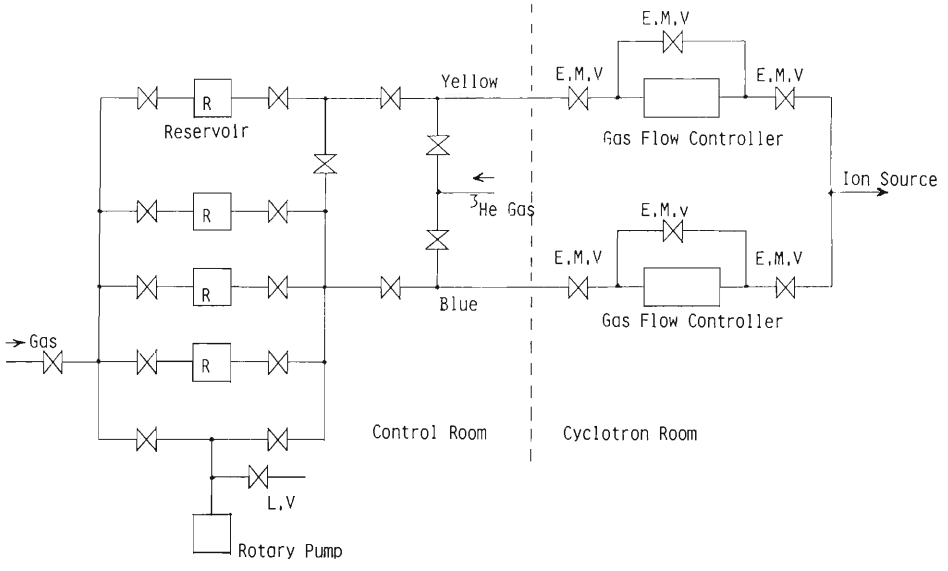

Fig. 1. A block diagram of the gas-feed system. Yellow line indicates a path of the main gas and blue line a path of the supporting gas.

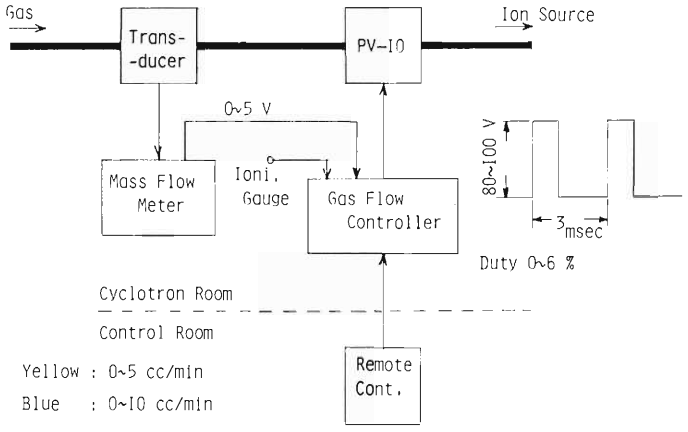

Fig. 2. A block diagram of the gas flow controller system.

mixing of gas. The main gas was decreased gradually and the supporting gas was increased to keep constant arc power and arc impedance. The beam intensity of heavy ions extracted from the cyclotron was measured with a gate drop probe at the entrance of the beam transport system.

Figures 3 and 4 show the beam intensity of 76 MeV C^{4+} when CO_2 and Ne gases are mixed, and 103 MeV O^{5+} when O_2 and Ar gases are mixed, respectively. In both cases optimum mixing rate of gases exists and the gas mixing is effective to increase the beam intensity. As the result of the test, it was found that the effect of gas mixing depends on the kind of the supporting gas. In the production of C^{4+} ions using CO_2 gas, Ne, Ar, and Kr gases were effective as supporting gases while He was not effective. In the case of O^{5+} using O_2 gas Ar gas was effective, but neither Ne nor Kr was effective. In the case of N^{5+} using N_2 gas, Ne and Ar gases were effective, but neither He nor Kr was effective. In the case of Ne^{6+} using Ne gas, no effective supporting gas was found. In all effective case, time duration of stable operation of the source was increased. We think from the result of the test that gas mixing is effective to stabilize the arc plasma in the ion source rather than for the beam intensity enhancement of heavy ions.

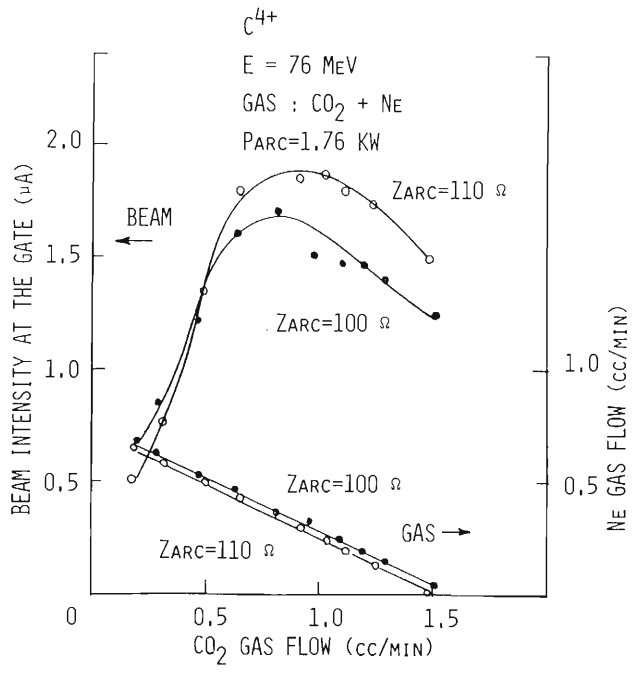

Fig. 3. The extracted beam intensity for 76 MeV C^{4+} at the gate and Ne gas flow to maintain Z_{arc} constant as a function of Co_2 gas flow.

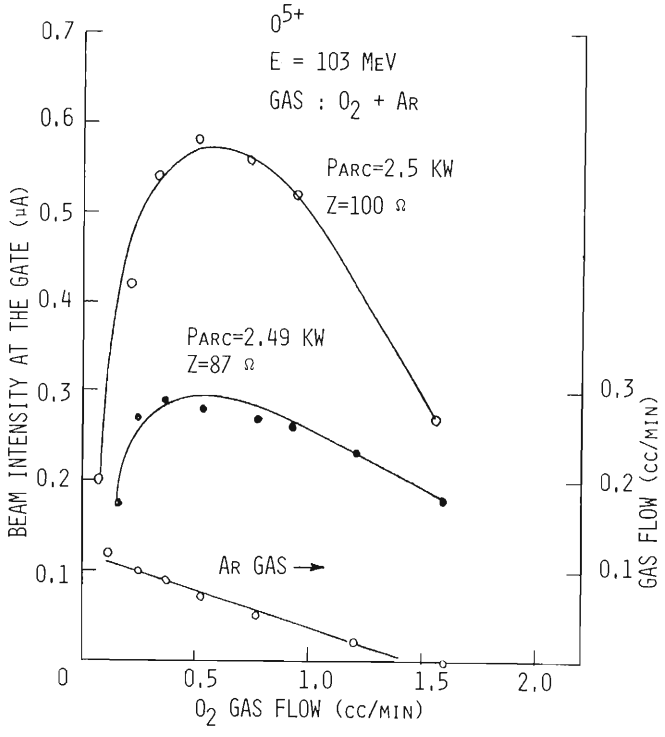

Fig. 4. The extracted beam intensity for 103 MeV O^{5+} at the gate and Ar gas flow to maintain Z_{arc} constant as a function of O_2 gas flow.

References

1) E.D. Hudson, G.A. Palmer, and C.L. Haley: IEEE Trans. Nucl. Sci., NS-24, 1950 (1977).
2) Y. Sakurada, G.D. Deharen, W.J. Walterscheid, S.M. Rielamowicz, R.L. Haisler, and H.W. Peeler: ibid., NS-26, 2175 (1975).
3) T. Kageyama, K. Ikegami, and I. Kohno: IPCR Cyclotron Progr. Rep., 14, 4 (1980).

Ⅳ-2. Beam Acceleration Test at RILAC

T. Kubo, T. Kambara, Y. Miyazawa, M. Hemmi,
Y. Gono, T. Inoue, T. Tonuma, M. Kase,
M. Yanokura, Y. Chiba, T. Fujisawa,
and M. Odera

In the spring of 1981, the beam acceleration test by synchronous excitation of six resonators was started to confirm the basic design of the heavy-ion linac (RILAC). Simplified control circuits[1] were fabricated for radio-frequency (RF) system[2] and were used to attain the stable acceleration. Ions of Ar^{4+} and N^{+} have been accelerated successfully at the frequency of 20 MHz.

(1) RF system

The beam acceleration synchronizing more than one resonator is difficult without the control circuits for the RF system.[3] As the installation of such control circuits is not completed, we made simplified ones to stabilize the operation of the RF system. Each of them includes, as described in detail in Ref. 1, an amplitude regulator of accelerating voltages, a semi-automatic tuner of the resonator and a phase shifter. Changes of the amplitude and phase of the accelerating voltages can be corrected by them.

Adopted acceleration frequency was 20 MHz, which corresponded to energy gain of 0.8 MeV/nucleon. Calculated RF voltages of the resonators for the Ar^{4+}- and N^{+}-ions are shown in Table 1, assuming that the phase angle for synchronized acceleration is −25 deg.

Table 1. Parameters of the RF system and the injector.

Ions		Ar^{4+}	N^{+}
Injector		225 kV	315 kV
Resonator	#1	90	126
	#2	100	140
	#3	115	161
	#4	125	175
	#5	140	196
	#6	150	210

(2) Beam acceleration

The ions produced in a PIG type ion source[4] were accelerated by an electrostatic injector,[5] and analyzed by two dipole magnets,[6] then led into the first resonator. The accelerating voltages of the injector are also shown in Table 1.

To confirm acceleration at the linac, it is necessary to measure the energy of the output beam. Two methods were available. One was measurement of the energy spectra by a Si detector placed

in the beam path. The other was an analysis of the beam by a switching (SW) magnet[7] installed downstream of the last resonator.

The former method is adequate to measure a small amount of the beam and was used in early stage of the acceleration test. For protection of the Si detector, the beam was collimated by a copper foil which was 15 μm in thickness and had a pinhole of 10 μm in diameter. The acceleration was optimized one by one from the first resonator, referring to the energy spectra. Parameters of the RF system (amplitude and phase) and those of focusing elements (Q-magnets) were adjusted so that the energy spectra would have a peak corresponding to the designed energy gain of excited resonators. Figure 1 shows an example of the optimized energy spectra of the N^+-ions accelerated when the first three resonators were excited. The peak found at the right side shows the ions accelerated synchronously, whose energy is 5.8 MeV. The peak at the left side, which has the energy of ions accelerated only by the injector, is supposed to be of atomic nitrogens neutralized by charge exchange process in the injection region. The energy spread of the accelerated ions is less than 1.7 % (FWHM).

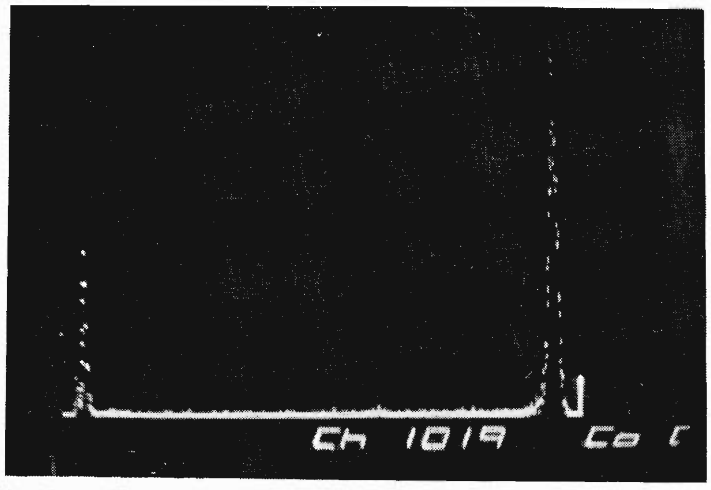

Fig. 1. Energy spectrum of the N^+-ions accelerated by the first three resonators.

Later, we confirmed the acceleration by the SW magnet as the beam current increased. The optimization procedure was similar to that of the former one except that the field of SW magnet was set according to the energy gain of excited resonators and the adjustments were made by referring to the beam current. Figure 2 shows an example of momentum spectrum of the Ar^{4+}-ions accelerated by all six resonators, which was measured by scanning the exciting current of the analyzer magnet[7] after the SW magnet. Energy obtained is 32 MeV and the energy spread is estimated to be about 1.5 % (FWHM).

The accelerated Ar^{4+}-ions were transported to A-1 and B-1 channels of target area.[7] Beam currents were more than 10 nA for each channel. Acceleration efficiency was obtained by comparing the beam current at the entrance of the first resonator with that at the end of the channel and was, so far, about 1 %.

The accelerated Ar^{4+}-ions were provided for experiments of atomic physics at the B-1 channel for the first time in autumn.

The acceleration of other ions (O^+, Xe^{8+}, etc.) and the acceleration at other frequencies are planned now.

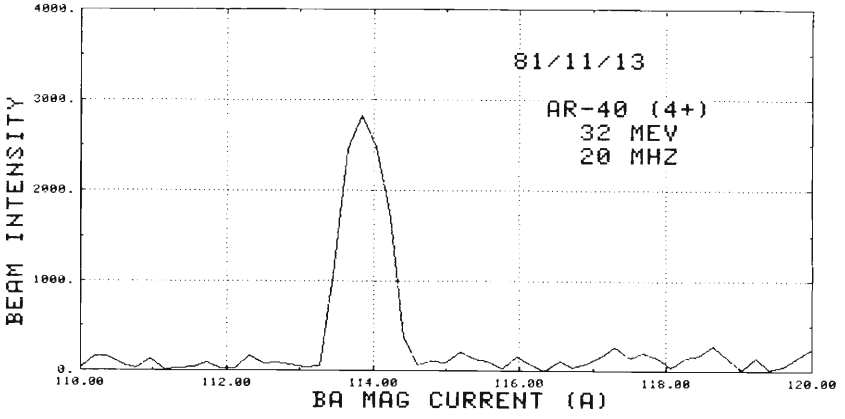

Fig. 2. Momentum spectrum of the Ar^{4+}-ions accelerated by all six resonators. The unit of vertical axis is arbitrary.

References

1) T. Kubo, M. Hemmi, and Y. Chiba: p.137 in this report.
2) T. Kubo and Y. Chiba: IPCR Cyclotron Progr. Rep., 14, 123 (1980).
3) Y. Chiba: ibid., p. 120.
4) M. Kase and Y. Miyazawa: ibid., p. 132.
5) M. Hemmi: ibid., 13, 145 (1979).
6) M. Kase, M. Hemmi, and S. Nakajima: ibid., p. 147.
7) M. Hemmi, Y. Miyazawa, and M. Odera: ibid., 14, 126 (1980).

Ⅳ-3. Performance of Light Link System for Control of Instruments on High Voltage Terminal

M. Hemmi

An optical fiber light link system which is insensitive to various electrical noises has been devised to control the instruments such as the ion source or vacuum pumps on the high voltage terminal, potential of which is as high as 500 kV. Since frequent on-off and fine tuning operation of the ion-source parameters from the control room is required, the usual mechanical control using the insulator rods has been abandoned in favor of an indirect control method which is more flexible. The method is based on the use of the optical link which transmits information through optical fibers by modulating infrared light.

(1) On-off signal channel

Usual method of the pulse code modulation was avoided, because puslive noises are numerous around the high voltage terminal where Corona or brush discharge is always present. Instead, a frequency modulation scheme has been adopted. The modulating frequency is chosen rather low and is between 500 and 2500 Hz. Mechanical tuning forks are used as the frequency discriminator in this audio-frequency range. The forks have an excellent characteristics as filter and are reliable, low cost and easy to tune. Figure 1 shows schematically the on-off control system using sinsoidally modulated light. At present, there are 32 channels for command signals from the control console. The number of the channels can be expanded up to 60 when necessary.

To avoid any error in the important operation, a double signal coincidence scheme is used for such command. In that DTMF (dual-tone multi-frequency) scheme only signals with coincident output from the two filters are accepted and addresses are specified by the two frequencies. For less important command, single frequency is assigned for each kind of operation. In Fig. 2, a block diagram of the on-off operation system is indicated. In that figure, in the down link channel

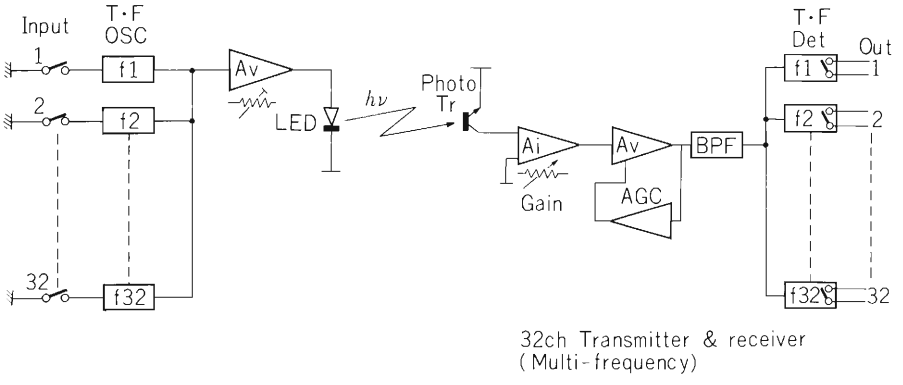

Fig. 1. Scheme of the optical link system which uses frequency modulation of light. T.F osc is the oscillators using tuning fork. Av is an amplifier. LED is a light emitting diode. hν is light flying in the optical fiber. Ai is also an amplifier. AGC, automatic gain control. BPF, band pass filter.

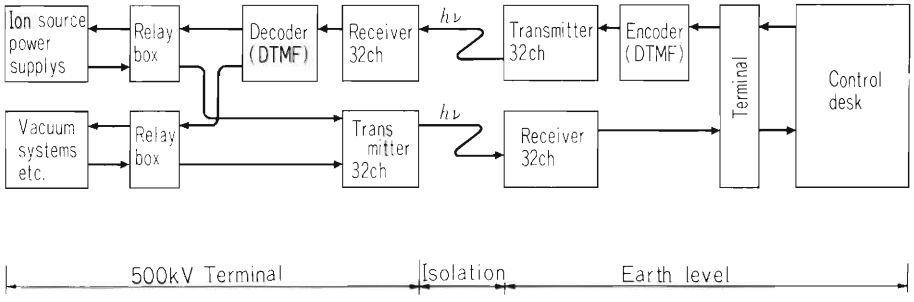

Fig. 2. Block diagram of the light link system for on-off operation.

which conveys the status information on the terminal, single frequency characterization scheme is solely used.

(2) Analog signal channel

We have not used the sophisticated multiplexer and ADC (analog to digital converter) combination. We have set up a simple and straight forward system using V/F (voltage to frequency converter) and F/V (frequency to voltage converter) circuits together with the LED (light emitting diode) and Photo-transistors. Each channel carries only one kind of analog signals as shown in Fig. 3. The scheme is very simple and its maintenance and expansion work needs no sophisticated technology. The conversion coefficients in this system are 100 mV/10 kHz for V/F and 10 kHz/10 V for F/V, accuracy being 10 bits.

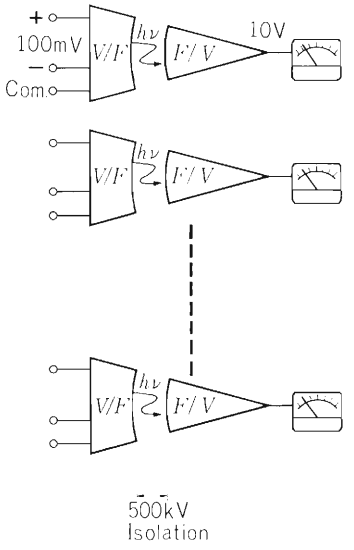

Fig. 3. High voltage isolation amplifier scheme for transmission of analog signals, using V/F and F/V converters.

(3) Selection of the optical fibers and mating of the connectors

Among the numerous brands of the fibers in the market, those having a large numerical aperture and of low cost were selected. Mating the connectors to the ends of the fiber cable was made by ourselves without difficulty.

As stated above, our optical data link system uses only standard parts found in the market and maintenance or expansion of the system is easy. Its structure is very simple and a high degree of reliability has been achieved. The system is found free of misoperation by virtue of the frequency modulation scheme using the tuning forks, especially, the DTMF method guarantees transmission of the important command without receiving perturbation from the electrical noises present in the injector room.

Ⅳ-4. Metal Ion Source

M. Kase, Y. Miyazawa, and T. Chiba

A metal ion source for the linac has been constructed and tested for Al, Ni, and Cu ions.

The source is of a hot cathode PIG type with a sputtering electrode.[1), 2)] Figure 1 shows schematically a cross sectional view of the metal ion source. The source is designed to be set on the same position in the magnet as the gas ion source described in Ref. 3. Therefore the structure of the metal ion source is almost identical to that of the gas ion source except for anode. The anode is composed of three parts: upper, center, and lower parts. The upper and lower anodes (A and B in Fig. 1) are made of copper and cooled by contacting with the water-cooled block (C in Fig. 1). The center anode (D in Fig. 1) is made of stainless steel and heated by arc plasmas up to around 300°C without being cooled during the operation in order to prevent deposition of sputtered material on the inside surface of the anode. A molybdenum plate with a beam slit (1 × 10 mm^2) is installed on one side of the center anode. On the opposite side of the beam slit, the sputtering electrode is inserted through a hole on the anode wall. The sputtering electrode is a rectangular block, 4 × 9 × 20 mm^3 in size. The electrode is made of the material to be charged in case of Cu and Al. For Ni, a 2 mm thick sheet of the material is soldered on a copper backing so as to prevent disturbance in the magnetic field. The sputtering electrode is supported by a water-cooled copper holder. The space between arc plasma and the sputtering electrode can be adjusted by moving the holder remotely from outside of the vacuum chamber with a set of some gears and rods. A negative voltage (0 ~ −1.5 kV) with respect to the anode can be applied to the sputtering electrode.

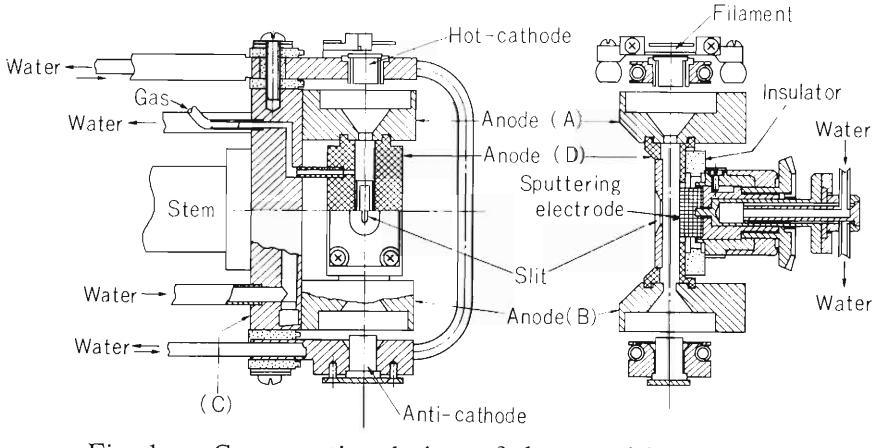

Fig. 1. Cross sectional view of the metal ion source.

The test of the metal ion source was carried out at a test bench of ion source which was constructed in 1979. An arrangement of the magnet and beam extraction system in the test bench is almost the same as that in the injector of the linac.[3)] Argon was used as supporting gas in the case of Ni and Cu, while neon was used in the case of Al because a value of mass-to-charge

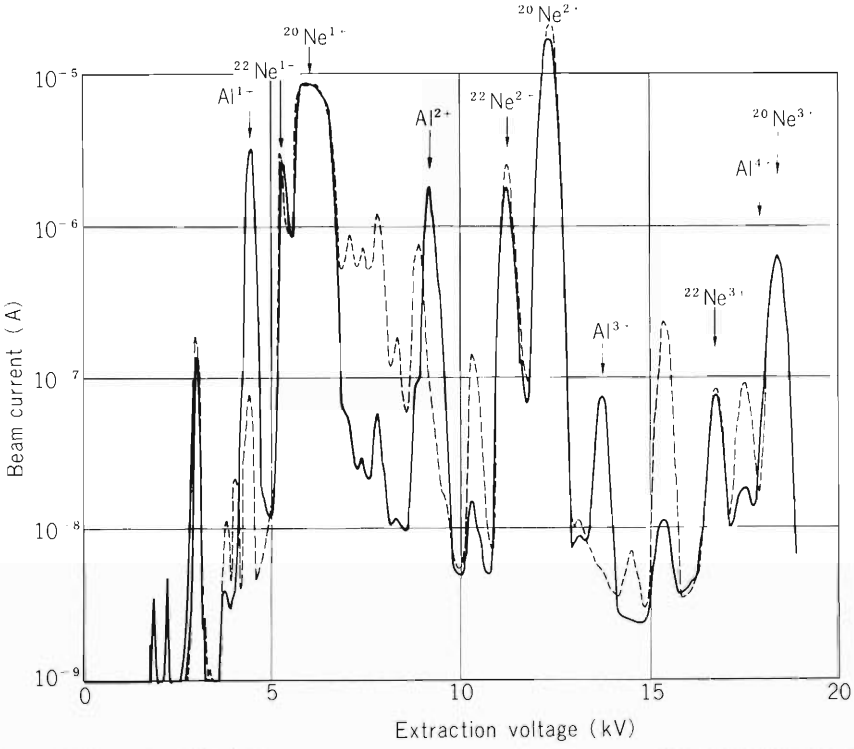

Fig. 2. The extracted beam current versus the extraction voltage when Al was charged. The magnetic field strength = 5.2 kG, the arc condition = 300 V × 0.5 A and the sputtering voltage = −300 V for the solid line and 0 V for the dashed line. The supporting gas was neon. The beam currents are measured with a Faraday cup (30 mmϕ aperture) located at the same position as that of the beam stopper in Fig. 2 of Ref. 3.

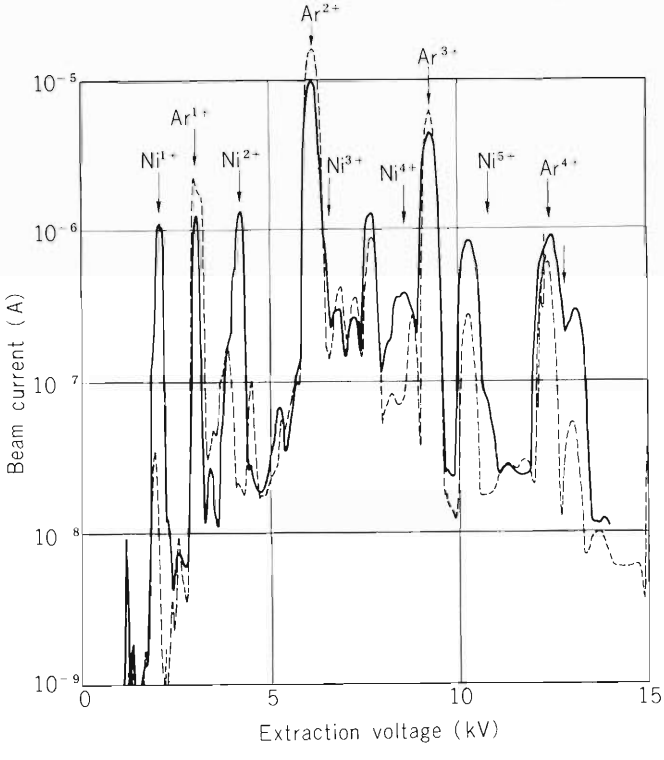

Fig. 3. The extracted beam current versus the extraction voltage when Ni was charged. The magnetic field strength = 5.2 kG, the arc condition = 420 V × 0.9 A and the sputtering voltage = −500 V for the solid line and 0 V for the dashed line. The supporting gas was argon.

ratio (m/q) for Al^{2+} is close to that for Ar^{3+}. The m/q spectra, when Al, Ni, and Cu were charged, are shown in Figs. 2, 3, and 4, respectively. In each figure, the m/q spectra when no voltage was applied to the sputtering electrode are shown by dashed lines.

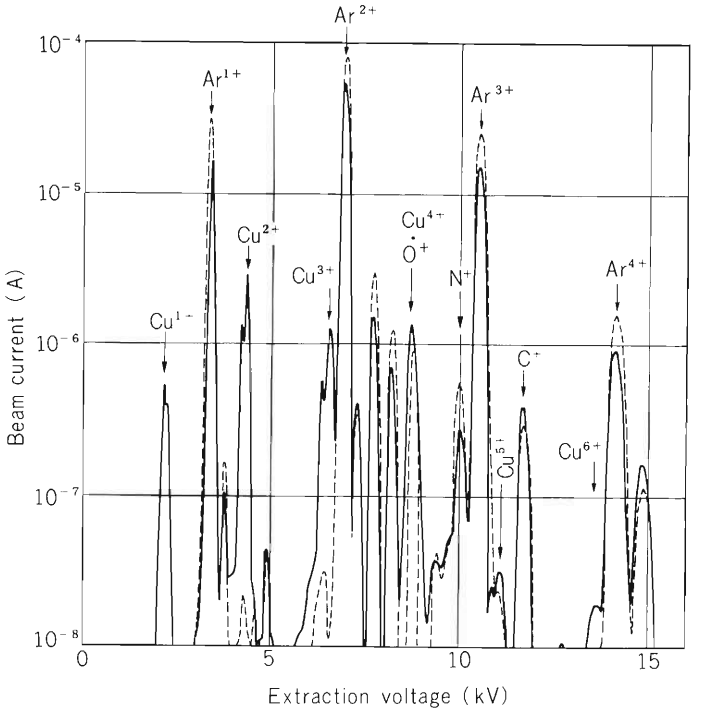

Fig. 4. The extracted beam current versus the extraction voltage when Cu was charged. The magnetic field strength = 4.3 kG, the arc condition = 400 V × 1.5 A and the sputtering voltage = −500 V for the solid line and 0 V for the dashed line. The supporting gas was argon.

References

1) H. Schulte, W. Jacoby, and B.H. Wolf: IEEE Trans. Nucl. Sci., NS-23, 1042 (1976).
2) K. Ikegami, T. Kageyama, and I. Kohno: Jpn. J. Appl. Phys., 19, 1745 (1980).
3) M. Kase and Y. Miyazawa: IPCR Cyclotron Progr. Rep., 14, 132 (1980).

Ⅳ-5. Construction of ECR Ion Source

M. Yanokura and M. Odera

Development of an electron-cyclotron resonance (ECR) ion source has been started to get multiply charged ions or high intensity beams of low-charge light ions. Figure 1 shows the test stand of the ECR ion source. The ion source has only one ECR cavity which is insulated from the other components and is kept at a positive high voltage up to 10 kV. A magnetron is used as an UHF power source and its output power is 1.6 kW (CW) at 2.45 GHz. The UHF power is supplied to the ECR cavity through an isolater, power monitor, EH tuner and RF window. Three diffusion pumps are installed in the test stand. One pump evacuates mainly the volume of the ECR cavity, and the other two pumps evacuate the volume of the beam extraction and analyzing systems. These systems, pumps and the UHF power source, are at the ground potential, and are insulated from the ECR cavity. The beam extracted from the ion source is focused by an einzel lense and analyzed by a magnet having a maximum B_ρ of 94.5 kGauss·cm. After analyzing, the beam current is measured with a Faraday cup.

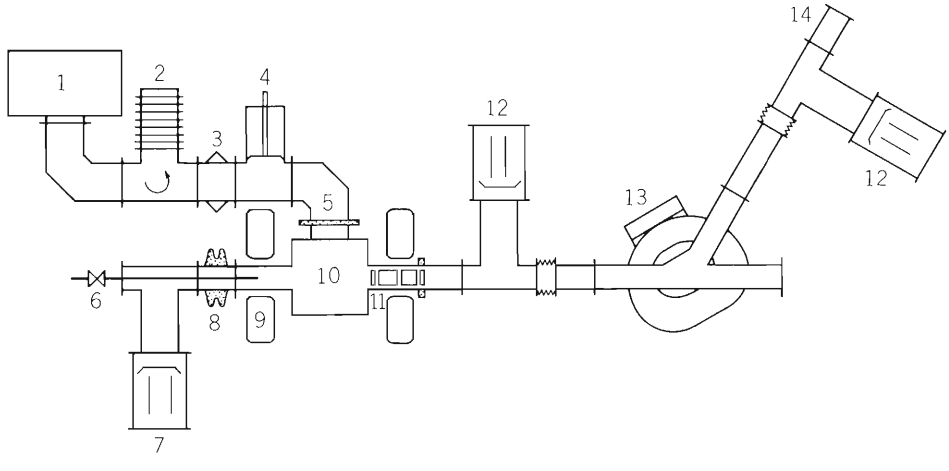

Fig. 1. Plan of the ECR ion source test stand. 1: 2.45 GHz magnetron, 2: isolater, 3: power monitor, 4: EH tuner, 5: RF window, 6: gas valve, 7: 600 L/s diffusion pump, 8: insulater, 9: main coil, 10: ECR cavity, 11: extractor and einzel lense, 12: 1500 L/s diffusion pump, 13: analyzing magnet, 14: Faraday cup.

This ECR ion source was tested using Ar gas. When Ar gas was fed into the ECR cavity at a flow rate of 1 cm^3/min, the pressure in the cavity was observed to be around 10^{-4} Torr. Plasma is seen to be formed in the cavity at a relatively low power level when the UHF power was supplied, and a few nA Ar^{2+} beam was measured at the Faraday cup. However, the plasma formed was not such that one would have expected in its distribution in the cavity. It is supposed that this result is due to the inadequate position and geometry of the vacuum window in the wave-guide. Improvement of the window is supposed to be necessary.

Ⅳ-6. Simplified Control Circuit for RILAC RF System

T. Kubo, M. Hemmi, and Y. Chiba

The amplitude and phase of the radio-frequency (RF) voltage generated in a resonator often change due to detuning of the resonator or shifting of the gain of amplifier. The control system for the RF system of RILAC,[1] described in a previous report,[2] was designed to include an automatic tuner and an amplitude and phase stabilizer. But it has not yet been installed as some modifications were found to be necessary. A simplified control circuit was fabricated as a temporary substitution for it and was used for the beam acceleration test.[3]

The RF system consists of six resonators combined with power amplifiers. Design of the control circuit is identical for each combination. Its schematic diagram is shown in Fig. 1.

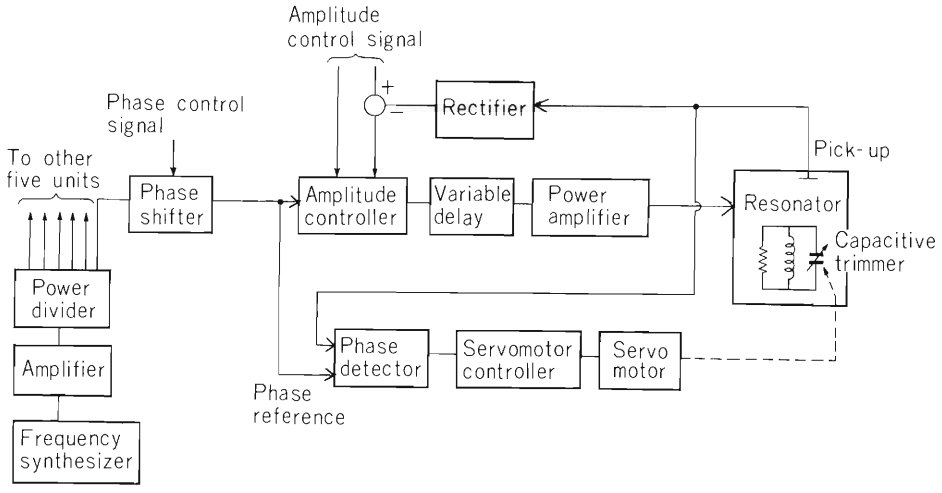

Fig. 1. Schematic diagram of the simplified control circuit.

The common signal for the system, applied as a drive signal of the amplifier and a phase reference, is provided by a frequency synthesizer and is distributed by a resistive power divider to six transmission lines which have identical electrical lengths. Each line provides the signal which has the identical amplitude and phase to the respective amplifiers.

The initial part of the control circuit is a phase shifter, which is composed of inductances and variable capacitive diodes. The phase of the drive signal can be adjusted by varying the bias voltage of the diodes and the adjustable range is 40 deg. The RF voltage of each resonator should have the same phase to accelerate ions synchronously. As this condition is almost satisfied by equalizing the length of the transmission line, the phase shifter is useful only when fine adjustments are necessary.

The amplitude of the RF voltage of the resonator is controlled by varying the attenuation of the drive signal with an attenuator included in the amplitude controller. A PIN diode is used as the attenuator which is continuously controllable by an external signal. To stabilize the amplitude, it can be driven by a rectified feedback signal from a voltage pick-up of the resonator.

Tuning of the resonator is maintained by a semi-automatic tuner. As this tuner cannot tune the resonator automatically by itself, the tuning should be made manually. It compares the phase of the RF voltage of the resonator with that of the phase reference by use of a double balanced mixer (DBM) as a phase detector and detects the detuning of the resonator as a phase change. The output of the phase detector controlls a servomotor and drives the capacitive trimmer of the resonator[1] to correct the phase change i.e. the detuning. Therefore, the phase of the RF voltage must be adjusted so that the phase detector will have the output of 0 V when the resonator is tuned (the DBM has the output of 0 V when the phase difference between input signals is 90 deg.) This adjustment is made by a variable delay after the amplitude controller. The tuner is not activated until these adjustments are completed and the normal RF voltage is generated.

The power amplifier can be driven with a pulse signal to tune the resonator. The capacitive trimmer is manually moved monitoring the pulse shape of the RF voltage of the resonator, until it becomes the normal shape as is shown in Fig. 2. Figure 3 shows an example of the pulse shape when the resonant frequency is slightly different from driving frequency.

Multipactoring phenomena can be easily overcome, if the resonator is tuned, by driving the amplifier with a signal which has enough amplitude and a fast rise time (less than a few microseconds).

The control circuits are linked to a control computer (HP-1000)[4] and can be operated by remote control.

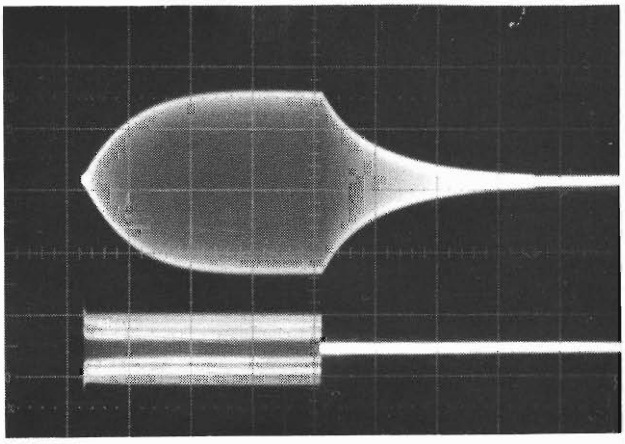

Fig. 2. The pulse shape of the RF voltage (upper) when the resonator is tuned and that of the drive signal (lower). The horizontal scale is 0.2 ms/div. and the vertical scale is arbitrary.

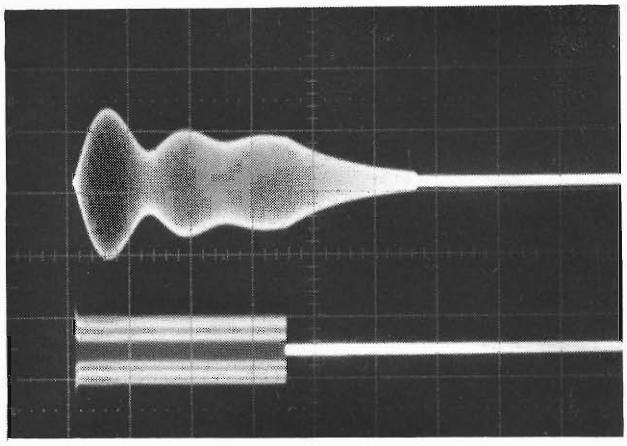

Fig 3. The pulse shape of the RF voltage (upper) when the resonator is off the resonance, and that of the drive signal (lower). See the caption of Fig. 2.

References

1) T. Kubo and Y. Chiba: IPCR Cyclotron Progr. Rep., 14, 123 (1980).
2) Y. Chiba: ibid., p. 120.
3) T. Kubo, T. Kambara, Y. Miyazawa, M. Hemmi, Y. Gono, T. Inoue, T. Tonuma, M. Kase, M. Yanokura, Y. Chiba, T. Fujisawa, and M. Odera: p. 128 in this report.
4) T. Kambara: IPCR Cyclotron Progr. Rep., 13, 134 (1979).

Ⅳ-7. Design of Compact Quadrupole Magnet

Y. Miyazawa and M. Hemmi

A compact quadrupole magnet of a moderate strength is frequently desired so that it can be inserted in the narrow space of the beam line to modify the orbit dynamics. One of the examples of such requirement is the change of beam characteristics on the targets. Another is the change of the beam property by a possible replacement of the ion source by a new type of source. Figure 1 shows a design which has an integrated strength of 75 kG for pole to pole gap of 25.4 mm and a pole length of 15 cm. The tape coil technique which has been improved and used extensively in the linear accelerator project is also used for this magnet. Table 1 is the specification of the magnet designed.

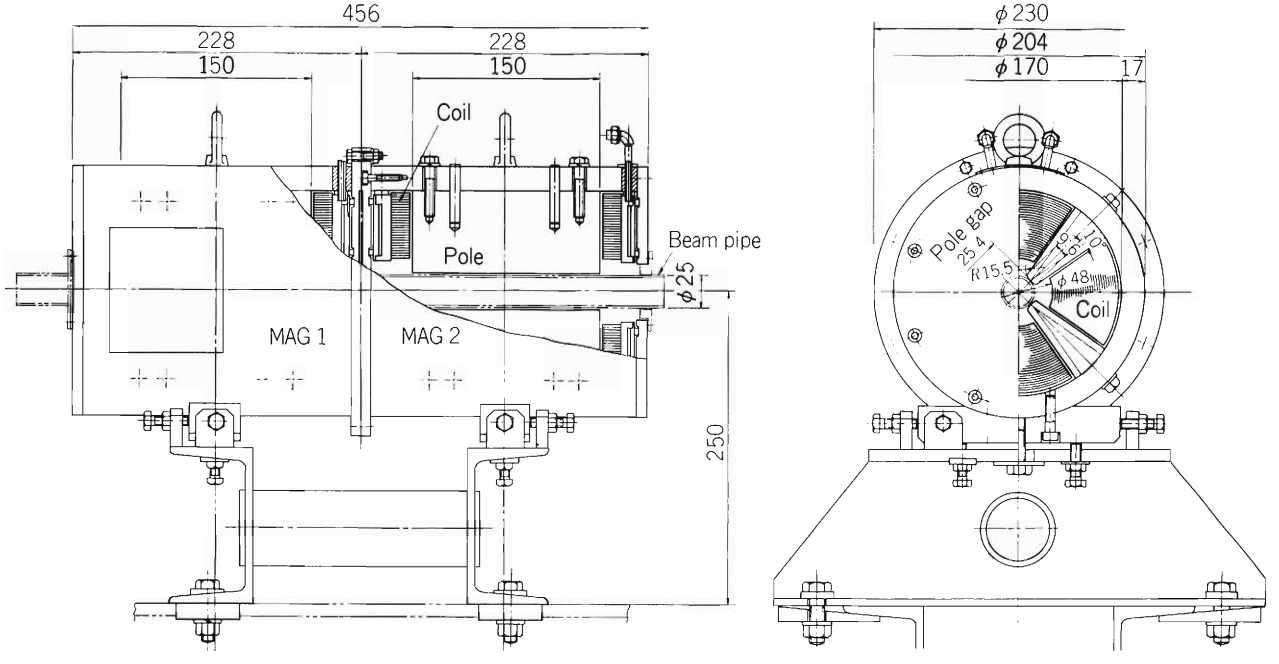

Fig. 1. Cross section of the doublet quadrupole magnet designed.

Table 1. Design specification of the quadrupole magnet.

Field gradient	5 kG/cm (maximum)
Pole length	15 cm
Aperture (pole to pole)	25.4 mm
Outer diameter	20.4 cm
Maximum ampere-turn	4000 AT
Power consumption	0.75 kW (maximum)
Weight	50 kg

Ⅳ-8. Simple Pepper-Pot Device for Beam Diagnostics

M. Hemmi, Y. Miyazawa, and T. Inoue

A simple pepper-pot device was fabricated and is being used to get a rough indication of the beam characteristics injected into the first cavity. Figure 1 shows its sketch showing the way of use in combination with a beam-profile monitor. It is found useful for tuning of beam parameters to have a simple and intuitive presentation of the beam emittance, not necessarily of very complete one, at the operation console. In Fig. 2 an example of the beam profile measured by the beam scanner is given. By knowing distances between peaks in that Figure, the degree of convergence can be estimated comparing with the hole distance in the pepper-pot plate. Two other emittance probes were also installed already in the injection beam line. We can get a complete information of the beam emittance by their use when necessary. However, in most of the beam steering procedure, the simple and quick presentation of the results of manipulation of the operator is useful and an exact measurement is scarecely needed. Together with a program to display on the CRT terminal of the control console the beam trajectory predicted in the later cavities by injection of the beam with the parameters estimated, the pepper-pot device has made the beam steering procedure much easier.

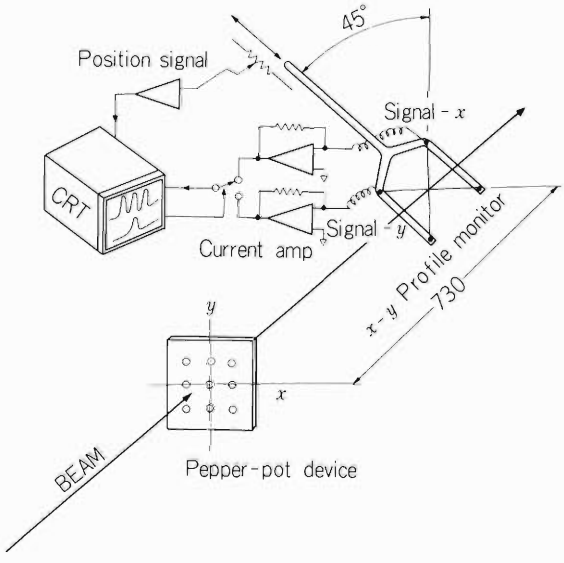

Fig. 1. Arrangement of the pepper-pot and a beam-profile monitor combination to measure beam property.

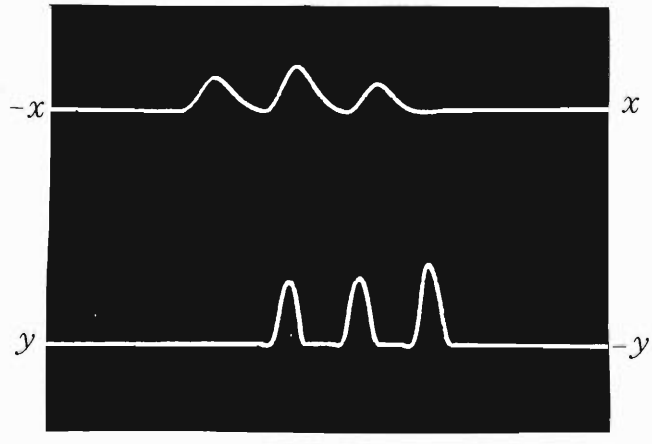

Fig. 2. An example of beam profile measured when the pepper-pot is inserted in the beam. Beam is Argon ion beam of energy 860 keV is used.

Ⅳ-9. Performance of Digital Emittance Measuring Device

I. Yokoyama, M. Kase, and T. Kambara

A multi-wire beam emittance measuring device was designed and fabricated last year.[1] The purpose is to obtain the detailed information of beam emittance quickly by the aid of the control computer HP-1000.[2] The device is composed of two beam probes, a driving system with pulse motors to move the probes and a circuit system with two microprocessors to measure and digitize the beam current. One of the two probes is for the measurement of emittance in the horizontal direction (x-direction) and the other is for that in the vertical direction (y-direction). One of the microprocessors is linked to the control computer via the HP-IB bus. The computer processes the data and displays the results.

The structure of the multi-wire sensor in the probe was modified and the performance of the device was tested with an actual beam in the beam injection line of the linac during 1981.

Figure 1 shows the schematic of the emittance measurement probe. The probe consists of a slit with 0.2 mm of width and 30 mm of length and a multi-wire beam sensor placed behind it at a distance of 75 mm. The multi-wire sensor consists of 30 wire strips made of Ni-Cr alloy evaporated on a 2 mm thick ceramic plate and also plated by thin gold. Each wire strip is 34 mm long and 80 μm wide and is placed in parallel at intervals of 40 μm. The sensor became more compact by the use of the evaporated wire strips than by the use of separated wires. Figure 2 shows the multi-wire sensor with the wire strips.

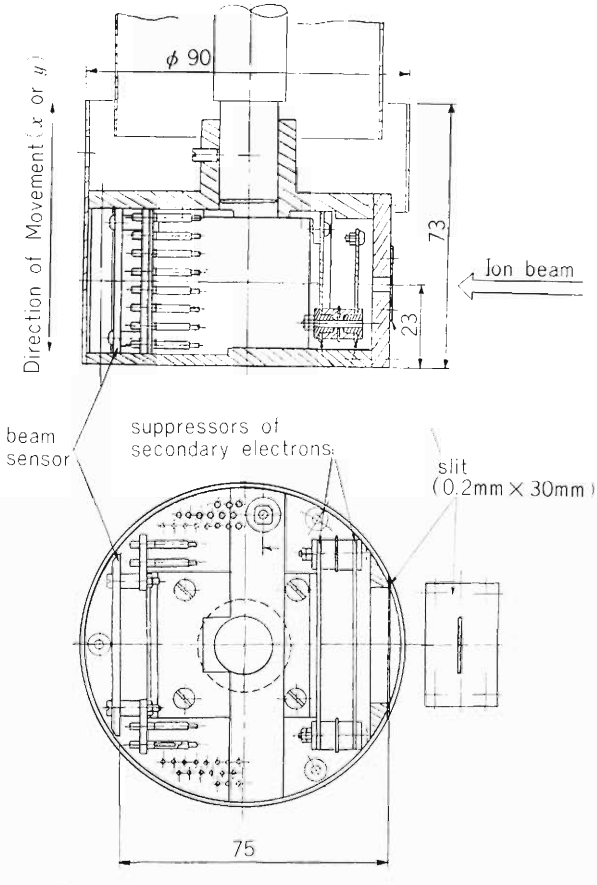

Fig. 1. Cross sectional view of the probe.

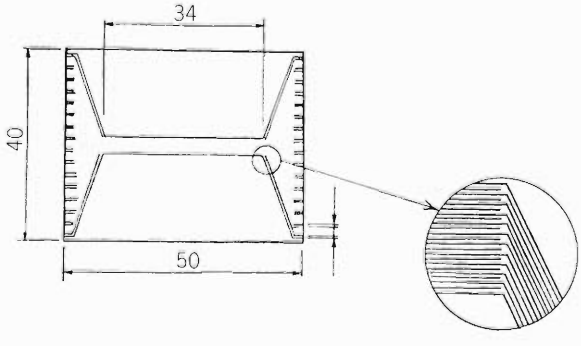

Fig. 2. Multi-wire beam sensor. Detailed drawing of the wire strips is shown in the circle.

A program "EMTN1" was developed for the control computer to interface to the device. From the CRT terminal of the computer, an operator sends a command to trigger the movement of the probe, to do a single or successive measurements and to transfer the data to the computer. Each command consists of two ASCII characters. Table 1 lists the commands and their functions.

Table 1. The commands to the microprocessor and their functions.

Command	Function
ZC	Zero drift check of the amplifiers
GC	Gain check of the amplifiers
XO, YO	Beam emittance measurement in one direction (x or y)
XY	Beam emittance measurement in both directions
IX, IY	Measurement of beam current of each wire at one probe position
D0	Transfer of zero drift check data to the computer
D1	Transfer of gain check data to the computer
D4	Transfer of measured data at one position by IX or IY command
D6	Transfer of emittance data for x-direction
D7	Transfer of emittance data for y-direction
D8	Transfer of emittance data for both directions

The drift of the zeros and the gains of the amplifiers for the wires can be checked for the correction of the measured data. The command ZC triggers the zero check and the command D0 triggers the transfer of the data to the computer. When the gain check is initiated by the command GC, a current of 60 nA is input to each amplifier from a current source, and the data are transferred to the computer by the command D1.

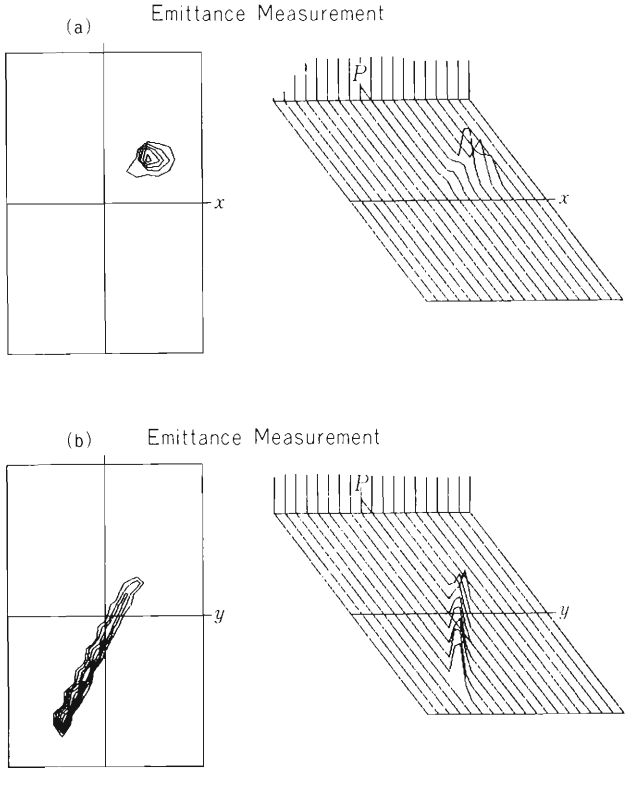

Fig. 3. Measured results of beam emittance displayed on graphic CRT display: (a) x-direction, (b) y-direction.

The command XO triggers the sequence of emittance measurement in the x-direction. The probe for the direction is moved horizontally and stepwise with intervals of 2 mm. At each stop, 30 data are obtained, which consists of the beam current of the 29 wires and the beam current of the probe itself. The probe stops at 19 positions for the measurement of the beam current and one position far from the beam for the zero check. Therefore the total number of the data from one measurement is 600. The data are digitized and stored in the memory of the microprocessor. The command D6 triggers the transfer of the stored data to the computer. If the command D6 is sent before the completion of the measurement, a message is displayed on the CRT screen showing that the device is busy. Each of the data sent to the computer is a numeral smaller than 2000. The resolution of the digitization is 0.1 nA at the most sensitive measurements. The time necessary to receive the data for each direction is about 59 seconds: about 9 seconds for moving the probe to the starting position of the measurements, and 50 seconds for the measurements at the 19 positions. After the measurements are completed, the microprocessor can receive the command D6 and send the data to the computer. It cannot start another sequence of measurement before the probe returns to the initial position, which takes additional 58 seconds. The command XY triggers successive measurements in the x- and y- directions. There is one power supply for the two pulse motors to move the two probes, and it must be switched over when the probe is changed, which takes about 10 seconds. Therefore it takes 174 seconds to receive the data in this case and 229 seconds to start another measurement.

After the computer receives the data, it temporarily stores them in a disc file. Then another program uses them for the numerical processing and displays the result on a graphic CRT. Figure 3(a) and (b) show the examples of the diagrams on the CRT. The data were taken for 315 keV N^{1+} beam at the injection line.

References

1) M. Saito, I. Yokoyama, M. Kase, T. Kambara, and M. Odera: IPCR Cyclotron Progr. Rep., 14, 138 (1980).
2) T. Kambara, S. Takeda, and M. Odera: ibid., p. 110.

Ⅳ-10. Single Arm Motor-Driven Slit System

T. Chiba and M. Odera

In the beam steering procedure through the accelerator or through the beam transport system of the accelerated ions, it is frequently desired to be able to adjust remotely the width of the slits at several locations along the course of the beam. On the other hand, there are many cases where no need is felt to fix the adjustable slits permanently to each location. After suitable prescriptions are established for beam manipulation around the position, the slits may be removed or replaced by simpler slits. Therefore, installation or removal of them should be simple. Sometimes, however, the space around the beam pipe is not enough to set the motor and driving mechanism on both right and left sides or above and below the slit-box. A simple and space-saving mechanism must be devised.

Figure 1 shows the slit system we have constructed to answer the requirements. In the Figure, a motor drives two opposite blades of the slit in the inverse directions at one time by

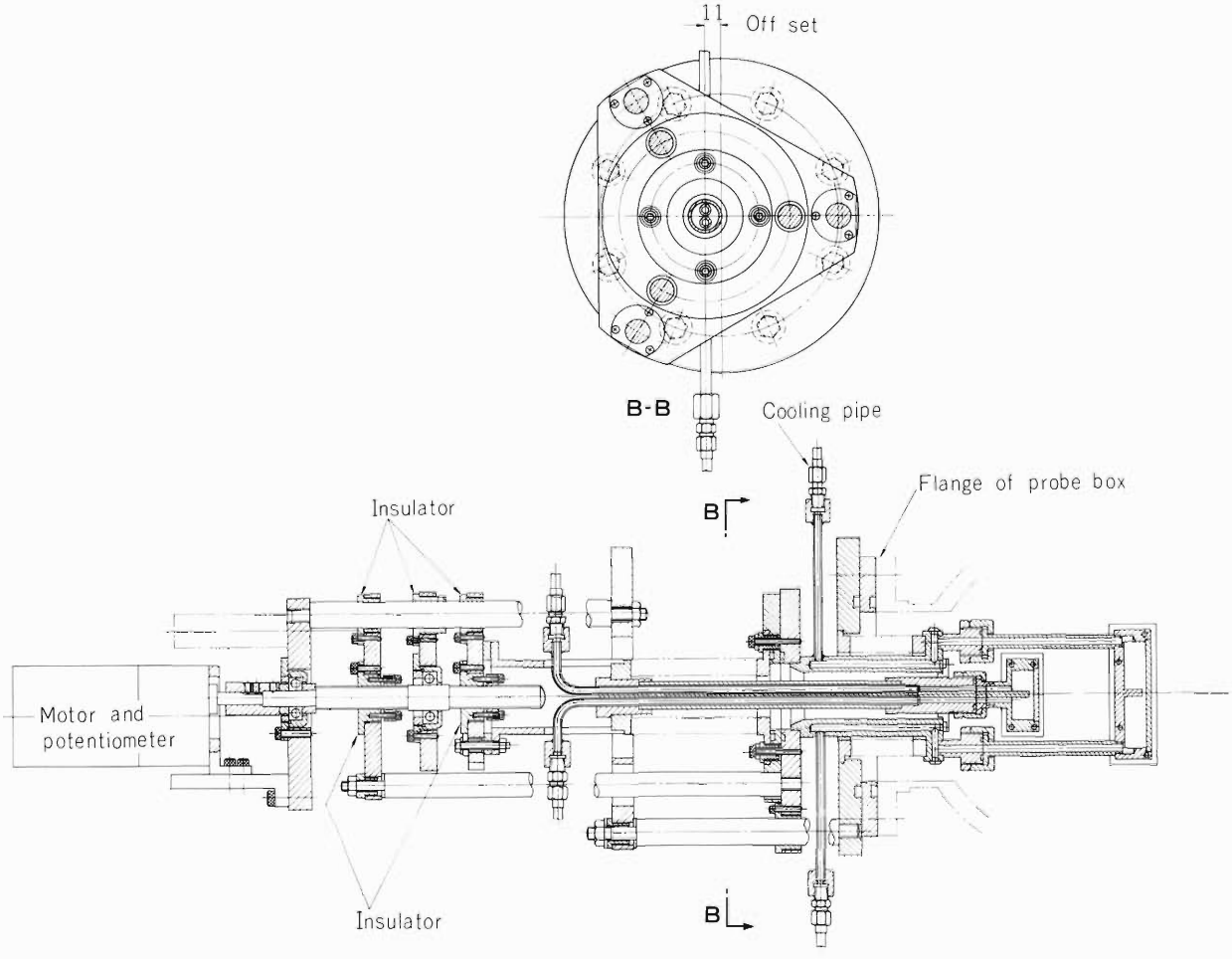

Fig. 1. Cross section of the motor-driven slit system.

rotating a shaft which has a right-handed screw cut on its half length and a left-handed screw on the other half. Therefore, only one side of the slit box is occupied by the driving motor to move two blades. Vacuum seals of the moving parts have welded bellows. The slit system is machined carefully so that the center of the slits or the closed position of the blades coincides with the center of the probe box accurately. The two blades move always symmetrically about this position. There is also an adjusting screw to allow shift of this position by a small amount. Each blade is cooled separately by circulating deionized water through the stem and the cylinder supporting blades. The axis of the driving shaft is offset from the center of the vacuum flange, so that two such slit assemblies can be inserted into the same probe box through the vertical and horizontal ports. The two pairs of slit together define a remotely adjustable rectangular window to the beam.

Ⅳ-11. Simple Low-Cost Profile Monitor

M. Hemmi and I. Yokoyama

A profile monitor which measures the transversal intensity distribution in the beam cross section is a valuable diagnostic tool for operation of any accelerator. In our linac, many profile monitors are also necessary along the beam line, i.e., on the injection beam line, between the cavities, and on the beam transport line in the experimental areas. Monitors of low cost, simple to use and reliable in operation are required to fulfill the demand.

Figure 1 shows the structure and way of use of the monitor we designed. The horizontal and vertical wires which sense the beam current are moved by a pneumatic actuator and scan the beam swiftly. Diameter of the wires is 0.2 mm. Signals are amplified by the head amplifiers set near each monitor, sent to the controle room and displayed on a memory oscilloscope in the operator's

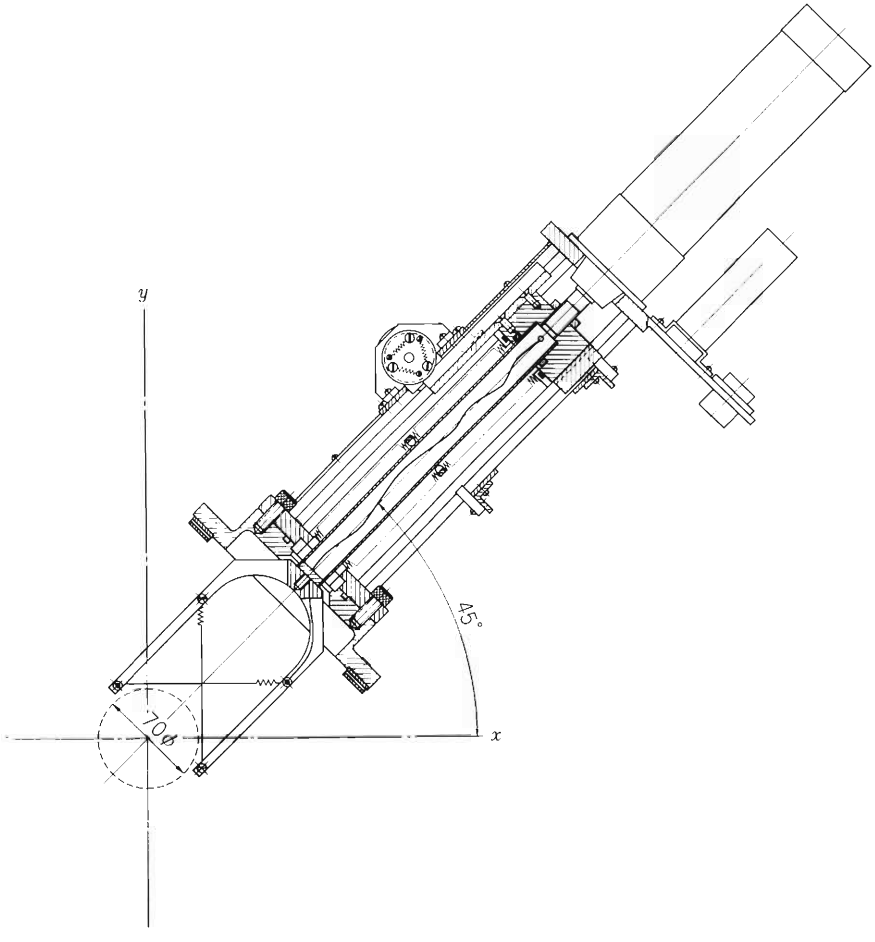

Fig. 1. Two-wire beam profile monitor. By thrusting the sensors in the direction making fourty-five degrees with respect to the horizontal plane, current densities in X and Y directions are measured easely within a few seconds. It is driven by a pneumatic cylinder.

console. The sensitivity of the amplifiers are adjustable remotely from the control room by four decades. Wider range of sensitivity is obtainable by locally attaching current shunt resistor to the amplifiers. Positions of the wires in the aperture of the beam pipe is given by an encoder made of a conductive plastic potentiometer mechanically coupled to the rod of the pneumatic actuator. The signal wires from the monitors in the various locations are connected to a switcher circuit in the control room. The interface circuit can receive up to 31 signals. Figure 2 shows the signal processing scheme schematically. Selection of the monitors to be displayed is made remotely by use of a microprocessor whose control sequence is given by a program written in its EPROM. Table 1 shows the specifications of the monitor.

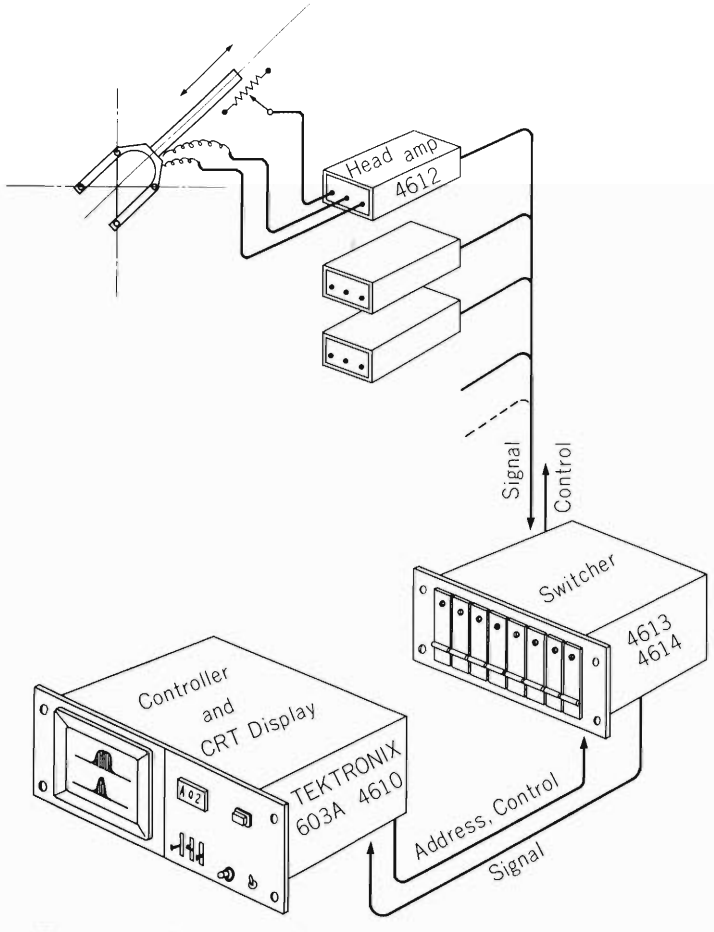

Fig. 2. Scheme of measurement and display.

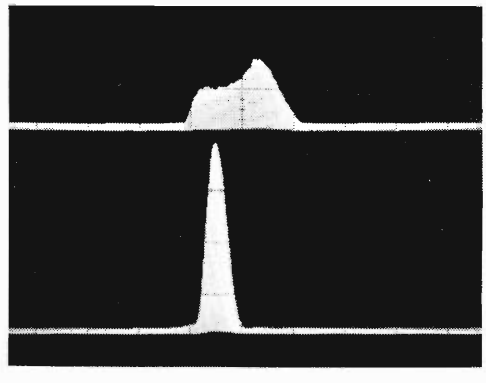

Fig. 3. An example of the beam profile at the entrance of first cavity.

Table 1. Specifications of the profile monitor.

Maximum sensitivity: 5×10^{-11} A per div. of CRT vertical scale
Response time of the head amplifiers: 5 msec in rising up to 90 % of the maximum
Drift of the amplifier system: less than 2×10^{-11} A
Scanning area: 70 mmϕ
Maximum error in position: less than 2 mm
Time required for single measurement: a few seconds (between 0.5 – 3 seconds)

Ⅳ-12. Beam Attenuation by Slit with V-Slots

M. Yanokura, T. Chiba, and M. Odera

Sometimes attenuation of beam by a large factor or formation of beam profile of very small diameter is necessitated. For instance, direct measurement of the beam energy by inserting a solid state detector into the beam path is required, in the tuning process of the linac, to find out if there exist some impurity ions mixed. In such a case the intensity of the beam must be greatly decreased in order not to destroy the cystalline structure of the silicon detector by heavy bombardment. Another example is the use of a beam of fine diameter to examine the complex structures of some materials such as the texture of alloys or structure of biological cells.

Figure 1 shows the cross section of the slit system. The overall structure resembles that of the motor driven slit system except a V-slot is cut in each blade and pulse motor is used to allow ajustment of the slit gap in fine steps.[1] Also the two blades are attached to the supporting stem and cylinder in such a way that the blades never collide with each other and the paired V-slots can form a small rectangular opening of only several micron in width when the heavy-ion beam is used.

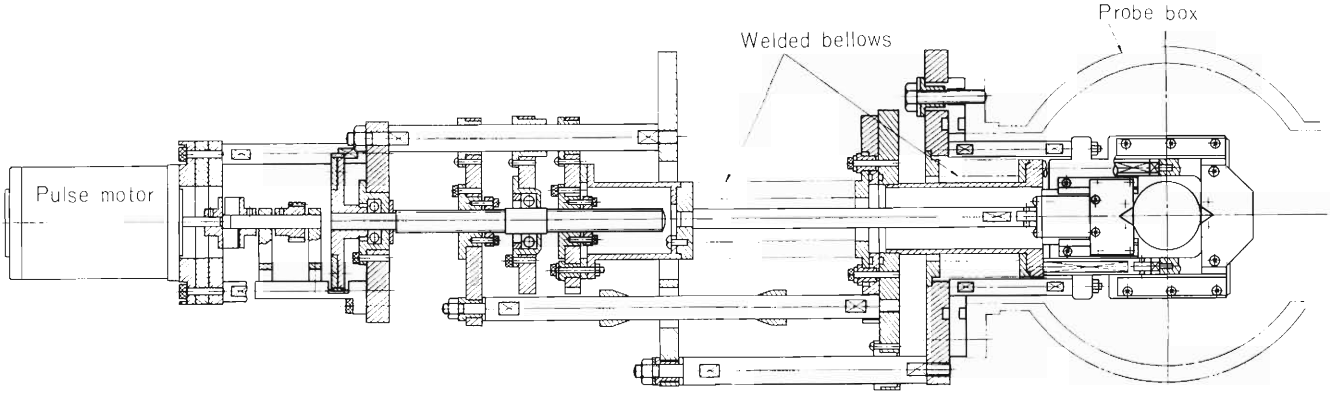

Fig. 1. Cross section of the beam attenuator.

Reference

1) T. Chiba and M. Odera: p. 144 in this report.

Ⅳ-13. Status of the RIKEN Separated Sector Cyclotron Project

H. Kamitsubo

The project for a separated-sector cyclotron (SSC) with K = 540 started at Riken in 1980. The SSC was planned to be an energy booster of the RILAC for acceleration of heavy ions. It will have another injector for light-ion acceleration and an AVF cyclotron with K = 90 will be installed for that purpose. A customary diagram of energy vs mass number for the present SSC is given in Fig. 1 together with those of the major facilities now under construction in the world. The ordinate gives the energy per nucleon as usual. The solid line labelled IPCR shows the maximum energies of ions when they are produced by a conventional PIG source, while the dotted line presents the expected maximum energies when ECR sources will be installed at the injectors. Typical examples of the operating parameters at the maximum energies of ions in the RILAC-SSC and the AVF-SSC combinations are listed in Table 1. Charge number, q_2, for the SSC corresponds to that of the optimal charge state after the ions pass through the foil strippers which will be placed between two injectors and the SSC.

The design study of the SSC is well in progress. Calculations of beam dynamics in the SSC have been extensively carried out. Computer codes for the calculation of the equilibrium and accelerated orbits, for the ray tracing calculation of the injection and extraction trajectories and for the simulation of the effects of harmonic field and defect in the isochronous field distribution in the SSC were newly developed.

It is recognized that the acceleration on the well-centered orbits is very important to get the beam of good quality. Conditions for well-centered acceleration were studied analytically and were

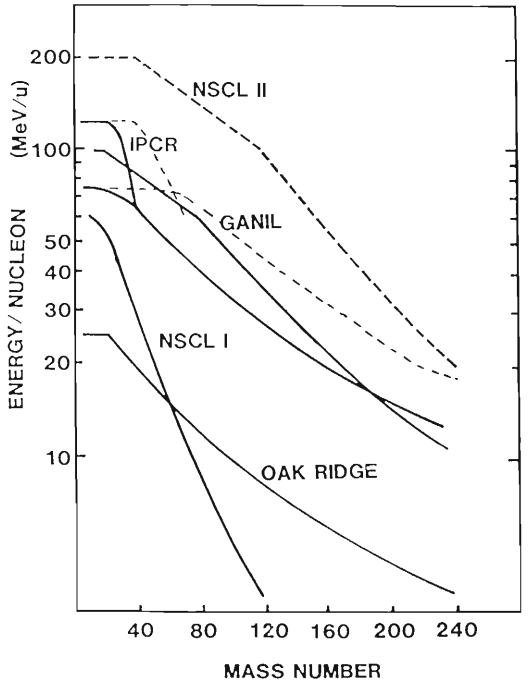

Fig. 1. Maximum beam energy vs. mass number of the RIKEN SSC together with those of heavy-ion accelerators now under construction in the world.
GANIL: Grands Accelerateur Nationale de Ion Loudes.
NSCL: National Superconducting Cyclotron Laboratory (Michigan)

Table 1. Examples of operating parameters at the maximum energies in the present accelerator complex.

	Ion	^{40}Ar	^{84}kr	^{132}Xe	^{238}U
Linac	Charge q_1	8^+	9^+	9^+	10^+
	m/q_1	5	9	15	24
	$F_{Acc.}$ (MHz)	43.3	33	26	20.4
	E (MeV/u)	3.8	2.2	1.36	0.84
SSC	Charge q_2	15^+	24^+	30^+	37^+
	m/q_2	2.7	3.5	4.4	6.4
	B_{Inj} (T)	1.45	1.45	1.43	1.64
	B_{Ext} (T)	1.55	1.5	1.46	1.66
	$F_{Orb.}$ (MHz)	4.8	3.67	2.88	2.27
	$F_{Acc.}$ (MHz)	43.3	33.0	26.0	20.4
	h	9	9	9	9
	E (MeV/u)	66.6	36.8	22.3	13.6

	Ion	$p(H_2)$	^3He	^{12}C
Cyclotron	Charge q_1	1^+	2^+	4^+
	m/q_1	2	1.5	3
	$F_{Orb.}$ (MHz)	7.37	7.37	6.51
	F_{RF} (MHz)	22.1	22.1	19.6
	B_{Ext} (T)	0.97	0.727	1.28
	E (MeV/u)	9	9	7
SSC	Charge q_2	1^+	2^+	6^+
	m/q_2	1	1.5	2
	B_{Inj} (T)	0.833	1.26	1.48
	B_{Ext} (T)	0.994	1.49	1.67
	$F_{Orb.}$ (MHz)	7.37	7.37	6.5
	$F_{Acc.}$ (MHz)	44.2	44.2	39.1
	h	6	6	6
	E (MeV/u)	184	184	134.6

verified by numerical calculations. According to these, the matching of the beam profile in the six dimensional phase space at the injection point should be well realized by adjusting the parameters of the beam transport line for injection. An alternative and more practical method was developed to use the first order harmonic field for bringing the injected beam onto the well-centered orbit.

Two of the sector magnets were ordered to Sumitomo Heavy Industry Co. The final design of the magnets was finished in last June after extensive calculations by the computer code TRIM and field measurements on the 1/4 scale model magnet. Number of the trim coils and the shape of their winding were so determined that the difference between the actual and ideal isochronous field distributions can be reduced to give no significant effects on the beam quality in the SSC. The first sector magnet will be completed at the end of next March and the second one in June. Field distributions inside the gaps of the magnets and in the valley region between both magnets will be measured next summer. Then the calculations of the beam dynamics in the SSC will be pursued again by using the measured field maps. The final design of the injection beam line will be done after that.

There will be installed two bending magnets, two magnetic inflection channels and an electrostatic inflector to bring the beam to the injection point in the SSC. A bending magnet is placed very close to the sector magnets. It should produce magnetic field up to 1.75 T and should be as small as possible. A full scale model was made and its performance characteristics were measured.

Design of the RF cavity is also in progress. It was decided that a half wave length resonator will be adopted for the RF system of the SSC. Characteristics such as resonance frequency, RF voltage distributions along the accelerating gap and the quality factor were measured for the half scale model. In order to analyze numerically the fundamental characteristics for cavities of the various shapes, a computer code has been developed to solve the Maxwell equations directly in three dimensional case.

Design of the vacuum system has been pursued during the past year. The chamber will be devided into eight sub-chambers and seals between them are amongst the most critical vacuum components of the SSC. Because of the space limitations, pneumatic seals will be adopted as vacuum seals between sub-chambers. Three 1/3 scale model of the pneumatic seal were made and have been tested to determine their performance characteristics.

Layout of the experimental area and the beam transport system was almost fixed. Radiation shielding has been extensively studied for the proposed layout. The beam transport lines to the experimental halls were designed to bring the beam in the achromatic or highly dispersive modes, and also in the isochronous mode. Detailed calculations of their characteristics were made using the computer code TRANSPORT.

Ⅳ-14. Some Results Obtained from Orbit Calculations

N. Nakanishi, A. Goto, and Y. Yano

Orbit calculations for beam dynamics in the RIKEN SSC have been done to study accelerated-beam properties. Some results are presented on the resonance effect in focusing frequencies, the imperfection effect in isochronous fields, and the effect of dee angle on the acceleration efficiency.

Focusing properties for various particles to be accelerated in the SSC are examined in the betatron frequency space. The sector angle of 50° was determined so as to give optimum focusing to various particles in the space. A 9 MeV proton beam, however, crosses two resonance lines: $\nu_r = 2\,\nu_z$ and $3\,\nu_r = 4$.[1] It is known that the former is a quadratic, non-linear, coupling resonance, and the latter a quadratic, non-linear, intrinsic resonance in the four-sector SSC. The proton beam encounters these resonances at energies of about 128 MeV and 165 MeV. Radial and axial half widths of the beam on the mid-line of an open valley are shown in Fig. 1. Only a slight change in width is observed through the acceleration process. The behavior of the phase space patterns at the vicinity of the $\nu_r = 2\,\nu_z$ (Walkinshaw) resonance is also examined, but harmful distortion in the patterns was not observed. According to these facts the influence by these resonances on beam qualities is considered to be very small at least in the case of 20 mm·mrad emittance. It is considered that the influence of these resonances is small because of a large energy gain per turn.

The influence of imperfection in isochronous fields has been investigated again.[2] Two types of isochronous field are adopted: a concentric type and a Gordon type. The concentric-type isochronous field which is calculated by program EQUIOT[3] is formed by multiplying a factor to the base field along a concentric circle which corresponds to a concentric-type trim coil. The

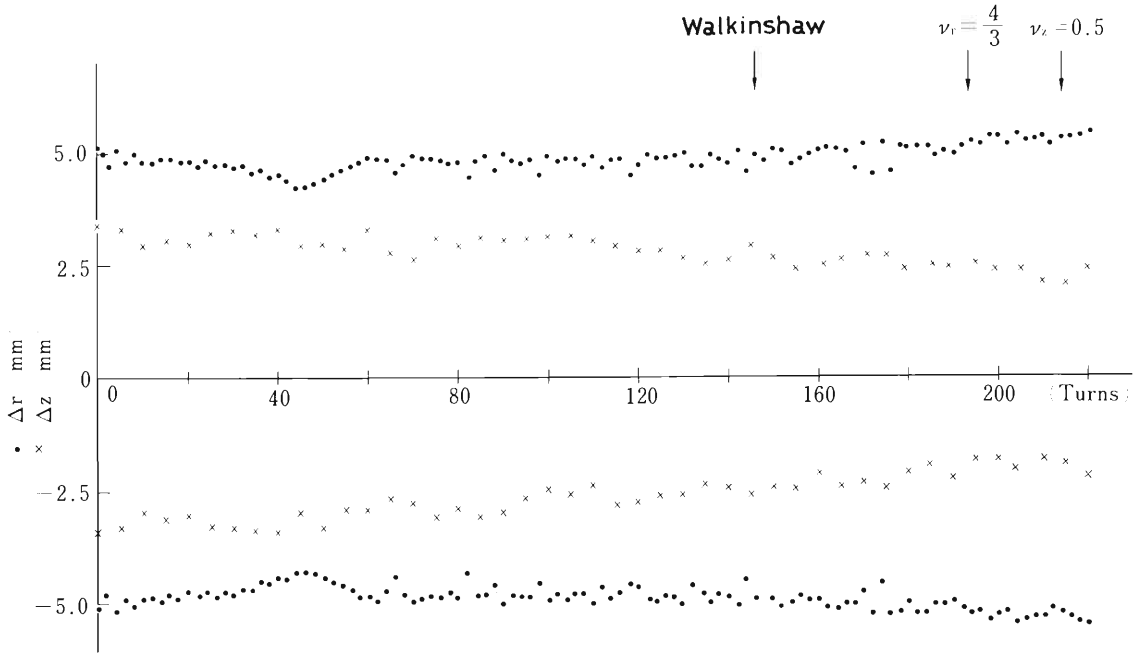

Fig. 1. Radial (•) and axial (×) half widths of 9 MeV proton beams.

Gordon-type field is formed by multiplying a factor to the base field along a certain line which corresponds to a Gordon-type trim coil. In the magnet region the line is a beam trajectory in a hard-edge approximation, and in the valley region it is a line normal to the magnet edge at the intersecting point of the edge with the trajectory.

The Gordon-type isochronous field is calculated by program EQUI2.[2] The program has been developed to get a Gordon-type isochronous field and to look for equilibrium orbits in that field. In order to estimate the influence of imperfection in each isochronous field, sinusoidal field perturbation which will be made by both types of trim coils are superimposed on the isochronous field. Energy spreads in a beam and phase slips of the central beam were calculated for various amounts of field perturbation and various wave length. Energy spreads show a similar tendency in both cases. It oscillates in the range between 2×10^{-4} and 5×10^{-4} at the field deviation of less than 0.13 %. The oscillation of the phase slip is fairly well leveled in the case of the concentric-type field, but in the case of the Gordon-type one it is straight-forwardly connected to that of imperfection in the amplitude and the wave length. Since the aspect of the energy spreads is considered to depend on the magnetic field configuration, the type of trim coils should be chosen so as to minimize the possible energy spread in the four-sector SSC. According to these calculations, it is supposed that the Gordon-type trim coils will be more suitable in the RIKEN SSC.

The angle of the delta-shape accelerating electrode was preliminary taken to be 20°, because the fundamental harmonic number h = 9. It has been confirmed that the choice is not wrong in view of stability in the phase space. In case of the SSC composed of four sector magnets, it is clear that the angle of 20° is not most efficient in the energy gain per turn, since an equilibrium

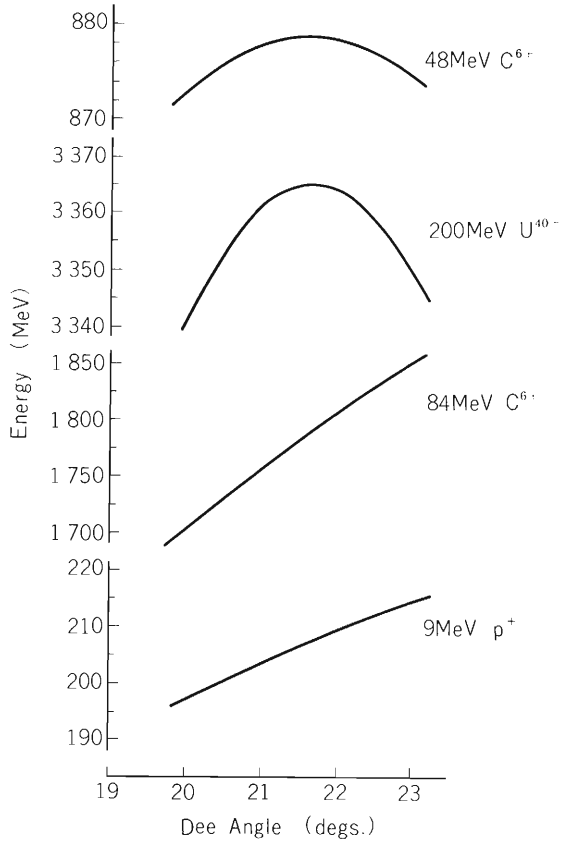

Fig. 2. Attainable energy versus dee angle for four injected beams.

orbit has a squared shape. Therefore, a numerical calculation was made in order to obtain the most suited angle. Figure 2 shows attainable energies for four typical beams of 48 MeV C^{6+}, 200 MeV U^{40+}, 9 MeV p^{+}, and 84 MeV C^{6+} at the turn numbers of 140, 80, 230, and 330, respectively. An accelerating voltage is assumed to be 250 kV. The harmonic number of the first two is 9 and that of the others is 6. It may be seen that the angle of 21.6° is most efficient. The change from 20° to 21.6° of angle brings about energy-gain increase of 0.8 % and 5.5 % for each acceleration mode. Accordingly the turn number can be reduced. Extensive examinations are now in progress.

References

1) N. Nakanishi, A. Goto, Y. Yano, and T. Wada: Proc. 9th Intern. Conf. on Cyclotron and their Applications, Caen (1981).
2) N. Nakanishi, A. Goto, and Y. Yano: Sci. Papers I.P.C.R., 75, 136 (1981).
3) N. Nakanishi: Reports I.P.C.R., (in Japanese), 57, 189 (1981).

Ⅳ-15. Formulation of Beam Centering Equation in a Separated Sector Cyclotron

Y. Yano, A. Goto, and N. Nakanishi

In order that a beam of good quality can be extracted from a separated sector cyclotron (SSC), the beam should be accelerated along a well-centered orbit inside the SSC. This well-centered orbit acceleration can be achieved when the central particle of the beam moves in the SSC as shown in Fig. 1. The essential feature of the motion is that the particle crosses the equilibrium orbit (E.O.) corresponding to its kinetic energy every time it reaches the mid-line of open valley, e.g. points A and D. R(i) and R(i + 1) represent the radial distances measured from the machine center to the i-th and (i + 1)-th E.O., respectively. In the case of a single-gap acceleration system, the particle would reach point B and leave the same point after gaining the energy. In our double-gap acceleration system, however, the particle is deflected by the accel. gap 1 and then is inflected by the accel. gap 2 as shown in the inset (Fig. 1). Because these deflection and inflection angles are almost the same, the treatment of this double-gap acceleration process can be simplified by describing the process in such a way that the particle reaches the point B and then leaves the point C after it gains the energy which is to be obtained by the passage of two acceleration gaps. The radial shift of the point C from the point B is given by $\epsilon(i)$.

Now let us consider the motion of the well-centered particle mentioned above on the radial phase space. The fact that eigen-ellipses for a certain E.O. given at mid-lines of four valleys are identical and they are erect ellipses makes the description much simpler. We can transform these

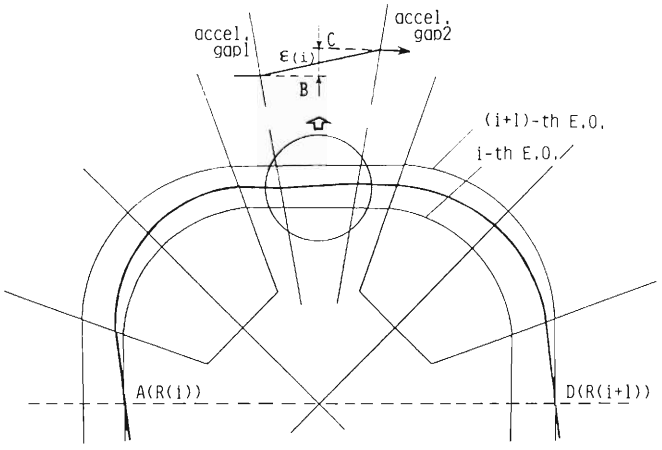

Fig. 1. Well-centered acceleration orbit (thick solid line). A particle moves clockwise and is accelerated by a couple of gaps in one dee (see the inset). The i-th and (i + 1)-th equilibrium orbits are also drawn. Leave the details to the text.

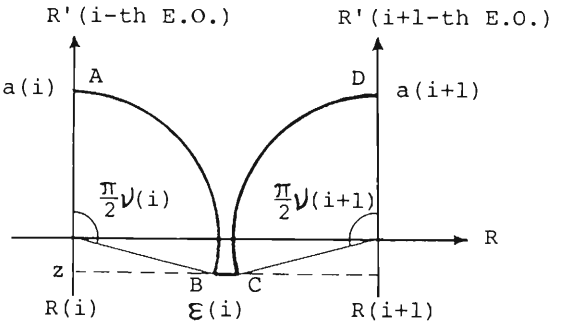

Fig. 2. Diagram describing motion of a well-centered particle on the radial phase space. Points (A-D) correspond to those in Fig. 1. Leave the details to the text.

ellipses into circles by multiplying an appropriate scaling factor to the values of angular divergence. This factor is given by r_0/r_0', where r_0 (radial displacement) and r_0' (angular divergence) represent the principal axes of the ellipse.

Figure 2 shows the diagram describing the motion of the well-centered particle on the radial phase space. The left (right) vertical axis (R′) gives the angular divergence for the i-th ((i+1)-th) E.O. which is properly scaled. The horizontal axis (R) represents the radial distance from the machine center to the E.O. of interest at the valley mid-line. This axis is common to all the E.O. considered. The particle which leaves the point A with the energy of E(i) and the angular divergence of a(i) moves along the circular arc AB and reaches the point B. Then it gets the energy gain of $\Delta E = E(i+1) - E(i)$ and the radial shift of $\epsilon(i)$ by the acceleration system. Afterwards the particle moves along the circular arc CD and reaches the point D. $\nu(i)$ and $\nu(i+1)$ represent the radial betatron frequencies for the i-th and (i+1)-th E.O., respectively.

From the diagram shown in Fig. 2, we can formulate an expression, which will be called "beam centering equation", for getting the well-centered acceleration orbit. This equation can be written in the form of

$$-z\left[\frac{1}{\tan\left[\frac{\pi}{2}\left\{\nu(i)-1\right\}\right]}+\frac{1}{\tan\left[\frac{\pi}{2}\left\{\nu(i+1)-1\right\}\right]}\right]+\varepsilon(i)=R(i+1)-R(i) \qquad (1)$$

with z indicated in Fig. 2. We assume that the trajectory between a couple of acceleration gaps can be approximated by a straight line and also that it cuts the mid-line of dee valley at right angles. These are fairly good assumptions because the magnetic field in the dee valley region is very low. Further, we assume that the particle crosses the mid-line of dee valley at the moment the RF voltage becomes null. Then we can get the following expressions:

$$\Delta E = 2g^{(1)} qV\left\{R^*\sec(\theta_{dee}/2)\right\}\sin(\Delta\theta)/\Delta\theta, \qquad (2)$$

$$\Delta\theta = g^{(2)}/R^*, \qquad (3)$$

$$\varepsilon(i) = g^{(3)}\left\{\Delta E/2E(i)\right\}R^*, \qquad (4)$$

$$R^* = R(i) + a(i)\sin\left\{\frac{\pi}{2}\nu(i)\right\} \qquad (5)$$

$$z = a(i)\cos\left\{\frac{\pi}{2}\nu(i)\right\}, \qquad (6)$$

$g^{(1)}$; $g^{(2)}$, and $g^{(3)}$ being given by use of the geometrical parameters for the sector magnets and RF resonator and the harmonic number of acceleration. q is the charge number of the particle, θ_{dee} the dee angle and V(x) the RF voltage given as a function of x, the distance measured along the mid-line of dee gap from the machine center. The term $\sin(\Delta\theta)/\Delta\theta$ in Eqn. (4) is introduced to take into account the transit-time effect due to the finite acceleration gap.

Ⅳ-16. Beam Centering and Related Problems in a Separated Sector Cyclotron

Y. Yano, A. Goto, and N. Nakanishi

We used the beam centering equation[1] to determine the conditions for centering the beam injected into the separated sector cyclotron. In applying this equation, the first condition is that a central particle of the beam must be injected at the radial position R(1) at an appropriate RF phase. This phase is calculated by the first-order transformation matrix theory. The second condition is that the central particle must be injected with the angular divergence given in the following way.

Assuming that $\nu(1) = \nu(2)$ and $R^* = R(1)$, the expression to obtain the necessary angular divergence a* (in actual unit) at injection point is deduced from the beam centering equation. This is written as

$$a^* = \left\{ R(2) - R(1) - \varepsilon(1) \right\} (r_0'/r_0) \left\{ 2\sin\left(\frac{\pi}{2}\nu(1)\right) \right\}. \qquad (1)$$

The right-hand side of Eqn. (1) is calculated from the isochronous field data and given RF voltage distribution of V(x).

The calculation of beam centering of $^{12}C^{6+}$ with the injection energy of 50.57 MeV was made as an example. We used the RF voltage distribution shown in Fig. 1. The voltage at R_{inj} was taken to be 250 kV. A fairly good result was obtained that the orbit center is injected onto the circle of radius of about 0.3 mm. Figure 2 shows the transformation of beam properties with the radius calculated by tracing four particles together with the central particle. These four particles exist on the eigen-ellipse of emittance of 20 π mm·mrad at injection point. The CP phase matching[2] was made. The time-varying magnetic field[3] induced by the radial distribution of RF

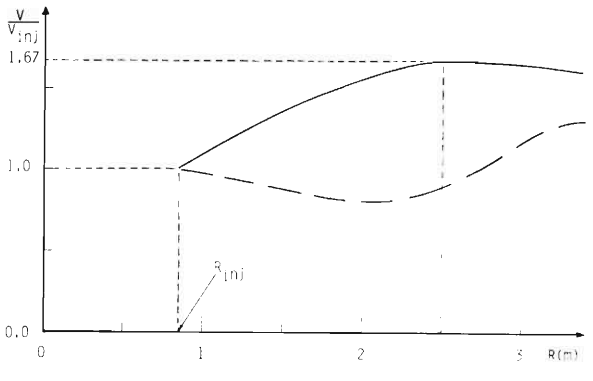

Fig. 1. Radial distribution of RF voltage used in the calculations of beam centering of $^{12}C^{6+}$ with injection energy of 50.57 MeV. R represents the distance measured along the mid-line of dee gap from the machine center. The RF voltage is normalized by the voltage at the position (R_{inj}) of the first acceleration orbit. The dashed curve shows the voltage distribution obtained by the present structure of RF resonator and the solid curve the resultant distribution calculated so that the beam centering equation can hold throughout the acceleration region of the SSC.

voltage was also taken into account.

Secondly, we calculated the RF voltage distribution which makes the beam centering equation hold exactly throughout the acceleration region. This distribution can be obtained by solving the equation iteratively by use of the isochronous field data. The resultant RF voltage distribution is shown in Fig. 1 (solid curve). In this case, the orbit center moves along the circle of radius of about 0.1 mm. Figure 3 shows the transformation of beam properties calculated by using the desired distribution. It can be seen that the energy resolution and the beam emittance at extraction point are improved considerably.

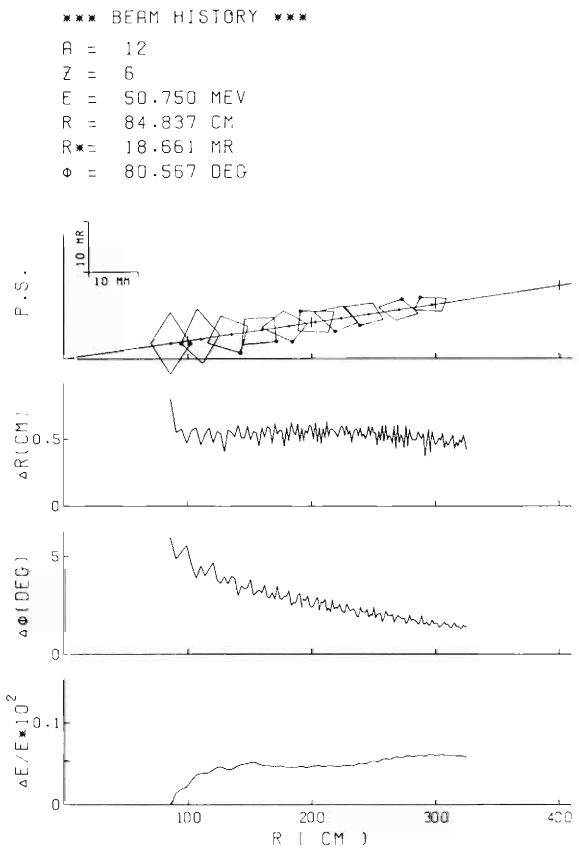

Fig. 2. Transformation of beam properties (radial emittance, full radial width, full phase width and energy resolution) calculated at the mid-line of open valley. Calculations were made using the RF voltage distribution given by the dashed curve in Fig. 1.

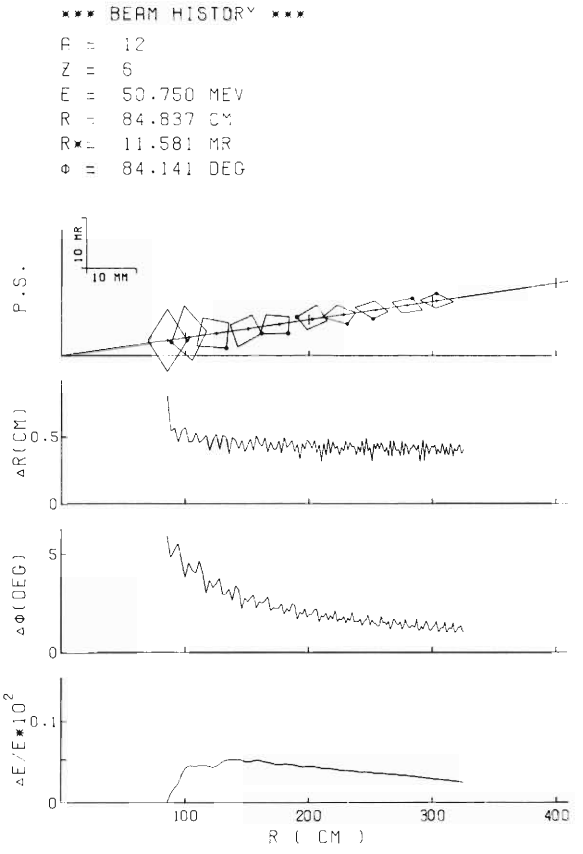

Fig. 3 Transformation of beam properties. Calculations were made using the RF voltage distribution given by the solid curve in Fig. 1.

References

1) Y. Yano, A. Goto, and N. Nakanishi: p. 155 in this report.
2) W.M. Schulte: "The Theory of Accelerated Particles in AVF Cyclotrons", Thesis, Eindhoven (1978).
3) W. Joho: Particle Accelerators, 6, 41 (1974).

Ⅳ-17. Design of Injection and Extraction Harmonic Coils for the RIKEN SSC

A. Goto, Y. Yano, and N. Nakanishi

Harmonic coils for the SSC were designed for beam centering in the injection region and for beam off-centering in the extraction region.[1] Using the numerical calculation programs,[2] the behavior of the orbit centers under the influence of the first harmonic field perturbations produced by these coils were investigated, and their optimal parameters were searched for.

It may happen that off-centering of the beam in the injection region occurs from following two causes: field distortion due to the injection elements and incorrect setting of these elements. Accordingly a harmonic coil is necessary to produce a magnetic field perturbation in the injection region in order to center the beam during the first several turns. In the extraction region the beam separation due to only acceleration is not enough for some of high energy light particles (e.g. 134 MeV/u $^{12}C^{6+}$). A magnetic field perturbation will also be required to enhance the turn separation in order that the single turn extraction can be achieved.

In surveying the beam behavior it is often convenient to calculate the motion of an orbit center instead of a particle itself. In the present calculation, the first harmonic field was superimposed onto the base field (isochronous field) and the motion of the orbit center was deduced by tracing a beam in the resultant field. The azimuthal distribution of the harmonic field, for example, which was used in the calculation is shown schematically in Fig. 1.

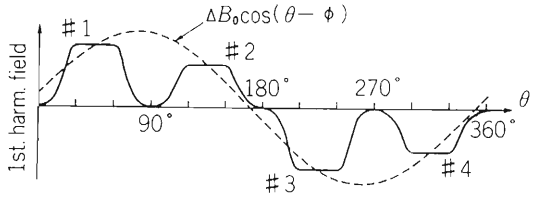

Fig. 1. Azimuthal distribution of the first harmonic field used in the calculation (solid line).

It is desirable to center the beam during about five particle revolutions or so, which correspond to a half turn of the orbit center ($\nu_r - 1 \cong 0.1$). For this reason we decided to divide all kinds of particles into three groups according to their orbit separations and to center them by three sets of harmonic coils, respectively. Thus we chose a typical particle for each group and calculated the motion of its orbit center in the presence of first harmonic field perturbation. They are 7 MeV/u $^{12}C^{6+}$, 4 MeV/u $^{12}C^{6+}$, and 0.84 MeV/u $^{238}U^{40+}$, whose orbit separations are smallest, medium and largest, respectively, among all the ions accelerated in our SSC. An off-centered beam was artificially given by putting the beam onto its equilibrium orbit at the injection point. The calculations were done using the code INJHARM.[2] The optimum positions of the three sets of harmonic coils were found to be at R_h (the radial position on the hill center line) = 101.5, 113.5, and 125.5 cm. The widths of these coils were taken to be 11.5 cm. In Fig. 2 is shown, as an example, the motion of the orbit center for the 0.84 MeV/u $^{238}U^{40+}$ beam, which was calculated in the harmonic field produced by the outermost coil. The dots stand for the orbit

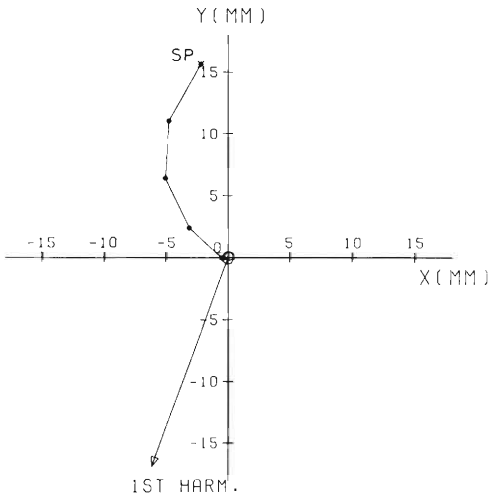

Fig. 2. Motion of the orbit center for the 0.84 MeV/u $^{238}U^{40+}$ beam in the injection region under the influence of the first harmonic field. The injection point is on the x-axis. The dots stand for the orbit centers and SP their starting point.

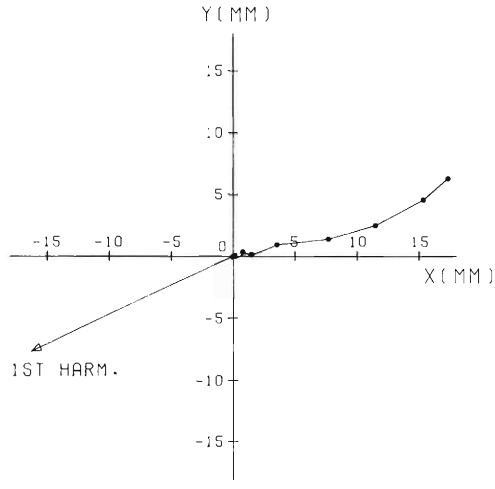

Fig. 3. Motion of the orbit center for the 134 MeV/u $^{12}C^{6+}$ beam in the extraction region under the influence of the first harmonic field. The entrance of EDC is positioned at about 15°. The dots stand for the orbit centers.

centers and the azimuthal position of the injection point is set to be 0°. One can see that the orbit center starting at the position about 15 mm apart from the cyclotron center is centered after about five particle revolutions. The strengths of the harmonic fields (and the azimuthal positions of their maximums) which are needed for centering the three beams were 10 Gauss (260°), 12 Gauss (255°), and 24 Gauss (250°), respectively.

We aimed to extract a beam before $\nu_r = 1$ resonance in order to avoid the strong radial defocusing of the extracted beam due to the fringe field of the sector magnets. The study was concentrated on the extraction of the 134 MeV/u $^{12}C^{6+}$ beam (the injection energy of 7 MeV/u) whose orbit separation is the smallest among all kinds of accelerated particles. The calculation was made using the code EXTHARM.[2] At first the well-centered orbit of the $^{12}C^{6+}$ beam was calculated using the code ACCEL[2] from the injection point up to the region where its radial distance is less than the extraction radius (373 cm on the hill center line) by about ten revolutions. The orbit center continues to stay at the cyclotron center during this acceleration. The beam parameters thus calculated were inputted into the code EXTHARM and then the parameters of the harmonic coil – its radial position, its field strength and direction – were searched for in order to obtain the beam separation large enough for single turn extraction. The optimum position of this harmonic coil was found to be at $R_h = 372$ cm, which is just inside the extraction radius. The orbit separation becomes larger, the steeper the field rise is; thus the narrower harmonic coil is more desirable. It was decided, therefore, to use the coil of 1.2 cm in width, which is made of a copper hollow conductor. Figure 3 shows the motion of the orbit center for the 134 MeV/u $^{12}C^{6+}$ beam, which was calculated in the first harmonic field produced by this coil. The dots stand for the orbit centers and the azimuthal position of the extraction point is set to be 0°. The entrance of the electric deflection channel (EDC) is positioned at about 15°. One can see that the

orbit center which stayed at the origin begins to move toward the entrance of EDC. The maximum displacement between two successive orbit centers is about 5 mm. In this case the strength of the field and the direction of its maximum are 100 Gauss and 205°, respectively. In Fig. 4 is shown the result of calculation of the transformation of beam ellipses on the valley center line (at 0°) with and without the first harmonic field mentioned above. It can be seen that the beam envelopes which were in contact with each other in the case of only acceleration can be separated with this harmonic field by about 5 mm at the extraction point. The septum of EDC will be located between 308th and 309th revolutions.

Further, we also use another harmonic coil of the same width just inside the above determined coil as an auxiliary one. Its radial position is at 370.6 cm.

These harmonic coils are also used as part of trim coils which consist of 29 pairs. Figure 5 presents the plan of the trim and harmonic coil set. We use three coils from No. 5 to No. 7 as harmonic coils for beam centering and two coils, No. 26 and No. 27, for beam off-centering. Coils numbered less than 8 are wound around the nose of the pole tip and the others around its back.

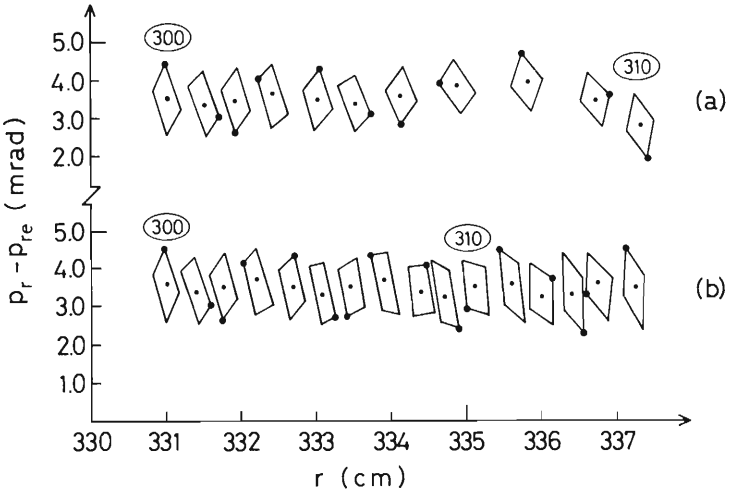

Fig 4. Radial phase space envelopes at 0° for the 134 MeV/u $^{12}C^{6+}$ beam in the extraction region, (a) with and (b) without the first harmonic field. The numbers refer to the revolutions of the beam. The beam emittance is taken to be 20 mm. mrad at the injection point.

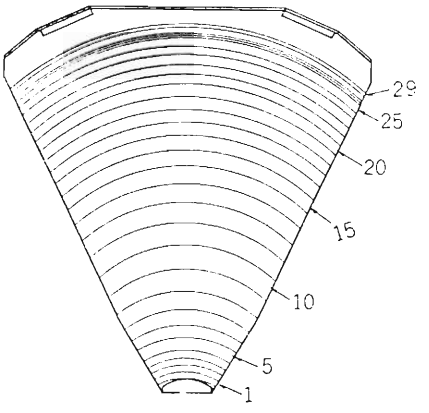

Fig. 5. Plan of the trim and harmonic coil set for the RIKEN SSC.

References

1) A. Goto, Y. Yano, and N. Nakanishi: Sci. Papers I.P.C.R., 75, 204 (1981).
2) A. Goto, H. Takebe, S. Motonaga, T. Wada, Y. Yano, N. Nakanishi, and Y. Tanaka: Reports I.P.C.R., (in Japanese), 57, 165 (1981).

IV-18. The Sector Magnet for the RIKEN SSC

S. Motonaga, H. Takebe, A. Goto, J. Fujita,
T. Wada, Y. Oikawa, I. Takeshita, and Y. Ikegami

The design of the sector magnet described in the previous progress report[1] was changed slightly. More detailed design work for the pole profile, configuration of the trim coils and vacuum seal between magnet and RF-cavity have been done during the year.

The profile of the magnetic field distribution should be such that the field will provide isochronism, focusing and orbital stability for the beam. Table 1 lists the final design parameters of the sector magnet. The four sector magnets will produce the magnetic field of 15.5 kG at maximum. The maximum magnetomotive force was estimated to be 1.35×10^5 A·T and the maximum power consumption in the four sector magnets is estimated to be 450 kW. The shape and geometrical size of sector magnet are shown in Fig. 1. Extremely tight tolerance limits

Table 1. Characteristics of SSC Magnets.

Number of sector magnet	4	Maximum magnetic field	15.5 kG
Sector angle	50°	Maximum magnetomotive force	1.35×10^5 A·T
Gap width	8 cm	Maximum current	1000 A
Injection mean radius	89.3 cm	Current stability	0.002 %
Extraction mean radius	356 cm	Maximum power	450 kW
Height of magnet	5.24 m	Number of trim coils	29 pairs × 4
Radial length of magnet	5.64 m	Maximum current	500 A
Total weight	2120 ton	Current stability	0.05 %
	(530 ton/one sector)	Total trim coil power	200 kW

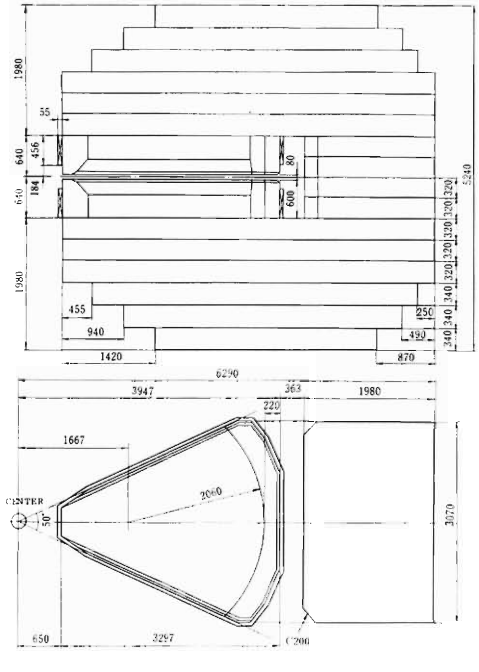

Fig. 1. Shape and geometrical size of the sector magnet.

are imposed on the magnetic field to obtain a high quality beam. The specified tolerances for the field stability, accuracy of machining and alignment for the construction of the magnet are as follows:

Stability of the magnetic field	10^{-5}
Maximum deviation from the isochronous field	10^{-4}
Relative error in gap distance of the four sector magnets	0.02 mm
Error in parallel setting of pole face	0.05 mm
Sector angle	$50.00^{\circ}\ ^{+0.02^{\circ}}_{-0.00}$
Misleveling of the four sectors magnets	0.1 mm
Error in positioning of the four sector magnets	0.1 mm
Error in parallel setting of trim coil assembly	1.0 mm
Error in positioning of the trim coils assembly	± 0.5 mm

The poles are triangular in shape with sector angle of 50° and length of 3.297 m along the center line. The pole-edge profile of side part in azimuthal direction was a modified B-constant type. Detailed design of the poles was performed on the basis of calculated magnetic field as well as measured field of the model magnet. The side of the central part as shown in Fig. 1 are cut away slightly to keep a wider space between the magnet and RF-resonator. Change of the effective boundary by this modification for this part was found to be small.

The yoke was divided into 16 slabs with maximum thickness of 340 mm for the convenience of the construction and transportation. The ratio of cross-sectional area of yoke to that of the pole base was 0.94.

Very homogeneous forged steel with carbon content of 0.01 % was used for the pole and rolled steel of 0.04 % carbon contents for the yoke of each magnet. Two poles of each sector magnet was prepared from a single ingot. Table 2 shows measured characteristics of the steel used.

Table 2. Measured characteristics of the low carbon steel (weight percent).

	C	Si	Mn	P	S	Cu	Al
Pole	0.01	0.001	0.08	0.013	0.002	0.01	0.018
	0.01	0.001	0.09	0.011	0.003	0.01	0.036
	0.01	0.001	0.10	0.011	0.002	0.01	0.031
Yoke	0.04	< 0.01	0.31	0.14			
	0.04	< 0.01	0.30	0.10			

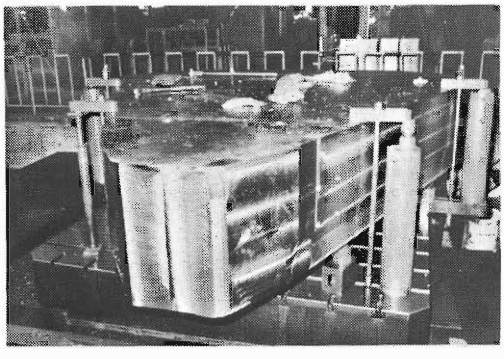

Fig. 2. Pole plate of the first magnet during machining using NC-machine.

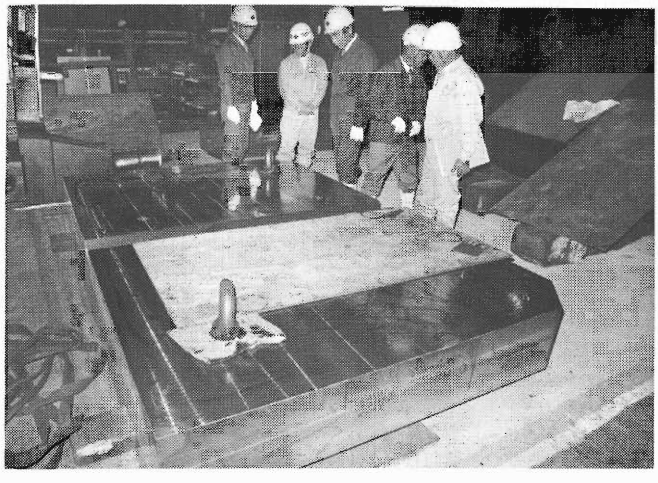

Fig. 3. Yoke slab of the first magnet during fabrication.

Fabrication of the first magnet started in July, 1981. Figures 2 and 3 show pole and yoke parts during machining.

The Main coil of one pole consists of 66 turns of hollow copper conductor for direct water cooling and made up of 11 units with 6 turns. They formed in size of 5.0 cm in thickness and 46.5 cm in height. Tape-winding with glassfiber reinforced epoxy resin was used for insulation between turns and to provide mechanical strength. Figure 4 shows the main coil of the first sector magnet. The main coils are located outside of the vacuum chamber.

Mechanical deformation of yoke and poles due to the magnetic force, gravitational force and atmospherical pressure was calculated by a computer code FEM-2.[3] The maximum deformation of 0.15 mm for pole face and vertical displacement of 0.25 mm at the front of pole tip were obtained. By applying 1 mm thick gap spacer between pole base and yoke, we could reduce the deformation to 0.1 mm, but the value of the vertical displacement was increased to 0.35 mm. Such displacement will entail no problem on the beam dynamics.

For forming the required isochronous field, 29 pairs of trimming coils will be mounted on the pole face. 5 pairs of them will also be used for the harmonic field formation. The radial width and positions of the trim coils were determined by using a computer optimization code developed by Goto.[4] The detailed design of the trim coils configuration is shown in Fig. 5. Trim coils consist of 6 mm thick copper plate and cooled by 6 X 12 mm hollow conductor welded to the copper plate. Each coil is flash-coated of fused aluminum oxide. Figure 6 shows one of the copper plate coated with Al_2O_3.

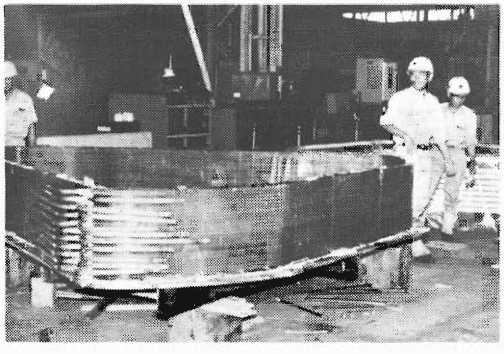

Fig. 4. Main coil of the first magnet.

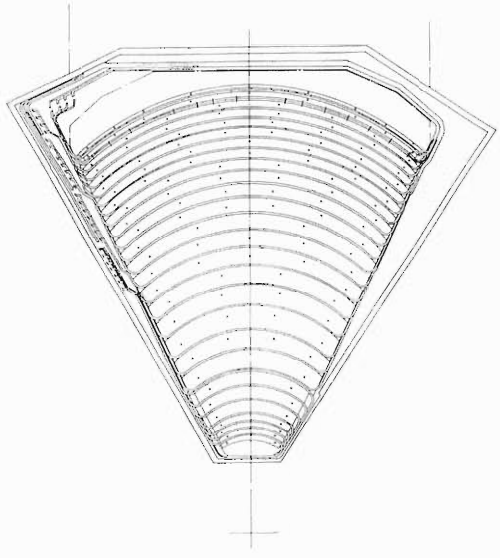

Fig. 5. Layout of the configuration of the trim coils.

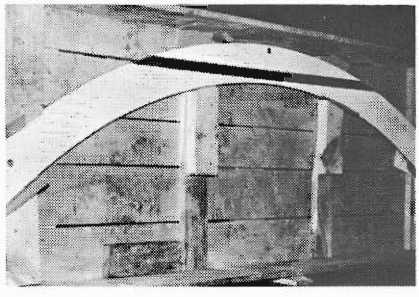

Fig. 6. Copper plate coated with aluminumed oxide.

The trim coils will be mounted directly on the pole face by bolts and enclosed with an auxiliary vacuum chamber. In order to reduce the magnetic perturbation due to bolt holes on the pole face, special bolts of soft iron welded onto stainless steel will be used. Cross-sectional view of the pole section is shown in Fig. 7.

The final design of equipment to map the field of the sector magnets was completed. This system employs

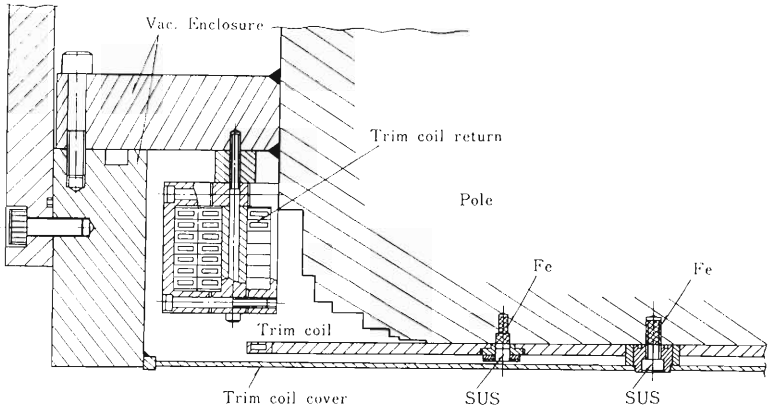

Fig. 7. Detailed cross-sectional view of the pole edge section.

21 Hall probes radially arranged, which measure the magnetic field between minimum and maximum radius as a function of the azimuthal position in the range of 360° with stepping mode. Operation of this system will be controlled by computer.

Fabrication of the sector magnets are progressing satisfactorily at present. In order to finalize the pole contour, preliminary measurement of edge field in the azimuthal direction will be performed at Sumitomo Heavy Industry's Work Shop in April, 1982.

References

1) S. Motonaga, H. Takebe, T. Wada, Y. Obana, J. Fujita, and Y. Ikegami: IPCR Cyclotron Progr. Rep., 14, 164 (1980).

2) H. Kumagai: Nucl. Instr. and Methods, 6, 213 (1960); S. Motonaga, Y. Miyazawa, N. Nakanishi, T. Tonuma, M. Hemmi, and T. Karasawa: Reports I.P.C.R., (in Japanese), 40, 1 (1964); T. Karasawa, S. Motonaga, Y. Miyazawa, and M. Hemmi: Proc. 1st Intern. Conf. on Magnet Technology, p. 239 (1965).

3) Y. Ikegami, T. Wada, M. Hara, and S. Motonaga: Reports I.P.C.R., (in Japanese), 57, 177 (1981).

4) A. Goto H. Takebe, S. Motonaga, T. Wada, Y. Yano, N. Nakanishi, and Y. Tanaka: ibid., p. 165.

IV-19. Structural Analysis of Sector Magnet by Finite Element Method

Y. Ikegami, T. Wada, and M. Hara

Finite element method (FEM) is widely used for the analysis of complex structures by the aid of digital computer.[1] We are using this method for the structural analyses of sector magnet, vacuum chamber and RF resonator.

Here the results for the sector magnet are presented. The deformation of the sector magnet by various forces acting on it was analyzed. The analysis has been done by using two-dimensional code (FEM-2)[2] because the data input is simple and fine element in FEM can be used, and the effects of slab structure of the yoke and a small gap in the pole base are investigated. The analysis by using three-dimensional code (SAP-5)[3] is in progress.

The dimension and size of the sector magnet are shown elsewhere.[4] The yoke is divided into 16 slabs for the convenience of construction and transportation. Table 1 lists the materials and their physical constants which are used in the present analysis. Three kinds of structures were investigated:

(1) A structure in which the whole magnet is treated as a solid by considering that the pole, yokes and the spacers are strongly pulled to each other by magnetic forces.

(2) A structure in which truss elements are inserted between the slabs by taking into account the slide between the slabs.

(3) A structure in which two small gaps of 1 mm are introduced in the pole bases in order to decrease the deformation of the pole.

Table 1. Materials and their physical constants.

Part	Material	Specific gravity	Young's modulus (kg/mm^2)	Poisson's ratio
Pole	Pure iron	7.87	21000	0.3
Yoke	Soft iron	7.70	21000	0.3
Spacer	SUS	8.03	21000	0.3

Figure 1 shows the subdivision of the sector magnet in the case of (1). Specifying the thickness of each element, the three-dimensional effects are included. The magnetic force loaded on the pole face elements are 9.75 kg/cm^2. The calculated deformations of the pole faces are shown in Fig. 2. Curve 1 is the result obtained using three spacers and curve 2 is that of only one spacer at innermost point of the pole face. The calculated deformations of the whole magnet for the case (3) are shown in Fig. 3. The solid and broken lines show the shapes before and after deformation, respectively. Figure 4 compares the deformation of pole faces for the above three cases. As can be seen from the comparison between curve 1 and 2, the deformation of the case of slab structure is about 4 times as large as that of the case of solid structure. In the real case, however, the deformation can be estimated to take the value between those two cases (about 0.1 mm). From the results for cases (2) and (3), it seems that the effect of pole base gap is not large. However, if the deformation of the pole base and pole face are compared, it can be seen that the deformation of the pole comes mainly from that of the part around the spacers. Figure 5 shows the deformations of the bases of upper and lower poles. It can be seen that deformations decrease by about 40 % and 70 % for the upper and lower poles, respectively, if small gaps are introduced in the pole bases. Figure 6 shows the stress distribution around the spacers. The maximum stress becomes a little smaller in the case of the structure with gaps. The maximum compression stress (13.84 kg/mm^2) is much smaller

than the allowed compression stress (52 kg/mm^2) and yield strength (21 kg/mm^2) of the stainless steel.

In the two-dimensional analysis, the deformation along azimuthal direction of this magnet cannot be calculated. We are now using SAP-5 code for the three-dimensional analysis. Figure 7 shows the subdivision for carrying out this calculation.

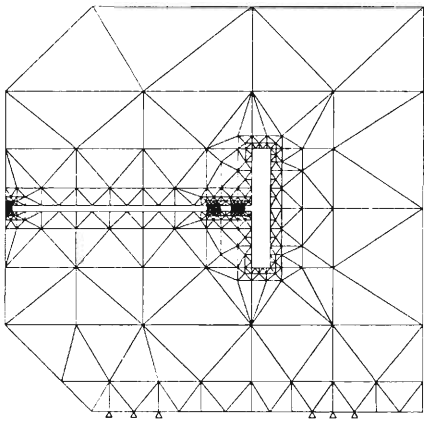

Fig. 1. Subdivisions of the sector magnet for case (1).

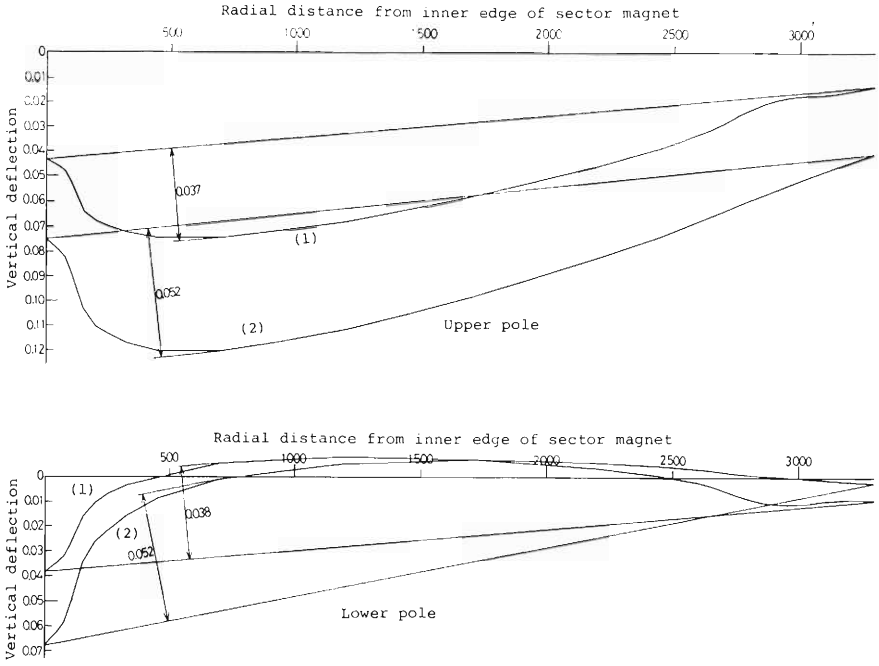

Fig. 2. Vertical deflections of the pole faces. Curves (1) and (2) show the results using three and one spacer, respectively.

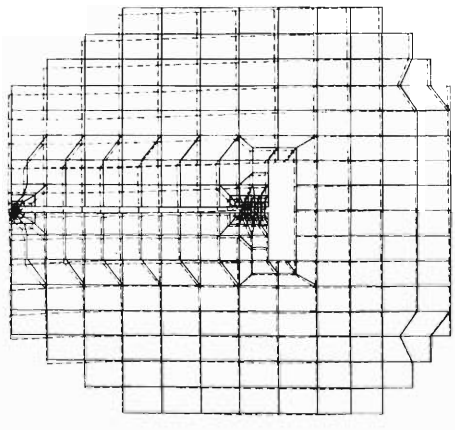

Fig. 3. The deformation of the whole magnet. The solid and broken lines show the shapes before and after deformation. Deformation is exaggerated by a factor of 200.

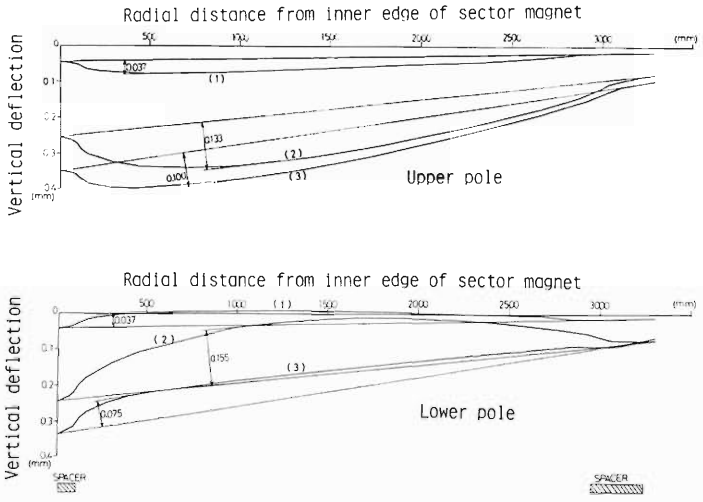

Fig 4. Vertical deflection of the pole faces in the three cases, (1), (2), and (3).

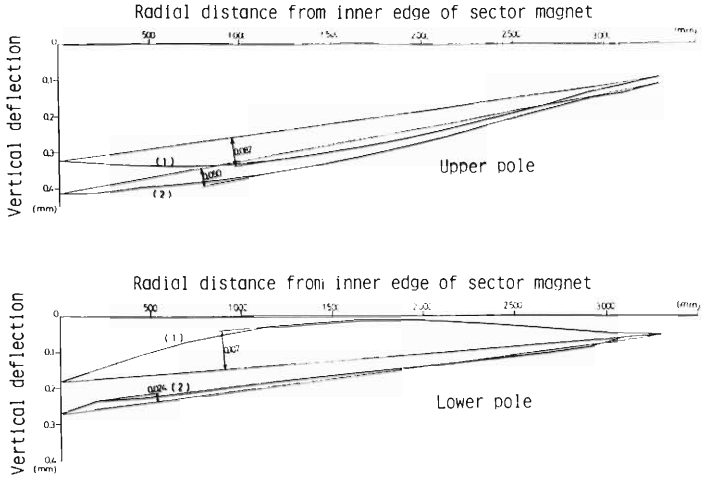

Fig. 5. Vertical deflection of the pole bases in the three cases, (1), (2), and (3).

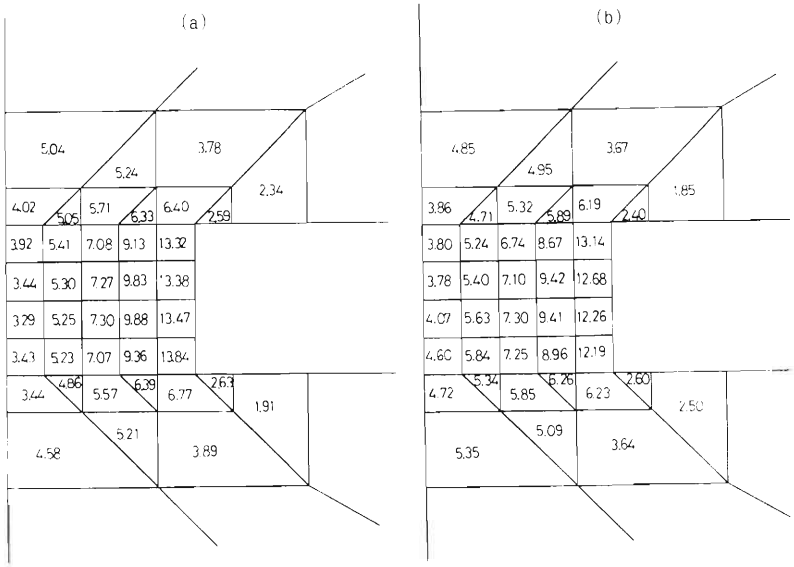

Fig 6. The distribution of stress (kg/mm^2) around the central spacer:
(a) no gap at the pole base.
(b) 1 mm gap at the pole base.

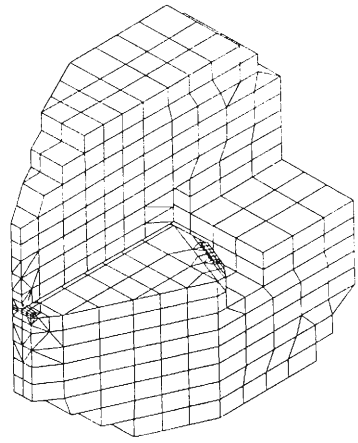

Fig. 7. Subdivisions for three dimensional analysis.

References

1) O.C. Zienkiewicz: "The Finite Element Method in Engineering Science", McGraw-Hill Publishing Co. Ltd., England (1971).
2) H. Togawa: "A Guide to Finite Element Method", Science Co. Ltd., Tokyo (1980).
3) K.J. Bathe and E.L. Wilson: SAP IV-A Structural Analysis Program for Static and Dynamic Response of Linear System, Report EERC 73-11, College of Engineering, University of California, Berkely, (June, 1973, revised Apr. 1974).
4) S. Motonaga, H. Takebe, T. Wada, A. Goto, J. Fujita, Y. Oikawa, I. Takeshita, and Y. Ikegami: 9th Intern. Conf. on Cyclotrons and their Applications, Caen, France, Sept. (1981).

Ⅳ-20. Model Test of the Trim Coil for the SSC

H. Takebe, T. Wada, I. Takeshita,
S. Motonaga, J. Fujita, and Y. Tanaka

Trim coil of the SSC sector magnet consists of 29 pair of coils. Each coil is made of a wide copper plate with a hollow conductor as seen in other report.[1] In the coils #1 to #7, electric currents are fed from hollow conductors to the copper plates at the outer edge points, while currents are fed at the inner points in the coils #8 to #29. To investigate the magnetic field distribution around the edge of this trim coils and the field deviation from the isochronous field of the sector magnet, a straight shape model of the trim coil has been prepared and the field is measured in 80 mm air gap of the H-type magnet. The results are compared with the calculations by

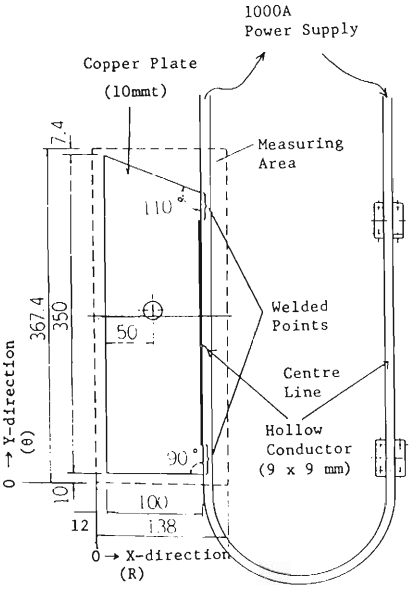

Fig. 1. Plan view of the model trim coil.

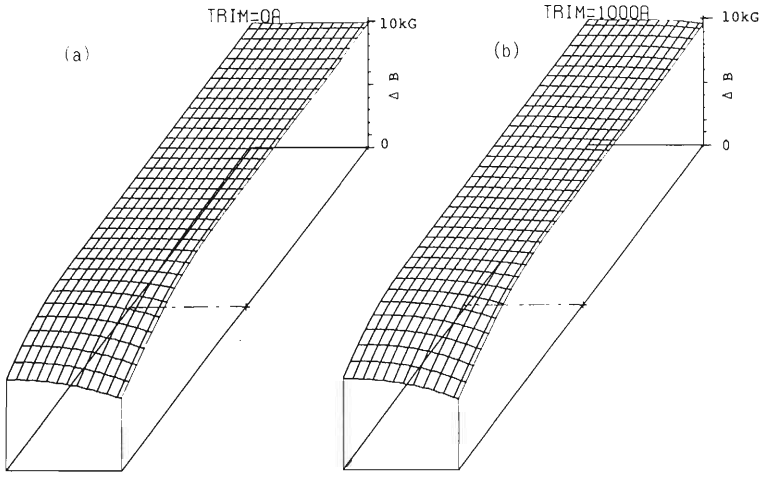

Fig. 2. Magnetic field maps measured at trim coil current of OA (a base field) (a), and 1000 A (b).

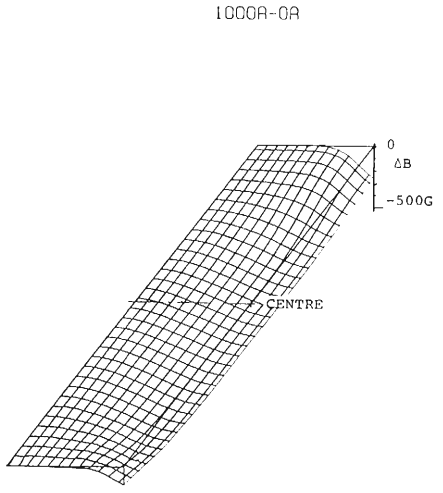

Fig. 3. Effective field produced by the trim coil. This is obtained by substracting the base field (Fig. 2-a) from the field of Fig. 2-b.

TRIM code[2] using a current distribution on the copper plate which is calculated by a finite element method (FEM).[3]

Figure 1 shows the model trim coil. Thickness of the copper plate is 10 mm and the hollow conductor (9 × 9 mm, hollow diameter = 6 mm) is welded by TIG method extending 30 mm on both the feed-in and feed-out sides of the copper plate. At the centre of the copper plate a hole is bored, because in the case of the SSC sector magnet there are hales for bolts to fix the trim coil on the pole face. One side of the copper plate is made in the shape of 110° cut as in the case of trim coils #1 to #7 of SSC magnet. The other is of 90° cut to compare the edge effect on the magnetic field. The magnetic field distribution has been measured by three Hall generators whose driver was controled by LSI-11 micro computer. The field was scanned by steps of 6 mm in both X and Y-directions in the area (138 mm × 368 mm) indicated by dashed line in Fig. 1. The X and Y-directions correspond to the radial and azimuthal direction in the SSC sector magnet.

Figure 2 (b) shows a measured map of the base field without the trim coil current and Fig. 2 (a) shows that with the current of 1000A. Difference of these two maps is the effective field of the trim coil. This is shown in Fig. 3.

As an accelerated particle continues to sense the magnetic field along the beam path (Y-direction), integrated value of the effective field is important around the edge region. These effective fields of 110° and 90° cut side of the trim coil were integrated along the Y-direction from the both edges to the centre line, respectively. Distributions of these integrated values (S) are shown in Fig. 4.

Effective field boundaries (EFB's) of the field produced by the trim coil were calculated by dividing these data (S) by the field values on the centre line indicated in Fig. 4. These EFB's on both sides are plotted in Fig. 5. The variation of the boundary curve along the X-direction for 110° cut is larger than that for 90° cut. This means that the outer lead type is not suitable for wide and short type trim coils. However, we adopted this type for trim coils #1 to #7 of the SSC because of geometrical condition of return lead lines.

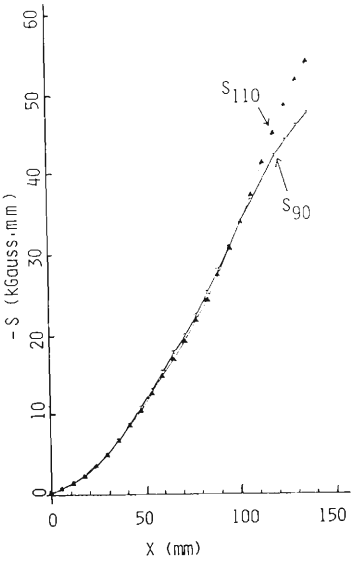

Fig. 4. Magnetic field distributions of effective field integrated along Y direction. S_{90} is integrated in the range of Y = 00 mm – 180.7 mm and S_{110} in the range of Y = 180.7 mm – 367.4 mm.

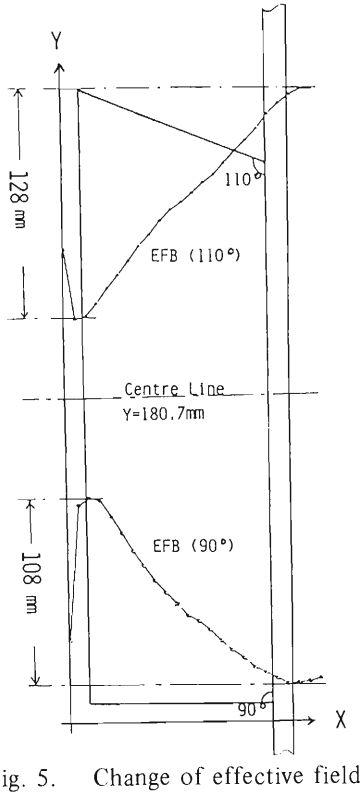

Fig. 5. Change of effective field boundary. This is obtained by dividing the integrated field strength S by the value at the centre lines.

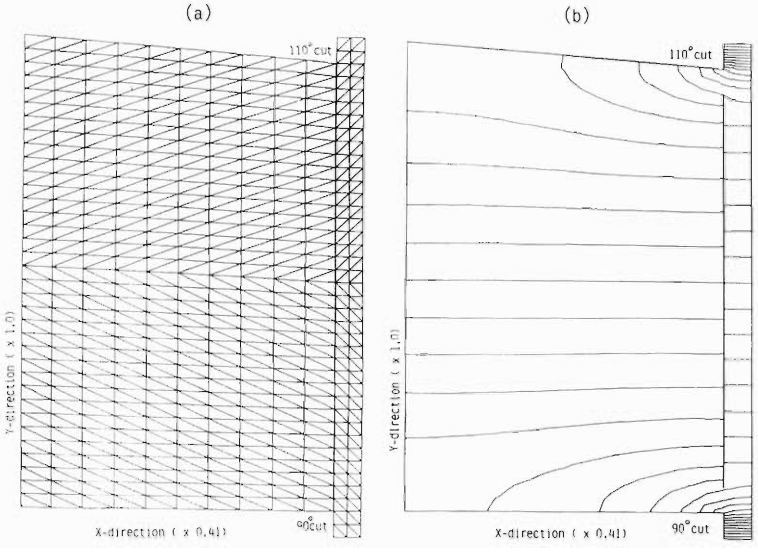

Fig. 6. (a) Mesh plot used in the FEM calculation of current distribution in the model trim coil. X-direction is magnified by a factor of 2.44. (b) Equipotential lines in the model trim coil.

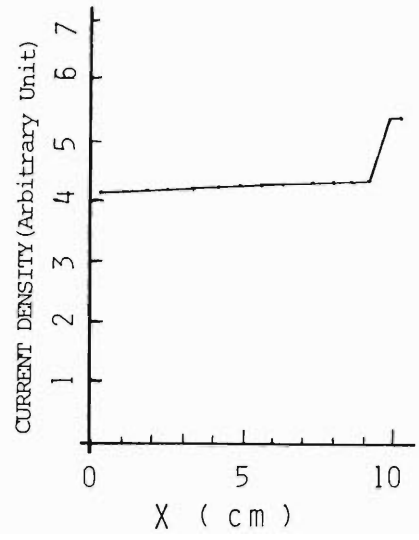

Fig. 7. Calculated current density distribution along the trim coil centre.

To calculate the current distribution on this model of the trim coil, FEM was used to solve Laplace equation. The mesh plot for this calculation is shown in Fig. 6 (a), and the resultant equipotential lines on the copper plate is shown in Fig. 6 (b). Figure 7 shows the current density distribution along the centre line of the trim coil. From this current distribution, the distribution of the magnetic field was calculated using a computer code TRIM. Figure 8 shows the distribution of the measured magnetic field along the X-directions as well as the calculated ones. It can be seen that the calculated field distribution on the centre line agrees well with the measured one. From this result we considered that the TRIM code is feasible in the design of the trim coil for the SSC. We estimated the field deviation from the isochronous field caused by the finite width of the trim coils in detail.

The H-type magnet used to generate the base field in this test has a pole piece different slightly in shape from that of the SSC sector magnet. Therefore, the effective field boundary measured in this test will be slightly different from that of the SSC sector magnet. In the design of the trim coil of the SSC, the data obtained in this test have to be modified to adopt to the real dimension of the SSC trim coils. Using this modified field and introducing the edge effect, the phase slip of an accelerated beam will be calculated.

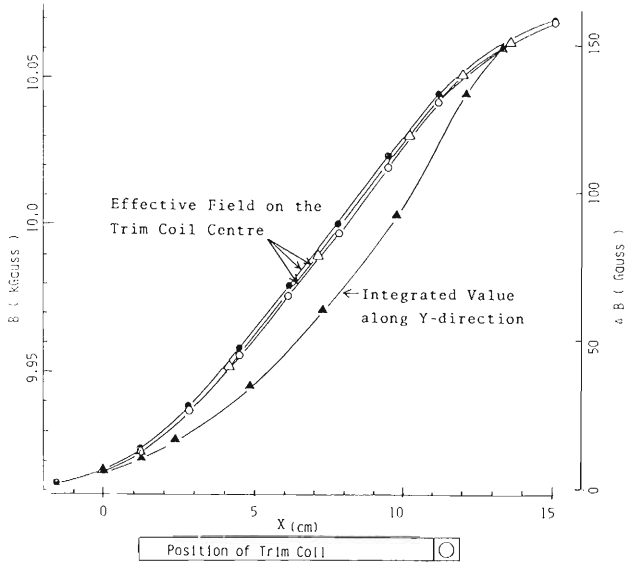

Fig. 8. Measured and calculated distributions of effective field in X-direction. ○: Calculation by TRIM code using the current density distribution in Fig. 7. △: Measured value. ●: Calculation by TRIM code using a constant current distribution. ▲: Integrated effective field of 110° cut along the Y-direction (this is normalized at both edge of the measured points in X-direction).

References

1) H. Takebe, A. Goto, S. Motonaga, T. Wada, Y. Oikawa, and I. Takeshita: p.173 in this report.
2) J.S. Colonais and J.H. Porst: Magnet Design Applications of the Magnetostatic Problem, called TRIM, UCRL-16382 (1965).
3) O.C. Zienkiewicz: The Finite Element Method in Engineering Science, McGrow-Hill Publishing Co. Ltd. (1971).

Ⅳ-21. Design of the Trim Coils for the RIKEN SSC

H. Takebe, A. Goto, S. Motonaga,
T. Wada, Y. Oikawa, and I. Takeshita

A final design of the trim coils for the SSC sector magnets was achieved on the basis of model measurements[1), 2)] and calculations.

The number of the trim coils and their radial positions were so determined that the deviation of the trim coils' field from the isochronous field should be less than 0.05 %. To perform the above requirement a computer code which can optimise the currents of the coils with a least squares method has been developed.[3)] Optimum currents can be obtained to minimize the following quantity:

$$Q = \sum_{i=1}^{N} Wi \left(\sum_{j=1}^{n_c} a_{ij} x_j + B_i^0 - B_i \right)^2 , \qquad (1)$$

where B_i^0 and B_i are the base field and the ideal isochronous field, respectively, at radial distance R_i. Here x_j is the current of the j-th trim coil, $a_{ij}\ x_j$ the field which is produced at R_i by the coil, and n_c the number of trim coils. N is the number of radial positions where the field data were taken and w_i the weighting factor. Here w_i's are so adjusted that the deviations of squares in Eqn. (1) become almost the same over the whole region of R_i. Furthermore, in this calculation the optimum value of the base field B_i^0 that minimizes the following quantity is automatically searched:

$$P = \sum_{j=1}^{n_c} K_j\ x_j^2 \qquad (2)$$

Here K_j is the weighting factor which prevents the particular current to become large. It was found that using this procedure the agreement between the field corrected by trim coils and the ideal isochronous field is fairly well improved. In this calculation it is possible to divide all the coils into any desired groups and to calculate their optimum currents under such a constraint that the coils belonging to each group have the same current. For base field and trim coil fields we used the values which were calculated with the TRIM code.[4)] It is noted here that the field step height of the trim coils varies with the strength of the base field. We thus modified the radial field distribution by the trim coil in such a way that the above effect can be taken into account. The field at radius R_i which is produced by the j-th trim coil is calculated by regarding the isochronous field at radius R_i as the base field. The field profiles thus obtained are presented in Fig. 1.

Because the radial increase of isochronous field is the largest for the 134 MeV/u $^{12}C^{6+}$ ion in the RIKEN SSC, we have designed the configuration of the trim coils in such a way that we can realize the isochronous field efficiently for this case. In this procedure, the following conditions were taken into account: (1) the current of

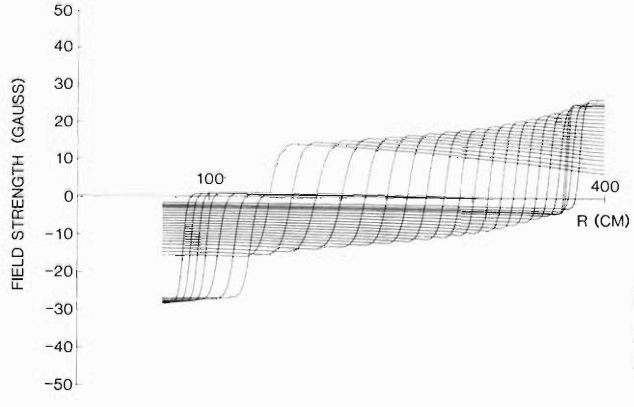

Fig. 1. Calculated magnetic field distribution formed by trim coils at the base field of 15.5 kG when each coil current is 100A.

Table 1. Radial positions and widths on sector centre lines and optimized currents of the trim coils for 184 MeV P, 71 MeV/u C^{6+}, 134 MeV/u C^{6+}, and 13.6 MeV/u $^{238}U^{40+}$. Each trim coil is connected to each power supply of the indicated type.

Trim coil		Particle and energy	P (184 MeV)	C^{6+} (71 MeV/u)	C^{6+} (134 MeV/u)	$^{238}U^{40+}$ (13.6 MeV/u)	Type of power supply	
No.	R (cm)	H (cm)	I (A)	I (A)	I (A)	I (A)		
1	78.0	5.0	149.61	178.09	34.74	76.04	C	
2	83.5	5.0	37.65	66.37	105.86	30.74	E	
3	89.0	5.5	8.15	20.12	38.31	6.71	E	
4	95.0	6.0	38.55	32.97	44.24	19.82	E	
5	101.5	11.5	72.20	69.05	129.28	30.42	C	Harmonic
6	113.5	11.5	93.85	60.19	211.68	19.62	C	Harmonic
7	125.5	11.5	109.17	115.43	200.03	128.02	C	Harmonic
8	137.5	16.5	226.96	140.47	340.78	41.03	B	
9	154.5	16.8	209.72	139.11	318.65	93.88	B	
10	171.8	20.0	303.96	182.79	484.74	97.89	A	Serial in 4-sectors' trim coils
11	192.3	18.5	303.96	182.79	484.74	97.89	A	Serial in 4-sectors' trim coils
12	211.3	16.6	313.46	189.47	494.24	95.37		Serial in 4-sectors' trim coils
13	228.4	15.3	313.46	189.47	494.24	95.37	A	Serial in 4-sectors' trim coils
14	244.2	14.5	324.80	182.99	503.07	76.22	A	Serial in 4-sectors' trim coils
15	259.2	13.5	324.80	182.99	503.07	76.22	A	Serial in 4-sectors' trim coils
16	273.2	12.3	321.19	164.36	495.48	76.57		Serial in 4-sectors' trim coils
17	286.0	11.3	321.19	164.36	495.48	76.57		Serial in 4-sectors' trim coils
18	297.8	10.4	321.62	158.50	481.89	68.84	A	Serial in 4-sectors' trim coils
19	308.7	9.8	321.62	158.50	481.89	68.84	A	Serial in 4-sectors' trim coils
20	319.0	9.3	322.60	150.86	481.74	66.04	A	Serial in 4-sectors' trim coils
21	328.8	8.6	322.60	150.86	481.74	66.04	A	Serial in 4-sectors' trim coils
22	337.9	8.3	323.62	146.45	482.31	68.78	A	Serial in 4-sectors' trim coils
23	346.7	7.8	328.01	146.46	479.54	69.82	B	
24	356.0	7.4	330.05	143.66	480.16	66.01	B	
25	362.9	6.9	337.19	147.67	480.98	77.20	B	
26	370.0	1.2	40.03	−1.02	54.39	−38.48	D	Harmonic
27	371.4	1.2	66.58	58.06	96.70	69.26	D	Harmonic
28	372.8	5.8	287.30	92.95	414.92	0.70	D	
29	379.1	4.2	275.19	136.97	341.55	83.30	B	

coils should change gradually with their radial position and (2) the maximum current should not exceed 500 A. Coils of 29 sets including 5 sets of harmonic coils[5] were found to be necessary. The radial positions and widths of the coils thus determined are tabulated in Table 1 together with the optimized currents for some typical ions. Some pairs of adjacent coils are connected in series. The currents required for isochronization on the 134 MeV/u $^{12}C^{6+}$ and 13.6 MeV/u $^{238}U^{40+}$ ions, respectively, give maximum and minimum values in our case. A plan of the trim coils is shown in Fig. 2. Three coils from No. 5 to No. 7 are used as harmonic coils for the beam centering and the two, No. 26 and No. 27, for the beam off-centering. Return leads of the coils No. 1 – 7 are wound around the nose of the pole and the others around its back. The coils are made of copper plates and are wound along equilibrium orbits in a hard-edge field distribution. The theoretical magnetic field produced by the coil configuration thus obtained agrees with the ideal isochronous field within difference of less than 0.05 % as shown in Fig. 3.

The connections of the leads were designed and the specifications of power supplies for the trim coils were determined using Table 1. We have decided to use five types of power supplies (types A – E) according to widths of the setting current of each trim coil. The voltages and currents of each type of power supply are listed in

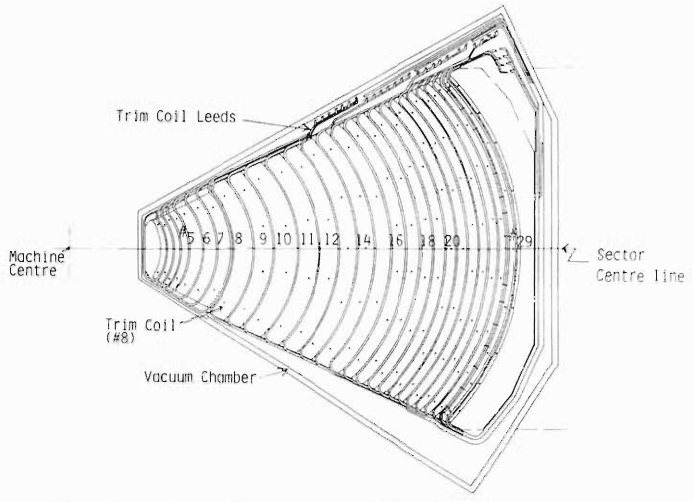

Fig. 2. Plan of the trim coils for the sector magnet.

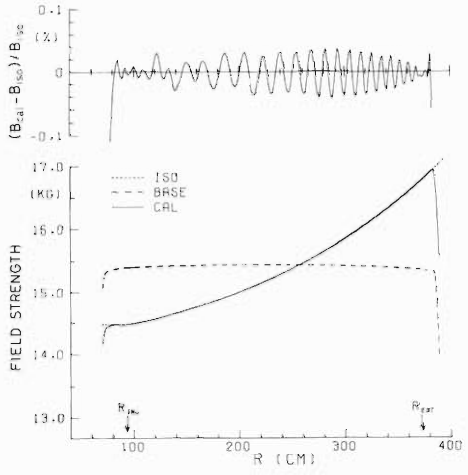

Fig. 3. Comparison of the magnetic field distribution formed by the trim coils with the isochronous field for acceleration of C^{6+} to 134 MeV/u.

Table 2. Specifications of five types fo power supplies for the trim coils of the four sector magnets. The number of total parameters to be set by computer is 71. Total power of the trim coils is estimated to be 192 kW.

Type		Min. ~ Max. Curr. (A)	Max. Volt.	Power (kW)	Bypass Curr. (A)	Number of blanchs	Number of P.S.	Total power (kW)
A	Bypass	50 ~ 500	205	103	30	7	1	103
B	control system	30 ~ 500	51	25.5	100	12	2	51
C	with	75 ~ 315	2.6	0.82		1	16	13.1
D	polarity	500 ~ 500	4	2.0		1	12	24
E	switch	100 ~ 70	0.9	0.1		1	12	1.2
Total					Parameters: 71			192

Table 2. The power supply of type A is used for the coils from No. 10 to No. 22. Coils No. 10 and No. 11, No 12, and No. 13, No. 14 and No. 15, No. 16, and No. 17, No. 18 and No. 19, No. 20, and No. 21 are each connected in series. Each of the above pairs and coil No. 22 are also connected in series through four sectors' trim coils, because the disturbance in the region from No. 8 to No. 22 coils due to the injection or extraction elements or the harmonic coils will be small enough. Furthermore, the differences of the currents between the adjacent pairs of these coils are less than 30 A. Therefore the currents of all these pairs are adjusted by a bypass control circuits as shown in Fig. 4. The number and the length of thick cables can be decreased in this method, resulting in an appreciable saving in power losses. This type of power supply has a transisterized regulator and a saturatable reactor.

One power supply of type B is used for coils No. 8, No. 9, and No. 29, and the other of type B for coils from No. 23 to No. 25. These coils are connected through bypass circuits in the same manner as in the case of type A power supply but are not in series through the four sectors' trim coils.

The other coils are excited by power supplies of types C, D and E with a polarity switch. They are connected to each power supply independently, because their currents differ by a large amount.

The currents are controlled by a computer with a 12 bits D/A converter using CAMAC system. The detailed specification of above power supplies will be written according to the results of field measurement for the real sector magnets and the trim coils.

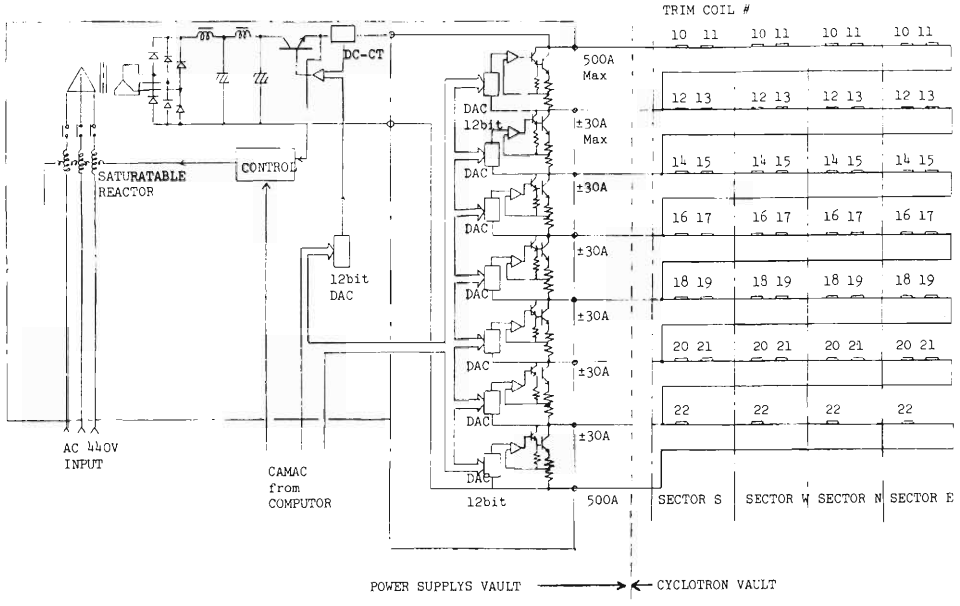

Fig. 4. Example of the schematic diagram of the trim coil power supply (type A) and electrical connection of the trim coil #10 to #22.

The trim coils will be made of 6 mm thick copper plates to which a 6 mm (t) × 12 mm (w) copper hollow conductor is welded partially by a TIG method, except for the coils No. 26 and No. 27 which consist of only hollow conductors. These hollow conductors are also used as return leads.

We decided to weld the hollow conductor to the inner side of the copper plate for the coils from No. 8 to No. 25, and No. 28 and No. 29, as a result of the model test measurement of a current distribution in the plate.[2] For the coils from No. 1 to No. 7, however, the hollow conductor is welded to the outer side of the plate because of the geometrical condition of the return lead. Each coil will be fixed to the pole face with specially made bolts.[6] The surface of the trim coil will be coated with aluminum oxide for insulation. The return lead will be taped with a Kapton sheet. The outgassing from these insulators does not pose serious problem because they are not installed in a high vacuum chamber but in a low (sub-) vacuum one.[6]

The trim coils are now under preparation by Sumitomo Heavy Industry Co., Ltd. and will be mounted on the sector magnets for the field measurement which will begin in the spring of 1982.

References

1) H. Takebe, S. Motonaga, T. Wada, J. Fujita, and K. Ogiwara: IPCR Cyclotron Progr. Rep., 13, 4 (1979).
2) H. Takebe, T. Wada, I. Takeshita, S. Motonaga, J. Fujita, and Y. Tanaka: p. 169 in this report.
3) A. Goto, H. Takebe, S. Motonaga, T. Wada, Y. Yano, N. Nakanishi, and Y. Tanaka: Reports I.P.C.R., (in Japanese), 56, 165 (1981).
4) J.S. Colonais and J.H. Porst: Magnet Design Applications of the Magnetostatics, call TRIM, UCRL-16382 (1965).
5) A. Goto, Y. Yano, and N. Nakanishi: p. 159 in this report.
6) S. Motonaga, H. Takebe, A. Goto, J. Fujita, T. Wada, Y. Oikawa, I. Takeshita, and Y. Ikegami: p. 162 in this report.

Ⅳ-22. Automatic Measuring System of Magnetic Field Distribution

J. Fujita, T. Wada, and H. Takebe

The LSI-11 microcomputer system mentioned before[1] is further expanded in its peripheral equipments and nearly full-automatic measurement of the magnetic field distribution is becoming possible. The latest system structure is shown in Fig. 1.

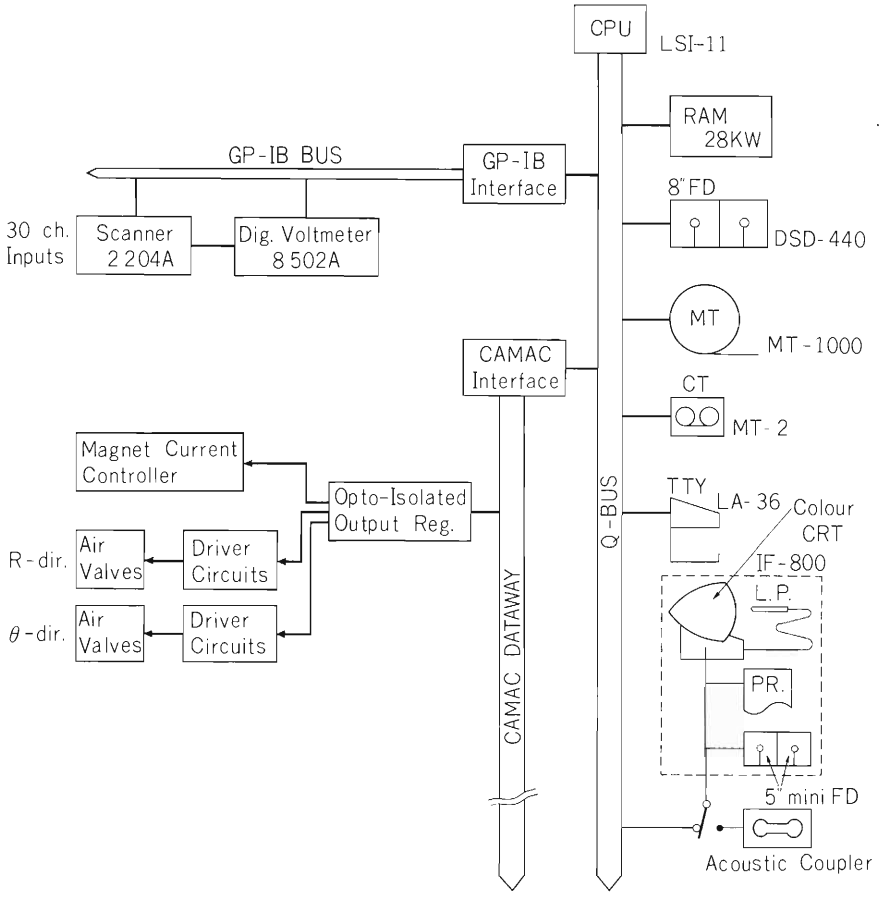

Fig. 1. Block diagram of automatic system for measurement of magnetic field distribution.

A Hall assembly, on which 20 elements are set in line to radial direction at an interval of 20 mm, measures the two dimensional field distribution by scanning both radial and azimuthal directions. It moves with mechanical stroke of a set of air cylinders actuated by the electromagnetic valves which are controlled by a CAMAC register. The output of the register is given via home made optical coupler to isolate noise. Position information of both directions is read into a 24 bits input register via rotary encoders.

A helical potentiometer which set an exciting current of magnet coils at each magnetic flux density is replaced by a digital-to-analogue converter (DAC). An output voltage of the DAC which is held in a thermally controlled oven has a temperature stability better than 10^{-4}/°C and is

controlled by two serial pulses of Up/Down and Clock from the above mentioned CAMAC output register.

Very small analogue voltages derived from 20 Hall elements, Pt-wire thermal sensors in the Hall assembly and a DC-CT transducer of the magnet coil current are multiplexed by a relay scanner FLUKE 2204A with 30 input channels and switching speed less than 14 msec, and measured by a digital voltmeter FLUKE 8502A. The scanner and voltmeter are serially connected on a common GP-IB bus.

A magnetic tape unit TEAC MT-1000 with a tape speed of 45 IPS and a record density of 1600 BPI is added to the LSI-11 bus in order to increase data storage capacity necessiated by progress of the automatic measuring system. A cassette tape unit with 15 IPS tape speed and 800 BPI record density can also be used.

An OKI IF-800 intelligent terminal is used for processing simple graphic demands and also serves as a tool for development of application programs. It can work also as a second terminal in the RT-11 multi-terminal monitor. The components of the IF-800 are 64 KB MOS RAM, dual 5 inch mini-floppy disks, a video display with graphic resolution of 200 X 640 dots, eight colour description and a light pen, and a keyboard printer. The IF-800 is connected to the LSI-11 by RS-232C serial lines. Signal transfer rate is selectable with a switch at 300 or 9600 Baud. The serial port in the IF-800 can be connected to a telephone via an acoustic coupler and make an exchange of data and programs with remote stations. The IF-800 is provided with BASIC and CP/M as operating system, and also utilities such as a screen editor and C-compiler which are developed by Dr. T. Soma of the Information Science Laboratory of our Institute to fit with the IF-800. The screen editor makes coding and change of source programs easy and speedy.

We are developing whole programs for various arrangements of measurement. The main part of the programs is written in FORTRAN and the remainders, especially for CAMAC modules, are written in Macro-assembly language as the subroutines of the FORTRAN programs. Those programs are expected to relieve one from the tedious work of measurements such as the watch of the instruments for hours.

Reference

1) J. Fujita, T. Wada, and H. Takebe: IPCR Cyclotron Progr. Rep., 14, 179 (1980).

Ⅳ-23. Beam Transport System for the RIKEN SSC (II)

Injecting Transfer Line

N. Kishida and Y. Yano

Construction of the separated sector cyclotron (SSC) is now in progress at RIKEN. As a result of the recent design work of the main building the position where the SSC is to be installed was altered from that given in a previous report.[1] Therefore the beam transport system between the SSC and preaccelerators (the heavy-ion linac already completed and the AVF cyclotron) has been reconsidered.

Layout of the accelerators is shown in Fig. 1. Their beam lines are not on the same horizontal

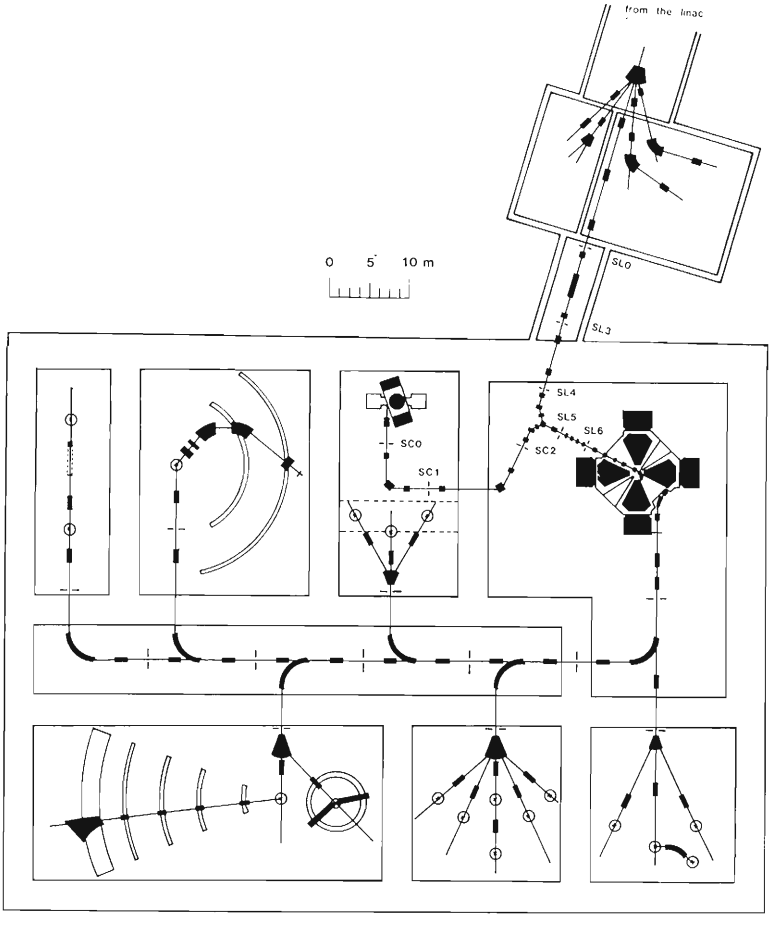

Fig. 1. The plan view of the beam transport system for the IPCR SSC. The beam levels of the SSC, the linac and the AVF cyclotron are not on the same horizontal plane. The median plane of the SSC is 12.5 m below the beam level of the linac and is 4 m below the median plane of the AVF cyclotron.

plane. The median plane of the SSC is to be 12.5 m below the beam level of the linac and 4.0 m below the median plane of the AVF cyclotron.

The perspective view of the redesigned beam transport system is shown in Fig. 2. Charge

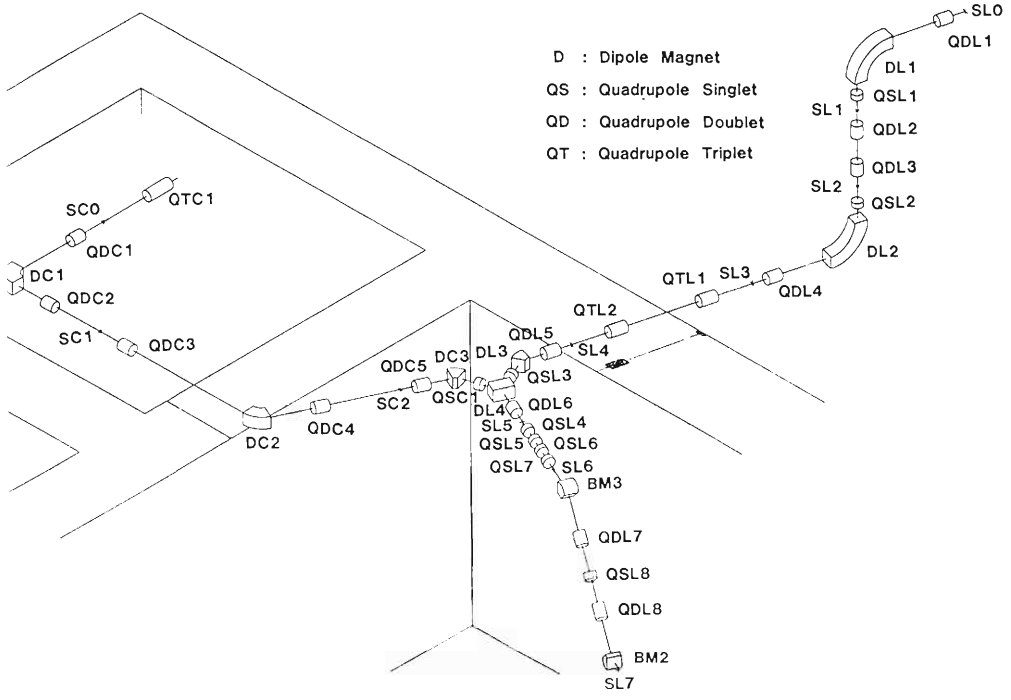

Fig. 2. Perspective view of the beam transport system between the linac and the SSC, and between the AVF cyclotron and the SSC. The vertical distance between SL0 and SL3 is 8.5 m and that between SL6 and SL7 is 4.0 m.

Table 1 (a). The beam matrices of the first- and second-order calculations for the system I at the beam injection point (TRANSPORT printout).

First-order						
0.0	0.285 CM					
0.0	2.154 MR	−0.002				
0.0	0.267 CM	−0.000	−0.000			
0.0	2.251 MR	−0.000	−0.000	−0.000		
0.0	3.004 CM	0.194	0.058	0.000	−0.000	
0.0	0.075 PC	0.214	0.000	−0.000	−0.000	0.909
Second-order						
0.057	0.296 CM					
0.111	2.177 MR	0.012				
0.006	0.267 CM	0.001	0.000			
0.041	2.644 MR	0.002	0.022	0.014		
−0.271	3.017 CM	0.161	0.058	−0.001	0.000	
0.0	0.075 PC	0.205	0.004	−0.000	0.001	0.905

Table 1 (b). The beam matrices of the first- and second-order calculations for the system II at the beam injection point (TRANSPORT printout).

First-order						
0.0	0.285 CM					
0.0	2.154 MR	−0.002				
0.0	0.267 CM	−0.000	0.000			
0.0	2.251 MR	−0.000	0.000	0.000		
0.0	3.995 CM	0.156	−0.078	−0.000	−0.000	
0.0	0.075 PC	0.214	−0.000	−0.000	−0.000	0.755
Second-order						
0.080	0.301 CM					
−0.526	2.238 MR	−0.055				
0.001	0.274 CM	0.001	−0.002			
0.000	2.756 MR	−0.002	−0.002	0.041		
−0.520	4.013 CM	0.141	−0.045	−0.000	−0.000	
0.0	0.075 PC	0.222	0.004	0.000	−0.000	0.752

stripping and charge selection parts are installed between SL0 and SL3 and between SC0 and SC1 to decrease the magnetic rigidity of preaccelerated ions and to increase the attainable maximum energy of the SSC. The transverse phase-space matching is performed in the section between SL5 and SL6, where the beam is achromatic. The dispersive beam from the AVF cyclotron is achromatized through the section between SC1 and SC2. In the following explanation we refer to the beam transport system from the linac (the AVF cyclotron) to the SSC as system I (system II).

The calculation of ion-optics in this system has been made to the second-order with the aid of the computer program TRANSPORT.[2] Table 1 presents the beam parameters (TRANSPORT outputs) at the beam injection point to the extent of the first- and second-order calculations for the system I and II. The ratios of the phase-space area of the first-order calculations to that of the second-order ones are tabulated in Table 2.

Table 2. The ratios of the phase-space area of the first-order calculations to that of the second-order ones for the system I and II at the beam injection point.

	On midplane	Off midplane
System I	1.05	1.17
System II	1.10	1.26

It is found that the first moments of the beams (centroid shift) are negligibly small. Furthermore the extents of the enlargements of the phase-space ellipses will give no troubles for the beam acceleration in the SSC.

The full discussion of this work has been published in Ref. 3.

References

1) N. Kishida, Y. Yano, and T. Wada: Sci. Papers I.P.C.R., 74, 105 (1980).
2) K.L. Brown, F. Rothacker, D.C. Carey, and C. Iselin: SLAC Report, No. 91, Rev. 1 (1974).
3) N. Kishida and Y. Yano: Sci. Papers I.P.C.R., 75, 214 (1981).

Ⅳ-24. Beam Extraction System for the RIKEN SSC (I)

N. Kishida, A. Goto, and Y. Yano

This report presents the layout of beam extraction system proposed on the basis of the calculated results for extraction trajectory orbit.

In designing the system, the following points were taken into account: (1) To realize single-turn extraction; (2) To extract the beam before crossing $\nu_r = 1$ resonance; (3) To use the extraction elements which can be manufactured without mechanical difficulty.

Heavy-ions and low-energy light-ions can be extracted by only RF acceleration. In the case of high energy light-ions, however, the separation of the beam on the extraction orbit from the beam on the last acceleration orbit is not sufficiently large for single-turn extraction. Therefore we use the first harmonic field perturbation to enlarge the beam separation in the extraction region and to realize the single-turn extraction for these ions. In this process we extract the beam before $\nu_r = 1$ resonance to avoid the strong radial defocusing of the extracted beam caused by the fringe field of the sector magnet. As for the detailed study on this procedure, see Ref. 1. The following two procedures were taken in determining arrangement of the extraction elements. Firstly, the extraction trajectory was calculated under the hard edge approximation of the magnetic field and no RF acceleration in such a way that the number of the elements and the power comsumption in each element could be minimized and that the beam separation enlarged. Secondly the extraction trajectory and the element arrangement were determined precisely using the numerical orbit calculation program EXTRACT,[2] where the realistic magnetic field was used and the first harmonic field perturbation was included. The beam which was traced numerically from the beam injection point was used as the beam entering into the extraction region in this calculation.

The extraction trajectory was investigated for 135 MeV/u $^{12}C^{6+}$ ion, since this has the highest magnetic and electric rigidity and the smallest beam separation and is, therefore, the most difficult to extract. The proposed extraction system consists of one electrostatic deflection channel (EDC), two magnetic deflection channels (MDC1 and MDC2) and two extraction bending magnets (EBM1 and EBM2). The layout of the extraction elements and their characteristics are shown in Fig. 1 and Table 1, respectively.

The beam width were estimated by tracing trajectories of five particles on six-dimensional phase-spaces using EXTRACT. Figure 2 shows the orbit separation between the extraction trajectory and the last acceleration trajectory. We then calculated the beam separation which is defined as the orbit separation minus the beam extents. The calculated separation gives sufficient space so that the extraction elements are expected to be safe from the heavy bombardment by the beam.

The maximum E.V. value of EDC was selected in such a way that spark-over will not occur. MDC's are composed of current septums and coils to self-compensate the field overshoot to the outside. EBM1 is the same type of magnet as BM1 used in a beam injection system.[3] A

window-frame type magnet without the outer return yoke is adopted as EBM2. Field optimization and mechanical design of each element is now in progress.

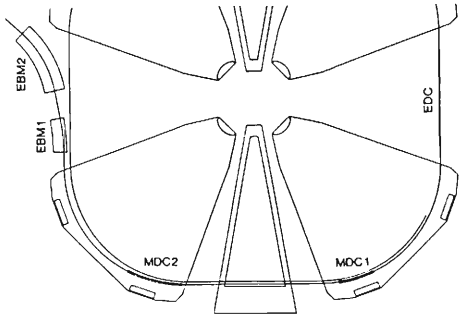

Fig. 1. Layout of the proposed extraction system together with the extraction orbit and the last acceleration orbit for 134 MeV/u $^{12}C^{6+}$ ion.

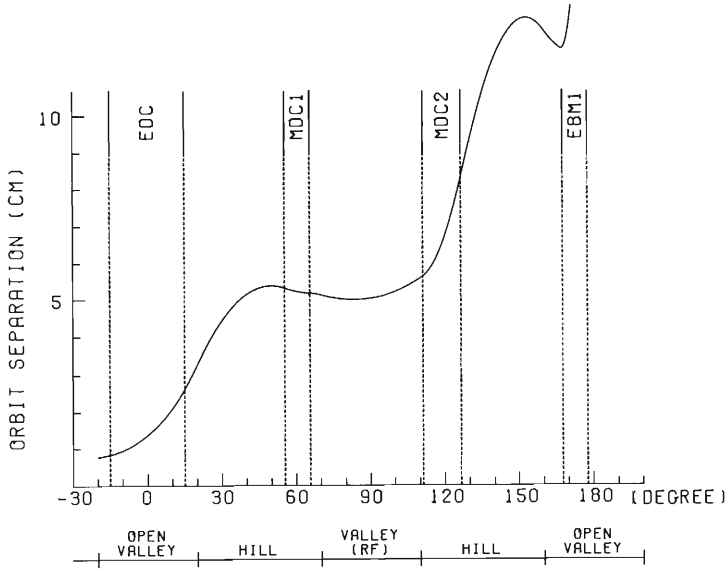

Fig. 2. Orbit separation between the extraction and the last acceleration orbits as a function of azimuthal position in the SSC.

Table 1. Characteristics of extraction elements.

Element	Bend angle (deg)	Aperture (cm) (H)	(V)	Radius (cm)	Maximum field	Face angle (deg) (entrance)	(exit)
EDC	0.79	2		linear	40 kV/cm		
MDC1	18	3	4	213	−0.5 kG	0	0
MDC2	25	3	4	230	−1.7 kG	0	0
EBM1	10	4	4.2	344	10 kG	0	0
EBM2	35	4	4	191	18 kG	0	0

References

1) A. Goto, Y. Yano, and N. Nakanishi: Sci. Papers I.P.C.R., 75, 204 (1981).
2) A. Goto: Reports I.P.C.R., (in Japanese), 57, 203 (1981).
3) Y. Yano, H. Takebe, S. Motonaga, T. Wada, J. Fujita, and A. Goto: Sci. Papers I.P.C.R., 75, 176 (1981).

Ⅳ-25. Model Study of Magnetic Inflection Channel for the SSC

H. Takebe, Y. Yano, S. Motonaga, T. Wada,
J. Fujita, Y. Ikegami, and M. Hosoyama

A couple of magnetic inflection channels (MIC1 and MIC2), which are used as the beam injection elements for the SSC, are inserted into a 50 mm available gap between the sector magnet poles.[1] They have to give field increases in ratios (A_0) of 8 % (MIC1) and 23 % (MIC2), respectively, to the sector field. They have not to give a large disturbance to the sector field.

A basic design of the MIC was made by using a computer code Trim.[2] We constructed a straight-shaped 1/1-scale model and tested it in the gap of an H-type magnet, which was a 1/3-scale model of the present 160 cm ordinary type cyclotron. The gap length was modified to 80 mm from 87 mm by placing a 7 mm thick iron plate on the lower pole.

A photograph of a top view of the model MIC is shown in Fig. 1, and a cross sectional view in Fig. 2. The iron shims are replaceable and their thickness can be selected to be 1 mm, 3 mm, and 5 mm. Four turns of the coils are divided into two pairs, each of which has two turns. The inner two turns compose coil A and the outer ones coil B. The compensation coil of four turns are wound on the left side of the MIC. The coils and iron shims are contained in a brass coil holder.

The coils are made of a 9 mm × 9 mm copper hollow conductor which has a water path of 6 mm in diameter. At the maximum current of 3 kA, the flow rate of cooling water amounts up to about 10 ℓ/min to keep the coil temperature at a moderate value. The conductors are insulated by Kapton film.

The magnetic field was measured by Hall generators of BHT-910 series (F.W. Bell Inc.). Three Hall generators were placed at intervals of 6 mm on a Hall assembly, as is shown in Fig. 3. As the temperature of the

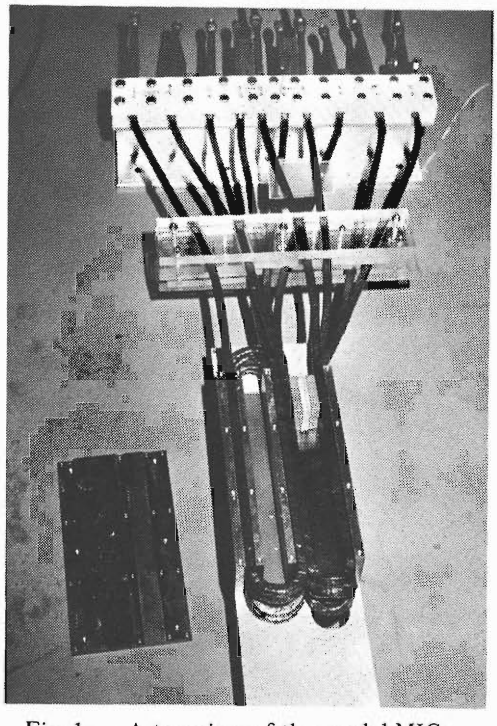

Fig. 1. A top view of the model MIC, which has a straight shape of 230 mm in length. The MIC coils are wound on the right side.

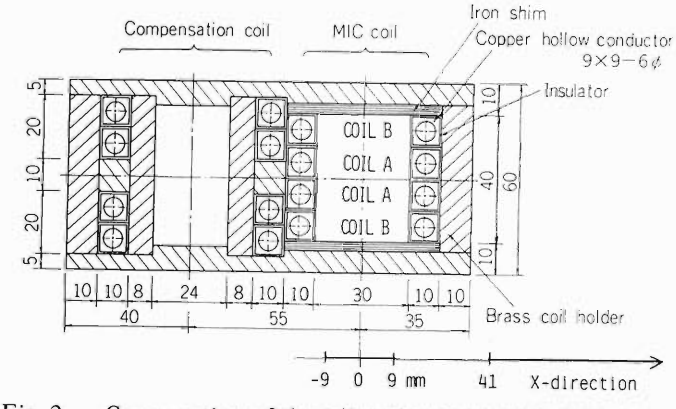

Fig. 2. Cross section of the 1/1-scale model MIC; dimensions in mm. Middle two turns of the MIC coils compose coil A, and top and bottom ones coil B.

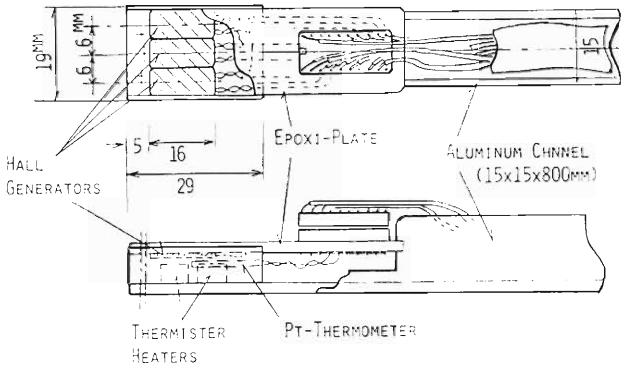

Fig. 3. Hall assembly mounted on a 15 mm X 15 mm aluminum channel. Three Hall generators (BHT-910) are placed at intervals of 6 mm with thermister heaters and a Pt-thermometer.

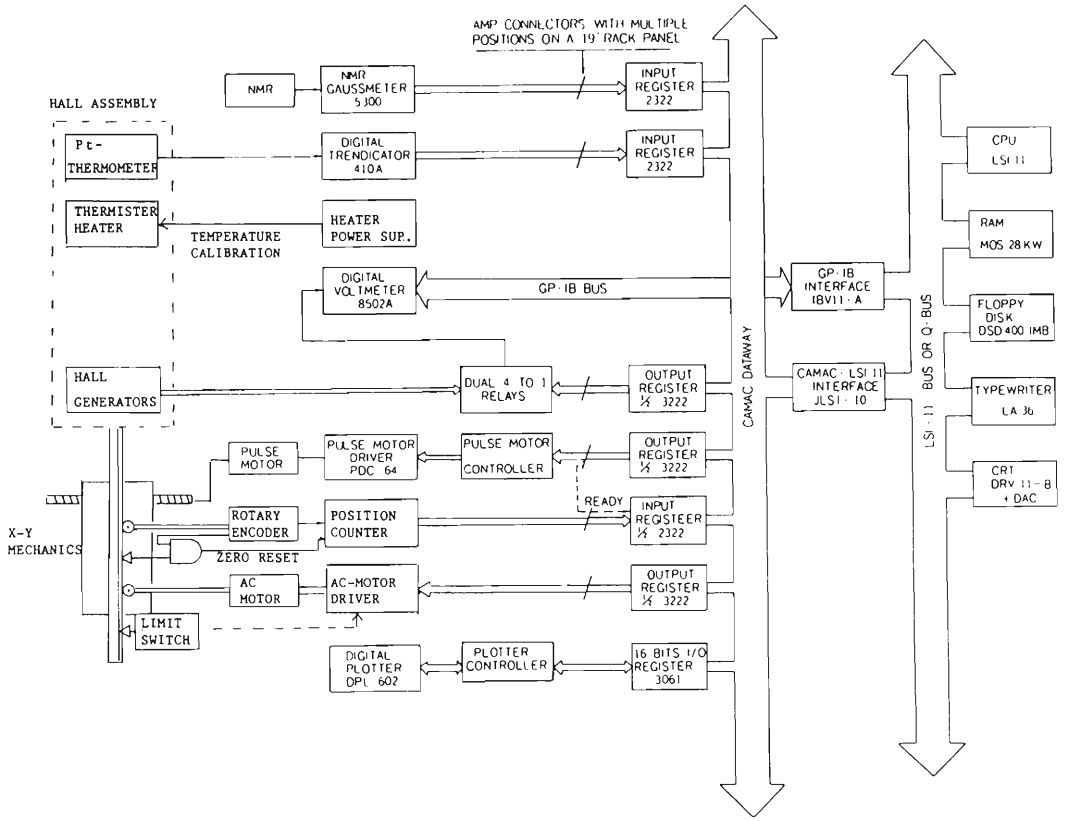

Fig. 4. Block diagram of the field measuring system. Measuring procedure except for setting a coil current is automatically controlled by the computer LSI-11.

Hall generators was not kept constant, we corrected the measured Hall output taking account of its temperature dependence, to obtain an accurate magnetic field strength.[3] Error of the measurement was within $\pm 1.5 \times 10^{-4}$ in relative value and $\pm 3 \times 10^{-4}$ in absolute value.

Figure 4 shows a block diagram of the measuring system. All the measuring procedure except for setting the coil current was done automatically by the computer (LSI-11).

Figure 5 shows some examples of measured field distributions inside the MIC at different currents. In order to obtain multipole components of these field distributions, the data were fitted to the following biquadrupole polynominal:

$$B_{MIC} = B_{base} \left\{ 1 + A_0 \left(1 + A_1 X + A_2 X^2 + A_3 X^3 + A_4 X^4 \right) \right\}$$

by using a least-squares method, where X indicates a transverse position from the MIC centre, in cm unit.

Figures 6 and 7 show examples of the field increase ratio, A_0, and sextupole component ϵ which is given by

$$\epsilon = A_0 A_2 / (A_0 + 1) \cdot$$

Data were obtained at the base field of 16 kG for the iron shim thickness of 5 mm (a), 3 mm (b), and 1 mm (c).

Results obtained when the coil A was used are shown in Fig. 6, and those with the coils A and B connected in series in Fig. 7. This latter arrangement will be called coil A & B. As shown in Fig. 6 (b), the sextupole component becomes zero at the current of 850 A, and A_0 is given as 9.3 %.

The sextupole component of the value within $\pm 1 \times 10^{-3}$ was supposed to be permissible for the ion-optical property of the beam.[4] Table 1 shows the field increase ratios (A_0) and the currents when the sextupole component is $+1 \times 10^{-3}$ and -1×10^{-3}. An available field increase ratio for each base field is shown in Fig. 8. The thick solid line indicates the maximum coil current for uniform MIC field. From this figure, we can conclude as follows:

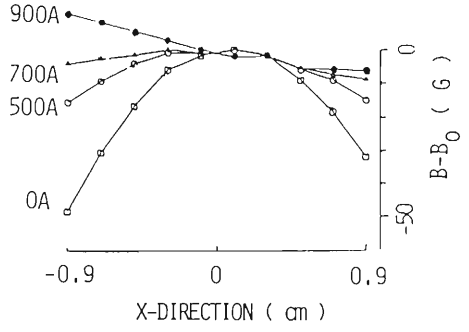

Fig. 5. Typical example of transverse field distributions inside the MIC at different current of the coil A. The iron shim of 3 mm in thickness was used. The base field was set to be 16 kG.

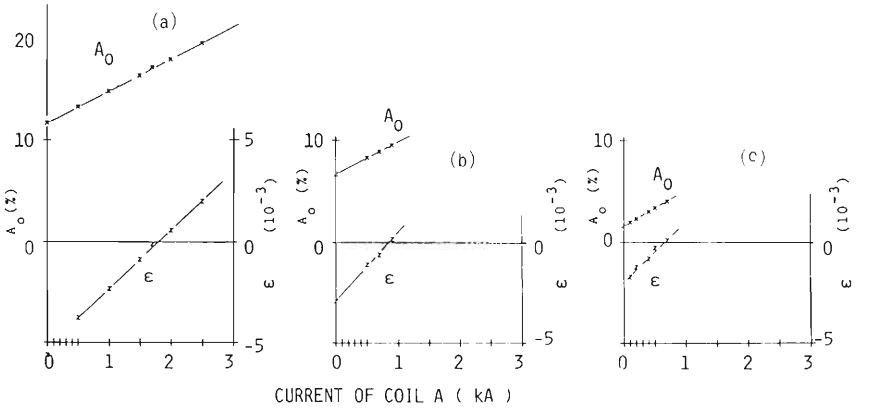

Fig. 6. Change of field increase ratio (A_0) and sextupole component (ϵ) with current of the coil A. Data was obtained at the base field of 16 kG for the iron shims of three different thickness: 5 mm (a), 3 mm (b), and 1 mm (c).

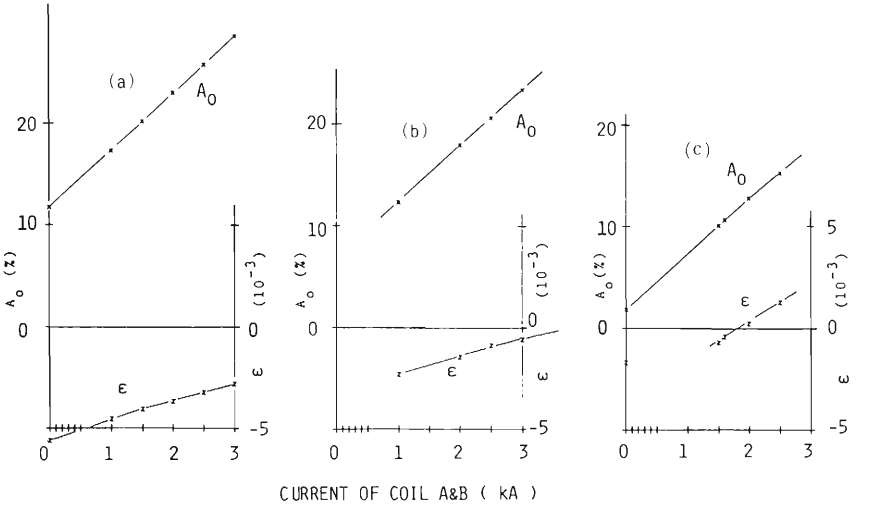

Fig. 7. Change of field increase ratio (A_0) and sextupole component (ϵ) with current of the coil A & B. Data was obtained at the base field of 16 kG.

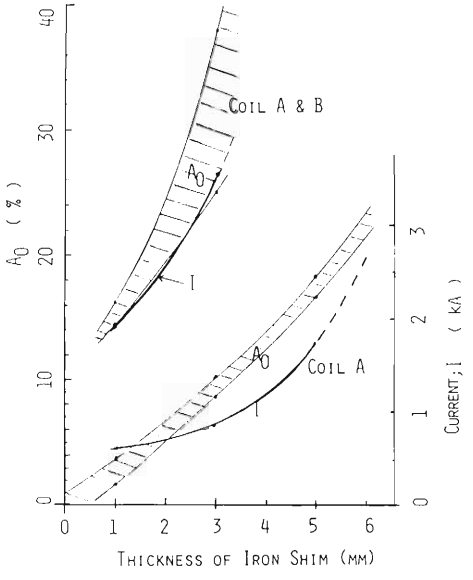

Fig. 8. Field increase ratio (A_0) corresponding to the case of $\epsilon = \pm 1 \times 10^{-3}$ at different base-field strengths (B_{base}). Data were obtained for coil A (a) and coil A & B (b). The shaded region indicates the values of A_0 which can be changed independently of the base field under the condition of $-1 \times 10^{-3} < \epsilon < 1 \times 10^{-3}$.

Table 1. Field increase ratios corresponding to the case of $\epsilon = +10^{-3}$ and -10^{-3}.

Coil A

Base (kG) \ Iron shim	ϵ	5mm $+1 \times 10^{-3}$	5mm -1×10^{-3}	3mm $+1 \times 10^{-3}$	3mm -1×10^{-3}	1mm $+1 \times 10^{-3}$	1mm -1×10^{-3}
6.209		18.5%	16.2	10.4	8.4	3.8	1.8
		660A	390A	380A	150A	230A	0A
10.022		19.1	16.7	10.7	8.6	5.0	1.8
		1200A	770A	670A	270A	580A	0A
12.924		19.0	16.6	10.7	8.5	4.8	2.3
		1600A	1000A	880A	330A	680A	90A
16.017		18.4	16.3	10.2	8.4	5.0	2.7
		2150A	1450A	1150A	550A	950A	300A

Coil A & B

Base (kG) \ Iron shim	ϵ	3mm $+1 \times 10^{-3}$	3mm 0.0	3mm -1×10^{-3}	1mm $+1 \times 10^{-3}$	1mm -1×10^{-3}
6.209			38.0%	19.4	31.7	6.8
			2000A	760A	2000A	330A
10.022			(38.2)	25.2	23.0	13.4
			3400A	1940A	2300A	1220A
12.924		(38.7)	30.8	22.5	19.0	12.4
		3900A	2800A	1660A	2400A	1450A
16.017		(37)	(28.5)	20.0	14.5	9.3
		5500A	3700A	2400A	2350A	1320A

The MIC1 should be composed of 2.6 mm thick iron shim and the coil A in order to get the field increase ratio of 8 %. The optimum current at base field of 16 kG is estimated to be 800 A.

On the other hand, MIC2 needs the field increase ratio of 23 %. Then it is necessary to use a 6 mm thick iron shim and the coil A. The maximum current is estimated to be about 2800 A. However it is also possible to use a 2.2 mm thick iron shim and the coil A & B. The maximum current is estimated to be of a similar value. The ampere-turns for the latter is twice as large as those for the former.

A disturbance outside the MIC and an effective field boundary change of the MIC are discribed elsewhere.[5)]

References

1) A. Goto, Y. Yano, T. Wada, and N. Nakanishi: Sci. Papers I.P.C.R., 74, 124 (1980).
2) J.S. Colonais and J.H. Porst: Magnet Design Applications of the Magnetostatic Problem, called TRIM UCRL-16382 (1965).
3) H. Takebe, Y. Yano, T. Wada, J. Fujita, Y. Obana, and S. Motonaga: IPCR Cyclotron Progr. Rep., 14, 176 (1980).
4) Y. Yano: Sci. Papers I.P.C.R., 74, 13 (1980).
5) H. Takebe, Y. Yano, S. Motonaga, T. Wada, J. Fujita, and Y. Ikegami: ibid., 75, 193 (1981).

Ⅳ-26. Calculation of RF Electromagnetic Field by Finite Element Method

M. Hara, T. Wada, and F. Kikuchi

In designing the RF resonators for accelerators, it is usual to evaluate RF characteristics on the basis of transmission line approximation or to depend on the experiments with scale models. Because the transmission line approximation is essentially one dimensional one, it is not useful to estimate the field distribution along the accelerating gap and to estimate the microscopic current density. In the model studies, it takes long time and requires large expense to build models.

In order to get a detailed analysis, we are now developing a computer code to calculate the electromagnetic field in an arbitrary three dimensional cavity resonator. As a first step we have developed two computer codes to evaluate the resonance frequency, electromagnetic field and other pertinent quantities by solving directly the Maxwell equations using finite element method.[1] One is for the field in a straight resonator with arbitrary cross section (H2DB) and the other for the axisymmetric field (HAX). In the former, scalar Helmholtz equation

$$\Delta^2 V + k^2 V = 0$$

is solved with Dirichlet and/or Neumann boundary conditions. In the latter, axisymmetric Helmholtz equation

$$\frac{\partial}{\partial r}\frac{1}{r}\frac{\partial}{\partial r}(rH_\theta) + \frac{\partial^2 H_\theta}{\partial z^2} + k^2 H_\theta = 0$$

is solved with Dirichlet and/or Neumann boundary conditions. In both cases, these equations reduce to the eigenvalue problems and both E and H modes can be treated. Resonance frequencies can be obtained from the eigenvalues, and the electromagnetic fields can be obtained from the eigenvectors or the derivatives of the eigenvectors. Several automatic mesh generation programs (MESH2D) are also developed for several typical problems. Using plot program (H2DPLOT), calculated results are displayed by the lines of electric or magnetic force. These codes, H2DB and HAX, are checked by calculating simple cases which can be solved analytically. For the axisymmetric case, calculated results by HAX are also compared with those by SUPERFISH.[2] As for the resonance frequency and the pattern of the lines of electric force, sufficient agreement is confirmed between HAX and SUPERFISH. The computation time by the code HAX was shorter than that by the code SUPERFISH.

Figure 1 shows the calculated results for single gap type resonator for the RIKEN SSC. Cut-off frequency and the RF electric field distribution along the accelerating gap are shown.

Recently, radio frequency quadrupole (RFQ) linear accelerator has attached much attention because of new focusing, bunching and accelerating structure. Model tests for the RFQ linac resonator were done at the Institute for Nuclear Study,[3] and we calculated the resonance frequencies and the lines of electric force. Figure 2 shows the results.

Alvarez type linac resonator was also investigated and the results are shown in Fig. 3.

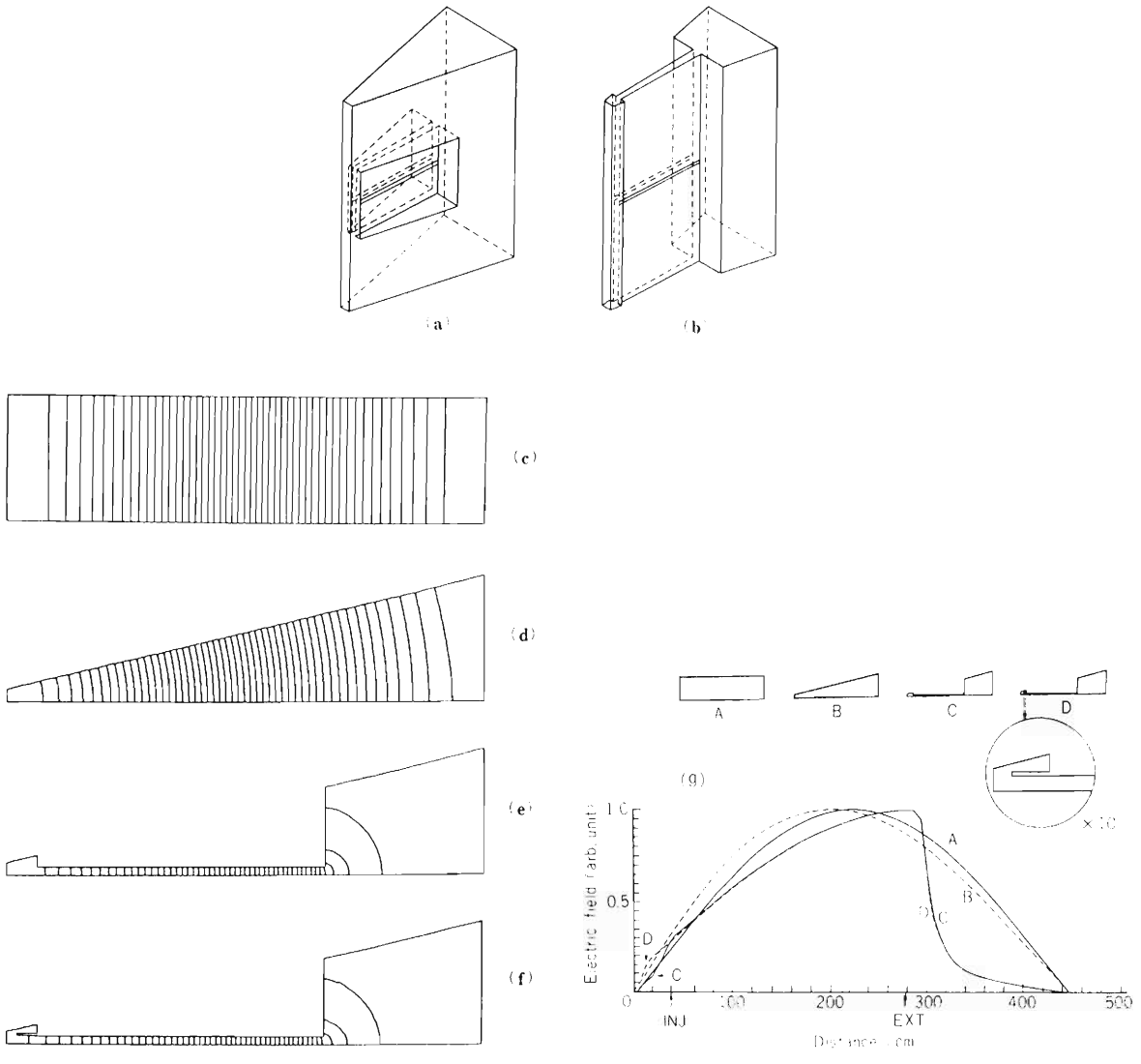

Fig. 1. Calculations for single gap resonators. These calculations are done using straight resonator model. Only half of the region is analyzed because of the symmetry condition.

(a) Schematic drawing of the single gap resonator designed for the RIKEN SSC.

(b) The straight resonator model by which fields are calculated.

(c) Rectangular model. Lines of electric force on the median plane are shown. NP = 1891 (number of nodal points), T_{cpu} = 127 s (CPU time)/5 modes (FACOM M200), f_{1c} = 33.332 MHz.

(d) Trapezoid model. Lines of electric force on the median plane are shown. NP = 1891, T_{cpu} = 111 s/5 modes, f_{1c} = 37.283 MHz.

(e) The model of the single gap resonator for the RIKEN SSC. NP = 1211, T_{cpu} = 56.8 s/5 modes, f_{1c} = 23.817 MHz.

(f) The same model as in (e) with vane attached. NP = 517, T_{cpu} = 22.4 s/5 modes, f_{1c} = 23.360 MHz.

(g) RF electric field distributions along the accelerating gap for the above models. Each distribution is normalized at maximum.

Cut-off frequencies decrease from model (d) to (f). Electric field at the injection radius increases from (c) to (d). Vane effects are the lowering of the cut-off frequency and the increase of the electric field near the vane.

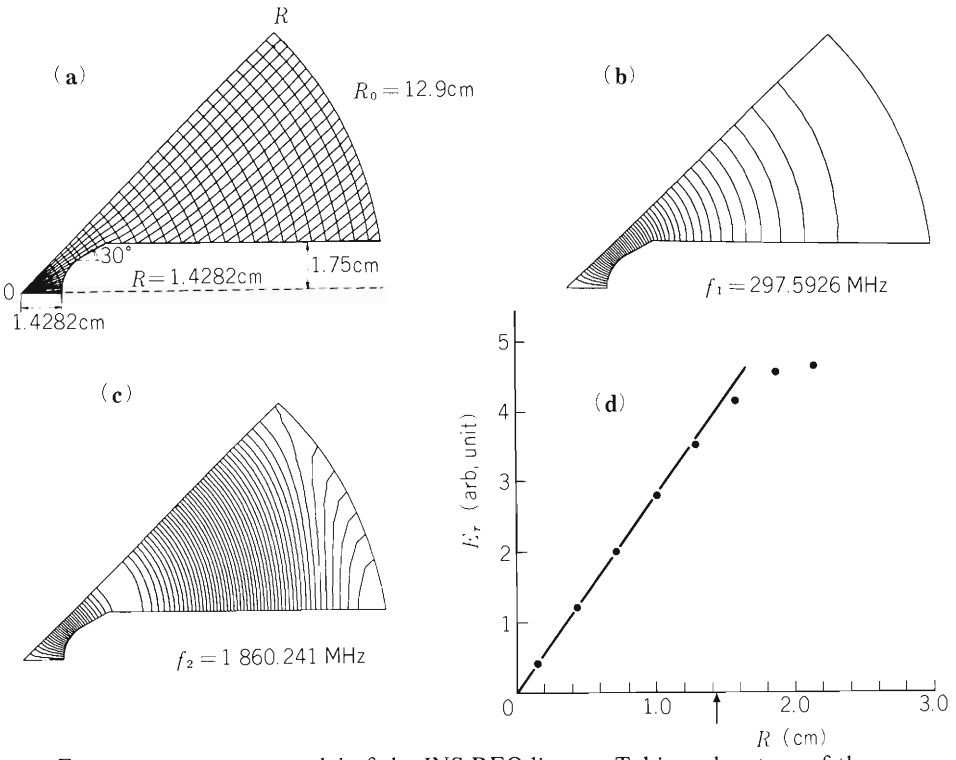

Fig. 2. Four vane resonator model of the INS RFQ linac. Taking advantage of the symmetry, only an octant region is analyzed.

(a) Subdivisions. The numbers of nodal points and elements are 428 and 409, respectively.

(b) Lines of electric force shown for H_{210} mode. Computation time is 45 s for five modes.

(c) The same for H_{220} mode.

(d) Calculated electric field distribution along the line OR in (a).

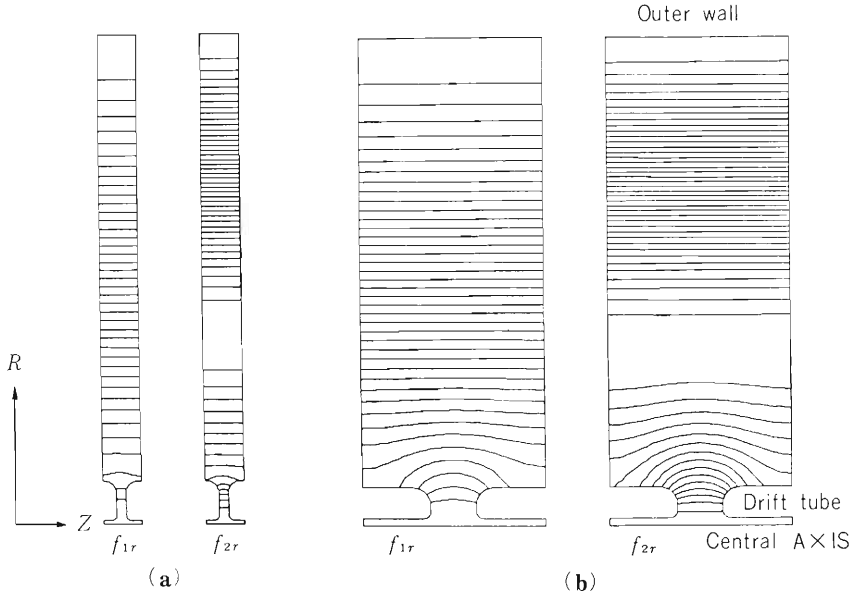

Fig. 3. Alvarez linac resonator

(a) Calculated lines of electric force for the first cell. The outer radius is 50 cm in length. $f_{1r} = 219.89$ MHz, $f_{2r} = 484.28$ MHz.

(b) Calculated lines of electric force for the last cell. The outer radius is 49.38 cm. $f_{1r} = 219.89$ MHz, $f_{2r} = 471.32$ MHz.

References

1) M. Hara, T. Wada, A. Toyama, and F. Kikuchi: Sci. Papers I.P.C.R., 75, 143 (1981).

2) K. Halbach and R. Holsinger: Particle Accelerators, 7, 213 (1976).

3) N. Tokuda, T. Nakanishi, N. Ueda, S. Arai, T. Katayama, and A. Noda: IEEE Trans. on N.S., NS-28, 3510 (1981).

Ⅳ-27. Model Study of RF Resonator for the RIKEN SSC

K. Ogiwara, M. Hara, and T. Fujisawa

The resonator for the RIKEN SSC is required to work in the frequency range of 17 to 45 MHz at the voltage of 250 kV (Maximum). In this resonator, the radial distribution of dee voltage is desired to be constant or radially increasing in order to realize good beam quality. The radial length of the accelerating gap should be more than 2.6 m corresponding to injection and extraction radii. In order to find the best structure of the resonator that satisfies the above conditions, calculations with transmission line approximation were carried out for half wave-length type resonator. From the calculations, it was found that the resonator satisfies the above conditions. On the basis of these calculations, a half scale model was constructed and the resonance frequencies, Q-values and radial distributions of RF electric field at the accelerating gap were measured.[1] To realize good radial distribution of RF electric field at the accelerating gap and also to make the size of the resonator small, earth panels were attached in the model resonator. Figure 1 shows the schematic view of the earth panels inside the model resonator. The resonance frequencies, Q-values and the radial distributions of RF electric field at the accelerating gap were measured.

Figure 2 shows the radial distributions of RF electric field at the accelerating gap measured by perturbation method.[2] Fairly good radial distributions were obtained at low frequencies (less than 50 MHz for the model) when the earth panels were used.

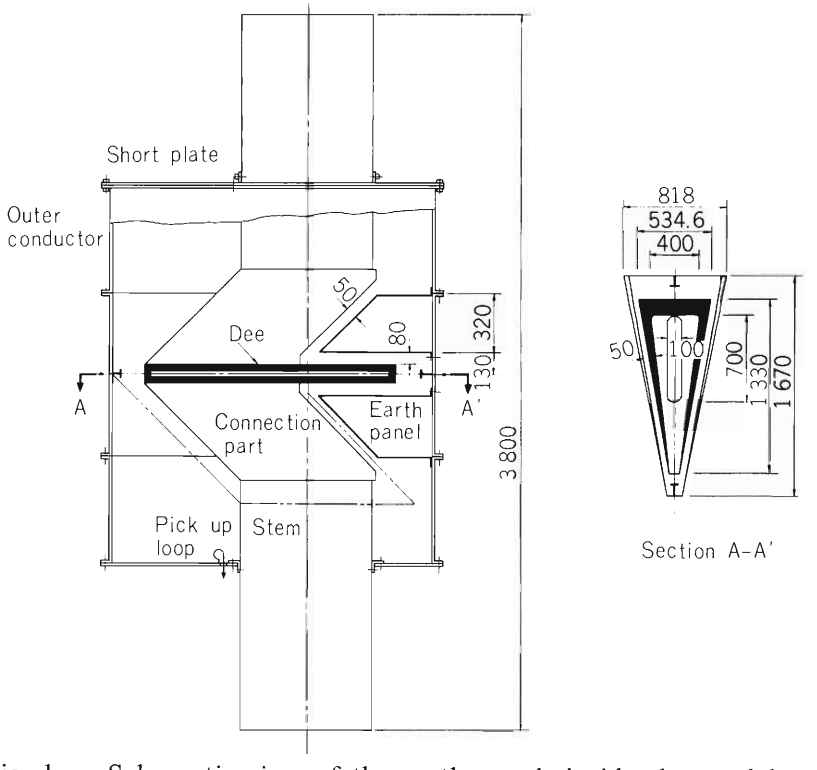

Fig. 1. Schematic view of the earth panels inside the model resonator. The earth panels were made of 0.3 mm-thick copper plates.

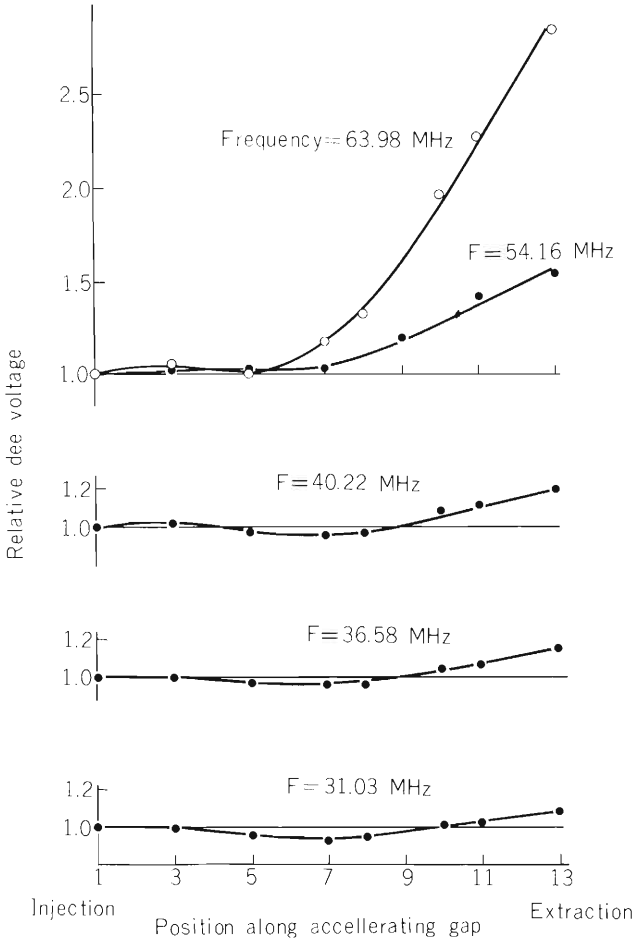

Fig. 2. Relative distributions of RF electric field along the accelerating gap for the model resonator which uses the earth panels. The distribution of the electric field at the extraction radius were improved.

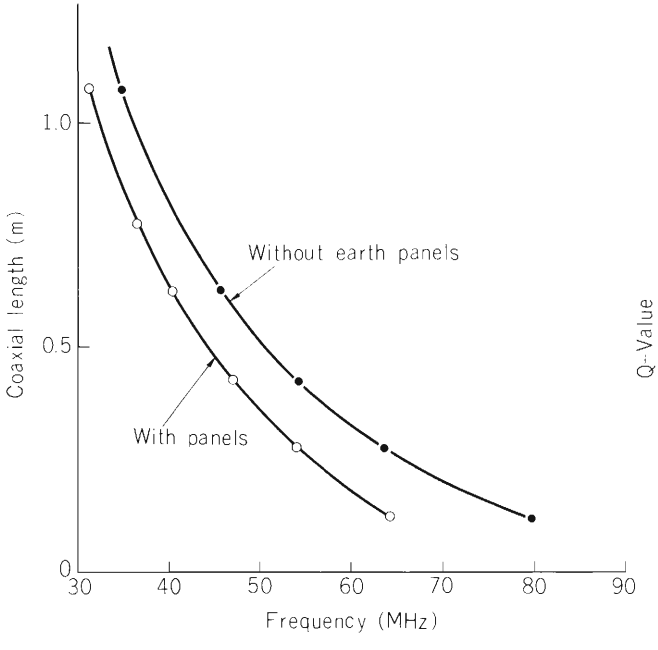

Fig. 3. Measured stem length.

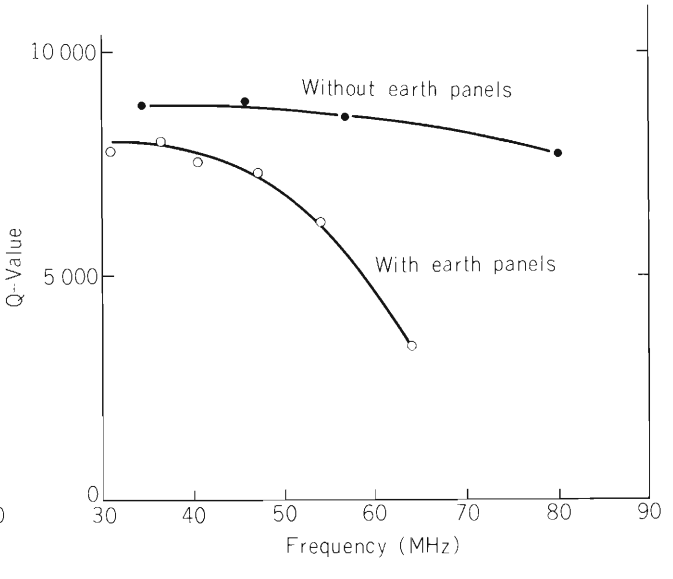

Fig. 4. Measured Q-values.

Figure 3 shows the stem length as a function of radio frequency. The stem length could be reduced by about 40 cm in this model by using the earth panels. This is equal to the 80 cm reduction in full-scale resonator.

Figure 4 shows the frequency dependence of the Q-values. The Q-value has maximum value at the lowest frequency when the earth panels are used and makes slow decrease as the frequency increases as shown in Fig. 4. From the result of these measurement, it was found that a half-wave type resonator using the movable shorting plates along with movable earth panels for frequency variation is desirable.

References

1) M. Hara, K. Ogiwara, and T. Fujisawa: IPCR Cyclotron Progr. Rep., 14, 182 (1980).
2) L.C. Maier, Jr. and J.C. Slater: J. Appl. Phys., 23, 68 (1952).

Ⅳ-28. New Method to Vary Resonant Frequency of Resonator for SSC

T. Fujisawa

The resonator for the IPCR SSC has been designed and the results of study by a model have been reported previously.[1] The resonator designed, however, has some disadvantages as follows:

1) The height of the resonator is very high (7 m).

2) The distance which the shorting plate must travel is long (2 m). Consequently, the total length of resonator including the mechanism to move the shorting plate becomes more than 11 m.

3) The maximum current density at the contact fingers of the shorting plate is estimated to be 70 A/cm at V_{dee} (voltage of dee) = 250 kV for 45 MHz. It is difficult to fabricate the fingers which endure such high current density.

Therefore, a new method to vary the resonant frequency is investigated. In Fig. 1, the new type resonator is shown. The resonant frequency is varied from 17 MHz to 45 MHz by moving the "movable box". The box does not make contact with the stem but contact only with the outer wall.

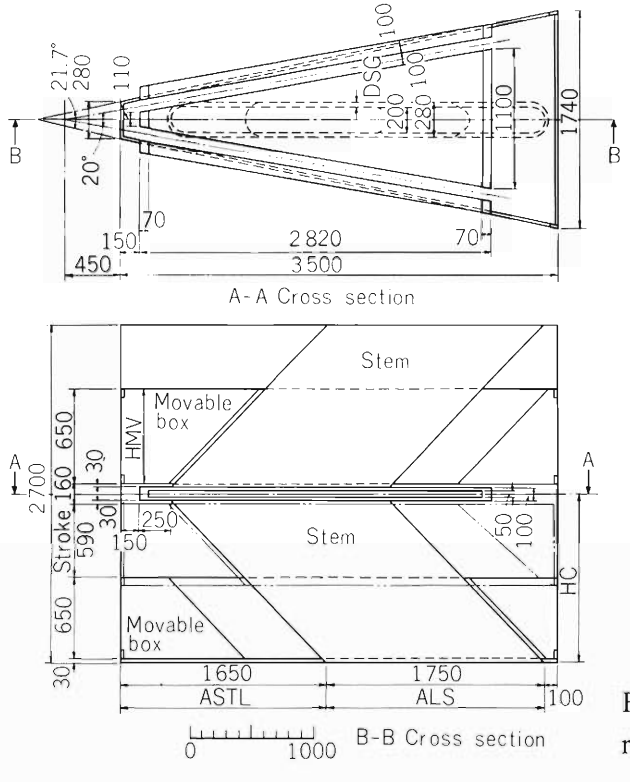

Fig. 1. Schematic view of the new type resonator.

The gap between the stem and box is 4 cm. This resonator has following merits:

1) The height is less than 3 m.

2) The distance which the box is moved is short (0.6 m).

3) The contact fingers are not at the location where the current density is maximum.

Figures 2 and 3 show the characteristics of the resonator calculated by the transmission line approximation. As shown in Fig. 2, the power loss at low frequency for V_{dee} = 250 kV is too high to realize this cavity. The dotted line in Fig. 2 shows the power loss assuming that the required dee voltage is proportional to the resonant frequency. In this case the power loss is not so high. This cavity can be used if high voltage such as 250 kV is not necessary at low frequencies.

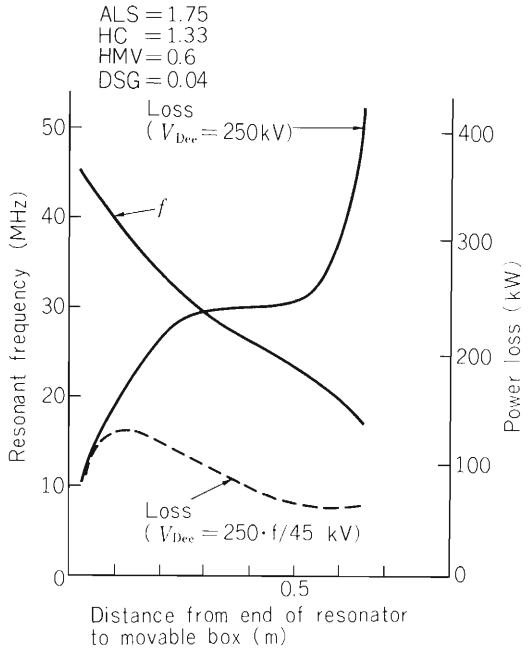

Fig. 2. Resonant frequency (f) and power loss calculated by the transmission line approximation. Parameters, ALS, HC, HMV, and DSG are shown in Fig. 1. The values of these parameters were determined to give the best characteristics of the resonator. The power loss is calculated at V_{dee} = 250 kV (real line) and V_{dee} = 250·f/45 kV (dotted line).

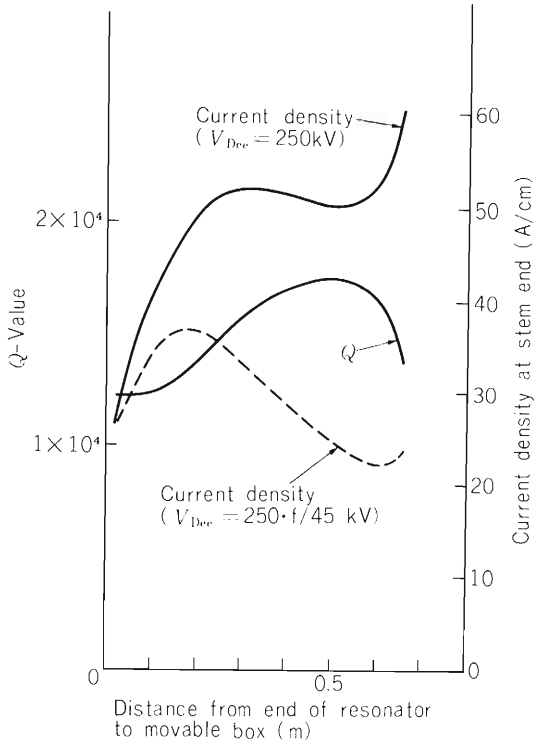

Fig. 3. Q-value and maximum current density at the stem end. See the caption of Fig. 2.

Reference

1) M. Hara, T. Fujisawa, and K. Ogiwara: Proc. 9th Intern. Conf. on Cyclotron and their Applications, Caen, Sept. (1981).

Ⅳ-29. Vacuum System of the SSC (I)

S. Nakajima, K. Ikegami, Y. Oikawa, and I. Takeshita

Design of the acceleration chamber of the IPCR SSC was changed from that previously reported.[1] The volume of the newly designed chamber[2] is approximately 65 m^3. The surface area exposed to the vacuum is about 750 m^2, whose composition is as follows:

Materials	Surface area
Stainless steel	~ 300 m^2
Copper	~ 440 m^2
Elastomer	~ 5 m^2
Total	~ 750 m^2

Pumping system for this chamber must satisfy following requirements:

1) Operating pressure $< 1 \times 10^{-7}$ Torr
2) Time allowed for roughing ~ 1 h
3) Time allowed to achieve operating pressure ~ 20 h.

The quantity of gas released from inner walls depends on quality and treatments of the surface materials. It will be $7 \sim 16 \times 10^{-3}$ Torr·ℓ/sec after 20 h pumping as is shown in Fig. 1.

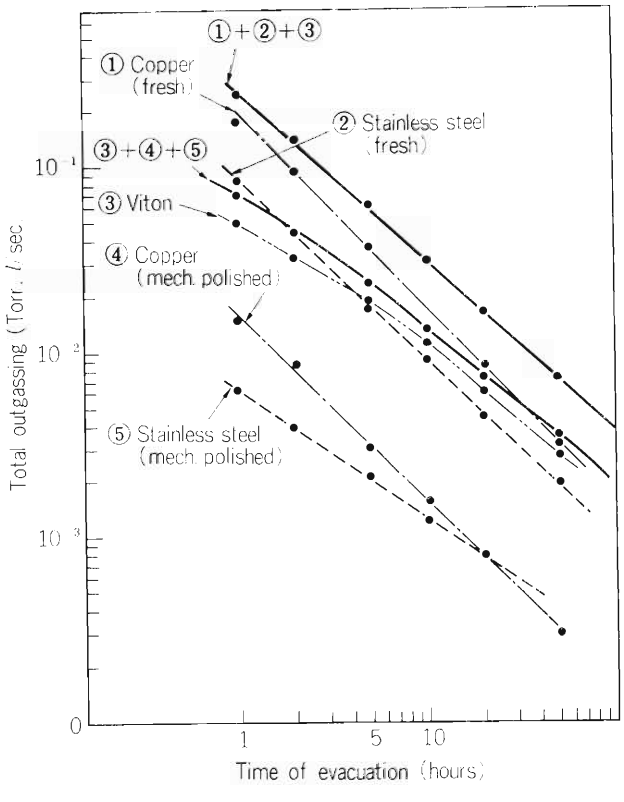

Fig. 1. The estimated total outgassing from materials of inner walls of the chamber. The outgassing from any other materials or components within the chamber is not included. Outgassing rates were obtained from the "vacuum Handbook" published by ULVAC corporation.

In addition, there is a gas load of $\sim 3 \times 10^{-3}$ Torr·ℓ/sec caused by the evolution of gas from various components within the chamber and the permeation of gas through the sealing elastomers. Therefore, an effective pumping speed of 11×10^{4} ℓ/sec, at least, is required to achieve a pressure lower than 1×10^{-7} Torr in the chamber. A combination of cryo-pumps and turbo-molecular pumps seems suitable for the pumping system to realize this condition. These pumps will be located in each valley chamber, in each RF resonator and in each space between the main magnet and the RF resonator. The coarse pumping will be done by four roughing pump units. Each of them is consisted of a rotary pump and a roots pump. Two of the units evacuate the RF resonators and the others evacuate both the valley chambers and the sub-vacuum chambers. A back up pumping system will be also necessary when one of the roughing units is not operational. An example of layout of the vacuum system is shown in Fig. 2.

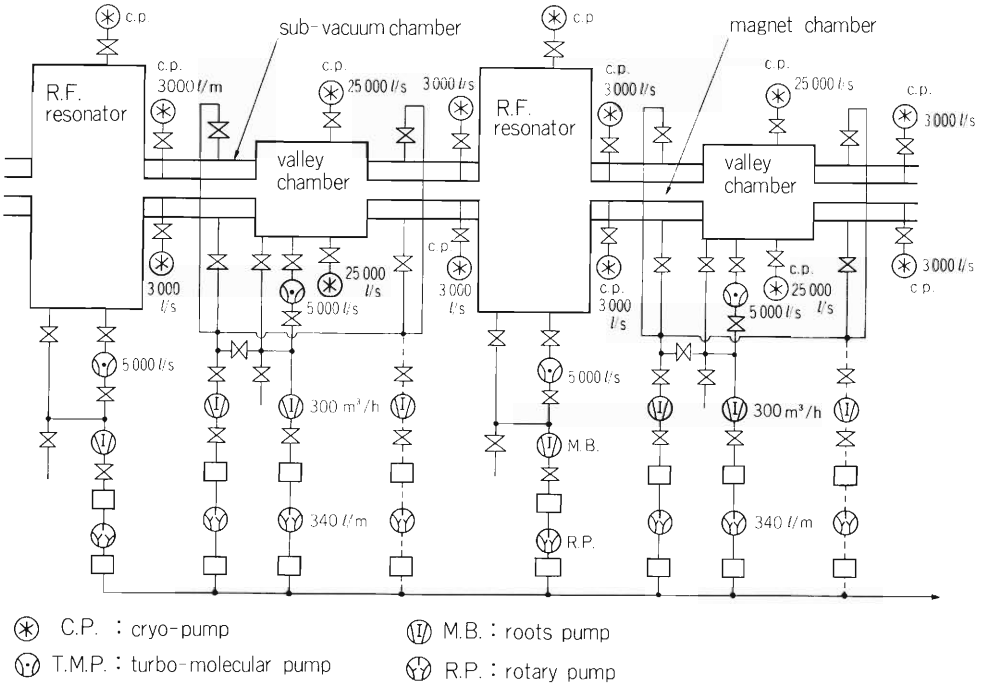

Fig. 2. Schematic drawing of a possible vacuum system.

References

1) K. Ikegami, S. Nakajima, and Y. Ikegami: IPCR Cyclotron Progr. Rep., 14, 198 (1980).
2) K. Ikegami, S. Nakajima, Y. Oikawa, and I. Takeshita: p. 200 in this report.
3) S. Nakajima and K. Ikegami: IPCR Cyclotron Progr. Rep., 14, 195 (1980).

Ⅳ-30. Vacuum System of the SSC (II)

K. Ikegami, S. Nakajima, Y. Oikawa, and I. Takeshita

(1) Vacuum chamber for the SSC

The design of the vacuum chamber for the SSC was changed from the monolithic structure[1] to the structure divided into 8 sections. One reason is that the RF resonators must be withdrawn backwards from the stationary position so that tuning and repair can be done easily, and another reason is that the operational equipment of the magnetic and electric injection channels, and of the beam diagnostic device of the injection system must be installed at the central region in the atmosphere.

In narrowly restricted space where bolt-nuts cannot be used, a sealing method with a pneumatic expansion seal[2] was considered to allow reasonable dimensional tolerances and to simplify the connecting and disconnecting procedures. This seal is especially adopted for sealing between RF resonator sections and magnet sections. Valley sections are connected to the magnet sections by using pneumatic expansion seal or lip welding.

The problem in evacuation is the evolution of gas from the surfaces of the chamber and equipments in it. Because a large quantity of gas is supposed to evolve from the pole faces, the main coils, and the field trimming coils, these components are placed outside of the chamber.

As the space available for the chamber in the pole gap is restricted, the chamber wall in that space could not be made thick enough to withstand atmospheric pressure. The chamber at the magnet sections is therefore surrounded with a sub-vacuum chamber which is evacuated to about 10^{-1} Torr to lessen the pressure difference on both sides of the wall. The thickness of the wall is 4 mm. The wall is fixed to the pole piece with O-ring seal interposed, by special bolts made of stainless steel and iron. The analysis of this structural behaviour is in progress using a finite element method.

The plan view of the chamber is shown in Fig. 1 and the vertical cross sectional view showing the connection between the magnet and the RF resonator sections in shown in Fig. 2. The chamber at the magnet section is also seen in this figure.

Geometric characteristics of the chamber are as follows:

total diameter		9 m
heights:	the valley section	60 cm
	the RF resonator section	740 cm
	the magnet section	5 cm
	the sub-vacuum chamber	38 cm
total volume		65 m^3

(2) Test of the pneumatic expansion seal

Three different types of 1/3 scale model of the seal were constructed to investigate the performance. Figure 3 shows a photograph of one of the model pneumatic expansion seals. The seal is fabricated by welding together two thin stainless-steel plates shaped like a race-track.

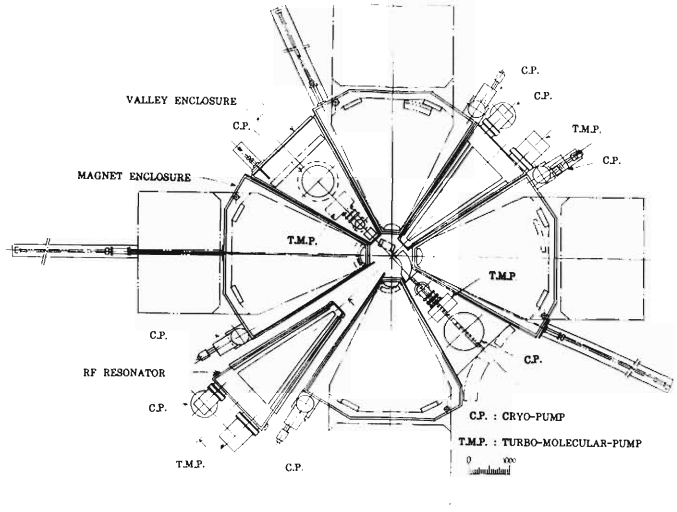

Fig. 1. Plan view of the vacuum chamber for the SSC.

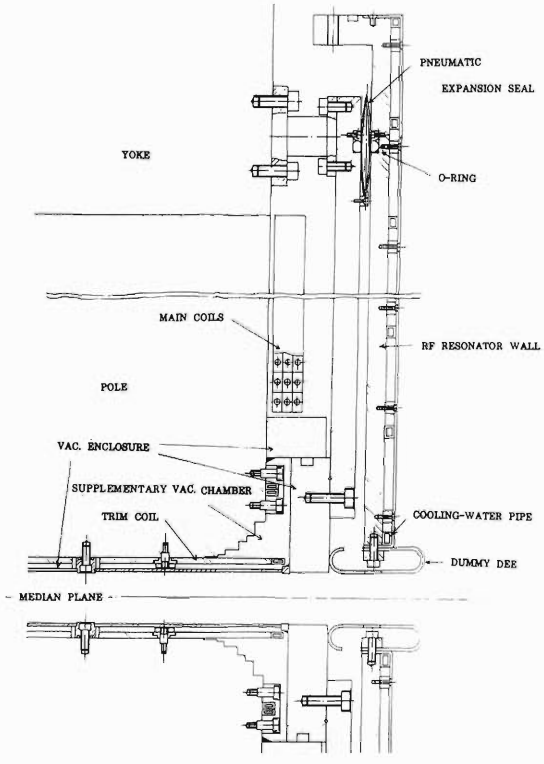

Fig. 2. Vertical cross section of the vacuum chamber showing the method of sealing between the magnet and the RF resonator sections.

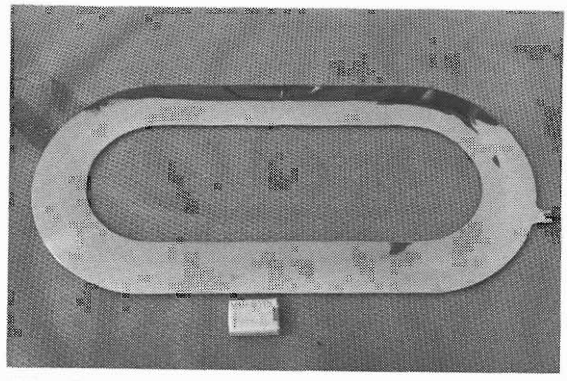

Fig. 3. A photograph of 1/3 scale model pneumatic expansion seal.

We measured the expanding length and the applied pressure required for the seal. Force applied to the O-ring is about 9 kg/cm when a single O-ring is used to seal. It was checked whether there is any leakage by using a He detector. Figure 4 shows the expanding length of each seal versus applied pressure. The expanding length of the seal was measured while the pressure was first increased gradually and then decreased gradually.

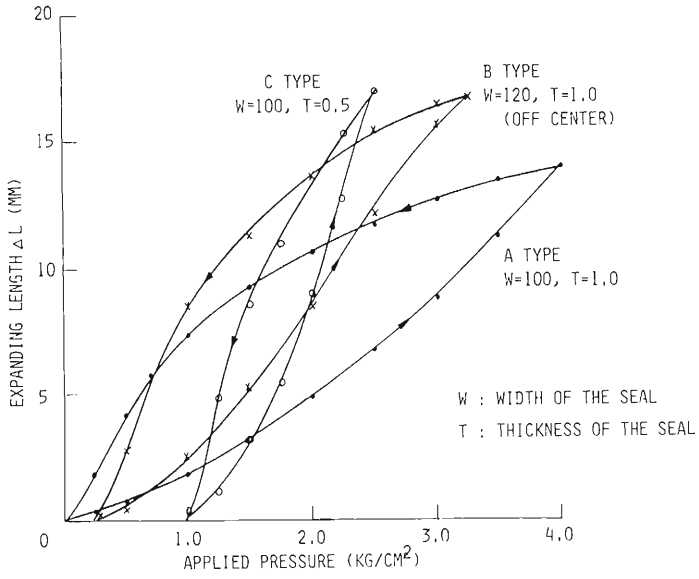

Fig. 4. The expanding length of three different types of seals versus applied pressure.

The gap between the magnet section and the RF resonator section is considered to be about 10 mm. As can be seen from Fig. 4, the pressure of 3.2 kg/cm^2 is needed in the case of A-type seal at a gap of 10 mm. Applied pressure was decreased gradually to the atmospheric pressure after the test chamber was evacuated to the pressure of less than 10^{-5} Torr. It was found that the seal was free from leakage against the variation of the applied pressure.

We conclude from the experimental results that the pneumatic expansion seal is useful for the vacuum chamber of the SSC.

The seal should be tested by repeated contraction and expansion to ensure reliable performance of the seal without loss of high vacuum-tightness due to fatigue of the material or welds.

References

1) K. Ikegami, S. Nakajima, and Y. Ikegami: IPCR Cyclotron Progr. Rep., 14, 198 (1980).
2) C.J. van Lamp: NAC/AR/80-01 Annual Rep., 3.4, p. 105 (1978).

Ⅳ-31. The SSC Beam Handling System

T. Inamura, N. Kishida, and H. Saito

A design study of the SSC beam handling system from the accelerator to the target areas has been made by taking into consideration the space available for the planned building. Here we describe a very versatile system that allows us to make full use of the beam quality regarding energy definition, time structure, and geometrical extent. Figure 1 shows the plan view of the system.

In designing the present system, special care has been taken to meet the following requirements:

(1) Symmetrical placing of standarized ion-optical elements;

(2) Achromatic, doubly telescopic transport;

(3) Monochromatic, doubly telescopic transport with a momentum resolution up to 20000;

(4) Isochronous, doubly telescopic transport.

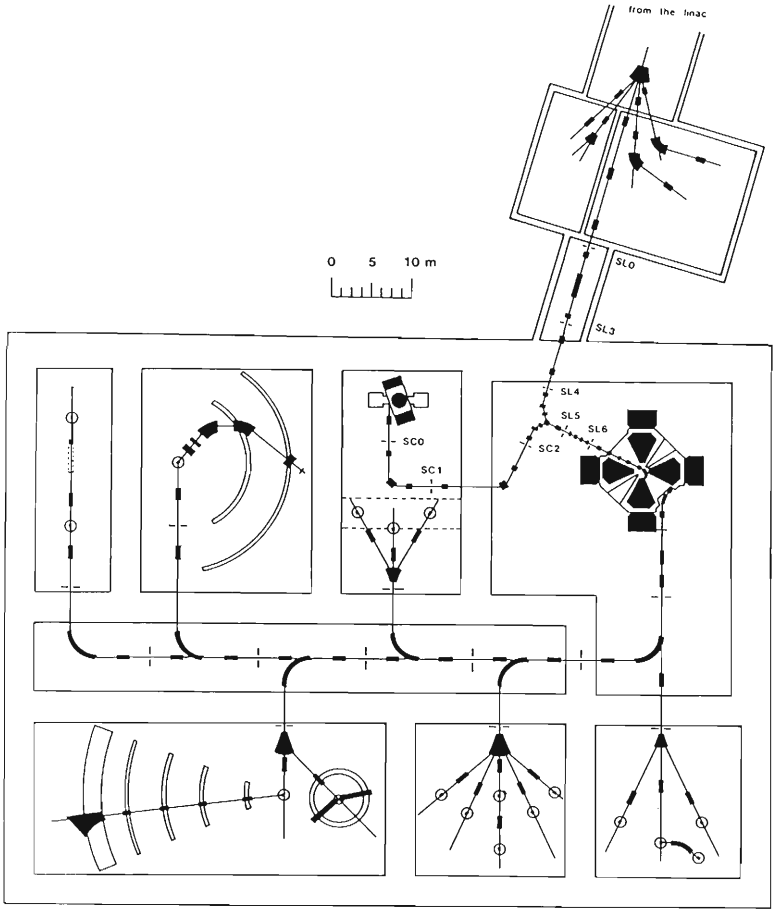

Fig. 1. The plan view of the beam handling system from the SSC to the target areas. S_0 is the source point of the system.

The first requirement obviously makes it easy to design the system and to calculate ion-optics. This assures that one can easily get any beam at any target station without making further calculations once he has got a certain beam at a target station. What he needs to know is only the magnetic rigidity of the beam. One must make every effort to avoid background radiation due to the stray beam produced during the beam preparation in the SSC Facilities. Because of this, it is essential to have an arrangement which allows easy preparation of the beam for any target station.

An achromatic, doubly telescopic system is most useful to get a high-intensity beam with a clearly defined geometrical extent at the target. In this mode the momentum spread of the initial beam does not affect the phase ellipse at the end of the system.

Much higher energy resolution than provided by the SSC will be needed, for example, in the experiments with a high resolution spectrometer. Therefore monochromator systems should be available for several target areas.

Time-of-flight experiments require sharp beam pulses. This means that the beam handling system should be isochronous so as to avoid the spreading out in time of the beam pulse due to the finite momentum distribution.

The design of the beam handling system is based on the following specifications of the beam from the SSC. Particles: Protons through ^{238}U, maximum magnetic rigidity $B\rho$ = 34.58 kG·m which corresponds to the case of 134.5 MeV/u $^{12}C^{6+}$;
Emittance: Between 1 π and 15 π mm·mrad in both planes;
Energy resolution: $E/\Delta E \gtrsim 1000$;
Time structure: Repetition rate of beam pulses 17 – 45 MHz, depending on the type of beam; time spread $\approx$ 200 ps.

Numerical calculations of the system were carried out using the computer code TRANSPORT.[1)]

The system consists of 90° bending magnets (B), quadrupole triplets (Q), and switching magnets (SW). It has mirror or anti-mirror symmetry, depending on the target area. Except in the case of the target area 2, the system works as a double monochromator whose energy resolution is 13000, i.e. 26000 in terms of momentum, when the slit width is 1 mm at the source point S_0 (See Fig. 1). Isochronous transport to the target areas 3, 4, and 5 is possible. For example, the time spread due to the flight from S_0 to the target area 3 is about 70 ps. Achromatic, doubly telescopic transport is guaranteed except to the target area 1. Figure 2 shows horizontal and vertical beam envelope plots for a 134.5 MeV/u ^{12}C beam in the case of achromatic, doubly telescopic transport to the target area 2.

The present design will be modified to meet shielding requirements, to provide more target stations, and to facilitate future expansion.

Technical data on the ion-optical elements are

(1) Bending magnets (B): 90° bending angle, radius ρ = 2.66 m, pole-face rotation = 26.6° for both entrance and exit sides, pole gap = 7.62 cm, homogeneous field $\leq$ 13 kG;
(2) Quadrupole triplets (Q): outer magnetic quadrupoles of effective length 25 cm, inner magnetic quadrupoles of effective length 45 cm, drift space between elements = 20 cm, aperture radius = 3.81 cm, maximum field gradient = 1.5 kG/cm;
(3) Switching magnets (SW): double-focussing switching magnets with 0° pole-face rotation and curved exit face are under consideration.

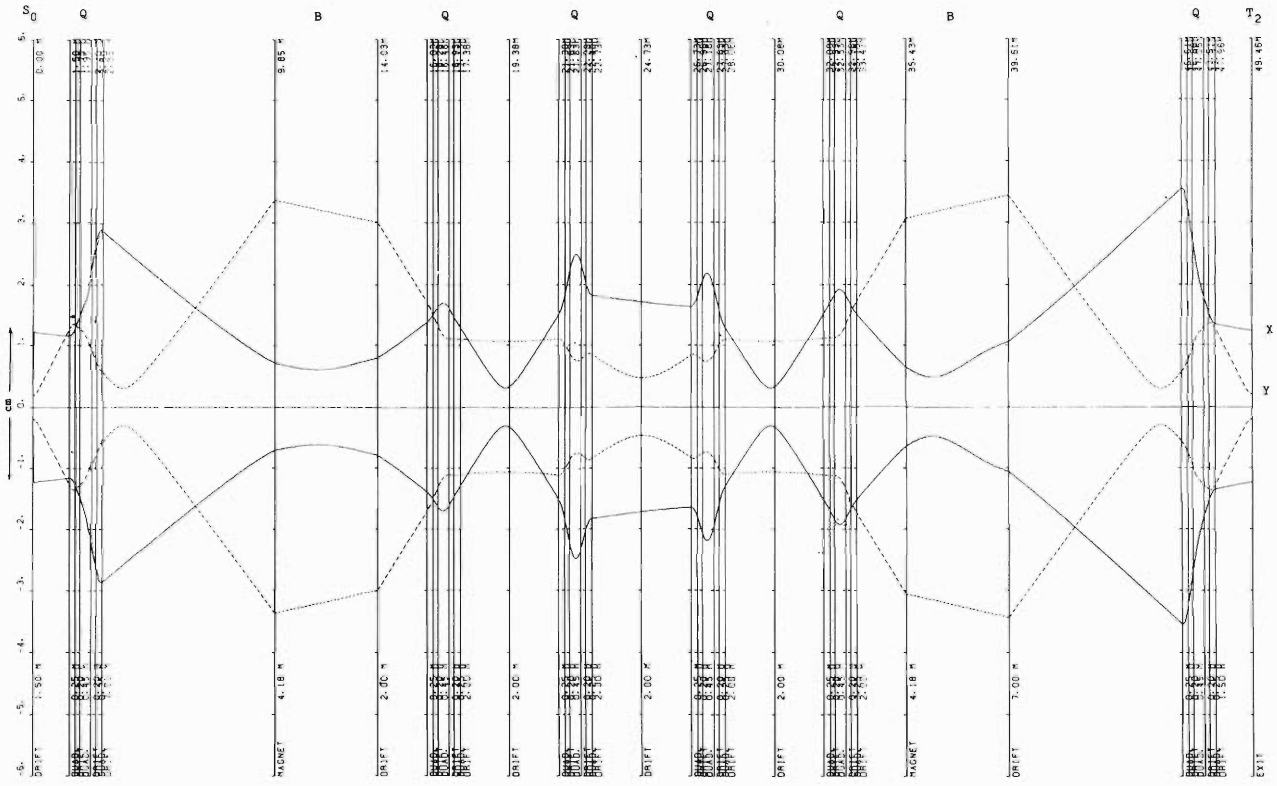

Fig 2. Horizontal (X) and vertical (Y) beam envelope plots for a 134.5 MeV/u, 15.3 π mm·mrad ^{12}C beam from the SSC to the target area 2 in the case of achromatic, doubly telescopic transport. This emittance is the largest value the beam of which can pass the beamline with an aperture radius of 3.81 cm without hitting the inside wall.

Reference

1) K.L. Brown and S.K. Howry: SLAC Report 91, Stanford (1970).

Ⅳ-32. Status of Radiation Shielding for the RIKEN SSC Facility

S. Fujita, S. Yamaji, and T. Shikata

In our previous report,[1] a calculation of the attenuation of neutrons passing through a thick concrete wall was carried out using absorption coefficients derived from half-value reduction thickness for high energy neutrons in the concrete.[2), 3)] However, as the contributions from inelastically scattered neutrons were neglected in our previous calculation, and, therefore, it did not include such factors as build-up factors in the absorption coefficient, it was supposed to be inaccurate. In the present report, the attenuation of neutrons in a concrete wall including the effects of inelastically scattered neutrons is re-evaluated using the results of calculations by Alsmiller et al.[4)] and by Roussin et al.,[5)] and the results are presented in a form available for the design of thickness of shielding wall. We assume that the density of concrete is 2.4 g/cm^3 and that the concrete contains $8.5 \cdot 10^{21}$ hydrogen atoms in cubic centimeters.

Their calculations on transport of monoenergetic neutrons normally incident on a semi-infinite thick slab shield were carried out with the discrete ordinates code ANISN. Alsmiller et al. calculated the transport through a thick slab of sillicon dioxide containing 5 % water by weight for neutrons of energies 50, 100, 200, 300, and 400 MeV, and Roussin et al. carried out a similar calculation for the case of concrete slab of the same thickness for neutrons of energies 15, 25, 50, and 75 MeV.

The geometrical arrangement used in our calculation for the source and the shield are shown in Fig. 1. Neutrons are those generated, as before,[1] from the reactions: 1) protons of energy 200 MeV incident on a thick aluminum target; 2) carbon ions of energy 135 MeV/A incident on a thick iron target; in both cases, beam currents are assumed to be 1 particle μA.

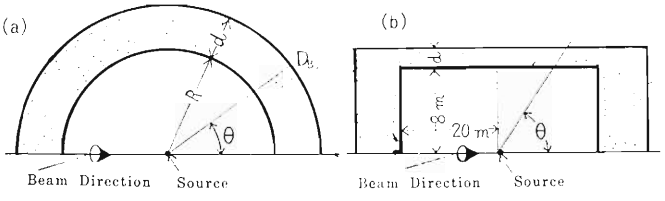

Fig. 1. Geometrical arrangement used for the calculation:
(a) hemi-spherical covering for the calculations of attenuation of neutron flux;
(b) cylindrical covering for the calculation of skyshine.

To begin with, in our shielding calculation, relation between neutron dose equivalent and depth into concrete slab is required for neutron energies up to 200 MeV. Then the ratio of the dose equivalent in the concrete slab with respect to that in silicon dioxide slab as a function of the depth was obtained by the results of Alsmiller et al. and of Roussin et al. at the incident energy of 50 MeV. We obtained the attenuation curves in the concrete slab for the incident energies of neutrons up to 200 MeV, multiplying the curves for the corresponding energies in silicon dioxide slab by the ratio obtained above. To make use of these curves for the calculation of attenuation of neutrons ejected from a point source, the following approximate expression of the dose equivalent D_B at the outer surface of a spherical covering of thickness d for a monoenergetic point source with strength ϕ_0 (n/sr) was derived:

$$D_B = D_B' \frac{\phi_0}{R^2} \frac{R^2}{(R+d)^2}, \qquad (1)$$

where, as shown in Fig. 1(a), R is the radius of the inner surface of the spherical covering, D_B' is the dose

equivalent at the depth d into the thick concrete slab for the case of the parallel neutron flux of density one neutron/cm^2 normally incident on it as obtained above. Calculating the quantities D_B for neutrons of various energies and summing them up, we obtained the dose equivalent on the outer surface of the spherical covering for the point source of neutrons ejected by the reactions mentioned above. If the directions of neutrons passing through the concrete covering are assumed to be unaltered from their initial directions, the dose equivalent at distance r ($r \geq R + d$) is easily determined. These results are shown in Fig. 2 together with the previous results. By means of these curves, one can easily design the shielding. The thickness of concrete wall can be reduced by using materials of high density. Then, after Smith,[6] we also get a dose-geometry contours for the design of a beam damp with iron and concrete. An example of such contours is shown in Fig. 3.

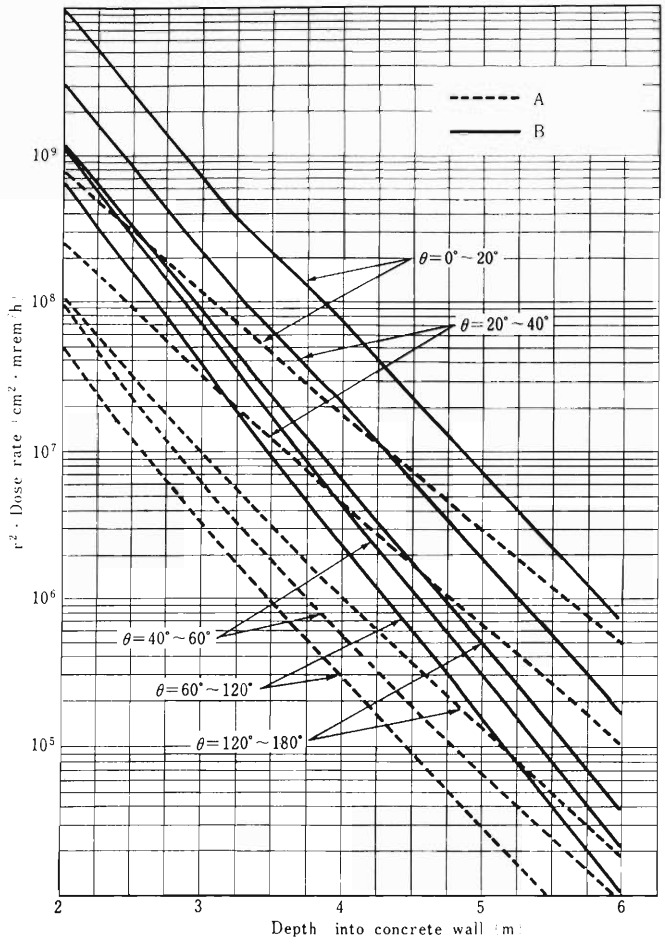

Fig. 2. Dose rate multiplied by r^2 vs. depth into concrete covering.

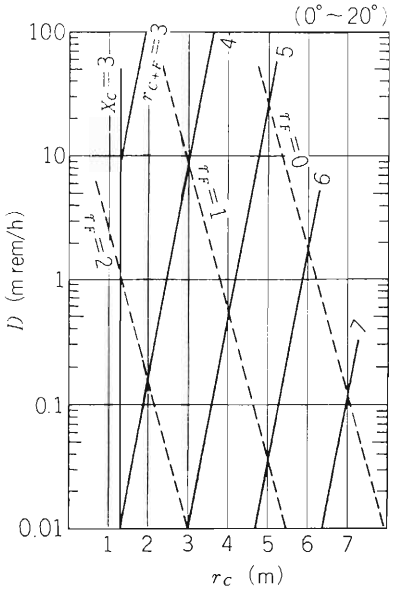

Fig. 3. Dose-geometry contours for 200 MeV protons (1μA) on a thick Al target ($0-20°$). Here, r_F is the thickness of the iron traversed, r_C is the thickness of concrete traversed, along a radius from the neutron source to the point of evaluation of the dose rate D, and r_{C+F} is equal to $r_F + r_C$. X_C is the thickness of concrete in mean free paths. This contour expresses the relation between dose rate D and thickness r_C with r_F or r_{C+F} as parameters. It is required that X_C be greater than 3, so that neutron equilibrium can be established in the concrete.

Calculation of the skyshine for a point neutron source enclosed by a cylindrical covering as shown in Fig. 1(b) was carried out by inserting the results shown in Fig. 2 into the empirical equation of Thomas.[6] The results are shown in Fig. 4 together with the previous results.[1] One can estimate the width of the roof required for getting severe condition of radiation level at the boundary with inhabitants at a distance of 100 m from the source as 4.5 m. This is for the extreme case that the machine is operating for 5000 h per year continuously with the maximum beam energy and beam intensity of 1 particle μA and that the shielding is performed only with the roof. However as beam damps are set at each terminal of the beam transport systems, the width of the roof might be considerably reduced.

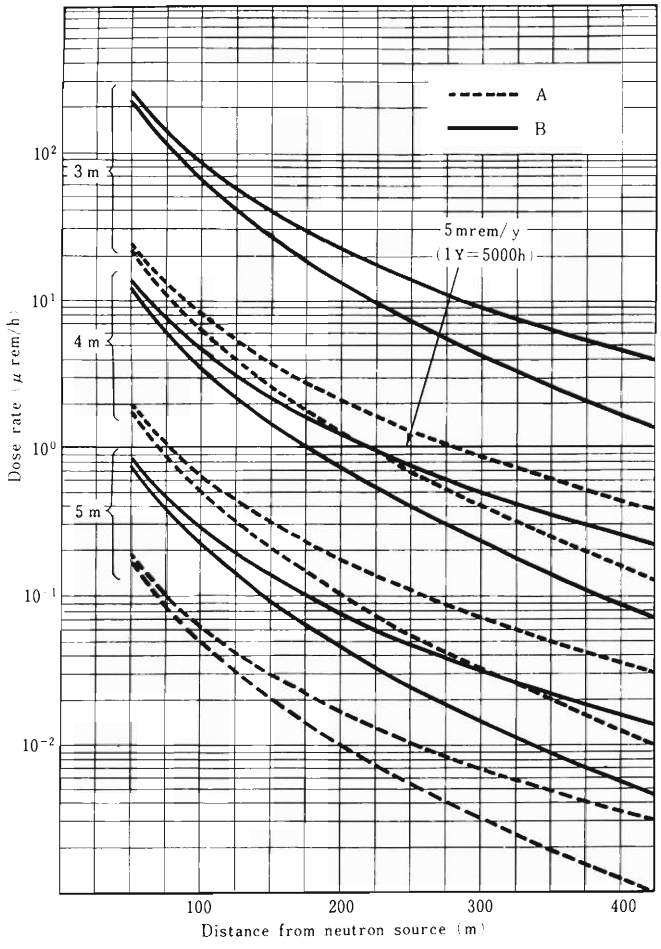

Fig. 4. Spatial distribution of neutron skyshine. Upper curves of each group with two curves correspond to the attenuation length λ = 850 m and lower ones correspond to λ = 267 m.

As is seen from Figs. 2 and 4, the radiation levels of the present results which include the effects of inelastically scattered neutrons are considerably higher than those of the previous results as was expected. However, in our present calculation, following several problems remain: 1) removal of the contribution due to the backscattered neutrons from the results; 2) consideration of the effect of the extremely large components at forward angles of the angular distribution of the source neutrons on Eqns. (1), and 3) improvement of the empirical equation of Thomas. When these problems are settled the required thickness of the shielding might be reduced to some extent.

References

1) S. Fujita, S. Yamaji, and T. Shikata: IPCR Cyclotron Progr. Rep., 14, 203 (1980).
2) R. Wallace: Nucl. Instr. Methods, 18・19, 405 (1962).
3) H.W. Patterson and R.H. Thomas: "Accelerator Health Physics", Academic Press, p. 442 (1973).
4) R.G. Alsmiller, Jr., F.R. Mynatt, J. Barish, and W.W. Engle, Jr.: Nucl. Instr. Methods, 72, 213 (1969).
5) R.W. Roussin, R.G. Alsmiller, Jr., and J. Barish: Nucl. Eng. Design, 24, 250 (1973).
6) H.A. Smith: IUCF Internal Rep., No. 74−6 (Radiation Shielding Note 1) (1974).

Ⅳ-33. Status of the Prototype Baby Cyclotron

T. Karasawa and T. Nozaki

In this year, the Prototype Baby Cyclotron at the National Nakano Chest Hospital in Tokyo has been operated for the production of ultra-short lived radioisotopes (^{11}C, ^{13}N, and ^{15}O). At the Muroran Plant of JSW Ltd and the Sano Plant of IDX Co., improvements on mechanical and electronical systems, respectively, were carried out successfully in manufacturing commercial type Baby Cyclotrons. These improvements made primarily for commercial type machines have also been applied to the prototype machine for higher beam intensities and for easy change of the acceleration particles from proton to deuteron.

The prototype machine was overhauled twice in the year. In the spring overhaul, new dees and dummy dees (each plate against dee) were installed; in the autumn overhaul, the handling device and center plug of lower magnetic pole were changed to those used in the commercial type machine.

Performance of the ion source for doubly charged helium ion (α-particles and $^{3}He^{++}$) was studied. It is well known that beam intensities of the multi-charged heavy ions increases with increasing arc power (arc current multiplied by arc voltage) and with decreasing gas pressure when the gas flow is enough to maintain the arc discharge. Our experimental results agree with these

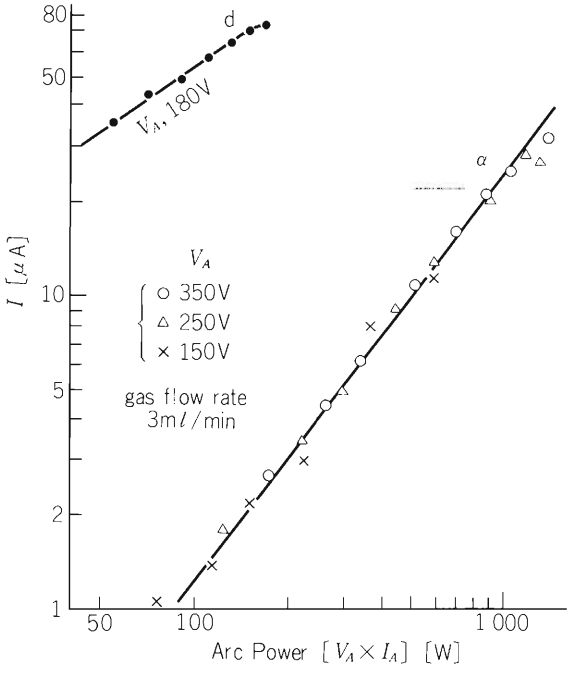

Fig. 1. Comparison of beam intensities between d and α-particles. I is the beam intensity at 20 cm radius for the same ion source and the same acceleration conditions except the magnetic field.

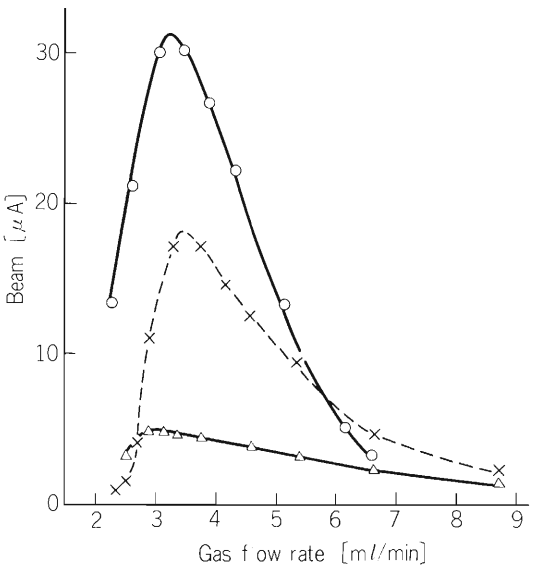

Fig. 2. Beam intensities at 10 cm radius vs. gas flow rate

Arc voltage: 250 V

○ (real): 2.8 A arc current

× (broken): 1.6 A arc current

△ (real): 0.6 A arc current

general tendencies, as shown in Figs. 1 and 2. This experimental result is useful in the ^{18}F production by the nuclear reaction $^{16}O(^{3}He, p)^{18}F$ on a natural water target as well as in activation analysis of oxygen by the same reaction.

Beam intensity distribution at the entrance window of the target box is critical in gas target bombardment. Autoradiographs of copper plates bombarded at this position were observed by a densitometer to give isodensity curves. A result is shown in Fig. 3 and Table 1.

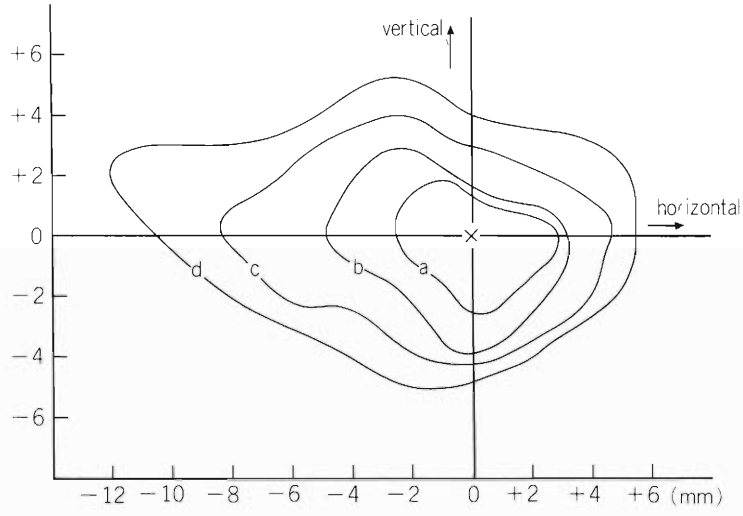

Fig. 3. Isodensity curve at the target box.

Table 1. Beam distribution at the target box.

	a	b	c	d
Beam intensity[a)]	68 %	45 %	23 %	10 %
Beam concentration[b)]	25 %	45 %	70 %	90 %
Beam density[c)]	20 $\mu A/cm^2$	11 $\mu A/cm^2$	7 $\mu A/cm^2$	4 $\mu A/cm^2$

a) Relative to peak intensity at the position of cross in Fig. 3.
b) Concentrated beam inside isodensity curve.
c) Average density between isodensity curves.

Routine diagnostic use of ^{11}CO and $^{11}CO_2$ has been continued. Photosynthesis mixture of ^{11}C glucose and fructose has been produced routinely and used for lung cancer identification and for some other purposes. An automatic synthesizer of this product is under construction and will be completed by the end of January, 1982.

The Kiliani synthesis of ^{11}C-labelled glucose-mannose mixture has been studied. By the use of glucose and mannose labelled with ^{14}C at the carbonyl positions, the ^{11}C Kiliani synthesis mixture was shown to be almost equally effective for the study of brain functions as ^{11}C glucose after being separated from the mixture. A process suitable for automated synthesis of the ^{11}C glucose-mannose has been established, and the automatic synthesizer has been designed.

Preparation of (^{11}C-methyl)-stearic acid from $^{11}CH_3I$ by the malonic acid synthesis has been studied. Hexacosanoic acid labelled with ^{11}C at the carboxylic carbon was prepared both by the Grignard reaction and the nitrile synthesis. The behaviour of this compound was studied for its possible use as a diagnostic tool for adenoleukodistrophy.[1)]

Aspartic acid labelled with no-carrier-added ^{11}C was prepared by the following two-step enzymatic synthesis: (1) reaction of $^{11}CO_2$ and phosphoenolpyruvic acid in the presence of phosphoenolpyruvate carboxylase to give ^{11}C oxaloacetic acid, and (2) conversion of the oxaloacetic acid into aspartic acid-^{11}C with the aid of glutamic acid and glutamate-oxaloacetate transaminase. In vivo distribution of this compound and catabolic rate of the ^{11}C atom into expired air were studied. Its diagnostic use is under consideration.

Reference

1) N. Sakuragawa, A. Matsui, M. Iio, S. Iida, T. Nozaki, M. Arima, E. Satoyoshi, and T. Karasawa: Intern. Symp. Leukodistrophy and Allied Diseases, Tokyo, Sept. (1981).

V. RADIATION MONITORING

1. Routine Monitoring

M. Koyama, K. Igarashi, I. Usuba,
S. Fujita, and I. Sakamoto

Results of routine radiation monitoring carried out on the cyclotron from April 1980 to March 1981 are described.

No remarkable change in leakage radiation and residual activities was observed during this period. Some aspects of the leakage radiation are described in the following report.

(1) Surface and air contamination

The surface contamination has been kept below 10^{-6} μCi/cm^2 on the floor of cyclotron room and the underground passage, and below 10^{-7} μCi/cm^2 in the experimental areas, hot laboratory and chemical laboratories. The contamination was wiped off twice a year, and immediately after this decontamination, the contamination on the floor of cyclotron room and the underground passage had been reduced to a value below 10^{-7} μCi/cm^2.

When the accelerating chamber was opened, slight contamination of the air in the cyclotron room was observed. The value of radioactivity concentration (beta-gamma) was 10^{-12} μCi/cm^3.

(2) Drainage

The radioactivity concentration of the drain water from the cyclotron building was found to

Table 1. Annual exposure dose received by the cyclotron workers from April 1980 to March 1981.

Workers	Number of persons				Total	Collective dose (man-mrem)
	Dose undetectable	10-100 (mrem)	101-300 (mrem)	>300 (mrem)		
Operators	1	7			8	220
Nuclear physicists	12	3			15	30
Accelerator physicists	17	3			20	120
Physicists in other fields	25	2		1	28	340
Nuclear chemists	6	4	5		15	1170
Biological chemists	6				6	
Health physicists	5				5	
Total	72	19	5	1	97	1880

Average annual dose per person: 19.4 mrem.

Maximum individual annual dose: 310 mrem.

be of the order of $10^{-6} - 10^{-7}$ μCi/cm^3. The total quantity of activities in the aqueous effluents in this period was about 50 μCi, and the radioactive nuclides found by the γ-ray spectrometry were mainly ^{65}Zn, ^{22}Na, and ^{58}Co.

(3) Personnel monitoring

The external exposure dose to personnel was measured with γ-ray and neutron film badges. The dose received during the present period by all the cyclotron workers is shown in Table 1. The collective γ-ray dose to all workers was 1880 man-mrem, while the collective dose owing to thermal and fast neutron exposures was too small to be detected. The collective dose to the cyclotron workers is about 82 % of the value in the preceding period.

In this period the average annual dose per person was 19.4 mrem, and the maximum individual annual dose was 310 mrem.

V-2. Leakage-Radiation Measurement at the Underground Passage

I. Sakamoto

Leakage radiation during operation of the cyclotron at the underground passage of the cyclotron building was measured. Leakage doses received from April 1980 to March 1981 by

Table 1. Leakage radiation dose (in mrem) at the underground passage from April 1980 at March 1981.

Radiation \ Point of observation[a)]	1	2
γ-rays (mrem)	2490	60
Thermal neutrons (mrem)	650	10
Fast neutrons (mrem)	740	60
Total (mrem)	3880	130

a) See the figure shown below.

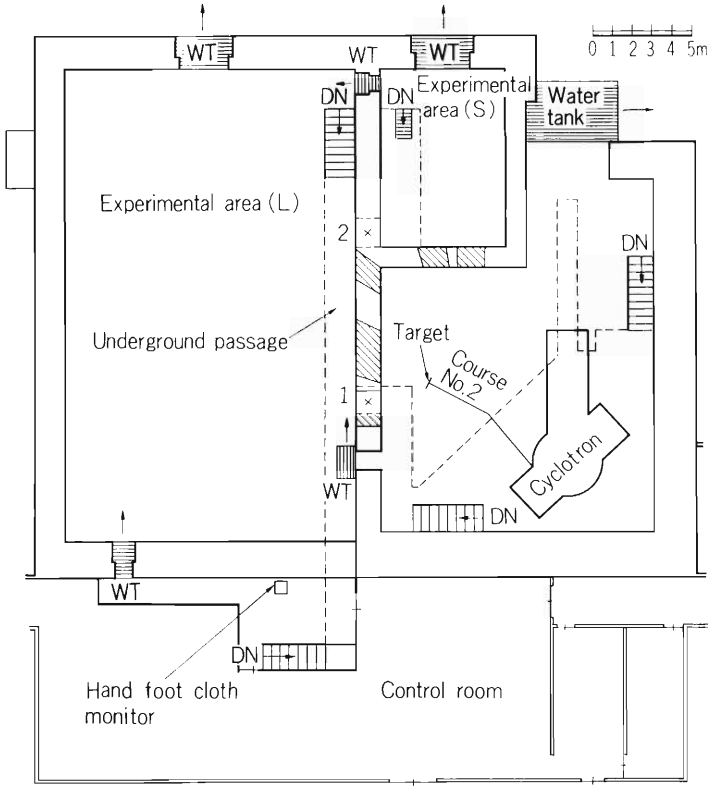

γ-ray and neutron film badges which were left at the underground passage, are shown in Table 1. The machine time allotted for deuteron acceleration was 36 h in this period.

As to the dose values at point No. 1 measured every month, the maximum dose of 790 mrem was observed in November. In this case, the values of gamma dose, thermal neutron dose and fast neutron dose were 460 mrem, 80 mrem and 250 mrem, respectively.

The neutron doses observed at point No. 1 in October, November, and March were larger than those in other months. The sum of neutron doses measured in the three months was 770 mrem, which was 55 % of the total neutron dose in this period. As a result of investigation, it was concluded that the increase of the neutron dose was mainly due to the 40 MeV α-particle bombardment on a GaAs and Sn plate at about $5-15$ μA in the beam course No. 2, where $5-10$ mCi of radioisotopes were produced in each month above mentioned by $^{75}As(\alpha, 2n)^{77}Br$ and $^{117}Sn(\alpha, 2n)^{119m}Te$ reactions.

V-3. Examination of Shielding Performance of Doors in the Linac Building

I. Sakamoto, M. Odera, Y. Chiba, M. Hemmi,
A. Shimamura, T. Inoue, I. Takeshita, and T. Hamada

The shield walls provided for the linac and the associated equipments are made of ordinary concrete of thickness 15 – 60 cm and able to keep the outside radiation levels (γ-rays plus neutrons) below the permissible value for non-occupational people even when a thick iron target is bombarded by carbon ions of 50 MeV at a current of 2×10^{13} ions per sec. The entrances to the injector vault, the accelerator vault and the experimental areas are equipped with shield doors which are made of ordinary concrete and of iron.

We examined all the six shield doors in the linac building, and found that they had the expected shielding performance. Details of the examination of the largest door are described below as an example.

The plan of the door and the arrangement for the measurement are shown in Fig. 1. 30 points were marked on the door as shown in Fig. 2 and at each point the transmission of γ-rays from a 29 mCi ^{137}Cs source was measured with a scintillation survey meter located at the opposite side of the door to the source and at a distance of 110 cm from the source.

The distribution of the measured dose rate is shown in Fig. 2. The door is made of 2.4cm thick iron and of 37.6cm thick ordinary concrete. The calculated dose rate, in this arrangement, is 0.057 mR/h. While the measured values of leakage dose rate almost agreed with calculated ones at right, those at left showed gradual increase with, which would be due to scattered γ-rays through opening between the door and the wall.

Since the main purpose of the examination was to check the presence of any defect such as holes in the concrete cast into the door, it is concluded that the door has the shielding performance expected.

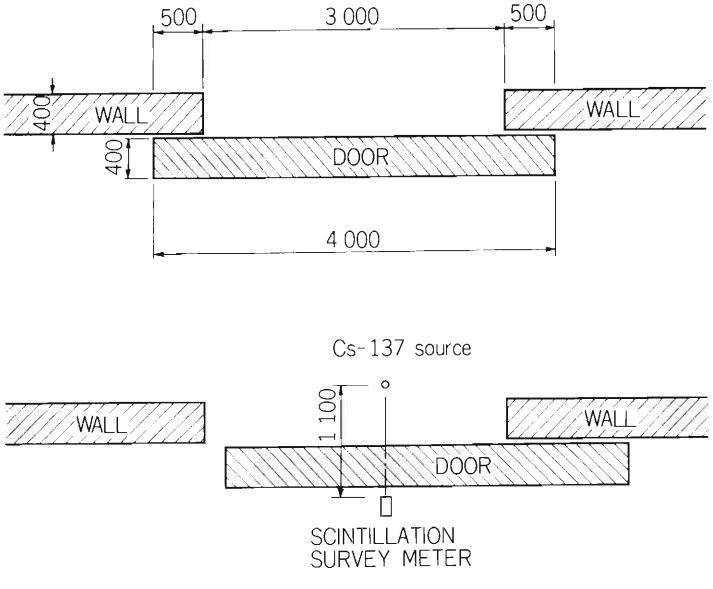

Fig. 1. Plan of the shield door (above) and the arrangement for the measurement (below).

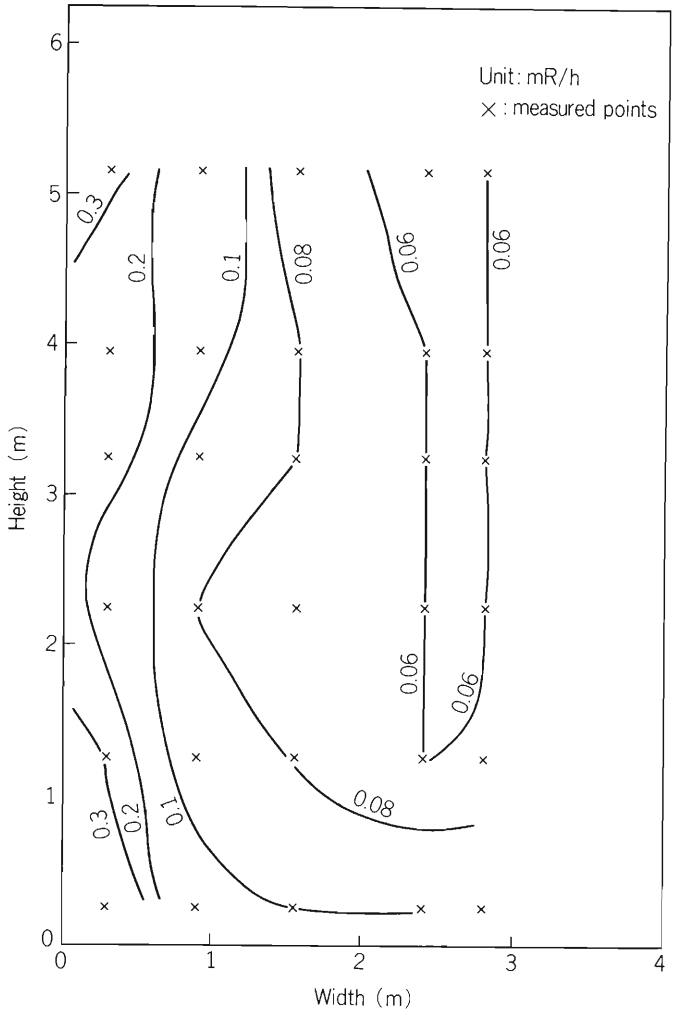

Fig. 2. Distribution of the measured dose rate of the shield door.

VI. LIST OF PUBLICATIONS

1. Machine development and accelerator physics

1) H. Kamitsubo: "IPCR Heavy Ion Accelerator Project. The Design of the Riken Separated Sector Cyclotron", Reports I.P.C.R., 57, 131 (1981).
2) Y. Obana, S. Motonaga, T. Wada, Y. Tanaka, and H. Takebe: "Design of the Sector Magnet for the RIKEN SSC (II)", Reports I.P.C.R., 57, 147 (1981).
3) S. Motonaga, T. Wada, Y. Obana, Y. Tanaka, and H. Takebe: "Design of the Sector Magnet for the RIKEN SSC (III). Final Design of the Magnet Pole Using a Computer Code Trim in 2-dimensional Approximation", Reports I.P.C.R., 57, 156 (1981).
4) A. Goto, H. Takebe, S. Motonaga, T. Wada, Y. Yano, N. Nakanishi, and Y. Tanaka: "Optimization of Currents and Configurations of Trim Coils for Sector Magnet", Reports I.P.C.R., 57, 165 (1981).
5) H. Takebe, T. Wada, I. Takeshita, S. Motonaga, J. Fujita, and Y. Tanaka: "Model Test of Trim Coils for Sector Magnet", Reports I.P.C.R., 57, 171 (1981).
6) Y. Ikegami, T. Wada, M. Hara, and S. Motonaga: "Structural Analyses of Sector Magnet by a Finite Element Method", Reports I.P.C.R., 57, 177 (1981).
7) N. Nakanishi: "Programs for Calculating Beam Orbits in Cyclotron (I)", Reports I.P.C.R., 57, 189 (1981).
8) A. Goto: "Programs for Calculating Beam Orbits in Cyclotron (II)", Reports I.P.C.R., 57, 203 (1981).
9) K. Ogiwara, M. Hara, and T. Fujisawa: "Design Study and Model Test of RF Resonator for the RIKEN SSC", Reports I.P.C.R., 57, 222 (1981).
10) S. Nakajima, K. Ikegami, Y. Oikawa, and I. Takeshita: "Design of the Vacuum System of the RIKEN SSC", Reports I.P.C.R., 57, 232 (1981).
11) S. Fujita, S. Yamaji, and T. Shikata: "Neutron Shielding for the RIKEN SSC", Reports I.P.C.R., 57, 239 (1981).
12) N. Nakanishi, A. Goto, and Y. Yano: "Isochronous Magnetic Field in a SSC and the Effect of Field Imperfection", Sci. Papers I.P.C.R., 75, 136 (1981).
13) M. Hara, T. Wada, A. Toyama, and F. Kikuchi: "Calculation of RF Electromagnetic Field by Finite Element Method", Sci. Papers I.P.C.R., 75, 143 (1981).
14) Y. Yano, H. Takebe, S. Motonaga, T. Wada, J. Fujita, and A. Goto: "Design and Model Study of Injection Bending Magnet for the RIKEN SSC", Sci. Papers I.P.C.R., 75, 176 (1981).
15) H. Takebe, Y. Yano, S. Motonaga, T. Wada, J. Fujita, and Y. Ikegami: "Model Study of Magnetic Inflection Channel for the RIKEN SSC", Sci. Papers I.P.C.R., 75, 193 (1981).
16) A. Goto, Y. Yano, and N. Nakanishi: "Design of Injection and Extraction Harmonic Coils for the RIKEN SSC", Sci. Papers I.P.C.R., 75, 204 (1981).
17) N. Kishida and Y. Yano: "Beam Transport System for the RIKEN SSC (II)", Sci. Papers I.P.C.R., 75, 214 (1981).
18) T. Inamura, N. Kishida, H. Saito, and M. Watanabe: "The RIKEN SSC Beam Handling System", Sci. Papers I.P.C.R., 75 236 (1981).

19) S. Motonaga, T. Wada, Y. Yano, H. Takebe, J. Fujita, Y. Ikegami, and N. Nakanishi: "The Sector Magnet for the IPCR SSC", IEEE Trans. Mag., MAG-17, 1836 (1981).

2. Nuclear physics and nuclear instrumentation

1) M. Ichimura, E. Takada, T. Yamaya, and K. Nagatani: "Reaction Mechanism of $^{12}C(^{16}O, \alpha)$: ^{12}C Transfer to Nuclear Molecular Resonances", Phys. Lett., 101B, 31 (1981).
2) H. Utsunomiya, T. Nomura, M. Ishihara, T. Sugitate, K. Ieki, and S. Kohmoto: "Angular-Momentum Transfer and Alignment Following Preequilibrium α-Particle Emission in the Reaction $^{209}Bi + ^{14}N$", Phys. Lett., 105B, 135 (1981).
3) S. Yamaji, A. Iwamoto, K. Harada, and S. Yoshida: "Microscopic Calculation of the Mass Diffusion Coefficient Using Linear Response Theory", Phys. Lett., 106B, 443 (1981).
4) Y. Gono, K. Hiruta, T. Nomura, M. Ishihara, H. Utsunomiya, T. Sugitate, and K. Ieki: "In-Beam α- and γ-Ray Spectroscopy for ^{214}Rn", J. Phys. Soc. Japan, 50, 377 (1981).
5) T. Fujisawa, N. Kishida, T. Kubo, T. Wada, Y. Toba, T. Hasegawa, M. Sekiguchi, N. Ueda, M. Yasue, F. Soga, H. Kamitsubo, M. Nakamura, K. Hatanaka, Y. Wakuta, T. Tanaka, and A. Nagao: "Analyzing Power-Polarization Inequality in the Inelastic Scattering of Protons on ^{12}C for Incident Energies from 22.0 to 29.0 MeV", J. Phys. Soc. Japan, 50, 3198 (1981).
6) H. Amakawa, A. Mori, H. Nishioka, K. Yazaki, and S. Yamaji: "Adiabatic Approximation for Deuteron Breakup Effect", Phys. Rev. C 23, 583 (1981).
7) M. Koike, K. Komura, H. Kawakami, M. Kanbe, G. Madiueme, S. Shibata, T. Fujisawa, and T. Wada: "Electric Monopole Transitions between 0^+ States in ^{102}Ru", Phys. Rev. C 24, 1611 (1981).
8) A. Ichimura and M. Ichimura: "Coupled Channel Analysis for the Anomaly of the $(^{18}O, ^{18}O^*)$ Reaction", Prog. Theoret. Phys., 66, 913 (1981).
9) M. Kawai, M. Ichimura, and N. Austern: "On the Relation between the Method of Coupled Channels and the Truncated Channel Coupling Array Formalism for Rearrangement Reactions", Z. Phys. A – Atom and Nuclei, 303, 215 (1981).
10) T. Inamura: "Is Massive Transfer Preequilibrium ?", Soryushiron Kenkyu, 63, C109 (1981).

3. Atomic and solid-state physics

1) H. Tawara, K. Ishii, and Y. Awaya: "Excitation, Ionization and Charge Transfer Processes about Inner-Shell Electrons", Atomic Physics by Using Accelerators, Study Group of Fundamental Atomic Process, p.25 (1981).
2) Y. Awaya: "Table of Accelerators Used for the Study of Atomic Physics", Atomic Physics by Using Accelerators, Study Group of Fundamental Atomic Process, p. 91 (1981).
3) Y. Awaya, H. Kumagai, and Y. Tendow: "An X-ray Crystal Spectrometer", The Handbook of Atomic Collisions – Apparatus –, Study Group of Fundamental Atomic Process, p. 194 (1981).

4) T. Tonuma, A. Yagishita, M. Kase, T. Kambara, Y. Awaya, and I. Kohno: "Multiple Ionization of Gas Targets by Ion Bombardment", Atomic Collision Research in Japan Progress Report, No. 7, p. 76 (1981).
5) T. Kambara, Y. Awaya, A. Hitachi, M. Kase, I. Kohno, and T. Tonuma: "X-Rays from Radiative Electron Capture Induced 110-MeV Ne-Ions", Atomic Collision Research in Japan Progress Report, No. 7, p. 78 (1981).
6) E. Yagi, A. Koyama, H. Sakairi, M. Iwaki, and R.R. Hasiguti: "Lattice Location of Ni Atoms Implanted into Al Crystals as Investigated by Means of Channeling Method", J. Phys. Soc. Japan, 50, 873 (1981).
7) H. Sakairi, E. Yagi, A. Koyama, and R.R. Hasiguti: "Atomic Replacement in Ordered Cu_3Au Alloy Irradiated with Protons, α-Particles and Carbon Ions from a Cyclotron", J. Phys. Soc. Japan, 50, 3023 (1981).
8) H. Kirihata and M. Uda: "Externally Quenched Air Counter for Low-energy Electron Emission Measurements", Rev. Sci. Instr., 52, 68 (1981).
9) E. Yagi, H. Bossy, K.P. Döring, M. Gladisch, D. Herlach, M. Matsui, H. Orth, G. zu Putlitz, A. Seeger, and J. Vetter: "Longitudinal Muon Spin Relaxation in α-Iron in High Magnetic Fields", Hyperfine Interaction, 8, 553 (1981).
10) H. Endo. M. Uda, and K. Maeda: "Influence of the Chemical Bond on the Intensities of F Kα X-Ray Satellites Produced by Electron and Photon Impacts", Phys. Rev. A 22, 1436 (1981).
11) M. Uda, H. Endo, K. Maeda, Y. Sasa, and M. Kobayashi: "Chemical Effect on F Kα X-Ray Satellites Produced by 6 MeV/amu P, α and C^{4+}", Z. Phys. A – Atom and Nuclei, 300, 1 (1981).
12) A. Yagishita: "Ionization Cross Sections of Krypton M-Subshells by Electron Impact", Phys. Lett., 87A, 30 (1981).
13) A. Yagishita, H. Hanashiro, S. Ohtani, and H. Suzuki: "The Kr $M_{2,3}M_{45}N_{23}$ Coster-Kronig Processes Following Electron Impact Ionization", J. Phys. B, 14, L777 (1981).

4. Radiochemistry, radiation chemistry and radiation biology

1) T. Nozaki, T. Karasawa, M. Io, K. Imamura, S. Iida, and H. Yoshida: "Present Status in the Use of the Prototype Baby Cyclotron", J. Label. Comp. & Radiopharm., 18, 181 (1981).
2) T. Nozaki and M. Iwamoto: "Some Fundamental Data Concerning the Formation of Low Z Radionuclides", J. Label. Comp. & Radiopharm., 18, 230 (1981).
3) T. Nozaki and M. Iwamoto: "Yield of ^{14}O for the Reactions $^{14}N(p, n)^{14}O$, $^{12}C(^3He, n)^{14}O$ and $^{12}C(\alpha, 2n)^{14}O$", Radiochim. Acta, 29, 57 (1981).
4) H. Muramatsu, H. Nakahara, and M. Yanokura: "Production of ^{119m}Sn by Alpha Particle Bombardment of ^{116}Cd and Its Carrier-free Separation", J. Inorg. Nucl. Chem., 43, 1727 (1981).
5) F. Ambe and S. Ambe: "A Site Distribution of Dilute ^{119}Sb and ^{119m}Te on Solidification of SnTe and SnSb by Mössbauer Emission Spectroscopy of ^{119}Sn", J. Chem. Phys., 75, 2463 (1981).

6) T. Tonuma, Y. Awaya, T. Kambara, H. Kumagai, M. Kase, A. Yagishita, and I Kohno: "Krypton Kβ/Kα Intensity Ratios for 6 MeV/amu Ion Bombardment", Inner-Shell and X-ray Physics of Atoms and Solids, Prenum Press, New York and London, p. 153 (1981).

(Papers Presented at Meetings)

1. Machine development and accelerator physics

1) N. Nakanishi, T. Wada, A. Goto, Y. Yano, S. Motonaga, and H. Kamitsubo: "Orbit Analysis 4 in the IPCR SSC", 36th Ann. Meeting of the Phys. Soc. Japan, Hiroshima, Mar. (1981).
2) A. Goto, Y. Yano, T. Wada, and N. Nakanishi: "Orbit Calculation of the Injection System for the RIKEN SSC", 36th Ann. Meeting of the Phys. Soc. Japan, Hiroshima, Apr. (1981).
3) M. Hara, T. Wada, T. Fujisawa, and K. Ogiwara: "Three Dimensional Analysis of RF Electromagnetic Field by Finite Element Method", 36th Ann. Meeting of the Phys. Soc. Japan, Hiroshima, Apr. (1981).
4) M. Hara, T. Wada, M. Odera, and F. Kikuchi: "Calculation of RF Cavities with Axial Symmetry by Finite Element Method", 6th Meeting on Linear Accelerator in Japan, Sapporo, July (1981).
5) Y. Yano, N. Kishida, H. Takebe, A. Goto, T. Wada, and S. Motonaga: "Beam Injection and Extraction System for the IPCR SSC", 9th Intern. Conf. on Cyclotrons and their Applications, Caen, France, Sept. (1981).
6) A. Goto, Y. Yano, N. Kishida, N. Nakanishi, and T. Wada: "Calculation of Injection and Extraction Orbits for the IPCR SSC", 9th Intern. Conf. on Cyclotron and their Applications, Caen, France, Sept. (1981).
7) S. Motonaga, H. Takebe, T. Wada, A. Goto, J. Fujita, Y. Oikawa, I. Takeshita, and Y. Ikegami: "The Sector Magnet for the IPCR SSC", 9th Intern. Conf. on Cyclotron and their Applications, Caen, France, Sept. (1981).
8) N. Nakanishi, A. Goto, Y. Yano, and T. Wada: "Beam Dynamics for the IPCR SSC", 9th Intern. Conf. on Cyclotron and their Applications, Caen, France, Sept. (1981).
9) M. Hara, T. Fujisawa, and K. Ogiwara: "The RF System for the IPCR SSC", 9th Intern. Conf. on Cyclotron and their Applications, Caen, France, Sept. (1981).
10) T. Fujisawa, M. Hara, and K. Ogiwara: "Method to Vary Resonant Frequency of Resonator of IPCR SSC", 1981 Fall Meeting of the Phys. Soc. Japan, Matsue, Sept. (1981).
11) N. Nakanishi, A. Goto, and Y. Yano: "Orbit Analysis 5", 1981 Fall Meeting of the Phys. Soc. Japan, Matsue, Oct. (1981).
12) A. Goto, H. Takebe, S. Motonaga, T. Wada, Y. Yano, and Y. Tanaka: "Design of the Trim Coils for the RIKEN SSC", 1981 Fall Meeting of the Phys. Soc. Japan, Matsue, Oct. (1981).
13) M. Hara, T. Wada, T. Fujisawa, K. Ogiwara, and F. Kikuchi: "Calculation of RF Electromagnetic Field by Finite Element Method", 1981 Fall Meeting of the Phys. Soc. Japan, Matsue, Oct. (1981).

14) T. Inamura, N. Kishida, and H. Saito: "A Design Study of the RIKEN SSC Beam Handling System", 1981 Fall Meeting of the Phys. Soc. Japan, Matsue, Oct. (1981).
15) Y. Yano, A. Goto, N. Nakanishi, T. Wada, and N. Kishida: "Beam Centering in the SSC", 1981 Fall Meeting of the Phys. Soc. Japan, Matsue, Oct. (1981).
16) M. Hara, T. Wada, and A. Toyama: "Calculation of RF Electromagnetic Field by Finite Element Method", Meeting on Calculation of Electromagnetic Field by Computer, Wako, Nov. (1981).

2. Nuclear physics and nuclear instrumentation

1) T. Inamura: "Is Massive Transfer Preequilibrium?", Symp. on Transport Phenomena in Heavy-Ion Reactions, INS, Tokyo, Feb. (1981).
2) T. Nomura: "Fast Light-Particle Emission and Preequilibrium Phenomena", Symp. on Heavy-Ion Nuclear Reaction, Tsukuba, Mar. (1981).
3) T. Inamura: "Massive Transfer", Symp. on Heavy-Ion Nuclear Reactions, Tsukuba, Mar. (1981).
4) T. Fujisawa, N. Kishida, T. Kubo, T. Wada, T. Hasegawa, M. Sekiguchi, N. Ueda, M. Yasue, F. Soga, H. Kamitsubo, M. Nakamura, K. Hatanaka, Y. Wakuta, T. Tanaka, A. Nagao, and Y. Toba: "Analyzing Power-Polarization Inequality in the Inelastic Scattering of Protons on ^{12}C for Incident Energies from 22.0 to 29.0 MeV", 36th Ann. Meeting of the Phys. Soc. Japan, Hiroshima, Mar. (1981).
5) A. Ichimura and M. Ichimura: The Normalization of the Channel Coupling Effect to the Optical Potential in Heavy-Ion Inelastic Scattering", 36th Ann. Meeting of the Phys. Soc. Japan, Hiroshima, Mar. (1981).
6) S. Yamaji, A. Iwamoto, K. Harada, and S. Yoshida: "Numerical Analysis of the ^{63}Cu + ^{197}Au Reaction", 36th Ann. Meeting of the Phys. Soc. Japan, Hiroshima, Apr. (1981).
7) Y. Nagame, I. Kohno, M. Yanokura, H. Nakahara, H. Kudo, and K. Sueki: "Heavy Particle Emissions in Reactions between ^{20}Ne + ^{50}Cr(II)", 36th Ann. Meeting of the Phys. Soc. Japan, Hiroshima, Apr. (1981).
8) K. Ieki, M. Ishihara, T. Nomura, S. Kohmoto, H. Utsunomiya, and T. Sugitate: "Light Particle Emission in Heavy-Ion Reaction", 36th Ann. Meeting of the Phys. Soc. Japan, Hiroshima, Apr. (1981).
9) T. Nomura: "Preequilibrium Phenomena in Heavy-Ion Reactions", Symp. on Nucleus-Nucleus Collision and Cluster Structure, Kyoto, Aug. (1981).
10) Y. Nagame, I. Kohno, H. Nakahara, M. Yanokura, H. Kudo, K. Sueki, and M. Takahashi: "Heavy Particle Emissions in Reactions between ^{20}Ne and ^{50}Cr, ^{54}Cr(III)", 1981 Fall Meeting of the Phys. Soc. Japan, Matsue, Oct. (1981).
11) S. Yamaji, A. Iwamoto, K. Harada, and S. Yoshida: "Mass Diffusion Coefficients in the Adiabatic Approximation", 1981 Fall Meeting of the Phys. Soc. Japan, Matsue, Oct. (1981).
12) H. Muramatsu, T. Miura, H. Nakahara, M. Fujioka, E. Tanaka, Y. Arai, and A. Hashizume: "Conversion Electron Measurements of ^{119}Sb Implanted Samples", 1981 Fall Meeting of the Phys. Soc. Japan, Matsue, Oct. (1981).
13) T. Inamura and M. Wakai: "Calculation of Gamma-Ray Multiplicity Moments

Associated with Massive Transfer Reactions", 1981 Fall Meeting of the Phys. Soc. Japan, Matsue, Oct. (1981).

14) M. Sasagase, Y. Gono, T. Kubo, Y. Itoh, S. Hayashibe, and M. Sugawara: "Search for the α-Particle Emission from High Spin Yrast Region", 1981 Fall Meeting of the Phys. Soc. Japan, Matsue, Oct. (1981).
15) M. Sasagase, H. Kumagai, M. Odera, T. Wada, and T. Inamura: "Data Processing System at RILAC", 1981 Fall Meeting of the Phys. Soc. Japan, Matsue, Oct. (1981).
16) K. Ieki, M. Ishihara, T. Inamura, and S. Kohmoto: "Light Particle Emission in Heavy-Ion Reaction 2", 1981 Fall Meeting of the Phys. Soc. Japan, Matsue, Oct. (1981).
17) A. Ichimura and M. Ichimura: "Extended Brink Model and its Derivation from Distorted Wave Born Approximation", 1981 Fall Meeting of the Phys. Soc. Japan, Matsue, Oct. (1981).
18) H. Muramatsu, T. Miura, H. Nakahara, M. Fujioka, E. Tanaka, Y. Arai, and A. Hashizume: "Chemical Effect on Outer-Shell Internal Conversion in ^{119}Sn", 25th Symp. on Radiochemistry, Tsukuba, Oct. (1981).
19) Y. Nagame, H. Kudo, K. Sueki, M. Takahashi, H. Nakahara, I. Kohno, and M. Yanokura: "Heavy-Ion Reactions between ^{20}Ne and ^{50}Cr, ^{54}Cr", 25th Symp. on Radiochemistry, Tsukuba, Oct. (1981).
20) K. Sueki, Y. Nagame, M. Takahashi, H. Nakahara, and I. Kohno: "Heavy-Ion Reaction between ^{14}N and ^{62}Ni", 25th Symp. on Radiochemistry, Tsukuba, Oct. (1981).

3. Atomic and solid-state physics

1) T. Nomura: "Fast Light-Particle Emission and Its Polarization", Proc. of Joint Meeting on Atomic Collision and Heavy-Ion Nuclear Reactions, Wako, Feb. (1981).
2) Y. Awaya: "On the Multiple Inner-Shell Ionization", Proc. of Joint Meeting on Atomic Collisions and Heavy-Ion Nuclear Reactions, Wako, Mar. (1981).
3) E. Yagi, H. Bossy, K.P. Döring, M. Gladisch, D. Herlach, H. Matsui, H. Orth, G. zu Putlitz, A. Seeger, and J. Vetter: "Diffusion of Positive Muons in α-Iron", Ann. Meeting of the Phys. Soc. Japan, Hiroshima, Mar. (1981).
4) A. Yagishita and T. Nakamura: "Design of Auger-Electron Spectrometer", Ann. Meeting of the Phys. Soc. Japan, Hiroshima, Mar. (1981).
5) A. Hitachi, H. Kumagai, and Y. Awaya: "A X-ray Crystal Spectrometer by Adopting a Position Sensitive Proportional Counter", Symp. of Position-Sensitive Radiation Detectors and Their Applications, Wako, Mar. (1981).
6) A. Hitachi, H. Kumagai, T. Katou, and Y. Awaya: "A Broad Range X-ray Crystal Spectrometer", Ann. Meeting of the Phys. Soc. Japan, Hiroshima, Apr. (1981).
7) A. Yagishita, H. Suzuki, S. Ohtani, and H. Hanashiro: The Kr $M_{2,3}M_{45}N_{23}$ and Ar $L_1L_{23}M_{23}$ Coster-Kronig Processes Following Electron Impact Ionization", XII Intern. Conf. on the Physics of Electronic and Atomic Collisions, Gatlinburg, July (1981).
8) Y. Awaya, A. Hitachi, H. Kumagai, T. Tonuma, T. Kambara, M. Kase, and A. Yagishita: "A Broad Range Crystal Spectrometer and X-rays Following Multiple Inner-Shell Ionizations", XII Intern. Conf. on the Physics of Electronic and Atomic Collisions, Gatlinburg, July (1981).

9) M. Uda, K. Maeda, Y. Sasa, and A. Koyama: "Chemical Effect on X-ray Spectra Produced by 2.4 MeV He^{++}", XII Intern. Conf. on the Physics of Electronic and Atomic Collisions, Gatlinburg, July (1981).

10) N. Shiotani, H. Narumi, H. Arai, K. Wakatsuki, Y. Sasa, and T. Mizoguchi: "Crystallization Processes of Amorphous Mg-Zn Alloys", 4th Intern. Conf. on Rapidly Quenched Metals, Sendai, Aug. (1981).

11) N. Shiotani, S. Tanigawa, H. Iriyama, and T. Mizoguchi: "Crystallization of Amorphous $Mg_{70}Zn_{30}$ Studied by Positron Annihilation", Intern. Conf. on Amorphous System Investigated by Nuclear Methods, Balatonfüred, Sept. (1981).

12) A. Hitachi, H. Kumagai, Y. Awaya, M. Kase, T. Kambara, T. Tonuma, and A. Yagishita: "The Measurement of X-rays Following Inner-Shell Ionizations by using a Broad Range Crystal Spectrometer", Fall Meeting of the Phys. Soc. Japan, Niigata, Oct. (1981).

13) A. Yagishita, H. Suzuki, S. Ohtani, and H. Hanashiro: "Read Effects on Kr MMN Coster- Kronig Processes Following Electron Impact Ionization", Fall Meeting of the Phys. Soc. Japan, Niigata, Oct. (1981).

14) A. Yagishita: "Ionization Cross Sections of Kr 3p- and 3d-subshells by Electron Impact", Fall Meeting of the Phys. Soc. Japan, Niigata, Oct. (1981).

15) K. Maeda, Y. Sasa, K. Fuwa, and M. Uda: "Chemical Effect on O Kα Spectra Induced by He Ions", Ann. Meeting of the Phys. Soc. Japan, Niigata, Oct. (1981).

16) M. Uda, K. Maeda, Y. Sasa, and A. Koyama: "Chemical Effect on Multiply Ionized X-ray Spectra", Ann. Meeting of the Phys. Soc. Japan, Niigata, Oct. (1981).

17) K. Fuwa, K. Fujima, and M. Uda: "Intensity Analysis of F Kα Satellites for Fluorine Compounds", Ann. Meeting of the Phys. Soc. Japan, Niigata, Oct. (1981).

18) M. Iwaki, O. Yoshio, T. Matsuda, K. Takahashi, and K. Yoshida: "Ion Implantation through Aluminum Deposited Iron Plates", 42th Fall Meeting of the Japan Soc. Appl. Phys., Fukui, Oct. (1981).

19) S. Sato, M. Iwaki, H. Sakairi, and I. Akiyama: "Ion Implantation in Diamond (I)", 42th Fall Meeting of the Japan Soc. Appl. Phys., Fukui, Oct. (1981).

20) K. Hirose, N. Yokoyama, N. Imajo, I. Odomari, K. Fuwa, and M. Uda: "Electronic Structures of Pd_2Si and PtSi Observed with ESCA", 42th Fall Meeting of the Japan Soc. Appl. Phys., Fukui, Oct. (1981).

21) T. Takahashi, Y. Awaya, T. Tonuma, H. Kumagai, K. Izumo, A. Hitachi, and A. Hashizume: "Energy Straggling of 5 – 7 MeV/amu C and He Ions", 42th Fall Meeting of the Japan Soc. Appl. Phys., Fukui, Oct. (1981).

22) Y. Awaya: "X-ray Spectroscopy and Ion-Induced X-rays", Symp. of Atomic Spectroscopy and Atomic Structure, Wako, Oct. (1981).

23) T. Takahashi: "Straggling of Heavy Ions", Symp. of Ion Beam Analysis, Wako, Oct. (1981).

24) N. Yamamoto, H. Shiraishi, H. Yoshida, H. Kamitsubo, I. Kohno, and T. Shikata: "Creep Properties in Helium Injected SUS 316 and γ'' Precipitation Strengthened Alloy ", 1981 Autumn Meeting of the Japan Institute of Metals, Kyoto, Nov. (1981).

25) H. Sakairi, E. Yagi, A. Koyama, and R.R. Hasiguti: "The Damage Function Based on

the Focusing Collision Model", Intern. Conf. (Yamada Conf. V) on Point Defects and Defect Interactions in Metals, Kyoto, Nov. (1981).

26) Y. Awaya: "Studies of Atomic Physics by Using Accelerators of Riken", Symp. of Studies by Using Accelerators, Wako, Dec. (1981).

4. Radiochemistry, radiation chemistry and radiation biology

1) S. Ambe and F. Ambe: "Mössbauer Emission Study of Defect ^{119}Sn Atoms in α-Irradiated SnSe", 43th National Meeting of the Chem. Soc. Japan, Tokyo, Apr. (1981).
2) T. Nozaki: "Charged Particle Activation Analysis", Japan-Taiwan Cojoint Meeting on the Use of Small Accelerators, Taipei, May (1981).
3) T. Nozaki: "Chemical Separation of ^{18}F as KBF_4 in Oxygen Analysis by the $^{16}O(^3He, p)^{18}F$ Reaction", Intern. Symp. Modern Trends in Activation Analysis, Toronto, June (1981).
4) Y. Itoh and T. Nozaki: "Depth Profiling of Oxygen by Activation with the $^{16}O(^3He, p)^{18}F$ Reaction", Intern. Symp. Modern Trends in Activation Analysis, Toronto, June (1981).
5) H. Emori, M. Umehara, M. Takeya, K. Nomura, Y. Terai, and T. Nozaki: "Determination of Oxygen in by ^{3}He Activation Analysis", 1981 Intern. Symp. on Gallium Arsenide and Related Compounds, Oiso, Sept. (1981).
6) S. Ambe, F. Ambe, and T. Okada: "Adsorption Kinetics of Carrier-free ^{119}Sb(V) onto α-Fe_2O_3", 25th Symp. on Radiochem., Tsukuba, Oct. (1981).
7) T. Masui, S. Muraoka, and T. Nozaki: "Determination of IR Absorption Coefficient of Nitrogen in Silicon by Charged Particle Activation", 25th Symp. on Radiochem., Tsukuba, Oct. (1981).
8) Y. Itoh and T. Nozaki: "Heat Treatment Behavior of Oxygen in Silicon as Measured by Charged Particle Activation Analysis", 160th Fall Meeting of the Electrochem. Soc., Denver, Oct. (1981).

Ⅶ. LIST OF OUTSIDE USERS AND THEIR THEMES

(Jan. – Dec. 1981)

1)	M. Watanabe and T. Usami "Radiochemical Analysis of B and ^{14}N in Si Crystal"	Toshiba R & D Center
2)	T. Abe "Radiochemical Analysis of C and ^{16}O in Si Crystal"	Shinetsu Semiconductor Co., Ltd.
3)	H. Emori "Radiochemical Analysis of ^{16}O in GaAs"	Mitsubishi Metal Co., Ltd.
4)	H. Nakahara and M. Takahashi "Production of ^{59}Co"	Faculty of Science, Tokyo Metropolitan Univ.
5)	K. Yuita "Production of ^{77}Br"	National Inst. of Agricultural Sciences
6)	Y. Homma "Production of ^{87m}Y"	Kyoritsu College of Pharmacy
7)	Y. Higashiguchi "Development of Ferritic Stainless Steel for Reactor"	Research Inst. for Iron, Steel and Other Metals, Tohoku Univ.
8)	K. Fukai and T. Furuta "Helium Implantation Effect on Creep Repture Properties of Modified 316 Stainless Steel for Reactor Material	Japan Atomic Energy Research Inst.
9)	T. Matsutani "Study of Effect by Bombarding High Energy Proton on a Solar Cell"	Electronic Parts Div., Sharp Co., Ltd.

10) S. Yoshida
"Study of Effect by Bombarding High Energy Proton on a Solar Cell"
LSI Research and Development Lab., Mitsubishi Electric Co., Ltd.

11) T. Fukushima
"Study of Effect by Bombarding High Energy Proton on I.C. and Transistor"
Kamakura Factory, Mitsubishi Electric Co., Ltd.

12) M. Hiranuma
"Photograph of Cyclotron Beam"
Nomura Research Inst.

VIII. LIST OF SEMINARS

(Jan. – Dec. 1981)

1) S. Yoshida, Tohoku Univ. (Sendai), 13 January
"Nuclear Reactions to Continuum Final States"

2) H. Ikegami, RCNP (Osaka), 24 January
"High Resolution Momentum – Mass Analyzer"

3) K. Shima, Tsukuba Univ. (Tsukuba), 17 February
"Charge Changing of Energetic Heavy Ions"

4) N. Onishi, Univ. of Tokyo (Tokyo), 24 February
"Wobbling Mode in High Spin States"

5) J. Grosset, Saclay (France), 3 March
"Time-Projection Counter for H.I. Reactions"

6) A. Policarpo, Univ. of Coimbra (Portugal), 9 March
"Photo-Ionization and Proportional Scintillation in Nuclear Radiation Detection"

7) T. Doke and T. Hayashi, Waseda Univ. (Tokyo), 9 March
"Isotope Identification by CR-39 Plastic Track Detectors"

8) I. Suzuki, Agency of Industrial Science and Technology (Tsukuba), 10 March
"Spectroscopy of (e, 2e) in Atomic and Molecular Physics"

9) F. Kikuchi, Univ. of Tokyo (Tokyo), 13 March
"On the Problems of the Finite Element Method"

10) K. Otsuka, JAERI (Tokai), 24 March
"Particle Emissions from the Preequilibrium States in the Heavy Ion Reactions and Recent Topics on the Application of IBM to Rotational Nuclei"

11) N. Takahashi, Texas A & M Univ. (USA), 8 April
"Massive Transfer Reactions on Light Targets on Their Relation to Molecular Resonances"

12) T. Watanabe, Univ. of Tokyo (Tokyo), 21 April
"Theory of Ion-Atom Collision"

13) R.D. Levine, The Hebrew Univ. Jerusalem (Israel), 28 April
"Surprisal Analysis: A Constrained Phase – Space Approach to Heavy Ion Collisions"

14) K. Sato, INS (Tokyo), 13 May
"RF System (MOPA) of the INS SF-Cyclotron"

15) H. Ohnuma, Tokyo Institute of Technology (Tokyo), 10 June
"Excitations to GT-States by (p, n) Reactions"

16) F. Soga, INS (Tokyo), 17 June
"Near-Threshold Pion Production from Nuclei by Proton Bombardment"

17) D.A. Swenson, LASL (USA), 24 June
"RFQ Linacs for Light- and Heavy- Ion Acceleration"

18) N. Takigawa, Tohoku Univ. (Sendai), 27 July
"Charge Equilibration in Deep Inelastic Heavy Ion Collision"

19) S. Honma, INS (Tokyo), 26 August
"Deuteron Emission from Reactions Induced by High Energy γ-Rays"

20) S. Ohtani, Nagoya Univ. (Nagoya), 8 September
"EBIS Ion Source and Atomic Collision Experiment using the Ion Source at Institute of Plasma Physics"

21) H. Hamagaki, INS (Tokyo), 9 September
"Present Status of the Experiment using HISS"

22) T. Fujita, Nihon Univ. (Tokyo), 13 October
"Projectile Fragmentation in High Energy Nucleus – Nucleus Collision"

23) D. Diamond, LBL (USA), 23 October
"Spectroscopy on High-Spin States with Continuum and Discrete γ-Rays"

24) I. Hamamoto, Nordita (Denmark), 26 October
"Rotation Properties of High-Spin States in Deformed Nuclei"

25) A. Iwamoto, JAERI (Tokai), 20 November
"Energy Spectra of α-Particles Emitted in the Preequilibrium Process"

26) I. Tanihara, INS (Tokyo), 25 November
"Two-Particle Correlations in High Energy Heavy Ion Collisions"

27) S. Ban, KEK (Tsukuba), 3 December
"On the Neutron Shielding"

IX. LIST OF PERSONNEL

Members of the Board

HAMADA Tatsuji 浜田達二
IMAMURA Masashi 今村昌
KOHNO Isao 河野功
NOZAKI Tadashi 野崎正 (Chairman)
SAKAIRI Hideo 坂入英雄
SHIMA Makoto 島誠
HASHIZUME Akira 橋爪朗
KAMITSUBO Hiromichi 上坪宏道
MORI Kazuo 森一夫
ODERA Masatoshi 小寺正俊
SEKIZAWA Hisashi 関沢尚
UDA Masayuki 宇田応之

Cyclotron Operation and Maintenance Group

FUJITA Shin 藤田新
KAGEYAMA Tadashi 影山正
KOHNO Isao 河野功
TAKEBE Hideki 武部英樹
IKEGAMI Kumio 池上九三男
KOHARA Shigeo 小原重夫
OGIWARA Kiyoshi 荻原清

Linac Operation and Maintenance Group

CHIBA Yoshiaki 千葉好昭
HEMMI Masatake 逸見政武
INOUE Toshihiko 井上敏彦
KASE Masayuki 加瀬昌之
MIYAZAWA Yoshitoshi 宮沢佳敏
YANOKURA Minoru 矢野倉実
GONO Yasuyuki 郷農靖之
IKEZAWA Eiji 池沢英二
KAMBARA Tadashi 神原正
KUBO Toshiyuki 久保敏幸
TONUMA Tadao 戸沼正雄

Scientific and Engineering Personnel

Cyclotron Laboratory

FUJISAWA Takashi 藤沢高志
GOTO Akira 後藤彰
ICHIMURA Atsushi 市村淳
INAMURA Takashi 稲村卓
KAMITSUBO Hiromichi 上坪宏道
KISHIDA Norio 岸田則生
KOHNO Isao 河野功
NAKAJIMA Shunji 中島諄二
NOMURA Toru 野村亨
SHIKATA Takashi 四方隆史
YAMAJI Shuhei 山路修平
FUJITA Jiro 藤田二郎
HARA Masahiro 原雅弘
IKEGAMI Yuji 池上祐司
ISHIHARA Masayasu 石原正泰
KARASAWA Takashi 唐沢孝
KOHMOTO Susumu 河本進
MOTONAGA Shoshichi 元永昭七
NAKANISHI Noriyoshi 中西紀喜
SAITO Haruko 斉藤晴子
WADA Takeshi 和田雄
YANO Yasushige 矢野安重

(Visitors)

HAYAKAWA Shunichiro 早川俊一郎 (Dept. Phys., Waseda Univ.)
HIRUTA Kotaro 蛭田幸太郎 (Dept. Phys., Tokyo Gakugei Univ.)
ICHIMURA Munetake 市村宗武 (Inst. Phys., College General Education, Univ. of Tokyo)

NAKAHARA Hiromichi 中原弘道 (Dept. Chem., Tokyo Metropolitan Univ.)
SATO Kenichi 佐藤憲一 (Dept. Phys., Tohoku College of Pharmacy)
SHIRAISHI Haruki 白石春樹 (Nat. Res. Inst. for Metals)
TAKEMASA Tadashi 武政尹士 (Dept. Phys., Saga Univ.)
TAKIGAWA Noboru 滝川昇 (Dept. Phys., Tohoku Univ.)
YOSHIDA Shiro 吉田思郎 (Dept. Phys., Tohoku Univ.)
UTSUNOMIYA Hiroaki 宇都宮弘章 (Inst. Nucl. Phys., Univ. of Tokyo)

(Students)

BAN Mitsuo 伴光男 (Facul. Sci. and Eng., Chuo Univ.)
HOSOYAMA Michio 細山三千男 (Facul. Sci. and Eng., Chuo Univ.)
IEKI Kazuo 家城和夫 (Dept. Phys., Kyoto Univ.)
MASHIYAMA Tsuguo 増山次男 (College of Hum. and Sci., Nihon Univ.)
NAGAME Yuichiro 永目諭一郎 (Dept. Chem., Tokyo Metropolitan Univ.)
OBANA Yoshiki 小花芳樹 (Dept. Phys., Chiba Univ.)
SUGITATE Toru 杉立徹 (Dept. Phys., Tokyo Inst. Technol.)
TANAKA Yasushi 田中保志 (Facul. Sci. and Eng., Chuo Univ.)
TOYAMA Akifumi 外山昭文 (College of Hum. and Sci., Nihon Univ.)
WATANABE Mitsuyuki 渡辺光幸 (College of Hum. and Sci., Nihon Univ.)

Linac Laboratory

CHIBA Yoshiaki 千葉好明
GONO Yasuyuki 郷農靖之
HOSHINO Kiichi 星野紀一
KAMBARA Tadashi 神原正
KUBO Toshiyuki 久保敏幸
ODERA Masatoshi 小寺正俊
TONUMA Tadao 戸沼正雄
YANOKURA Minoru 矢野倉実
CHIBA Toshiya 千葉利哉
HEMMI Masatake 逸見政武
INOUE Toshihiko 井上敏彦
KASE Masayuki 加瀬昌之
MIYAZAWA Yoshitoshi 宮沢佳敏
SASAGASE Masaji 笹ヶ瀬正二
YAGISHITA Akira 柳下明

(Visitors)

DOKE Tadayoshi 道家忠義 (Sci. and Eng. Res. Lab., Waseda Univ.)
EJIRI Hiroyasu 江尻宏泰 (Dept. Phys., Osaka Univ.)
FUKUZAWA Fumio 福沢文雄 (Dept. Nucl. Eng., Kyoto Univ.)
HARADA Kichinosuke 原田吉之助 (Japan Atomic Energy Res. Inst.)
HAYASHIBE Shogo 林部昭吾 (Dept. Phys., Tohoku Univ.)
HISATAKE Kazuo 久武和夫 (Tokyo Inst. Technol.)
ISHII Keishi 石井慶之 (Dept. Nucl. Eng., Kyoto Univ.)
ITO Noriaki 伊藤慶昭 (Dept. Crystalline Materials, Nagoya Univ.)
KAWAI Nanao 河合七雄 (Osaka Univ.)
MASUDA Kozo 升田公三 (Tsukuba Univ.)
MATSUI Masao 松井正夫 (Nagaoka Sci. and Tech. Univ.)
MORITA Susumu 森田右 (College of Eng., Hosei Univ.)
OHNO Shinichi 大野新一 (Japan Atomic Energy Res. Inst.)
OZAWA Kunio 小沢国夫 (Japan Atomic Energy Res. Inst.)
SAKISAKA Masakatsu 向坂正勝 (Dept. Nucl. Eng., Kyoto Univ.)
TAKEDA Shigeru 竹田繁 (Nat. Lab. High Energy Phys.)

TAWARA Hiroyuki 俵　博之 (Dept. Nucl. Eng., Kyushu Univ.)
TSURUBUCHI Seiji 鶴淵誠二 (Dept. Eng., Tokyo Univ. Agric. Tech.)
YOSHIZAWA Yasukazu 吉沢康和 (Dept. Phys., Hiroshima Univ.)

Radiation Laboratory

AWAYA Yohko 粟屋容子
HAMADA Tatsuji 浜田達二
HASHIZUME Akira 橋爪朗
HITACHI Akira 日出章
IZUMO Koichi 出雲光一
KATOU Takeo 加藤武雄
KONNO Satoshi 金野智
KUMAGAI Hidekazu 熊谷秀和
OKANO Masaharu 岡野真治
TAKAHASHI Tan 高橋旦
TENDOW Yoshihiko 天道芳彦

(Visitors)

DOKE Tadayoshi 道家忠義 (Sci. and Eng. Res. Lab., Waseda Univ.)
FUJIOKA Manabu 藤岡学 (Dept. Phys., Tohoku Univ.)
HAYASHIBE Shogo 林部昭吾 (Dept. Phys., Tohoku Univ.)
ISHII Keizo 石井慶造 (Cyclotron, Tohoku Univ.)
MIURA Taichi 三浦太一 (Dept. Chem., Tokyo Metropolitan Univ.)
MURAMATSU Hisakazu 村松久和 (Dept. Chem., Tokyo Metropolitan Univ.)
MORITA Susumu 森田将 (College of Eng., Hosei Univ.)
NAGAHARA Teruaki 永原照明 (Inst. Atomic Energy, Rikkyo Univ.)
TAWARA Hiroyuki 俵　博之 (Dept. Nucl. Eng., Kyushu Univ.)
WATANABE Tsutomu 渡辺力 (Dept. Eng., Univ. of Tokyo)

Thermonuclear Fusion Laboratory

ANDO Kozo 安藤剛三
MORI Kazuo 森一夫

Metal Physics Laboratory

KOYAMA Akio 小山昭雄
SHIOTANI Nobuhiro 塩谷亘弘
YAGI Eiichi 八木栄一

Magnetic Materials Laboratory

ASAI Kichizo 浅井吉蔵
OKADA Takuya 岡田卓也
SAKAI Nobuhiko 坂井信彦
SEKIZAWA Hisashi 関沢尚

Solid-State Chemistry Laboratory

ENDO Hiroshi 遠藤寛
KOBAYASHI Masayoshi 小林雅義
MAEDA Kuniko 前田邦子
SASA Yoshihiko 佐々嘉彦
UDA Masayuki 宇田応之

(Visitor)

ODOMARI Iwao 大泊巌

(Students)

FUWA Koh 不 破 耕 (School of Sci. Eng., Waseda Univ.)
HIROSE Kazuyuki 広 瀬 和 之 (School of Sci. Eng., Waseda Univ.)
IMAJO Nobuhiko 今 城 信 彦 (School of Sci. Eng., Waseda Univ.)
YOKOYAMA Natsuki 横 山 夏 樹 (School of Sci. Eng., Waseda Univ.)

Radiochemistry Laboratory

AMBE Fumitoshi 安 部 文 敏
AMBE Shizuko 安 部 静 子
ARATANI Michi 荒 谷 美 智
ITO Yoshiko 伊 東 芳 子
IWAMOTO Masako 岩 本 正 子
NOZAKI Tadashi 野 崎 正
TERAI Yoshiro 寺 井 善 郎

(Visitors)

SUGITA Yoshimitsu 杉 田 吉 充 (Dept. Phys., Toyama Univ.)
TAKI Ko 滝 幸 (Dept. Hygen., Kitazato Univ.)
USAMI Katsuhisa 宇佐美 勝 久 (Hitachi Res. Lab., Hitachi Ltd.)

Radiation Chemistry Laboratory

IMAMURA Masashi 今 村 昌
KIMURA Kazuie 木 村 一 宇

Radiobiology Laboratory

HATTORI Yukihiko 服 部 行 彦
KANEKO Ichiro 金 子 一 郎
KITAYAMA Shigeru 北 山 滋
NAKANO Kazushiro 中 野 和 城
NISHIMURA Tetsuji 西 村 哲 治
YATAGAI Fumio 谷田貝 文 夫

(Visitor)

OHNO Tadao 大 野 忠 夫 (National Inst. Radiological Sciences)

(Students)

EGUCHI Kiyomi 江 口 清 美 (Dept. Medicine, Tsukuba Univ.)
INADA Tetsuo 稲 田 哲 雄 (Dept. Medicine, Tsukuba Univ.)

Safety Control Affairs Office

IGARASHI Kazui 五十嵐 一 戊
KOYAMA Masashi 小 山 政 史
MIYAGAWA Makoto 宮 川 真 言
SAKAMOTO Ichiro 坂 本 一 郎
USUBA Isao 薄 葉 勲

Beam Analysis Center

IWAKI Masaya 岩 木 正 哉
SAKAIRI Hideo 坂 入 英 雄

AUTHOR INDEX

RIKEN Accelerator Progress Report

理化学研究所加速器年次報告　第15巻（1981）

印　刷　昭和57年（1982）3月25日
発　行　昭和57年（1982）3月31日
発行者　理化学研究所
代表者　宮　島　龍　興
〒351　埼玉県和光市広沢2番1号
電話（0484）62－1111
編集者　理化学研究所加速器運営委員会
印刷所　丸星印刷株式会社
〒130 東京都墨田区亀沢1丁目3番3号

定価 4,000円

理化学研究所

埼玉県　和光市　広沢